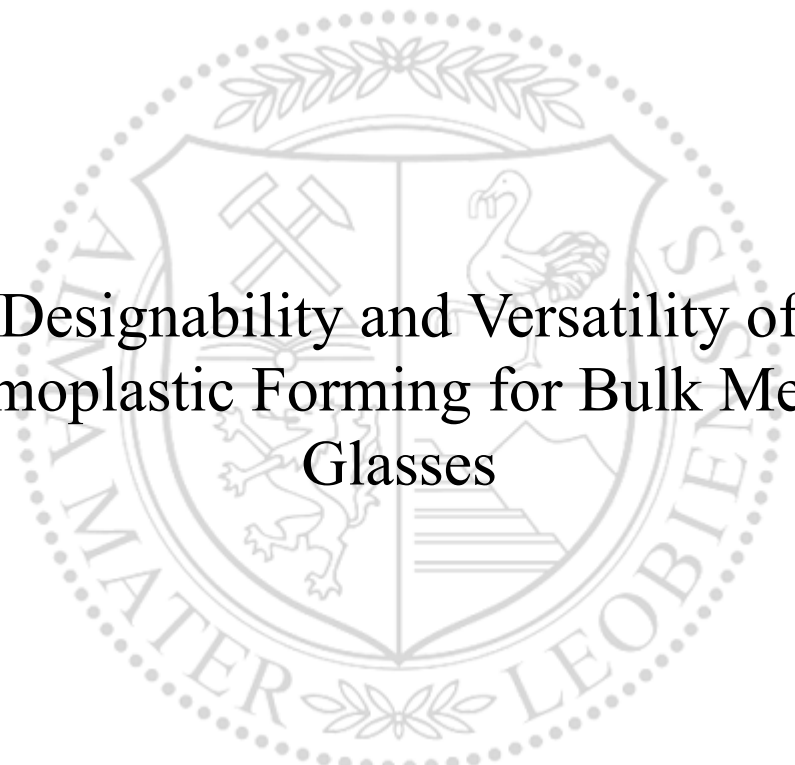




Chair of Materials Physics

Doctoral Thesis



Designability and Versatility of
Thermoplastic Forming for Bulk Metallic
Glasses

Fei-Fan Cai, M.Sc. (hons)

July 2024



AFFIDAVIT

I declare on oath that I wrote this thesis independently, did not use any sources and aids other than those specified, have fully and truthfully reported the use of generative methods and models of artificial intelligence, and did not otherwise use any other unauthorized aids.

I declare that I have read, understood and complied with the "Good Scientific Practice" of the Montanuniversität Leoben.

Furthermore, I declare that the electronic and printed versions of the submitted thesis are identical in form and content.

Date 15.07.2024

Fei-Fan Cai

Signature Author
Fei-Fan Cai

This work has received funding from the European Union's Horizon 2020 research and innovation programme under the Marie Skłodowska-Curie grant agreement No. 861046 (BIOREMIA).

Copyright © 2024 by Fei-Fan Cai. All rights reserved.

Montanuniversität Leoben

Department of Materials Science, Chair of Materials Physics

Jahnstraße 12

8700 Leoben

Austria

Acknowledgements

”Teamwork is the ability to work together toward a common vision. The ability to direct individual accomplishments toward organizational objectives. It is the fuel that allows common people to attain uncommon results.” – Andrew Carnegie.

Science is a collaborative process more than ever in the modern era, especially when it comes to interdisciplinary topics. Therefore, I want to take this opportunity to thank collaborators and colleagues, as well as family and friends, who have contributed in some way to the creation of this work. These acknowledgments are not necessarily complete in case I might have forgotten someone by accident.

First and foremost, I want to express my sincere gratitude to my supervisors, **Prof. Jürgen Eckert** and **Dr. Florian Spieckermann**, at *Chair of Materials Physics, Montanuniversität Leoben*. Their kind guidance, continuous support, and encouragement are key elements that motivate my Ph.D. career and research. And special thanks to my mentor, **Prof. Christian Teichert**, for his insights, immense knowledge, and willingness to assist. I could not have imagined having better supervisors and mentor in my Ph.D. I always knew that they believed in me and wanted the best for me.

I would like to extend my thanks to **BIOREMIA-ETN**, supported by the European Union’s Horizon 2020 research and innovation program under the Marie Skłodowska-Curie grant agreement No. 861046. I deeply appreciate **BIOREMIA-ETN** for providing such a fantastic training network and an interesting research project. It’s my pleasure to meet and work with all ESRs and PIs. Special thanks to all collaborators host and support my secondments:

- **Dr. Udo Greiser, Dr. Patrick Duffy, and David Z. Pérez** at *Ashland Specialties Ireland Ltd.*
- **Prof. Tadhg Ó’Cróinín** at *University College Dublin.*
- **Prof. Jan Schroers, Dr. Sungwoo Sohn, Naijia Liu, and Arindam Raj** at *Yale University.*
- **Prof. Carme Nogués and Dr. Andreu Blanquer** at *Universitat Autònoma de Barcelona.*

It is worth noting that many experiments in this thesis were accomplished with the support of collaborators. Without their effort, it’s impossible to complete such an interdisciplinary topic. The following list aims to endorse their contributions.

Material characterizations:

- High-resolution transmission electron microscopy (HRTEM) and selected area electron diffraction (SAED): **Dr. Zhuo Chen** and **Prof. Zaoli Zhang** at *Erich Schmid Institute of Materials Science, Austrian Academy of Sciences, Austria.*

- Scanning electron microscopy (SEM): **Lukas Schweiger** at *Department of Materials Science, Chair of Materials Physics, Montanuniversität Leoben, Austria.*
- Linear sweep voltammetry (LSV), electrochemical impedance spectroscopy (EIS), and cyclic voltammetry (CV): **Selin Gümrückü** and **Dr. Baran Sarac** at *Erich Schmid Institute of Materials Science, Austrian Academy of Sciences, Austria.*
- Contact angle measurement: **Prof. Christian Teichert** at *Department Physics Mechanics and Electrical Engineering, Chair of Physics, Montanuniversität Leoben, Austria.*
- Resonant ultrasound spectroscopy (RUS): **Miguel B. Costa** and **Prof. A. Lindsay Greer** at *Department of Materials Science & Metallurgy, University of Cambridge, UK.*
- X-ray photoelectron spectroscopy (XPS): **Adnan Akman**, **Dr. Martin Hantusch**, and **Dr. Annett Gebert** at *Leibniz Institute for Solid State and Materials Research, Germany.*

In vitro studies:

- Alamar blue assay, live/dead staining, DAPI/phalloidin staining, and SEM imaging (Saos-2 cells): **Dr. Andreu Blanquer** and **Prof. Carme Nogués** at *Departament de Biologia Cel·lular, Fisiologia i Immunologia, Universitat Autònoma de Barcelona.*
- Crystal Violet assay (S. Aureus): **David Z. Pérez** and **Prof. Tadhg Ó'Cróinín** at *School of Biomolecular and Biomedical Science, University College Dublin.*
- AFM imaging (S. Aureus): **Prof. Brian Rodriguez** at *School of Physics, University College Dublin.*
- Live/dead staining (S. Aureus): **Adam Turner** and **Prof. Margarita Trobos** at *Department of Biomaterials, University of Gothenburg.*

Finally, I want to appreciate my colleagues at *Erich Schmid Institute of Materials Science of the Austrian Academy of Sciences (ESI)*, especially **Dr. Baran Sarac** and **Dr. Parthiban Ramasamy**, for their practical insights into thermoplastic forming (TPF) and casting of bulk metallic glasses (BMGs). Further thanks to all technicians at ESI for their immense support and trustworthy advice. I would like to thank my family and friends for their accompaniment and for having my back.

Abstract

Bulk metallic glasses (BMGs) are a novel class of metallic alloys possessing amorphous structures that set them apart from traditional crystalline alloys. The amorphous structure of BMGs lacks crystalline defects, such as grain boundaries, twins, and dislocations, resulting in their desirable properties, including high elasticity, hardness, toughness, good wear resistance, and good corrosion resistance. However, the requirement of BMGs in rapid cooling restricts the fabrication of complex shapes through casting, limiting their practical applications. Luckily, BMGs can be shaped and patterned through thermoplastic forming (TPF) by viscous flow deformation when heated to the supercool liquid region (SCLR). Therefore, the present thesis aims to enhance the practicality and functionality of BMGs through TPF approaches.

The first focus targets “designability”. It was believed that “*BMGs can not be deformed and patterned once the materials are crystallized.*” The concerns about the crystallization during TPF are the loss of deformability and mechanical properties of BMGs. This work uses $\text{Ti}_{40}\text{Zr}_{10}\text{Cu}_{34}\text{Pd}_{14}\text{Sn}_2$ BMG to demonstrate that “*if the initial crystallization event is the formation of nanocrystals, the BMGs can still be shaped and patterned via TPF, even with the nanocrystallization.*” A TPF strategy of allowing nanocrystallization during the process is implemented to create surface patterns from macro- to nano-scales and hierarchical structures integrating micro- and nano-patterns on the same surface. Moreover, the study suggests that $\text{Ti}_{40}\text{Zr}_{10}\text{Cu}_{34}\text{Pd}_{14}\text{Sn}_2$ BMG possesses crystallization tolerance to TPF, and slight crystallization is allowed before losing its mechanical properties.

The second focus demonstrates the “versatility” for biomedical applications. In-vitro assays using Saos-2 cell lines were tested on four different surface topographies of $\text{Ti}_{40}\text{Zr}_{10}\text{Cu}_{34}\text{Pd}_{14}\text{Sn}_2$ BMG, including: (a) Flat (mirror-polished), (b) Micro-pattern (2.5 μm square protuberances), (c) Nano-pattern (400 nm protrusions), (d) Hierarchical-pattern (400 nm protrusions on 2.5 μm square protuberances). Based on the findings of in-vitro studies, two potential biomedical applications of TPF patterned $\text{Ti}_{40}\text{Zr}_{10}\text{Cu}_{34}\text{Pd}_{14}\text{Sn}_2$ BMG are then suggested: (i) Dental or orthopedic tissue implants and (ii) a toolbox for studying cell response on rigid and ordered surfaces.

The final focus combines the “designability” and “versatility” for catalytic applications. The hydrogen evolution reaction (HER) performance of $\text{Pt}_{57.5}\text{Cu}_{14.7}\text{Ni}_{5.3}\text{P}_{22.5}$ BMG with flat, micro-patterned, and nano-patterned surfaces is explored. The nano-patterned Pt-BMG exhibits long-term stability and self-improving behavior after 1000 linear sweep voltammetry (LSV) cycles. Surface characterizations indicate that a layer of Cu_xO foam was formed on top of the nano-patterned surface after 1000 LSV cycles. The formation of Cu_xO foam is explained by a three-step process involving Cu dissolution of Pt-BMG and dynamic hydrogen bubble templating (DHBT) electrodeposition without using copper salt.

The present thesis reveals the prospect of utilizing the TPF process for a wide range of mediocre glass forming systems and semi-crystalline composites into surface-enhanced functional materials without sacrificing mechanical properties. Beyond implant applications, biocompatible BMGs provide a toolbox for studying cell response on rigid and ordered surfaces in biomedical research. TPF-patterned BMGs combining dynamic bubble templating electrodeposition could be a feasible strategy to synthesize metal or metal-oxide foams for catalytic applications.

Kurzfassung

Massive Metallische Gläser (Bulk Metallic Glass, 'BMG') sind eine neue Klasse metallischer Legierungen, die sich durch ihre amorphe Struktur von herkömmlichen kristallinen Legierungen unterscheiden. Die amorphe Struktur von BMGs weist keine kristallinen Defekte wie Korngrenzen, Zwillinge und Versetzungen auf, was zu ihren wünschenswerten Eigenschaften führt, darunter hohe Elastizität, Härte, Zähigkeit, gute Verschleißfestigkeit und gute Korrosionsbeständigkeit. Da BMG jedoch schnell abgekühlt werden muss, ist die Herstellung komplexer Formen durch Gießen nur begrenzt möglich, was ihre praktischen Anwendungen einschränkt. Glücklicherweise können BMGs durch thermoplastische Umformung (TPF) durch viskose Fließverformung geformt und modelliert werden, wenn sie auf den Bereich der unterkühlten Flüssigkeit (SCLR) erhitzt werden. Daher zielt die vorliegende Arbeit darauf ab, die praktische Anwendbarkeit und Funktionalität von BMGs durch TPF-Ansätze zu verbessern.

Der erste Schwerpunkt liegt auf der „Designfähigkeit“. Es wurde angenommen, dass *“BMGs nicht verformt und strukturiert werden können, sobald die Materialien kristallisiert sind.”* Die Bedenken bezüglich der Kristallisation während der TPF sind der Verlust der Verformbarkeit und der mechanischen Eigenschaften von BMGs. In dieser Arbeit wird $\text{Ti}_{40}\text{Zr}_{10}\text{Cu}_{34}\text{Pd}_{14}\text{Sn}_2$ BMG verwendet, um zu zeigen, dass *“wenn das anfängliche Kristallisationsereignis die Bildung von Nanokristallen ist, die BMGs immer noch mittels TPF geformt und strukturiert werden können, sogar mit der Nanokristallisation.”* Eine TPF-Strategie, die eine Nanokristallisation während des Prozesses ermöglicht, wird eingesetzt, um Oberflächenmuster von der Makro- bis zur Nanoskala und hierarchische Strukturen zu erzeugen, die Mikro- und Nanomuster auf derselben Oberfläche integrieren. Darüber hinaus legt die Studie nahe, dass $\text{Ti}_{40}\text{Zr}_{10}\text{Cu}_{34}\text{Pd}_{14}\text{Sn}_2$ BMG eine Kristallisationstoleranz gegenüber TPF besitzen und eine leichte Kristallisation möglich ist, bevor sie ihre mechanischen Eigenschaften verlieren.

Der zweite Schwerpunkt demonstriert die „Vielseitigkeit“ für biomedizinische Anwendungen. In-vitro-Assays mit Saos-2-Zelllinien wurden an vier verschiedenen Oberflächentopografien von $\text{Ti}_{40}\text{Zr}_{10}\text{Cu}_{34}\text{Pd}_{14}\text{Sn}_2$ BMG getestet, darunter: (a) flach (spiegelpoliert), (b) Mikromuster (2,5 μm große quadratische Erhebungen), (c) Nanomuster (400 nm große Erhebungen), (d) hierarchisches Muster (400 nm große Erhebungen auf 2,5 μm großen quadratischen Erhebungen). Auf der Grundlage der Ergebnisse von In-vitro-Studien werden zwei potenzielle biomedizinische Anwendungen von TPF-gemustertem $\text{Ti}_{40}\text{Zr}_{10}\text{Cu}_{34}\text{Pd}_{14}\text{Sn}_2$ BMG vorgeschlagen: (i) Implantate für zahnmedizinisches oder orthopädisches Gewebe und (ii) ein Instrumentarium zur Untersuchung der Zellreaktion auf starren und geordneten Oberflächen.

Der letzte Schwerpunkt ist die Kombination von „Designfähigkeit“ und „Vielseitigkeit“ für katalytische Anwendungen. Die Leistung der Wasserstoffentwicklungsreaktion (HER) von $\text{Pt}_{57.5}\text{Cu}_{14.7}\text{Ni}_{5.3}\text{P}_{22.5}$ BMG mit flachen, mikrostrukturierten und nanostrukturierten Oberflächen wird erforscht. Das nano-strukturierte Pt-BMG zeigt Langzeitstabilität und selbstverbesserndes Verhalten nach 1000 LSV-Zyklen (Linear Sweep Voltammetry). Oberflächencharakterisierungen zeigen, dass sich nach 1000 LSV-Zyklen eine Schicht aus Cu_xO -Schaum auf der nanostrukturierten Oberfläche gebildet hat. Die Bildung des Cu_xO -Schaums wird durch einen dreistufigen Prozess erklärt, der die Cu-Auflösung von Pt-BMG und die dynamische Wasserstoffblasen-Templating (DHBT)-Elektroabscheidung ohne Verwendung von Kupfersalz umfasst.

Die vorliegende Arbeit zeigt die Möglichkeit auf, das TPF-Verfahren für eine breite Palette mittelmäßiger glasbildender Systeme und teilkristalliner Verbundwerkstoffe in oberflächenverbesserte Funktionswerkstoffe zu verwandeln, ohne dass die mechanischen Eigenschaften darunter leiden. Über Implantatanwendungen hinaus bieten biokompatible BMGs einen Werkzeugkasten für die Untersuchung von Zellreaktionen auf starren und geordneten Oberflächen in der biomedizinischen Forschung. TPF-gemusterte BMGs mit einer Kombination aus dynamischer Blasenschablonierung und Elektroabscheidung könnten eine praktikable Strategie zur Synthese von Metall- oder Metalloxidschäumen für katalytische Anwendungen sein.

List of Abbreviations and Symbols

AFM	Atomic force microscopy
AMP	Antimicrobial peptide
BMG	Bulk metallic glass
CHT	Continuous heat transformation
CLSM	Confocal laser scanning microscopy
CV	Cyclic voltammetry
DMA	Dynamic mechanical analysis
DSC	Differential scanning calorimetry
EIS	Electrochemical impedance spectroscopy
FBR	Foreign body reaction
GFA	Glass-forming ability
HCP	Hexagonal close packed
HER	Hydrogen evolution reaction
HRTEM	High-resolution transmission electron microscopy
IAI	Implant-associated infection
LSV	Linear sweep voltammetry
OCP	Open circuit potential
OER	Oxygen evolution reaction
OM	Optical microscopy
RUS	Resonant ultrasound spectroscopy
SAED	Selected area (electron) diffraction
SCL	Supercooled liquid
SCLR	Supercooled liquid region
SEM	Scanning electron microscope
TPF	Thermoplastic forming
TPN	Thermoplastic net-shaping
TTT	Time-temperature-transformation
T_g	Glass transition temperature

T _x	Crystallization temperature
WCA	Water contact angle
XPS	X-ray photoelectron spectroscopy
XRD	X-ray diffraction

Contents

Acknowledgements	II
Abstract	IV
Kurzfassung	VI
List of Abbreviations and Symbols	VIII
1 Introduction and Aims	1
2 State of the Art	2
2.1 Bulk Metallic Glasses	2
2.1.1 Structural Characteristics of Amorphous Metals.....	2
2.1.2 From Metallic Glasses to Bulk Metallic Glasses.....	3
2.1.3 Properties and Applications of Bulk Metallic Glasses	5
2.1.4 Fabrication of Bulk Metallic Glasses	6
2.2 Thermoplastic Forming of Bulk Metallic Glasses	7
2.2.1 Fundamental Principle of Thermoplastic Forming.....	7
2.2.2 Potential Applications.....	9
2.3 Metallic Biomaterials with Anti-Biofilm Properties.....	10
2.4 Electrocatalysts in Hydrogen Production.....	14
3 Motivation and Problem Statement	17
3.1 Can't Metallic Glasses Be Deformed and Patterned Once Crystallized?	17
3.2 Limited Materials for Biological Research on Rigid-Ordered Surfaces	19
3.3 Pt-Based Bulk Metallic Glasses for Hydrogen Production.....	20
4 Major Materials and Methods	22
4.1 Materials	22
4.1.1 Bulk Metallic Glasses.....	22
4.1.2 Bioresorbable Polymers.....	23
4.1.3 Templates for TPF	23
4.2 Casting of Ti-BMGs	24
4.2.1 Arc Melter Apparatus	24
4.2.2 Fabrication of Ti-BMGs	25
4.2.3 Optimization of Copper Mold for Disk Fabrication	25
4.3 Thermoplastic Forming of BMGs.....	27
4.3.1 Original Apparatus Based on Zwick Type 1382	27
4.3.2 Upgraded Apparatus Based on Zwick Z100.....	28
4.3.3 Summarized TPF Process Parameters	30
4.4 Material Characterization.....	31
4.5 In-Vitro Study	31
4.6 Materials and Methods of Unpublished Results	32

4.6.1	Spin Coating of Bioresorbable Polymers	32
5	Discussion and Summary of Scientific Contributions.....	34
5.1	Thermoplastic Forming of Ti-BMGs with Nanocrystallization	34
5.1.1	TPF Can Shape and Pattern BMGs Even with Nanocrystallization.....	34
5.1.2	Crystallization Tolerance in $Ti_{40}Zr_{10}Cu_{34}Pd_{14}Sn_2$ BMG for Mechanical Properties	36
5.2	Patterned Ti-BMGs for Biomedical Applications	38
5.2.1	Biocompatibility of $Ti_{40}Zr_{10}Cu_{34}Pd_{14}Sn_2$ BMGs for Hard Tissue Implants	38
5.2.2	TPF-Patterned Ti-BMGs as a Toolbox for Studying Cell-Surface Interaction	39
5.3	Patterned Pt-BMGs as Catalysts for Hydrogen Evolution Reactions	41
5.3.1	Influence of Surface Topographies on Electrocatalytic Performance	42
5.3.2	Stability Test of 1000 LSV Cycles for Nano-patterned Pt-BMG	43
5.4	Unpublished Contributions	47
5.4.1	Cell Response on PDLA-PEG Coated $Ti_{40}Zr_{10}Cu_{34}Pd_{14}Sn_2$ BMGs.....	47
5.4.2	Staphylococcus Aureus on $Ti_{40}Zr_{10}Cu_{34}Pd_{14}Sn_2$ BMGs	48
5.4.3	Hedgehog-like Hierarchical Structure on Pd-BMGs.....	50
6	Conclusions and Outlook.....	53
	References	54
	Publications and Appendix.....	69
A.	List of Included Publications.....	69
B.	My Contribution to the Included Publications	69
C.	Publication I	70
D.	Publication II.....	89
E.	Publication III.....	117
	Appendix.....	148

1 Introduction and Aims

Bulk metallic glasses (BMGs) are a novel class of metallic alloys possessing liquid-like amorphous structures as opposed to traditional crystalline alloys.[1–3] The amorphous structure is achieved by rapidly cooling the metallic melt to avoid crystallization.[2–4] The first metallic glass (MG), Au₇₅Si₂₅ alloy, dates back to 1960 by Klement et al.[5] Due to the requirement of ultrafast cooling rates (10^4 – 10^6 K/s), metallic glasses could only be achieved in the form of thin ribbons (<100 μm) or small particles back then.[5–7] It was not until the 1980s that the bulk form of metallic glasses (with minimum dimension exceeding 1 mm), so-called bulk metallic glasses (BMGs), could be realized with noble metal-based ternary alloy systems thanks to their lower critical cooling rates (< 100 K/s).[4,6,8] Around the 1990s, Akihisa Inoue and co-workers at Tohoku University discovered multicomponent alloy systems based on Fe, Co, Ni, Ti, Zr, Mg, and Cu, booming the research in the BMG world.[9,10]

In terms of applications, the amorphous structure of BMGs benefits from lacking crystalline defects, such as grain boundaries, twins, and dislocations, resulting in superior properties such as near-theoretical strength, high elasticity, high hardness, high toughness, good wear resistance, and corrosion resistance making them promising structural materials.[2,3,6,8,11] In NASA's space exploration program, applications of BMGs include solar wind collectors, spacecraft shielding, and anti-backlash gears.[12–15] More applications of BMGs beyond structural materials continue to be discovered.[4,16–18] The requirement of BMGs in rapid cooling restricts the fabrication of complex shapes through casting.[19,20] Luckily, BMGs can be shaped and patterned through thermoplastic forming (TPF), thanks to their amorphous nature.[1,19,21] Therefore, the present thesis aims to enhance the practicality and functionality of BMGs through TPF approaches, including (1) shaping BMGs even with nanocrystallization, (2) using TPF-patterned Ti-BMGs to study cell behavior on rigid and ordered surfaces, (3) synergizing TPF-patterned BMGs and dynamic bubble templating to fabricate metal or metal-oxide foams.

The present thesis consists of six parts: Following the introduction in **Chapter 1**, **Chapter 2** provides the principle knowledge from materials and process techniques to intended applications. **Chapter 3** points out the challenges in processing BMGs via TPF, fabricating rigid and ordered surface topography for biomedical research, and an unexplored application of TPF patterned Pt-BMGs. **Chapter 4** dives into the major materials and methods applied in the present thesis, including know-how in engineering aspects. **Chapter 5** summarizes the key findings of published works. Moreover, unpublished results are presented in this chapter. **Chapter 6** wraps up the designability and versatility of TPF-processed BMGs and discusses prospects for future research. Lastly, the **Publications and Appendix** section lists the two published plus one submitted manuscripts in international peer-reviewed journals and appends developed protocols and installation manuals for devices.

2 State of the Art

In order to provide comprehensive background knowledge to this thesis, this chapter will start with the fundamental knowledge of the materials – bulk metallic glasses (BMGs) and the process – thermoplastic forming (TPF). Afterward, the intended applications, such as hard tissue implants and electrocatalysts in hydrogen production, will be briefly introduced.

2.1 Bulk Metallic Glasses

2.1.1 Structural Characteristics of Amorphous Metals

Most metallic alloys in the environment are crystalline metals whose atoms are most tightly packed in a three-dimensional periodic pattern.[2,22] The three-dimensional periodic pattern comprises the simplest repeating units called unit cells. Hence, crystalline metals possess long-range order and regular atomic arrangement.[2,11,22] In comparison, amorphous metals, also known as metallic glasses, feature amorphous structures fabricated by rapid cooling.[2,3,22,22] It can be imagined that when alloys are heated to their liquid phase, the system has more space, and atoms can move randomly. Once the rapid cooling takes place, atoms do not have sufficient time to move and diffuse to form their most stable and closed-packed structures – crystals. Instead, the molten alloys are frozen fast enough that atoms are densely packed that they can no longer easily rearrange themselves and maintain their liquid-like disorder arrangements, i.e., frozen supercooled metallic liquids.[2,3,22] Therefore, amorphous metals have glass-like structures with short-range order and random atomic packing.[2,3,11,22] A comparison between amorphous and crystalline metals is shown in Figure 1.

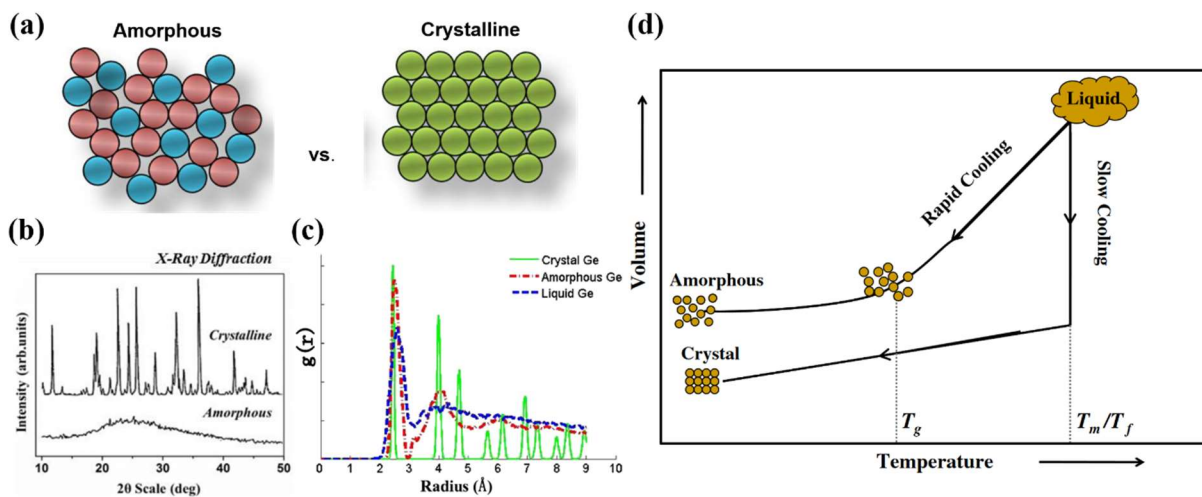


Figure 1: (a) Schematic illustration of amorphous and crystalline structures. Adapted from [23]. (b) Typical X-ray patterns of crystalline and amorphous materials. Adapted from [24]. (c) Radial distribution function (RDF) of the monocrystalline, liquid, and amorphous germanium from molecular dynamics simulation.[25] (d) Comparison of volume in amorphous and crystalline structures induced from different cooling paths.[26]

In practice, disorder in amorphous metals can be determined by (1) structural characterizations and (2) thermodynamic measurements. Structural characterizations such as X-ray diffraction (XRD) and transmission electron microscopy (TEM) access the microstructure directly via diffraction or imaging. Diffraction experiments measure the intensity of the scattered radiation of the material based on Bragg's law, as demonstrated in Figure 1(b).[2,23,27] Broad and diffuse peaks in the XRD patterns are typically used to indicate the existence of an amorphous phase.[2,28] The Fourier transformation of diffraction data is the radial distribution function of the structure, which describes important features of the atomic arrangements (Figure 1(c)).[2] It should be noted that even though XRD is a common and less expensive method, it has some limitations.[2,28] Crystalline phase fractions of ≤ 5 vol.% and nanocrystals with small grain sizes of ≤ 10 nm are often not detectable by XRD.[2,28]

Furthermore, disorder in amorphous metals can be examined thermodynamically through glass formation, such as differential scanning calorimetry (DSC) and differential thermal analysis (DTA).[2] As illustrated in Figure 1(d), the change of volume or enthalpy as a function of temperature during cooling can be used to describe the glass formation. When cooling slowly below melting/freezing temperature (T_m/T_f), the molten alloys will crystallize, leading to a discontinuous change in the extensive properties, like volume or enthalpy.[2,29,30] On the contrary, if cooling rapidly below T_m/T_f , the molten alloys transit into the vitreous state with a continuous transformation happening in the volume or enthalpy. This is a process also known as glass formation. The glass transition temperature (T_g) divides the undercooled liquid and the frozen solid (glass), traditionally designated when the viscosity of the undercooled liquid reaches a value of 10^{12} Pa s.[2,11,30] It is worth noting that the glass formation region and T_g are controlled by dynamic behavior and are thus highly dependent on the cooling rate.

2.1.2 From Metallic Glasses to Bulk Metallic Glasses

MGs were fabricated in the form of thin ribbons and small particles due to the requirement of an ultrafast cooling rate, which limits its application. Hence, BMGs allowing a slower cooling rate and having a section thickness of at least a few millimeters were developed. In order to formulate the alloy systems with the enhanced glass-forming ability (GFA) to synthesize BMGs, Inoue introduced three basic empirical rules as follows: [2,7,9]

1. The alloy must contain multiple components of at least three chemical elements. As the number of components in the alloy system increases, the glass formation becomes more accessible.
2. Among the component elements of the alloy, there should be a notable difference in atomic size. It is suggested that the atomic size differences between the primary constituent elements should be larger than 12%.

- There should be negative mixing enthalpy for the primary constituent elements in the alloy system.

The first rule considers the thermodynamic and kinetic aspects of glass formation, and the second rule takes into account the topological aspects, such as the structure and packing of atoms. The last rule eases the mixing of atoms and the forming of a homogeneous glassy phase.[2]

From the outcome point of view, BMGs should have the following important properties:[2]

- As illustrated in Figure 2, BMGs can be produced at slow solidification rates, typically 10^3 K s^{-1} or less, allowing them to be produced from casting, water-quenching, and even 3D printing.
- BMGs can be fabricated into forms with large thicknesses or diameters, a minimum of about 1 mm, which improves their practicality.
- BMGs have a large supercooled liquid region (SCLR), which is the difference between the glass transition temperature (T_g) and the crystallization temperature (T_x). The large SCLR ($\Delta T_x = T_x - T_g$) usually ranges from a few tens of degrees to more than one hundred degrees, promoting the processability of BMGs.

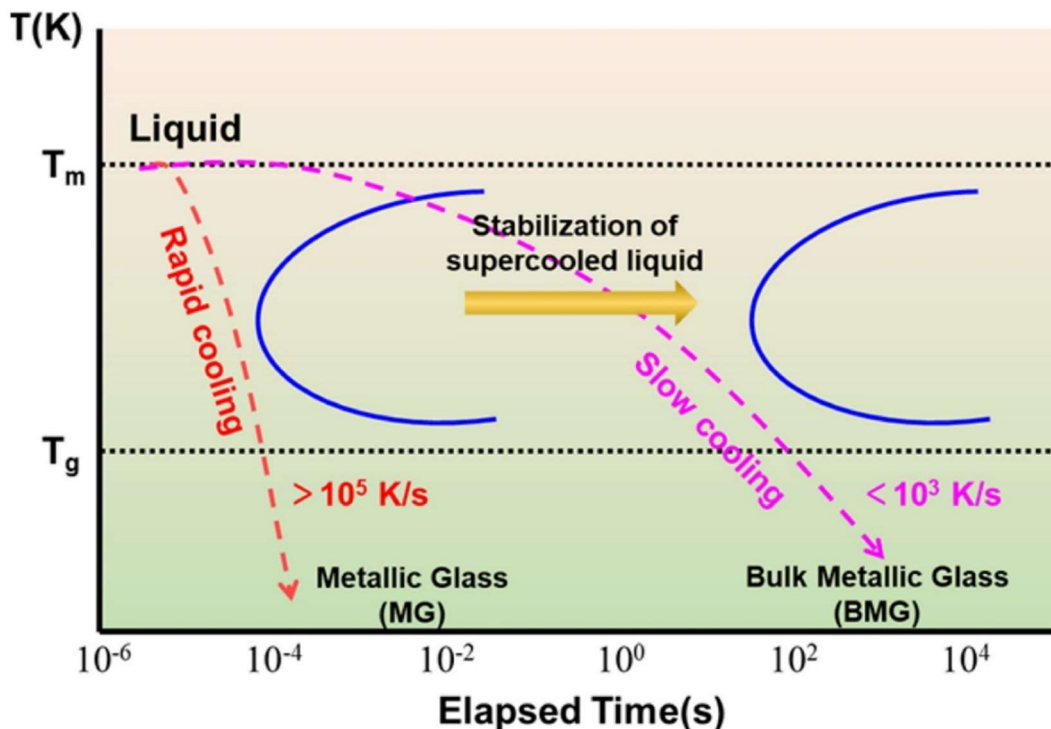


Figure 2: Schematic TTT diagram of MGs and BMGs with corresponding cooling paths illustrating the improvement of BMGs over MGs in terms of cooling rate.[31]

2.1.3 Properties and Applications of Bulk Metallic Glasses

BMGs possess superior properties over their crystalline counterparts, such as low elastic modulus, high strength and high fracture toughness, high elasticity, high hardness, outstanding wear resistance and corrosion resistance, and excellent soft magnetic properties, thanks to the absence of long-range order, dislocation, grain boundary, and other traditional lattice defects in their amorphous structures (Figure 3(a)).[2,4,8,18] For example, the elastic limit in BMGs is typically 2%, which is four times more than that of titanium, aluminum, and conventional steel alloys.[2,4] Because BMGs lack a crystal structure, there is no dislocation mechanism for plastic deformation; combined with their high elastic limit, tensile strength, and fracture toughness, BMGs are particularly suitable for applications requiring large storage of elastic energy, such as high-performance springs, tennis racket frames and golf clubs and casings of electronics (Figure 3(b)).[2,4,8] BMGs also find their place in space exploration with the previously mentioned high strength and wear resistance, as well as the fact that they do not get brittle in extremely cold conditions, allowing them to turn under strong torque even under $-200\text{ }^{\circ}\text{C}$ without lubricant, which will preserve precious battery power in space (Figure 3(c)).[32]

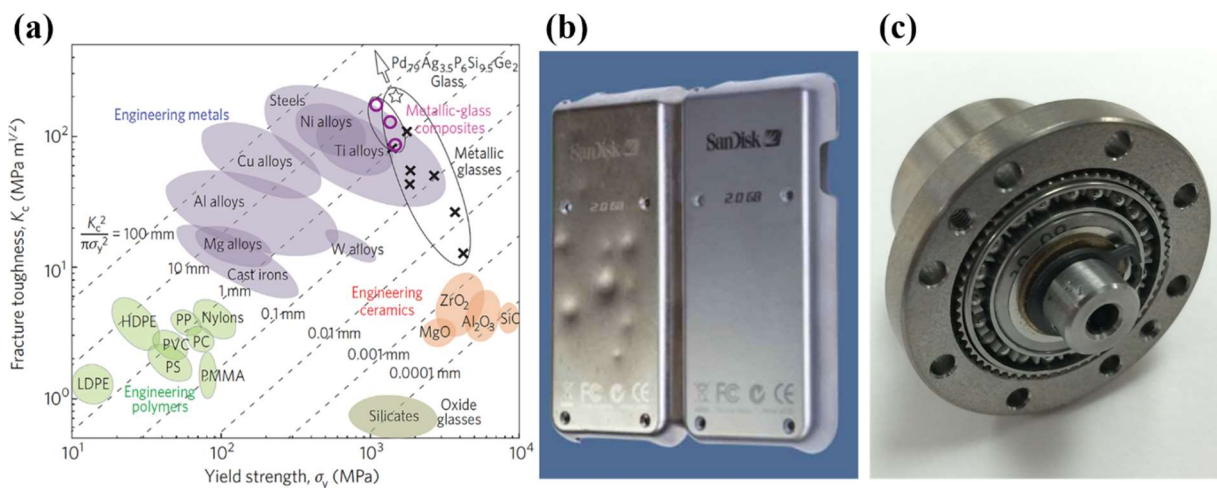


Figure 3: Properties and applications of BMGs: (a) Ashby plot of yield strength and fracture toughness for various engineering materials illustrating that MGs achieved both high fracture toughness and high yield strength over conventional materials.[33] (b) A comparison shows that traditional crystalline alloys (left) can be dented while BMGs (right) can not be dented.[34] (c) A NASA project developed strain wave gears made from BMGs, which are suitable for extreme conditions in space applications.[32]

BMGs based on biocompatible elements, such as Ti, Zr, and Pt, have attracted substantial interest in biomedical applications. For example, for dental and orthopedic implants, BMGs have favorable properties like high corrosion resistance, wear resistance, lower Young's modulus, and higher elasticity, making them potential biomaterials compared to traditional crystalline alloys.[35–38] Enhanced elastic behavior and reduced Young's modulus are expected to mitigate the stress-shielding effects when contacting bone tissues.[35,39,40] Moreover, biodegradable BMGs based on Ca, Mg, Zn, and Sr can be applied as temporary

implant materials to provide temporary fixation or mechanical support for injured tissues and match their degradation rate to the healing process of the host tissues, targeting the medical treatment without secondary surgeries.[36]

Another highlight of BMGs is their high formability and dimensional accuracy because BMGs exhibit almost no volume shrinkage upon solidification during the casting process due to the absence of first-order phase transformations during the liquid-to-solid transitions.[2,4,8] Hence, BMGs can be cast to net shape with a significant reduction in post-processing and have complex shapes with high dimensional requirements.[2,4,8] Furthermore, BMGs show unique superplasticity within the SCLR, where they start to behave less like a solid and more like a liquid.[1,3,6,8,41] This property makes BMGs ideal for precise and net-shaping different geometries by thermoplastic forming (TPF), which can also be applied in micro- and nano-replication.[6,8] More details about TPF and the superplasticity of BMGs within SCLR will be introduced in section 2.2. Thanks to the advantageous properties of BMGs, more research is devoted to utilizing them in many areas, such as electronics, aviation, aerospace, machinery, microelectronics, and medical devices.[4]

2.1.4 Fabrication of Bulk Metallic Glasses

Before introducing the methods to produce real “bulk” MGs, it is worth mentioning the melt spinning technique, which is applied to produce a ribbon form of MGs because researchers produce ribbons firstly to screen the potential composition and study their properties and crystallization behavior before proceeding to fabricate their bulk forms.[2,42] The alloy is melted inductively in a crucible, and then argon pressure is used to push the melted alloy onto a spinning copper drum through a small hole in the crucible, where the melted alloy solidifies at a cooling rate of around 10^6 K/s to form the MG ribbon.[2,8]

Copper mold casting is one of the most common methods to fabricate BMGs.[2] In principle, the alloy is melted and then exerted into a copper mold, where the melted alloy contacts the copper mold to cool and solidify quickly because of the rapid heat extraction.[2,15] There are many variations in copper mold casting depending on their melting methods and the driving force to exert the melted alloy into the mold. For instance, the alloy can be melted using induction heating or arc melting. An example of the driving force is utilizing the pressure difference between the melting site and the casting site. Either applying high pressure in the melting site to “push” the melted alloy into the casting mold or creating low pressure in the casting site to “pull” the melt into the mold. Methods like high-pressure die casting, ejection casting, and suction casting are all following this pressure differential principle.[2,19] Different driving forces can also be adapted to fabricate BMGs, such as gravity in tilt casting and centrifugal force in centrifugal casting.[43,44]

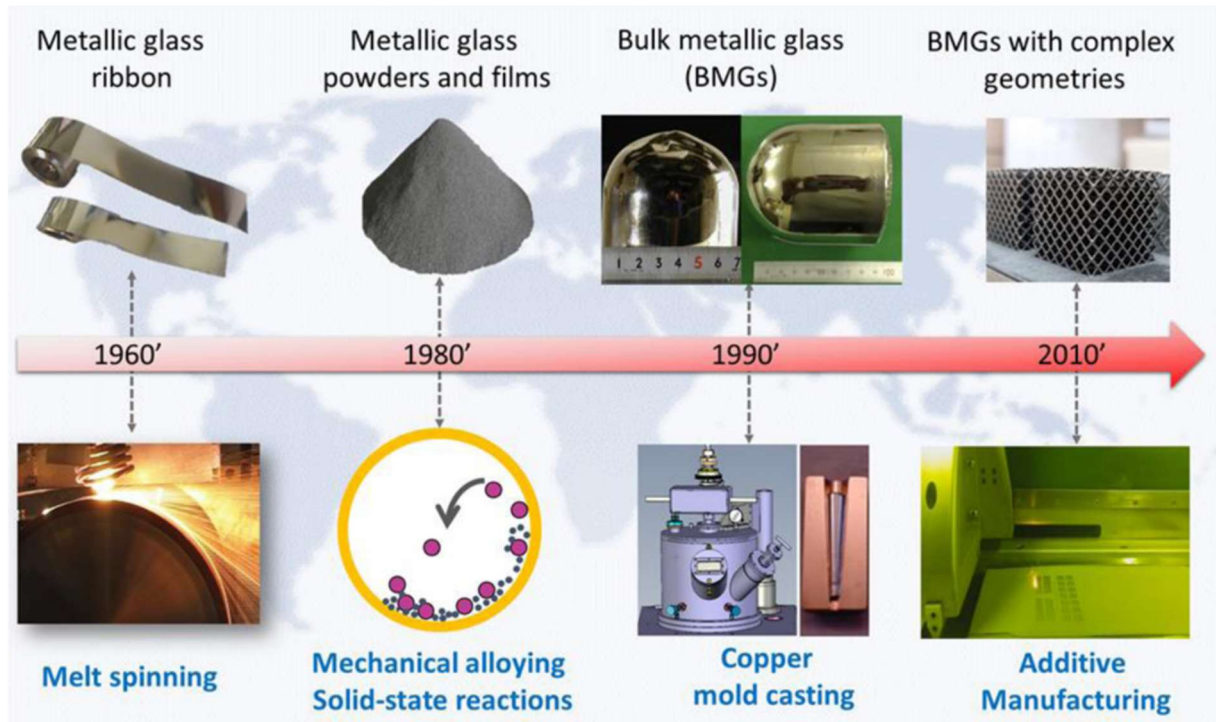


Figure 4: Progress in fabrication techniques for MGs and BMGs.[31]

Powder metallurgy approaches can be used to create BMGs while avoiding the dilemma between casting size and cooling rate.[2,18] The concept is to produce amorphous powders first via mechanical alloying or gas atomization and then consolidate amorphous powders into bulk samples using methods such as hot extrusion, hot isostatic pressing, and spark plasma sintering.[2,18] Thanks to the advances in 3D printing technology since the last decade, additive manufacturing methods based on powder feedstock such as selective laser melting (SLM), laser-engineered net shaping (LENS), thermal spray 3D printing (TS3DP), and non-powder feedstock (ex: wires, ribbons, rods, and pellets) such as laser foil 3D printing (LF3DP), fused filament fabrication (FFF), laser forward transfer 3D printing (LFT3D) are developed to fabricate BMGs and improve their applicability.[31,45]

2.2 Thermoplastic Forming of Bulk Metallic Glasses

2.2.1 Fundamental Principle of Thermoplastic Forming

Generally, BMGs have poor ductility and formability at room temperature because their plastic deformation tends to be localized in sharp shear bands.[41] Luckily, it was found that when BMGs are heated to their SCLR, the region between glass transition temperature (T_g) and crystallization temperature (T_x), their viscosity is reduced significantly, and the material can be deformed by viscous flow before crystallization takes place.[1,6,19,41] As demonstrated in Figure 5(a), in the SCLR ($\Delta T = T_x - T_g$), BMGs can be shaped and molded much like (thermo)plastics via a thermo-mechanical processes known as thermoplastic forming (TPF),

which has different nomenclature such as thermoplastic net-shaping, hot forming, hot embossing, superplastic forming, and viscous flow forming.[6,22,46]

The operating principle of TPF can be explained in a time-temperature-transformation (TTT) diagram, as shown in Figure 5(b): **Segment 1** is the rapid cooling path to form a BMG from melted alloy. In **Segment 2**, the BMG is reheated into its SCLR, where its viscosity decreases and the material gradually softens. **Segment 3** is the forming step, where external forces, such as compression, extrusion, rolling, injection molding, and blow molding, are applied to shape the material into the desired shape. It is important that **Segment 3** does not intersect the crystallization nose; otherwise, the BMG will crystallize. Finally, the BMG is cooled below T_g in **Segment 4**, and fast cooling is not required after TPF.[1,3]

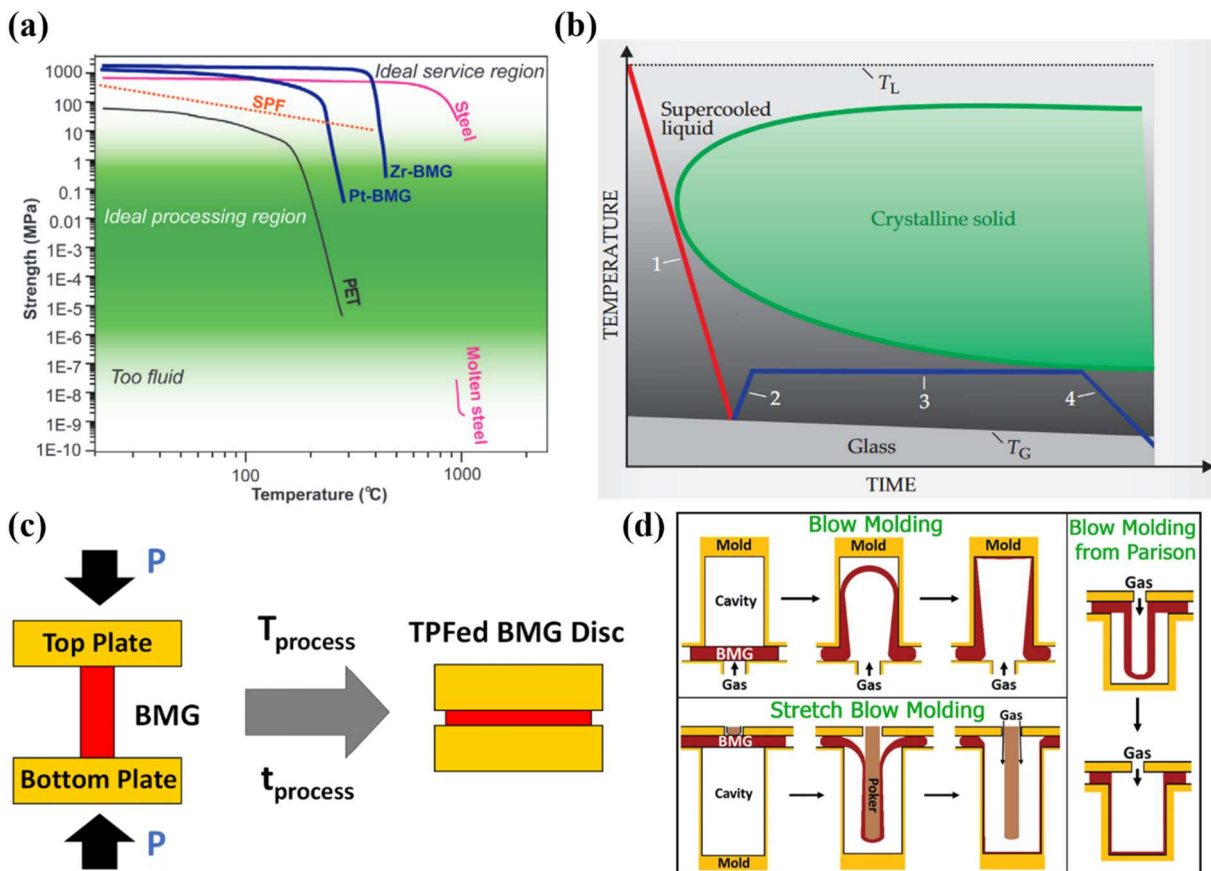


Figure 5: (a) Comparison of processability for conventional steel, SPF alloys, plastics, and BMG via the temperature-dependent strength curves.[47] (b) Typical TPF processing route in TTT diagram.[3] (c) Schematic illustration of compression-based TPF.[1] (d) Blow molding with various strategies developed by J. Schroers and collaborators.[48]

In implementation practice, the most basic setup for TPF is compression molding, as displayed in Figure 5(c), in which the BMG is placed between two molds and squeezed by applied pressure.[1] This setup can deform a BMG rod into a BMG disk and due to its simplicity to conduct, this method is applied to explore the formability of BMGs.[21] For example, a standardized method to characterize the formability of a BMG in its SCLR is introduced by J.

Schroers.[49] By adding templates on the BMG disks, the compression molding can be adopted to create patterned surfaces on BMGs.[50] With a sequential TPF patterning process, a multitier pattern integrating features in multiple length scales can be achieved on the BMG surface.[46]

As mentioned above, TPF can be executed in versatile forming strategies beyond compression molding, such as extrusion, rolling, injection molding, blow molding, and thermoplastic drawing. For instance, as shown in Figure 5(d), blow molding has been developed with different strategies to achieve high aspect ratio open shape structures with overall strains exceeding 2000% from sheet-like BMG feedstock.[48] All these developments enable net-shape complex articles from BMGs, offering highly practical and effective methods to realize a broad commercial application of BMGs.

2.2.2 Potential Applications

Thanks to the versatile forming strategies of TPF, BMGs can be shaped and patterned from macro- to nano- and even atomic scales, as demonstrated in Figure 6. In the macro-scale (m to mm), BMGs can be processed into wires, screws, covers, containers, casings, housings, tubing, and bellows via compression molding, hot rolling, thermoplastic extrusion, and blow molding.[1,47,48,51,52] In the field of miniature fabrication, micro-sized BMG components, such as gears, tweezers, scalpels, stents, and springs, can be created by combining miniature molding and subsequent planarization techniques.[1,53–55] Micro- and nano-patterns can be imprinted on the BMG surfaces via micro- and nano-molding, while sequential TPF patterning methods can achieve multitier surface patterns joining multiple-length scales.[11,46,53,56,57] The typical micro- and nano-patterns are micro-pyramids, micro-bumps, micro-grooves, nanorod, nano-grooves, nano-wires and nano-pits.[11,46,50,51,53,56–58] In atomic scale, surfaces exhibiting atomic-level smoothness with a roughness smaller than 2 Å are achieved by compression molding of BMGs on mica.[1,59] This work suggests that surface oxidation can be removed from the forming area by the lateral flow of the supercooled liquid, showing the possibility of joining BMGs by thermoplastic methods, which has been later achieved and reported by Chen et al. [59–61]

Thanks to the versatility and designability of TPF, in addition to being structural materials, the TPF-processed BMGs have many functional applications, ranging from wettability, structural color, sensors, and electronics to catalysis and biomedical applications.[1,18,62,63] For example, biomedical applications include Zr-, Ti-, Mg-, Fe-BMGs for cardiovascular stents and bone implants,[18] patterned Pt-BMG nanorods for glucose sensors,[64] nanopatterned Pt-BMGs for engineering cellular response,[58] Pt-BMG microneedles/tubes for drug injections,[65,66] and MG-based fiber probes for neural stimulation and recording in neuroscience.[67,68] In catalyst applications, nanostructures created by TPF can enhance catalytic performance due to their strong specific surface area and

large number of active sites. Gao et al. demonstrate that nanorod-patterned Pd-BMG has an enhanced catalytic activity towards hydrogen evolution reaction (HER) with self-stabilizing catalytic activity over a long-term operation.[69] Carmo et al. reveal that nanowire-patterned Pt-BMG has superior electrocatalytic behaviors toward carbon monoxide, oxidation, methanol oxidation, and ethanol oxidation.[70]

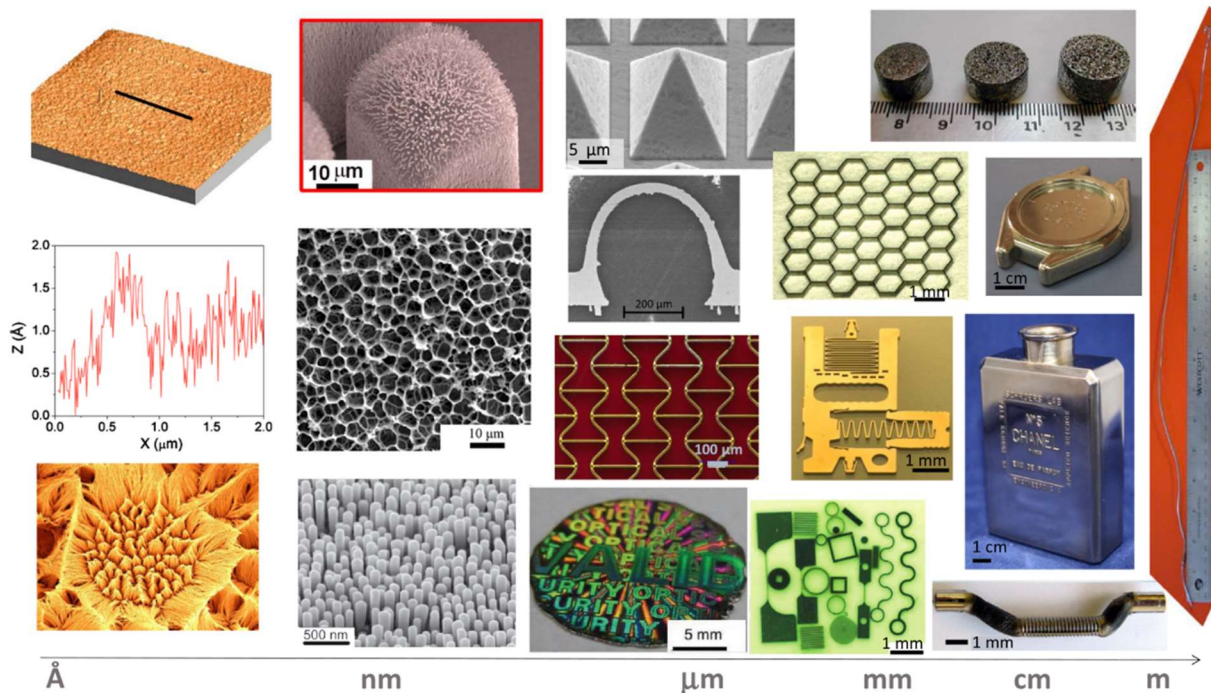


Figure 6: Thermoplastic forming can be applied to process BMGs on multiple scales, ranging from macro-scale down to atomic-scale and from the whole shape to surface modification.[1,46,47,51–53,56,59,70–74]

More and more applications from TPF-processed BMGs have been explored, such as nanopatterned surfaces with anti-reflective behavior,[10] micropatterned superhydrophobic surfaces,[75,76] nanowires for photoinduced heat conversion,[77] surface transfer for micro-optics,[53] blow molding of microelectromechanical systems (MEMS) resonators,[51,78] multifunctional wave springs,[79] and even using BMGs as a filler material for joining metals.[80] Therefore, TPF process BMGs show their potential in a wide range of applications.

2.3 Metallic Biomaterials with Anti-Biofilm Properties

Improvements in medical health care during the past decades have led to increased use of implants, while increased medical progress and biological demands dictate the requirements of implants.[81] Metallic biomaterials have a long history in medical applications and have been widely used in hard tissue implants (orthopedic fixations, spinal fixations, joint replacements, dental implants), cardiovascular devices (cardiac pacemakers, defibrillators, blood conduits, stents, artificial heart valves) and even neurovascular implants (aneurysm

clips), as exposed in Figure 7(a).[81,82] Due to the annual implantation of more than 1.7 million cardiovascular devices and 1 million orthopedic implants worldwide, the global implant industry was expected to reach \$21.5 billion in cardiovascular devices and \$55.8 billion in orthopedic implants in 2020.[82–85] The use of metallic biomaterials is expected to rise more in the near future.

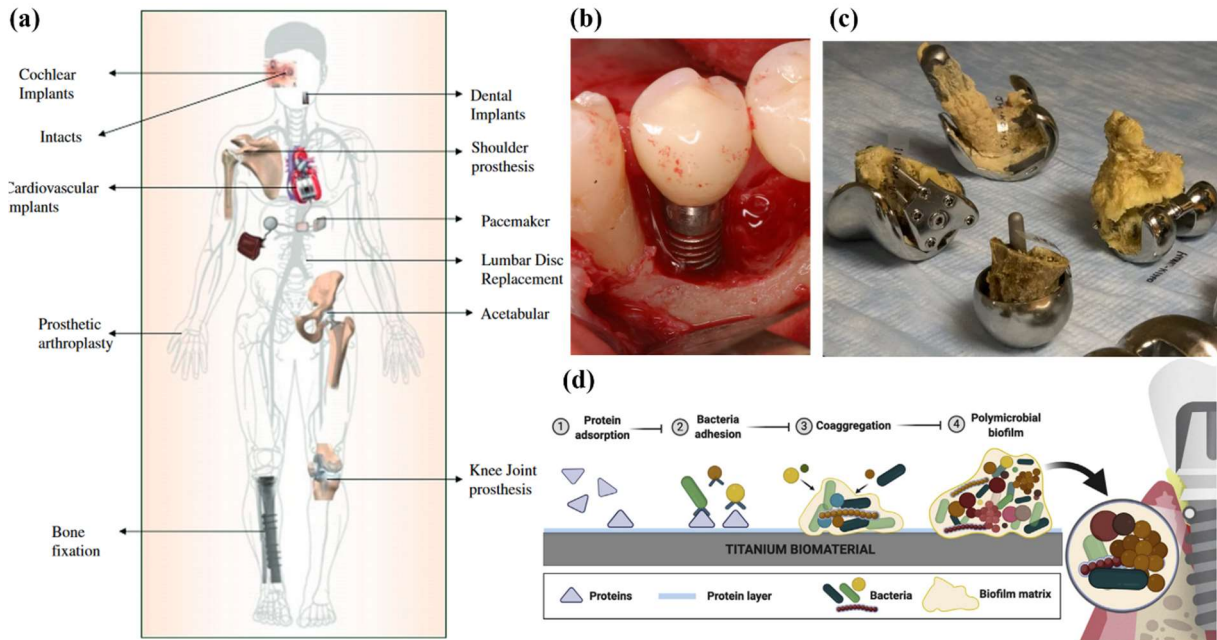


Figure 7: Metallic implants and implant-associated infections: (a) Metallic biomaterials for implant applications.[81] (b) Infection causes bone loss around dental implants.[86] (c) Removed knee implants from patients due to IAIs.[87] (d) Stages of biofilm formation on implant surfaces.[88]

The increased number of implants also increases the cases of implant-associated infections (IAI), which cause significant threats to patients, such as implant loosening, chronic pain, immobility, osteomyelitis, and even mortality (Figure 7(b-c)).[82,88–95] The main reason of IAI is that implants are often detected as “foreign bodies” by the host immune system and activate immune responses, so-called foreign body reaction (FBR), leading to a local immune-compromised environment in the surrounding tissue and providing a foothold to pathogenic bacteria to colonize the implant surface which further forms hard-to-eradicate biofilms.[82,96] Even with systemic antibiotic therapy before surgery, surgical procedures carry a risk of infection, with incidence ranging from 0.5% to 4% for total hip and knee implants.[95] Furthermore, these implants inevitably increase the risk of infection when left in the body for an extended period.[97] IAI occurrence is even higher in cases of revision surgeries on failed implants, the infection rates after surgical revision considerably increase up to 40% than after primary replacement.[82,95] IAI has a considerable clinical incidence, accompanying morbidity and mortality, and high economic costs shared across all implant and device categories.[82,90,95] According to recent studies, the combined annual hospital costs associated with hip and knee periprosthetic joint infection (PJI) alone will reach \$ 1.85 billion

in the United States by 2030.[98,99] Therefore, developing implant materials with anti-biofilm properties is imminent and indispensable.

A legendary military strategist, Sun Tzu, once said, “To know your enemy, you must become your enemy.” and “If you know the enemy and know yourself, you need not fear the result of a hundred battles.”.[100] To help the host tissue win the fight against biofilm on the implant surface, it is essential to understand how pathogenic bacteria attach and form biofilm on the surface. Figure 7(d) illustrates four main stages of biofilm formation on titanium implants:[88]

- (1) Proteins adsorb on the implant surface, forming a protein layer responsible for mediating subsequent cellular events, including microbial and host cell attachment, through adhesin-receptor interactions.[88,101,102]
- (2) Early colonizing bacteria as planktonic (free-floating) microbial recognize protein pellicle receptors and adhere to the surface via binding to the protein layer. Thus, protein pellicle receptors can selectively promote the accumulation of specific microbial species on exposed surfaces.[88,101,102]
- (3) After initial microbial adhesion, bacteria in the monolayer proliferate locally and secrete extracellular polymeric substances (EPS) including polysaccharides, proteins, extracellular DNA (eDNA) which are the building blocks for biofilm. Different microbial species also interacts to each other to facilitate biofilm accumulation and maturation by co-aggregation processes.[88,101,102]
- (4) The synergistic interaction between organisms continues to build the biofilm structure, forming a three-dimensional extracellular matrix called polymicrobial biofilm. Biofilm as a protective matrix for bacteria not only enhances microbial interaction and cooperation but also blocks bacteria from immune cells and antibiotics. Thus, removing a biofilm is incredibly challenging after a biofilm has formed and matured.[88,101,102]

It is worth noting that bacteria in the biofilm can be dispersed and revert to a planktonic state, spreading infection by floating in the surrounding liquids and initiating a new biofilm formation cycle.[101] The most causative pathogens in IAs are Staphylococci, such as *Staphylococcus aureus* and *Staphylococcus epidermidis*, and other common ones include enterococci and *Pseudomonas aeruginosa*. [92,103–105]

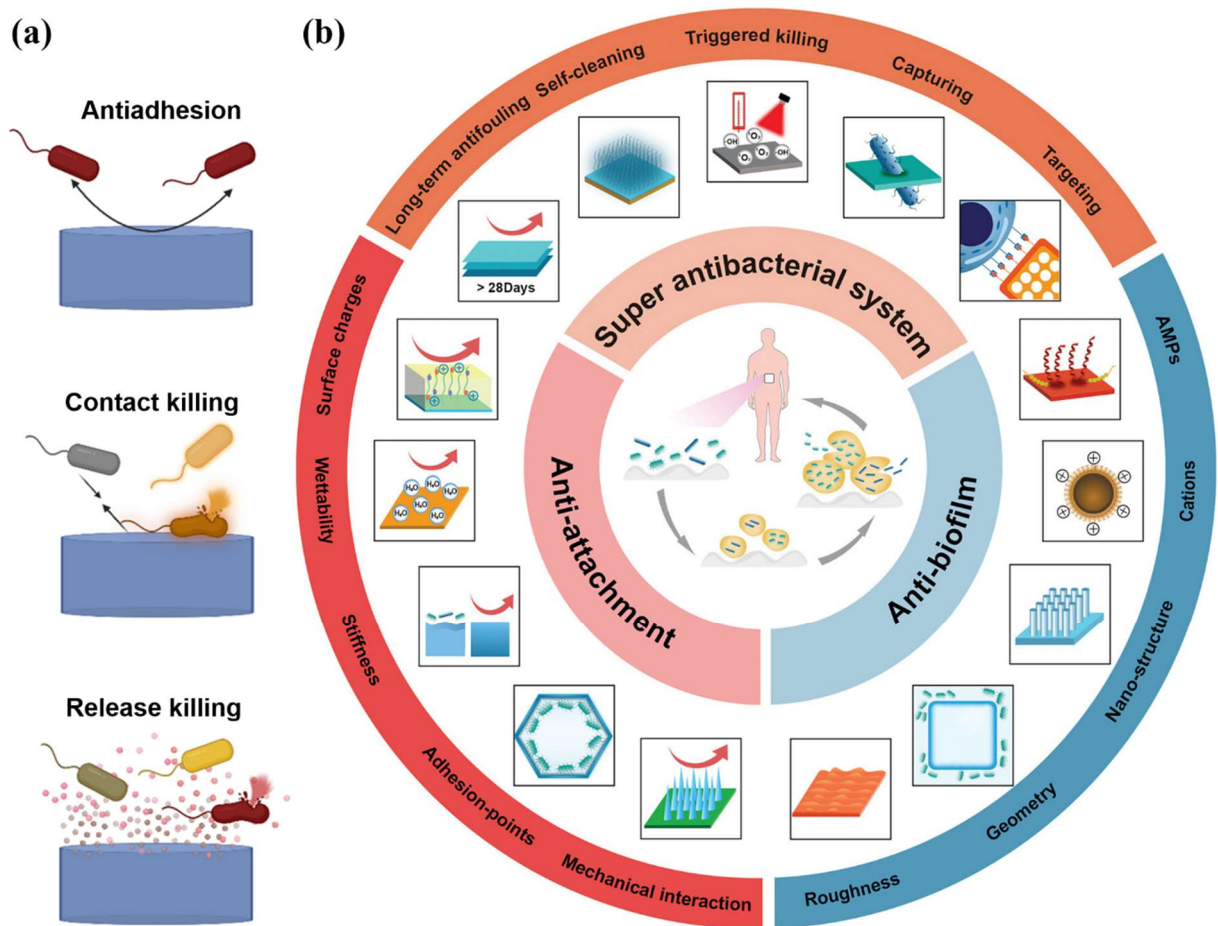


Figure 8: Designs to assign antibacterial properties on implant surfaces (a) Main mechanisms to enhance antibacterial properties. Adapted from [106]. (b) An overview of antibacterial material surface design, including key aspects against bacterial adhesion (left), various effects to resist biofilm (right), and antibacterial systems combining multiple strategies for clinical therapy.[107]

The current therapies for IAIs are heavily rely on antibiotics which leads to the emergence of antibiotic-resistant bacterial strains, such as methicillin-resistant *Staphylococcus aureus* (MRSA).[103] Therefore, more researchers are working on biomaterials with antimicrobial properties in order to find material-based solutions for IAIs. As illustrated in Figure 8(a), there are three main mechanisms to achieve antibacterial properties on the implant surfaces:

- (i) **Antiadhesion:** The implant surfaces with antifouling and antiadhesive properties minimize bacterial adhesion, a critical stage for biofilm formation. These surfaces aim to prevent bacterial adhesion and biofilm formation without actively killing bacteria.[108–110] Antiadhesion can be achieved by controlling wettability and steric or electrostatic repulsions. Examples are surface topography with micro- and nanostructure or polymeric coating with hydrophilicity or super-hydrophobicity.[88,104,108–110]
- (ii) **Contact killing:** The implant surfaces utilize physical approaches, such as electrostatic action and mechano-bactericidal mechanism, to damage bacterial cell

walls and kill bacteria without releasing antibacterial agents. Surfaces modified with nanostructures, antimicrobial peptides (AMPs), photocatalytic substances and ion implantations are examples [97,104,108–112]

- (iii) Release killing: The implant surfaces are loaded with antibacterial agents, which are released locally to kill the planktonic bacteria in the surroundings after implantation. Common antibacterial agents are metal ions, AMPs and drugs.[107,108,113]

In practice, antibacterial implant surfaces can be realized through surface modifications (Figure 8(b)) or directly using intrinsic antibacterial materials that already have antibacterial and bactericidal properties without further surface modification.[105] An example of intrinsic antibacterial materials is using micro-alloying as a strategy to modulate antibacterial ion release from bulk materials.[114] It is worth noting that different antibacterial mechanisms and strategies have their own pros and cons, and most importantly, antibacterial surfaces should minimize adverse effects on host tissues. Hence, an ideal implant surfaces can be accomplished by integrating multiple antibacterial strategies. The current strategies mainly suffer from three major disadvantages, including short lifetime, cytotoxicity to surrounding tissue, and antimicrobial resistance.[107] Therefore, the development of materials combining long-term antibacterial effects and targeting capabilities on pathogens while preserving good biocompatibility is essential for human well-being.

2.4 Electrocatalysts in Hydrogen Production

Since the rise of the traditional energy crisis and the increasing awareness of environmental and climate problems, it is inevitable to change the energy structure and raise the proportion of renewable energy to ensure the sustainable development of human society.[115,116] The development of renewable and sustainable green energy, like solar, wind, tidal, and hydrogen, has attracted extensive attention.[117] Hydrogen (H_2) is regarded as a prospective energy carrier because of its nontoxic, pollution-free, good thermal conductivity, high utilization rate, and high calorific value (140 MJ/kg), making it a promising energy carrier as a fuel for both storage and transportation.[115–117] Overall, there are three industrial options for hydrogen generation: methane steam reforming, coal gasification, and water electrolysis.[116] However, water electrolysis, especially the hydrogen evolution reaction (HER), is a more environmentally friendly and sustainable option compared to the other two. Since hydrogen production through water splitting has to overcome its intrinsically slow kinetics and large overpotential, making it economically impractical for large-scale use.[118–120] Thus, in order to lower energy consumption and increase energy conversion efficiency, electrocatalysts with small overpotentials must be developed.[121]

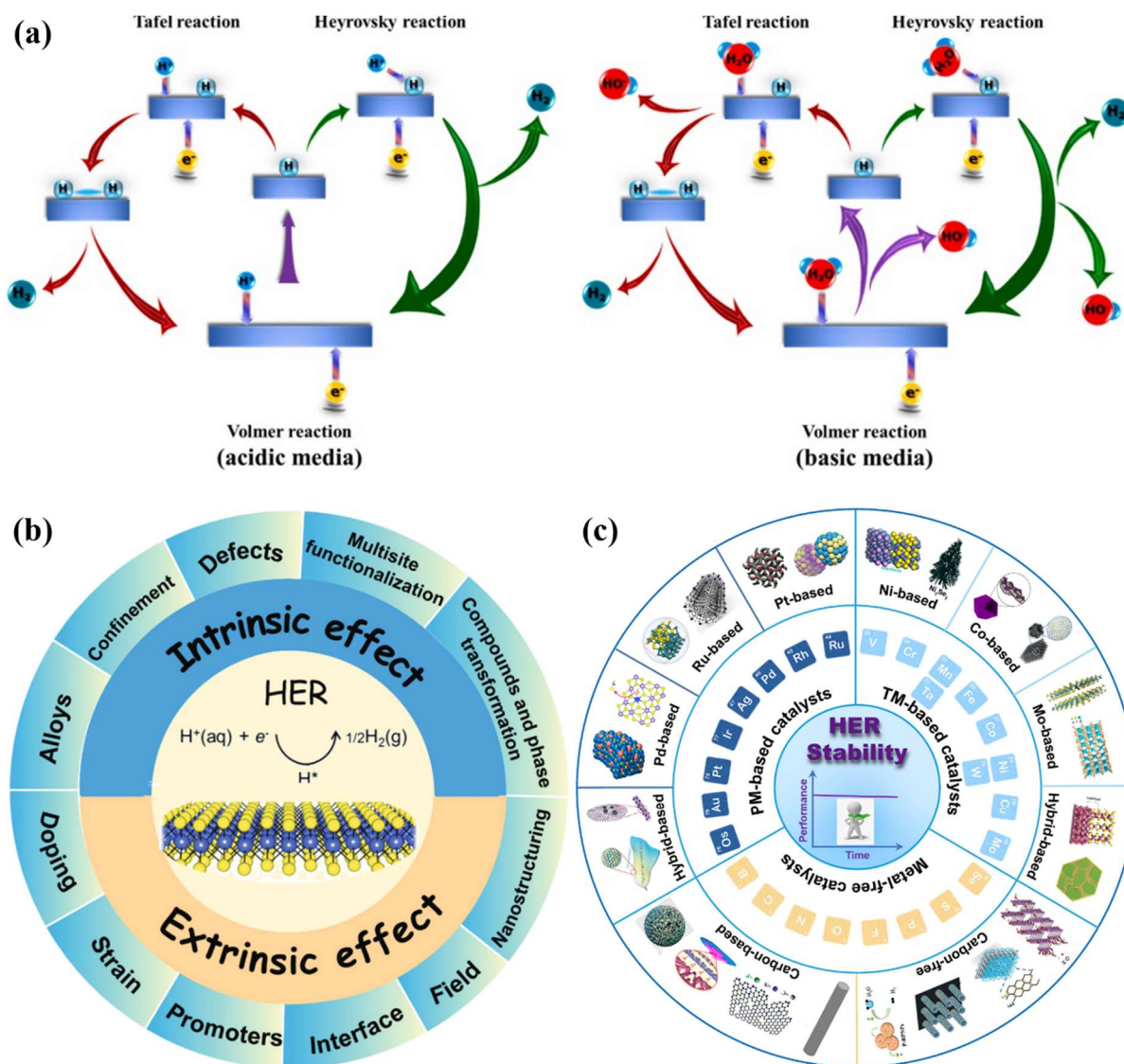


Figure 9: Electrocatalysts for hydrogen evolution reaction (HER): (a) Roles of electrocatalysts in HER mechanism in acidic (left) and base solutions (right).[122] (b) Strategies to improve HER electrocatalysts.[115] (c) HER electrocatalysts based on various material systems have been proposed.[116]

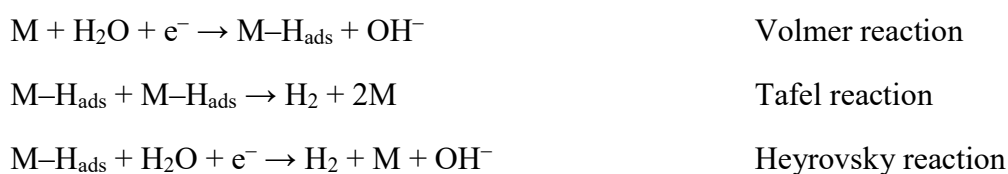
There are two half-reactions in water electrolysis: HER at the cathode generates hydrogen (H₂), and oxygen evolution reaction (OER) at the anode generates oxygen (O₂).[123] Generally, HER contains two consecutive electrochemical steps in both acidic and alkaline solutions via Volmer-Heyrovsky or Volmer-Tafel pathways, as shown in Figure 9(a).[122–124] The first step is the Volmer reaction, where a proton is adsorbed on the active site of the electrocatalyst and couples with an electron provided by the external circuit, yielding an intermediate adsorbed hydrogen (H* or M–H_{ads}) atom.[122,124] In the second step, H₂ can be generated by either the Tafel reaction, in which two adjacent adsorbed hydrogen atoms are directly combined to form H₂ (Volmer-Tafel pathway), or Heyrovsky reaction, in which another proton in acidic electrolytes or water molecule in base electrolytes diffuses to the adsorbed

hydrogen atom and then reacts with an electron to form H₂ (Volmer-Heyrovsky pathway).[116,122–124]

In acid solution:



In base solution:



Notably, the adsorbed protons depend highly on the electrolyte and play a critical role in HER. For example, protons appear as hydronium ions (H₃O⁺) in acidic solutions such as H₂SO₄. In contrast, water molecules (H₂O) are the proton source in base solutions such as KOH or neutral solutions such as phosphate buffer electrolyte.[122,123]

Electrocatalysts with superior HER performance have typical properties like high intrinsic activity, large specific surface area, and fast electron/hydrogen/water transport.[115] As illustrated in Figure 9(b), in order to achieve good overall catalytic performance, an ideal design of electrocatalysts should coordinate intrinsic effects and extrinsic assistance to synergistically maximize intrinsic activity, exposed active sites, and electron/hydrogen/water transports.[115] The intrinsic effects include alloys, compounds and phase transformation, defects, confinement, and multisite functionalization, while extrinsic effects cover strain effects, heteroatom doping, promoters, nanostructuring, interface, and field effects.[115]

Currently, the benchmark for HER electrocatalysts is still Pt-based metals because of their ideal adsorption of hydrogen, which facilitates both the adsorption of active hydrogen species and the desorption of hydrogen molecules.[116] However, noble metal (Pt, Ru, and Ir)-based electrocatalysts suffer from their scarcity, high cost, and poor stability in highly acidic and alkaline electrolytes.[116,118,123] As demonstrated in Figure 9(c), electrocatalysts based on various material systems are proposed in order to develop HER catalysts for large-scale applications with low production cost, high Earth abundance, long-term electrocatalytic stability, high electrical conductivity, and efficient electrocatalytic performance.[115,116,118] Nevertheless, improving the electrocatalytic activity and durability of HER catalysts remains a challenge.

3 Motivation and Problem Statement

3.1 Can't Metallic Glasses Be Deformed and Patterned Once Crystallized?

As mentioned in section 2.2, the basic concept of thermoplastic forming of BMGs is that amorphous BMGs can be deformed and patterned via Newtonian viscous flow when reheated into their SCLR. It was believed that the TTT curves of the material define the processing window of TPF, and it was crucial to avoid intersecting the nose-shaped crystallization curves during the whole TPF process. The main concerns about the crystallization during TPF are (i) loss of the deformability and (ii) loss of the mechanical properties of BMGs.

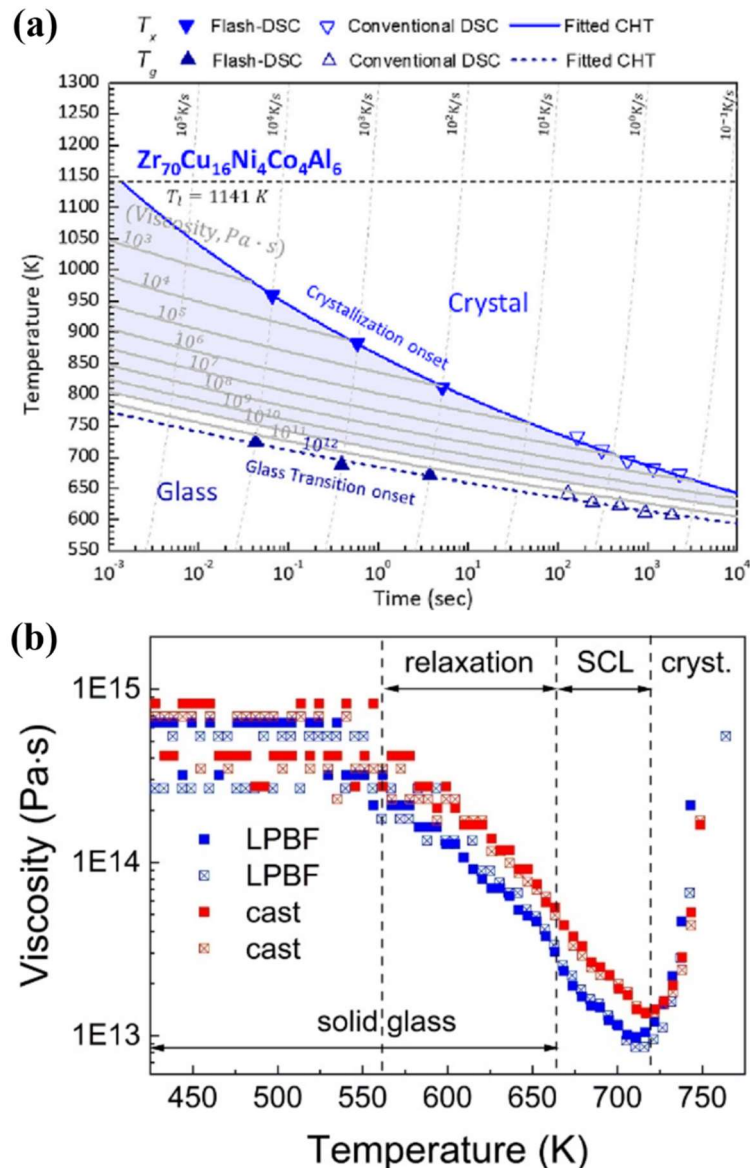


Figure 10: (a) Continuous heating transformation (CHT) curves with iso-viscosity contours for $Zr_{70}Cu_{16}Ni_4Co_4Al_6$ MG.[125] (b) The temperature dependence of viscosity for $Zr_{52.5}Cu_{17.9}Ni_{14.6}Al_{10}Ti_5$ BMG. As temperature increases, the viscosity of BMG drops in the relaxation and SCL regions but then increases suddenly due to the crystallization.[1,126]

Regarding the loss of the deformability of BMGs, it is worth noting that the selection of processing temperature simultaneously influences the crystallization time and viscosity of BMGs. Ideally, the TPF processing path should provide (i) a sufficiently wide processing window without triggering the crystallization and low enough viscosity to deform the material. As shown in Figure 10(a), within the SCLR, the higher processing temperature leads to a shorter crystallization time (disadvantageous) and lower viscosity (beneficial). Furthermore, as demonstrated in Figure 10(b), the viscosity of BMGs reduces strongly in the relaxation and SCL regions, followed by an abrupt increase in viscosity due to the crystallization, causing the material to lose its liquid-like behavior.[1,126] Hence, the material cannot be deformed anymore once it is crystallized.[1,21]

Concerning the loss of mechanical properties of BMGs after the TPF process, several studies report that the hardness increased, and embrittlement occurred on the processed materials.[3,127–130] For instance, Monfared et al. showed that even though the material remains amorphous after the TPF process, the TPF processed $Zr_{58.5}Cu_{15.6}Ni_{12.8}Al_{10.3}Nb_{2.8}$ MGs have higher hardness values than the original material, and the hardness is increased with higher forming temperature (Figure 11(a)).[127] The study concluded that this increase in hardness is owing to the annihilation of the free volume in the amorphous material during the TPF.[127]

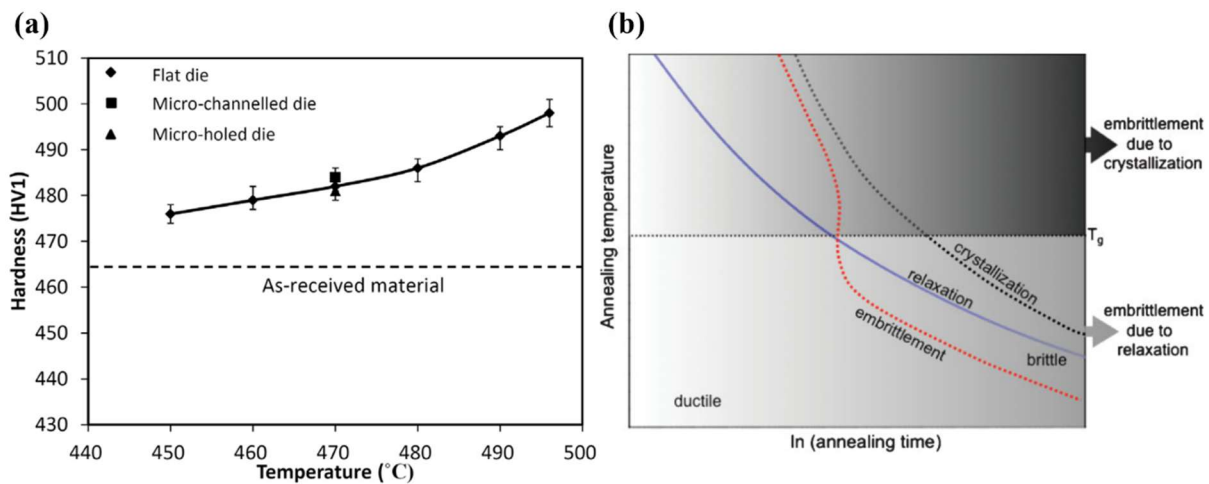


Figure 11: (a) Hardness (HV1) change of $Zr_{58.5}Cu_{15.6}Ni_{12.8}Al_{10.3}Nb_{2.8}$ MG after thermoplastic forming at different temperatures.[127] (b) A schematic illustration of the embrittlement kinetics in BMGs with respect to annealing temperature and time. The embrittlement of BMGs originates from the structural relaxation when annealed below T_g and the crystallization when annealed above T_g .[19,128]

The temperature exposure during TPF processes can cause embrittlement in BMGs.[1,3,19,128,129] Figure 11(b) illustrates how structural relaxation actuates the embrittlement when annealing below T_g .[19,128] When annealing above T_g , crystallization dominates the embrittlement, and even the early stages of the crystallization process cause considerable embrittlement.[1,19,128] Furthermore, annealing was also found to affect the elastic constants of BMGs.[19,128,131] Therefore, it was believed that the fabrication of BMG

parts via TPF must refrain from crystallization to avoid noticeably embrittling the material and loss of mechanical properties.[1,3,19,41,126]

3.2 Limited Materials for Biological Research on Rigid-Ordered Surfaces

The surface topography of the implants plays an essential role in their osseointegration and anti-biofilm properties due to their influence on protein adsorption and cell behavior. [40,132–134] First, surface topography can deeply modify surface–protein interactions and thus change the amount, binding strength, orientation, and conformation of the adsorbed protein.[135] The adsorbed protein covering the surface can define subsequent cell adhesion.[40,134,136] On the other hand, numerous studies demonstrate how cells can sense their surroundings and use mechanotransduction to translate mechanical cues like topography and stiffness into biochemical signals that regulate cell response and function.[134,137–142] In terms of antimicrobial properties, several studies demonstrate that micro- and nano-scale topographies can reduce bacteria adhesion, which is crucial for hard-tissue implant applications.[107,143]

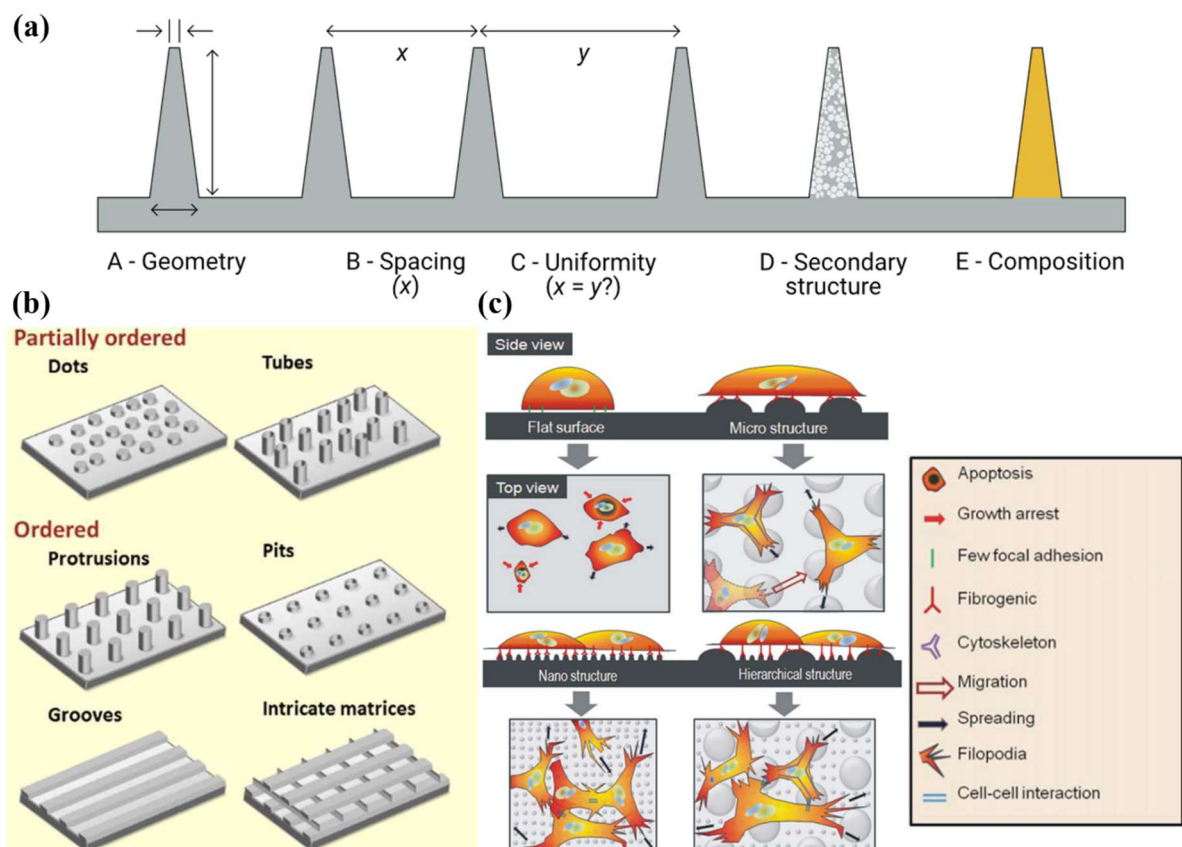


Figure 12: Various strategies to optimize the pattern design for implant surfaces: (a) Design parameters for surface patterns.[144] (b) Schematic illustration of representative partially ordered and ordered surface patterns.[134] (c) Schematic illustration of the effects of various surface patterns on cellular activities, including flat surface, micro-, nano-, and hierarchical structured surfaces.[145]

On a deeper level, further research tempts to understand how pattern parameters, such as the geometry, dimension, aspect ratio, repeat spacing, and uniformity of a patterned surface, can substantially influence cell attachment, migration, proliferation, and differentiation with various cell types (Figure 12).[35,134,145–148] Generally, micro-structured substrates can alter cell morphology and cytoskeletal structure, while nano-structured surfaces can affect cell functions, especially proliferation, differentiation, and alignment.[35,145] Furthermore, there are also reports that multimodal surface topography, such as hierarchical structures, influences protein adsorption with both, micro- and nano-features. For example, micro-roughness enhanced protein adsorption, which is expected to occur due to the presence of additional active sites and features for a larger specific surface area.[135,149] At the same time, nano-roughness has no clear effect on adsorption, but its aspect ratio can affect protein conformation and orientation.[135,150,151]

Currently, highly ordered patterns are primarily created with polymeric substrates, and less research on cell responses has been done on rigid- and ordered-patterned surfaces.[134] Most studies on patterned Ti-alloys rely on chemical and laser-based approaches to achieve hierarchical topography, in which uncontrollable roughness is a primary challenge. Compared with arbitrary roughness, surface topography with well-defined dimensions makes it simple to qualify and quantify the effect of a designated surface feature on a specific cell or bacterial behavior.[35,58,134] Transferring beneficial patterns studied from soft materials onto metallic implant surfaces while maintaining fidelity is still challenging. Therefore, Publication II showcases surface patterning with multi-length-scale features on BMGs using TPF, broadening the possibility of studying cell behavior on rigid and ordered surfaces.[35]

3.3 Pt-Based Bulk Metallic Glasses for Hydrogen Production

Platinum (Pt)-based materials have been proven to be the most efficient catalysts for hydrogen evolution reaction (HER).[118,152,153] According to experimental and theoretical calculation studies, Pt element achieves high HER catalytic activity thanks to the most approachable zero hydrogen absorption energy, which is illustrated in the experimental “volcano plot” (Figure 13).[118,152,154] The volcano plot shows that Pt has both a high exchange current density (catalytic activity) and intermediate metal–hydrogen bond strength (moderate strength of Pt–H bonding) to be the most promising HER catalysts.[118,152,154] However, the high cost, poor stability, and scarcity of Pt severely limit their vast utilization.[118,152,154–156]

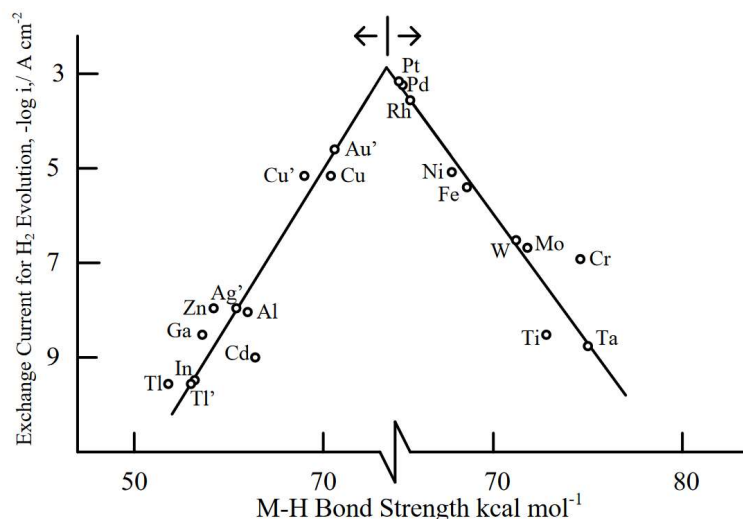


Figure 13: Experimental Volcano plot for HER: Exchange current density as a function of the hydrogen adsorption energy of metal–hydrogen bonds for pure metals.[152,157]

Noble metal-based BMGs, such as those based on Pt and Pd, can easily be molded and patterned via the TPF process when heated up to supercool liquid region (SCLR) and have been applied to jewelry and implant applications.[1,2,70,114,158,159] Additionally, BMGs could be a strategy to ease the financial burden of noble elements by forming alloys with other inexpensive metals and lowering noble metal loading.[118,158]

In the context of electrocatalytic application, several studies demonstrated the advantageous properties of TPF-nanostructured Pt-based BMGs in hydrogen oxidation (HOR), oxygen reduction (ORR), and methanol oxidation (MOR).[70,159,160] In terms of HER application, studies showed that Pd-based BMG catalysts, such as Pd_{40.5}Ni_{40.5}Si_{4.5}P_{14.5} BMG with hierarchical nanostructures, Pd₄₀Ni₁₀Cu₃₀P₂₀ MG ribbons, and nanoporous amorphous Pd-Cu-S, exhibit two peculiar features: (i) a self-stabilizing tendency of long-term static overpotentials to achieve specific current densities and (ii) enhanced electrocatalytic activity during the long-term cyclic voltammetry (CV) tests.[17,69,161,162] Both phenomena from Pd-based BMG catalysts are beneficial, in contrast to the declining trend of activity observed in polycrystalline Pd-alloys.[17,159,161–165] Additionally, a hybrid catalyst that embeds Pt nanoparticles on a nanowire-patterned Pd₄₀Ni₁₀Cu₃₀P₂₀ BMG matrix has improved long-term stability and activity in HER.[153,158]

The majority of Pt-based BMG electrocatalytic research is currently concentrated on the hydrogen oxidation reaction in fuel cell applications, where Pt-based BMG catalyst exhibits exceptional durability and activity.[12,21,22,32] The puzzle of Pt-based BMGs for HER in hydrogen production still needs to be discovered.[153] Therefore, in Publication III, the electrocatalytic performance of Pt_{57.5}Cu_{14.7}Ni_{5.3}P_{22.5} BMG (Pt-BMG) with plain, microrod, and nanorod surfaces in hydrogen production via HER was explored.[153] In-depth studies found that the nano-patterned Pt-BMG possesses enhanced catalytic activity and long-term stability for HER due to the in-situ formation of Cu_xO foam on top of the Pt-BMG nanorods.[153]

4 Major Materials and Methods

4.1 Materials

4.1.1 Bulk Metallic Glasses

Ti₄₀Zr₁₀Cu₃₄Pd₁₄Sn₂ BMG

Aiming for dental and orthopedic applications, Ti₄₀Zr₁₀Cu₃₄Pd₁₄Sn₂ BMG (at%) is chosen to study creating surface patterns using the TPF technique. Ti₄₀Zr₁₀Cu₃₄Pd₁₄Sn₂ BMG is based on a well-explored Ti₄₀Zr₁₀Cu₃₆Pd₁₄ BMG, but 2 at.% of copper is replaced by tin. The original Ti₄₀Zr₁₀Cu₃₆Pd₁₄ BMG has shown satisfactory biocompatibility, and compared with the benchmark Ti-6Al-4V alloy, it has good corrosion resistance (a higher corrosion potential and a lower corrosion rate), relatively higher strength, and lower Young's modulus.[16,166–168] Hence, Ti₄₀Zr₁₀Cu₃₆Pd₁₄ BMG is a promising material for dental implants. However, the Ti₄₀Zr₁₀Cu₃₆Pd₁₄ BMG has some disadvantages for the TPF process, such as a narrow SCLR ($\Delta T_x = 47$ °C) and low fragility.[56,169,170] The material has only roughly one order of magnitude of viscosity reduction in the SCLR and, thus, is very hard to deform by the viscous flow deformation during the TPF process.[21,56,170] In addition, the annealing time before crystallization begins is short, leading to a short TPF processing window of Ti₄₀Zr₁₀Cu₃₆Pd₁₄ BMG because BMGs cannot be deformed once fully crystallized.[21] By substituting Cu with 2 at.% Sn, the Ti₄₀Zr₁₀Cu₃₄Pd₁₄Sn₂ BMG has a better GFA and a larger SCLR ($\Delta T_x = 55$ °C) before crystallization compared with Ti₄₀Zr₁₀Cu₃₆Pd₁₄ BMG, thanks to the effective control of the nucleation of crystalline phases.[169,171–174] As a result, the Ti₄₀Zr₁₀Cu₃₄Pd₁₄Sn₂ BMG has a greater potential to be processed via TPF than Ti₄₀Zr₁₀Cu₃₆Pd₁₄ BMG.[21] The comparison of DSC curves between Ti₄₀Zr₁₀Cu₃₆Pd₁₄ and Ti₄₀Zr₁₀Cu₃₄Pd₁₄Sn₂ BMGs is shown in Figure 14(a). The Ti₄₀Zr₁₀Cu₃₄Pd₁₄Sn₂ BMGs were fabricated in-house; see section 4.2.2 for details.

Pt_{57.5}Cu_{14.7}Ni_{5.3}P_{22.5} and Pd₄₃Cu₂₇Ni₁₀P₂₀ BMGs

Both Pt_{57.5}Cu_{14.7}Ni_{5.3}P_{22.5} (Pt-BMG) and Pd₄₃Cu₂₇Ni₁₀P₂₀ (Pd-BMG) used in this thesis were provided by PX Services SA and produced via induction-melting and tilt-casting. The feedstocks with nominal composition Pt_{57.5}Cu_{14.7}Ni_{5.3}P_{22.5} and Pd₄₃Cu₂₇Ni₁₀P₂₀ (at%) were alloyed using high-purity components (> 99.95%) in an induction furnace, which minimizes P losses from evaporation. The alloyed feedstock was then cast into a BMG rod with a 6 mm diameter and 100 mm length by tilt-casting into a copper mold.[153] All melting and casting operations were done in a high-purity argon-protective atmosphere, and no fluxing chemicals were introduced. Disks of 1.5 mm in thickness were cut from the as-cast rod. To confirm the amorphous structure of the whole as-cast rod, XRD was performed on the disks from the bottom, middle, and top sections using a Bruker D2 Phaser and Co K_α radiation ($\lambda = 0.17889$ nm).[153] The DSC curves of Pt-BMG and Pd-BMG are illustrated in Figure 14(b).

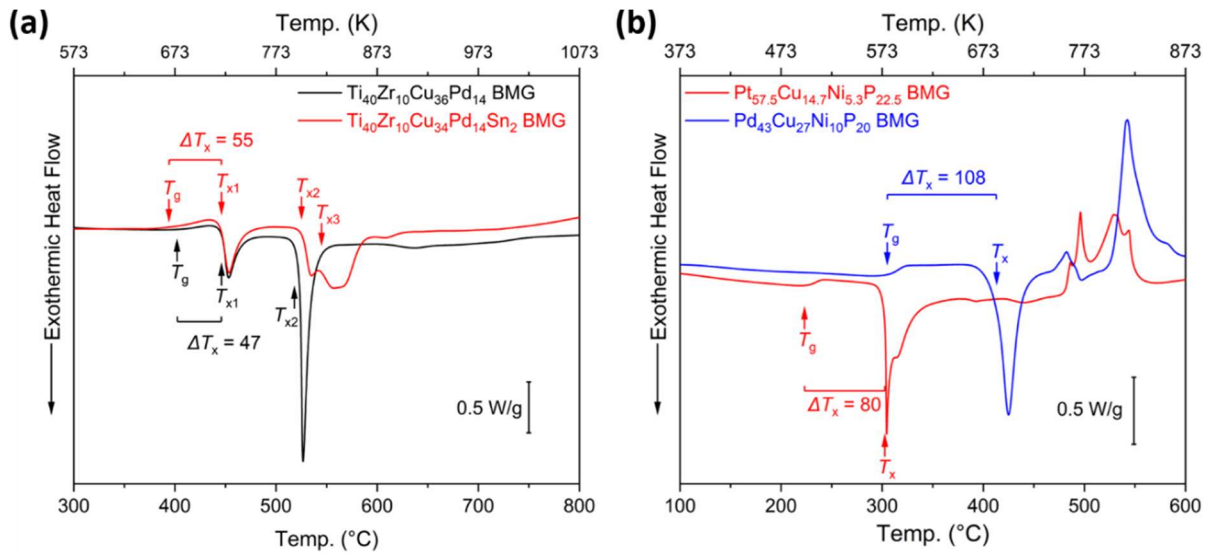


Figure 14: DSC curves from constant-rate heating (20 °C/min) measurements: (a) comparison of $\text{Ti}_{40}\text{Zr}_{10}\text{Cu}_{34}\text{Pd}_{12}\text{Sn}_2$ and $\text{Ti}_{40}\text{Zr}_{10}\text{Cu}_{36}\text{Pd}_{14}$ BMGs, (b) comparison of $\text{Pt}_{57.5}\text{Cu}_{14.7}\text{Ni}_{5.3}\text{P}_{22.5}$ and $\text{Pd}_{43}\text{Cu}_{27}\text{Ni}_{10}\text{P}_{20}$ BMGs.

4.1.2 Bioresorbable Polymers

The bioresorbable polymers poly(D,L-Lactide-co-PEG5000) (PDLLA-PEG) used for spin-coated samples were synthesized by Ashland Specialties Ireland Ltd.

4.1.3 Templates for TPF

Table 1 summarizes various patterning molds implemented in the TPF processes.

Table 1: A summarized list of templates used in this thesis.

Section	Material	Features	Supplier
Publication I [21]	W720 tool steel	An array of 300 μm cubes with 300 μm gaps	Customized at workshop ^[1]
	Macro-porous silicon	5 μm pore diameter and 12 mm interpore distance	SmartMembranes GmbH
Publication II [35]	Macro-porous silicon	2.5 μm pore diameter and 4.2 μm interpore distance	SmartMembranes GmbH
	Nano-porous alumina	400 nm pore diameter and 480 nm interpore distance	
Publication III [153]	Macro-porous silicon	2.5 μm pore diameter and 4.2 μm interpore distance	SmartMembranes GmbH
	Nano-porous alumina	90 nm pore diameter and 125 nm interpore distance	
5.4.3	Macro-porous silicon	1 μm pore diameter and 1.5 μm interpore distance	SmartMembranes GmbH
	Nano-porous alumina	40 nm pore diameter and $10^{-12} \sim 10^{-8}$ pore density	InRedox LLC

[1]: The W720 tool steel templates were fabricated using wire-cut electrical discharge machining (EDM MV1200S, Mitsubishi Electric Europe B.V.).

4.2 Casting of Ti-BMGs

4.2.1 Arc Melter Apparatus

An integrated system with plasma arc melting and suction casting (Arc Melter AM 500, Edmund Bühler GmbH) is utilized to prepare $Ti_{40}Zr_{10}Cu_{34}Pd_{14}Sn_2$ master ingots and BMG samples (fabrication details see section 4.2.2). The photo of the basic setup of the arc melter is shown in Figure 15(a). The arc melter requires four supplementary elements for the operation: (i) power supplier, (ii) recirculating water-cooling chiller, (3) inert gas bottle, and (iv) vacuum pump.[175] A power supply allows arc ignition without touching the sample, which is suitable for preparing high-purity metallic alloys.[175] The recirculating water-cooling chiller has a loop flow internally through the copper crucible plate (Figure 15(b)) and the water-cooled tungsten electrode.[175] The inert gas bottle provides Argon gas as the shielding gas during the melting.[175] The vacuum pump includes the rotary and the diffusion units to remove the pollution and the reactive gases from the melting chamber.[175] To ignite the arc without contact, the power supplier has an inverter section equipped with a high-frequency facility to strike a spark between the electrode and the crucible; plus, the shielding gas creates a conductive path, thereby starting the melting arc.[175] The melting arc formed between the electrode and the metals to produce heat, melting the metals in the crucible to form an alloy.

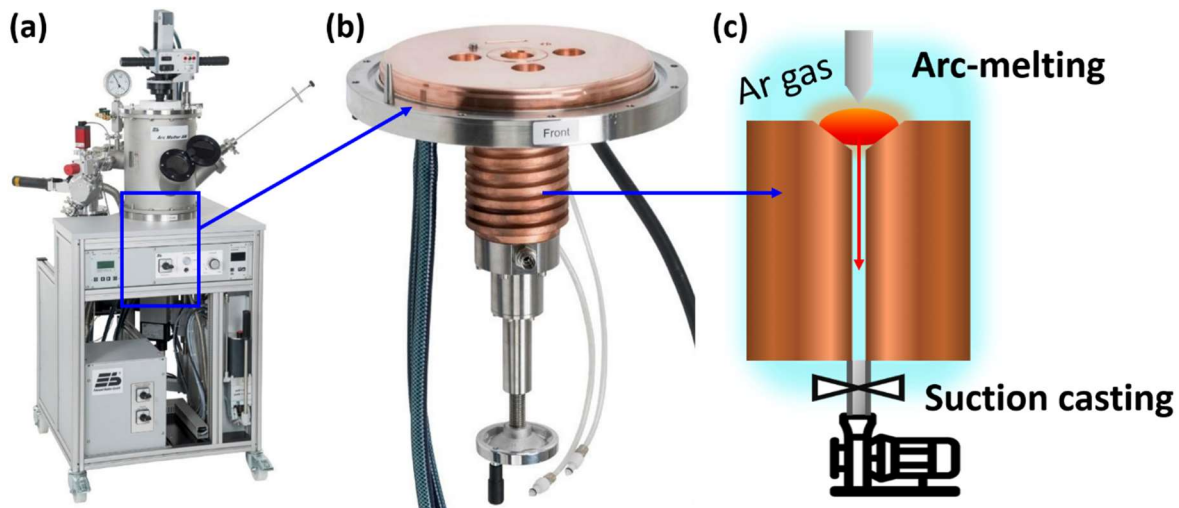


Figure 15: The integrated system with plasma arc melting and suction casting: (a) Arc Melter AM 500.[176] (b) Copper crucible plate with suction casting components.[177] (c) illustration of suction casting.

The suction-casting components are installed under the copper crucible plate, as illustrated in Figure 15(c). The essential components are (i) copper mold, (ii) control valve, and (iii) suction chamber. The copper mold is mounted right below the copper crucible plate, then

the control valve, and finally, the suction chamber. The suction chamber was under vacuum condition using the vacuum pump before casting. Therefore, the suction chamber has lower air pressure than the melting chamber. After the master alloy is properly re-melt, the control valve is opened to let the lower air pressure in the suction chamber ‘‘suck’’ the metal melt into the copper mold.

4.2.2 Fabrication of Ti-BMGs

The $\text{Ti}_{40}\text{Zr}_{10}\text{Cu}_{34}\text{Pd}_{14}\text{Sn}_2$ BMGs were produced using an arc-melter with a suction casting option (Arc Melter AM 500, Edmund Bühler GmbH). Firstly, the master ingots with nominal composition $\text{Ti}_{40}\text{Zr}_{10}\text{Cu}_{34}\text{Pd}_{14}\text{Sn}_2$ (at%) were prepared by melting and mixing pure elements (purities: Ti: 99.995%; Zr: 99.95%; Cu 99.999%; Pd 99.9%; Sn: 99.99%) by arc-melting. Each ingot was melted above the liquidus temperature for five times to ensure homogeneity. The ingot is then cast into the desired geometry, such as a rod and a disk, by copper mold suction casting. The same arc-melting apparatus, operated in a Ti-gettered Ar environment, was used for both master ingot preparation and suction casting. The optimized parameters for casting $\text{Ti}_{40}\text{Zr}_{10}\text{Cu}_{34}\text{Pd}_{14}\text{Sn}_2$ BMGs into various dimensions are summarized in Table 2.

Table 1: Optimized parameters for suction-casting $\text{Ti}_{40}\text{Zr}_{10}\text{Cu}_{34}\text{Pd}_{14}\text{Sn}_2$ BMG disks.

Dimension (Thickness x Diameter)	Ingot Mass (g)	Barometric Pressure in Chamber (bar)	Melt Current (A)	Throttle (turns)
2.5 mm x 12 mm	2.85	-0.1	130 ~ 135	10
2.0 mm x 12 mm	2.80	-0.1	130	10
1.0 mm x 12 mm	1.20	-0.1	100	10

Depending on the geometry and the following experiments, the as-cast Ti-BMGs were cut differently. The as-cast Ti-BMG rods were cut to the desired thickness for DSC analysis and deformability test using a Struers Accutom 50 device.[21] For the surface patterning experiments, the as-cast Ti-BMGs disks with 2.5 mm thickness were sliced in of half the thickness using a wire-cut electrical discharge machining (EDM MV1200S, Mitsubishi Electric Europe B.V.) and then mirror-polished to a thin disk with a thickness around 1 mm and surface roughness (Ra) less than 1 μm . The polish step eliminated potential surface crystallization and oxidation, ensuring the surfaces were parallel for the TPF processing.

4.2.3 Optimization of Copper Mold for Disk Fabrication

A good copper mold design is essential to cast BMGs. The main functions of copper molds are (i) controlling the final shape of the casting and (ii) cooling down the casting quickly enough to avoid crystallization. In order to have final samples suitable for in-vitro biological

assays, which require at least 10 mm in diameter and around 1 mm in thickness, the mold was designed to cast BMGs into disk shape. The final design of the copper mold to fabricate BMG disks is displayed in Figure 16(a). There are four main components in this mold design:

- (1) Ingot holder: The place holds the ingot to re-melt the master alloy.
- (2) Upper mold (cope): This part includes a tunnel connected to the ingot holder, allowing the melted alloy to flow into the mold.
- (3) Spacer: The spacer controls the thickness and shape of the disk.
- (4) Lower mold (drag): This part includes air passages allowing the Argon gas from the melting chamber to flow into the vacuum chamber underneath the mold.

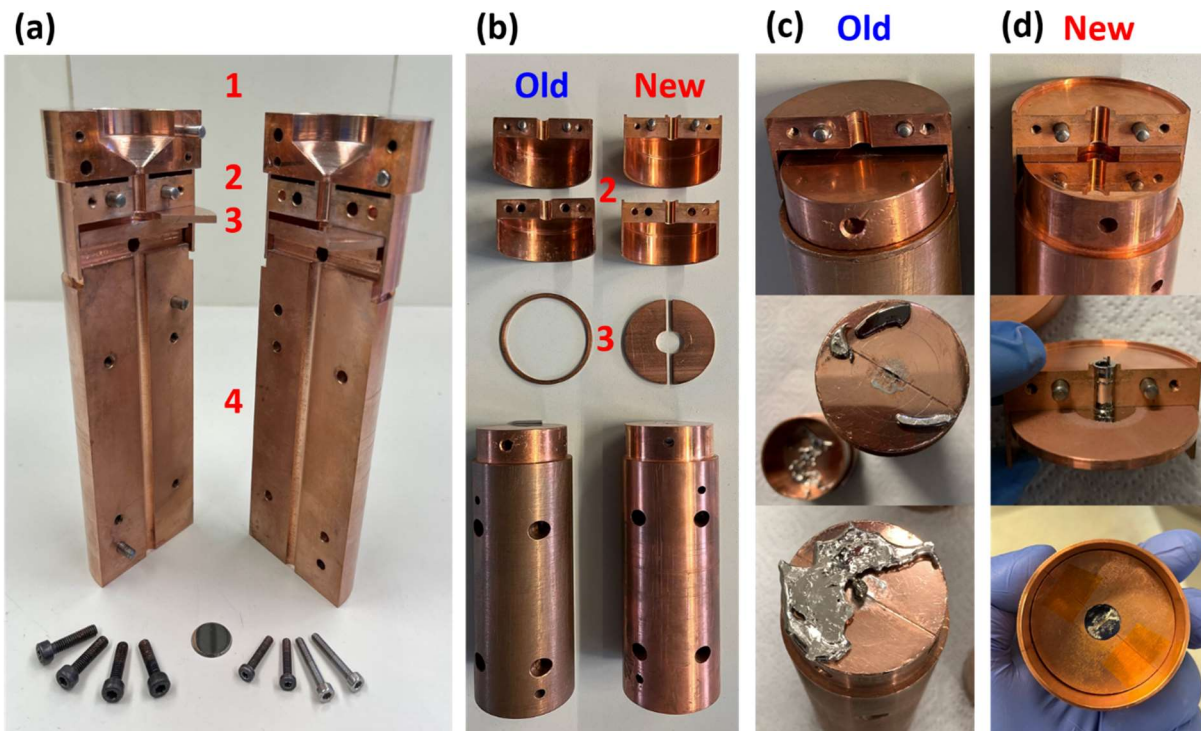


Figure 16: (a) The final design of the copper mold and a Ti-BMG disk in the center. (b) Disassembly photo of old and new copper molds. A detail view of casting space in the mold and the final casting products of the (c) old and (d) new designs.

Compared with the original mold, this new design has gone through serial optimizations, as shown in Figure 16(b). There are two main evolutions in the new design. The new upper mold (2) features a notch to create a gap between the ingot holder. This gap hinders the heat conduction from the ingot holder to keep the mold cold when melting the ingot. The other evolution is the spacer (3). The old spacer is a copper ring installed on the outer side of the lower mold, and the upper mold stands on the spacer to create the casting space in the upper mold. The main issue with the old spacer is that the copper ring can only define the casting thickness but fails to control the shape of the final casting, as revealed in Figure 16(c).

On the contrary, the new spacer comprises two half-piece gaskets installed inside the upper mold. There are three advantages of this new design (Figure 16(d)): (i) precise control of

casting shape and thickness, (ii) improved cooling rate of the casting by creating more contact area, and (iii) more tolerance for casting parameters such as heating current and chamber pressure. Lastly, the design of two half-piece gaskets is economically beneficial because it can be customized to cast in different shapes, such as square plates and gears, without changing other mold components.

4.3 Thermoplastic Forming of BMGs

All BMG disks were ground and mirror-polished to a thickness of about 1 mm and surface roughness (Ra) of less than 1 μm to eliminate potential surface oxidation and ensure the parallel surfaces required for further TPF processing.

4.3.1 Original Apparatus Based on Zwick Type 1382

In the first publication, the fundamental layout of the TPF process includes a compression test machine (Zwick Type 1382) with a custom vacuum chamber, a vacuum pump, and a resistance heating sheath surrounding the chamber (Heraeus Type 19.519.000), as demonstrated in Figure 17.[21]

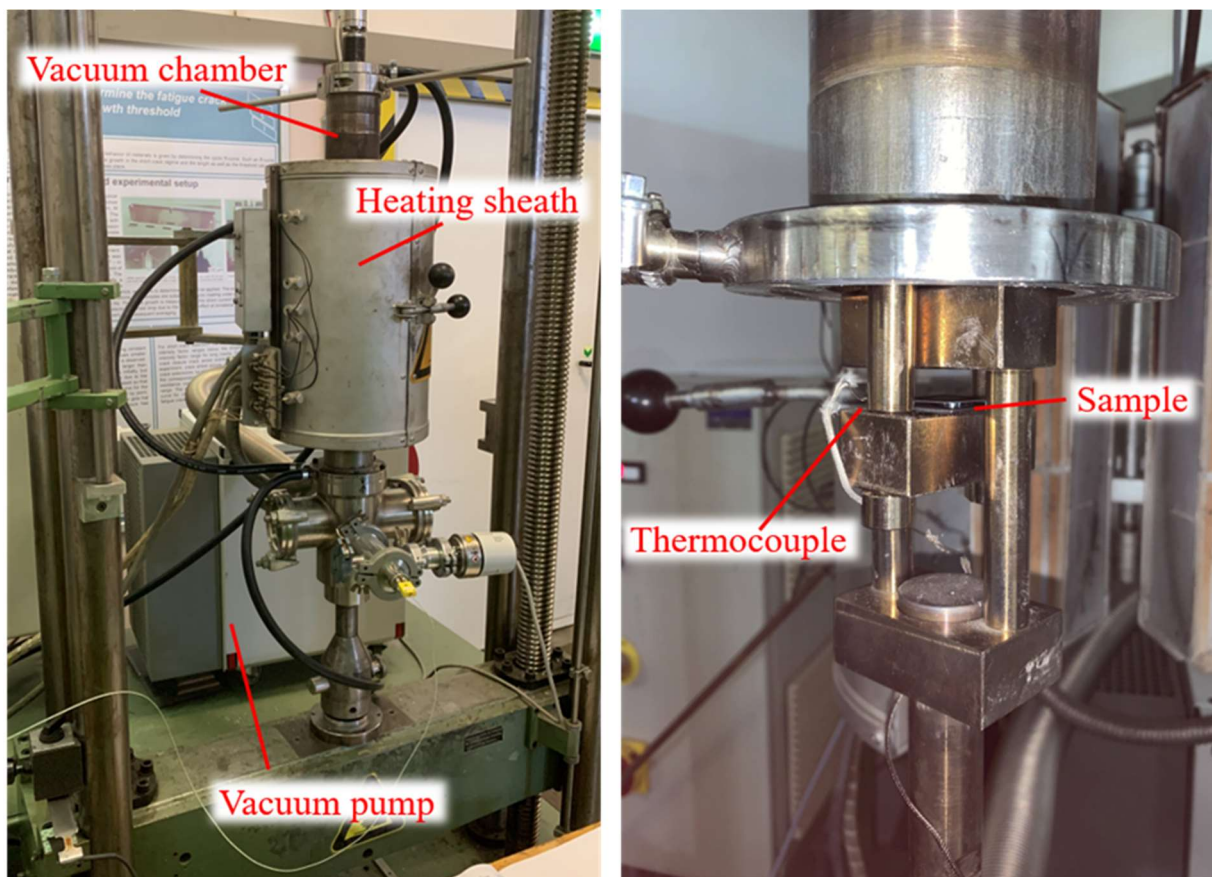


Figure 17: The apparatus of thermoplastic forming (TPF) process used in the first publication.[21] Because of the configuration of the shaft components, the compression test machine drives in a tensile direction to apply compressive stress to the sample.

To alleviate the influence of oxidation throughout the material flow, the TPF process was executed in an enclosed chamber under vacuum (4×10^{-4} mbar) conditions.[21] The heating sheath heated the vacuum chamber to the targeted temperature between 430 °C and 450 °C with an average heating rate of around 6.8 °C/min.[21] Additionally, to prevent undesired dynamic impact, a preload of 1 kN was applied to the specimen before the sample reached the targeted temperature.[21] When the sample reached the processing temperature, the load was gradually increased to the highest load of 10 kN with a loading rate in the range of 4.5 ~ 7.5 N/s and held for a predetermined duration.[21] The force, temperature, and displacement of the process were monitored and recorded on a computer using the LabVIEW system design program.[21]

This apparatus realizes the basic research on the TPF process for Ti-BMGs. However, there are several drawbacks to this setup:

- The maximum force of this compression test machine is only 10kN, which means it can apply only pressure of 127 MPa on a 10 mm diameter disk.
- The target force is manually controlled by a knob adding uncertainty to the reproducibility, and loading rate control is almost impossible.
- The sample must be pre-installed into the enclosed chamber, then the heating sheath is placed to heat the vacuum chamber. This means the sample needs to heat along with the whole system, costing the TPF process window of BMGs.
- The sample is heated indirectly by the heating sheath through the vacuum chamber, resulting in a long heating-up stage (at least 1 hour to achieve 400 °C), and the sample temperature is prone to overshooting.
- The pull-to-compress configuration is not mechanically stable, resulting in poor pressure distribution.

Due to the above-mentioned drawbacks, upgrading the TPF apparatus was crucial to level up the TPF research. More details are revealed in section 4.3.2.

4.3.2 Upgraded Apparatus Based on Zwick Z100

An upgraded TPF apparatus (Figure 18) was utilized in Publications II and III.[35,153] This new apparatus design was inspired by the prior research by Prof. Jan Schroers and colleagues at Yale University.[50,178] The entire system is built around a compression testing machine (Zwick Z100, ZwickRoell GmbH & Co. KG) and customized components such as upper and lower anvils fitted with heating cartridges, thermocouples, a PID controller, and water-cooling circulation.[35,153] The anvils have preserved holes to fit heating cartridges and thermocouples. The thermocouples send live time signals to the PID controller for temperature control. The most significant improvement of our setup over the apparatus at Yale University is adding a water-cooling circulation system. The apparatus at Yale University lacked a proper cooling system to eliminate the heat transfer from anvils to the loading cells, which caused the

compression testing machine to malfunction during long-term experiments. Our water-cooling circulation system can effectively keep the loading cells cool even after 6 hours of operation at 400 °C. A manual, including the installation and operation of this ad-hoc TPF apparatus, is attached in the Appendix.

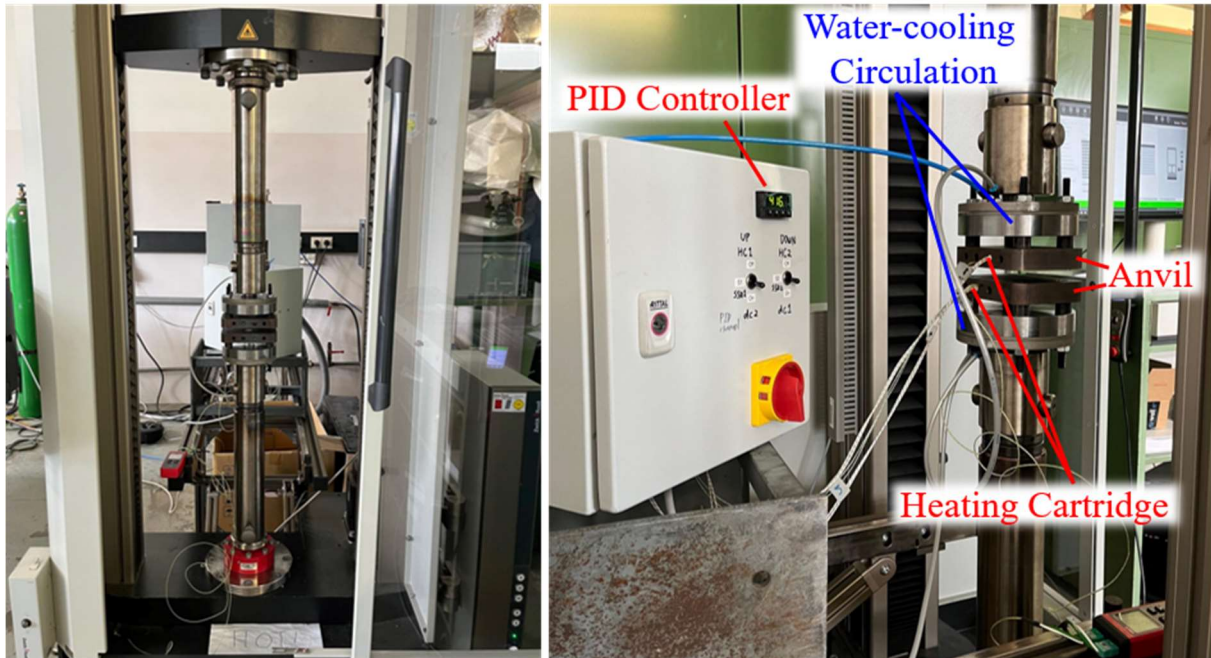


Figure 18: The upgraded apparatus of thermoplastic forming (TPF) process used in Publication II and III.[35,153]

This upgraded apparatus based on Zwick Z100 have significant improvements over the original apparatus based on Zwick Type 1382:

- The maximum force is raised to 100 kN, which can deliver 1.27 GPa pressure on a 10 mm diameter disk. This pressure is 10 times higher than that of the previous apparatus.
- The target force and loading rate are pre-programmed and computer-controlled. The loading rate can be regulated either by force or by displacement. All these features significantly improve the reproducibility.
- Without the enclosed vacuum chamber, the sample can be inserted after the anvils achieve the target temperature, saving the TPF process window of BMGs.
- The sample is heated directly by the anvils. Hence, the sample temperature can achieve 400 °C within 1 minute. Furthermore, the anvils take around 20 min to 400 °C, at least 60% faster than the original apparatus.
- The rigid and stable components, such as force-delivering shaft and anvils, ensure good pressure distribution on the sample surface.

Thanks to all the above improvements, Ni-free Ti-BMG disks with nano-patterns and hierarchical structures via TPF were accomplished as described in Publication II.[35]

4.3.3 Summarized TPF Process Parameters

All TPF process parameters applied in this thesis are summarized in Table 3.

Table 2: Summarized TPF process parameters

Section	Material	Temp. (°C)	Max. Force (kN)	Load Rate (kN/min)	Hold Time (min)	Step	TPF Apparatus (section)	Comment
Publication I	Ti ₄₀ Zr ₁₀ Cu ₃₄ Pd ₁₄ Sn ₂	~440	10	0.27 ~ 0.45	40	-	4.3.1	Deformability test
		~440	10	0.27 ~ 0.45	~20	-	4.3.1	Macro-pattern (300 μm)
		~440	10	0.27 ~ 0.45	~10	-	4.3.1	Micro-pattern (5 μm)
Publication II	Ti ₄₀ Zr ₁₀ Cu ₃₄ Pd ₁₄ Sn ₂	410	90	15	4	-	4.3.2	Micro-pattern (2.5 μm)
		410	90	90	9	-	4.3.2	Nano-pattern (400 nm)
		418	90	90	9	1	4.3.2	Hierarchical Structure
		410	90	15	4	2	4.3.2	(400 nm + 2.5 μm)
Publication III	Pt _{57.5} Cu _{14.7} Ni _{5.3} P _{22.5}	253	5.6	5.6	10	-	4.3.2	Flat
		253	1.4	0.7	4	-	4.3.2	Micro-pattern (2.5 μm)
		253	5.6	5.6	6	-	4.3.2	Nano-pattern (90 nm)
5.4.3	Pd ₄₃ Cu ₂₇ Ni ₁₀ P ₂₀	340	5.6	11.2	10	1	Yale	Hierarchical Structure
		340	5.6	0.7	10	2	Yale	(40 nm + 1 μm)

4.4 Material Characterization

The material characterization methods used in this thesis can be classified into five categories, as illustrated in Figure 19. These five categories are (i) structural properties, (ii) thermal properties, (iii) surface properties, (iv) mechanical properties, and (v) electrochemical properties. The experimental methods were adjusted and optimized depending on the scope of each publication. Therefore, detailed information about the methods is described for each publication in section Publications and Appendix.

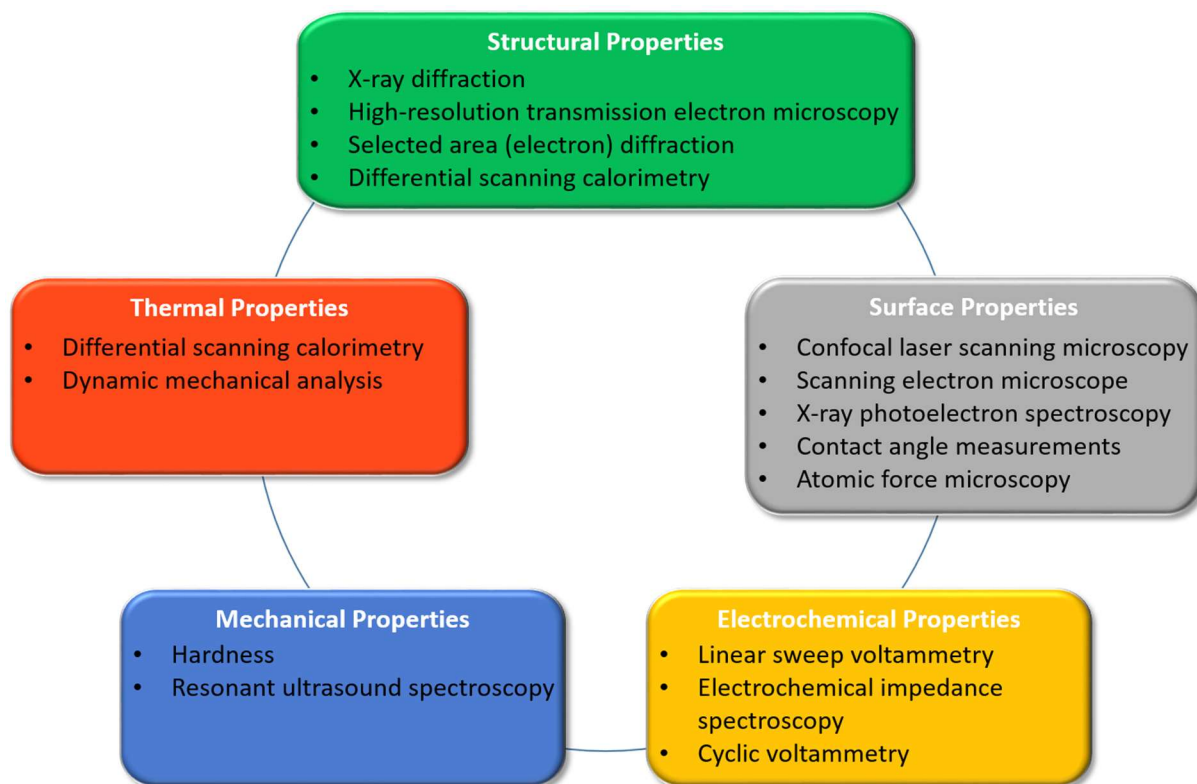


Figure 19: Summary of material characterization techniques used in this thesis.

4.5 In-Vitro Study

The in-vitro studies in this thesis are summarized into a coordinate plane with four quadrants and illustrated in Figure 20. The x-axis distinguishes the cell culture and microbial culture. Methods on the positive x-axis (i.e., Quadrant I and IV) are carried out with host cells, while those on the negative x-axis (i.e., Quadrant II and III) are conducted with bacteria. The y-axis separates the methods by imaging analysis and colorimetric assays. Imaging analysis on the positive y-axis (i.e., Quadrant I and II) directly observes cell and bacterial morphology, distribution, and live-dead physiological states via OM, SEM, fluorescence microscopy, and AFM. It is worth noting that taking multiple images on various regions of the sample is critical for imaging analysis due to the heterogeneous distribution of cells and bacteria on the whole surface. Colorimetric assays on the negative y-axis (i.e., Quadrant III and IV) assess the

concentration of a specific chemical compound in a solution by reading spectral absorbance at a given wavelength with the aid of a color reagent and a colorimeter (spectrophotometer) offering a quantitative estimation on cell growth and viability or biofilm formation.[179]

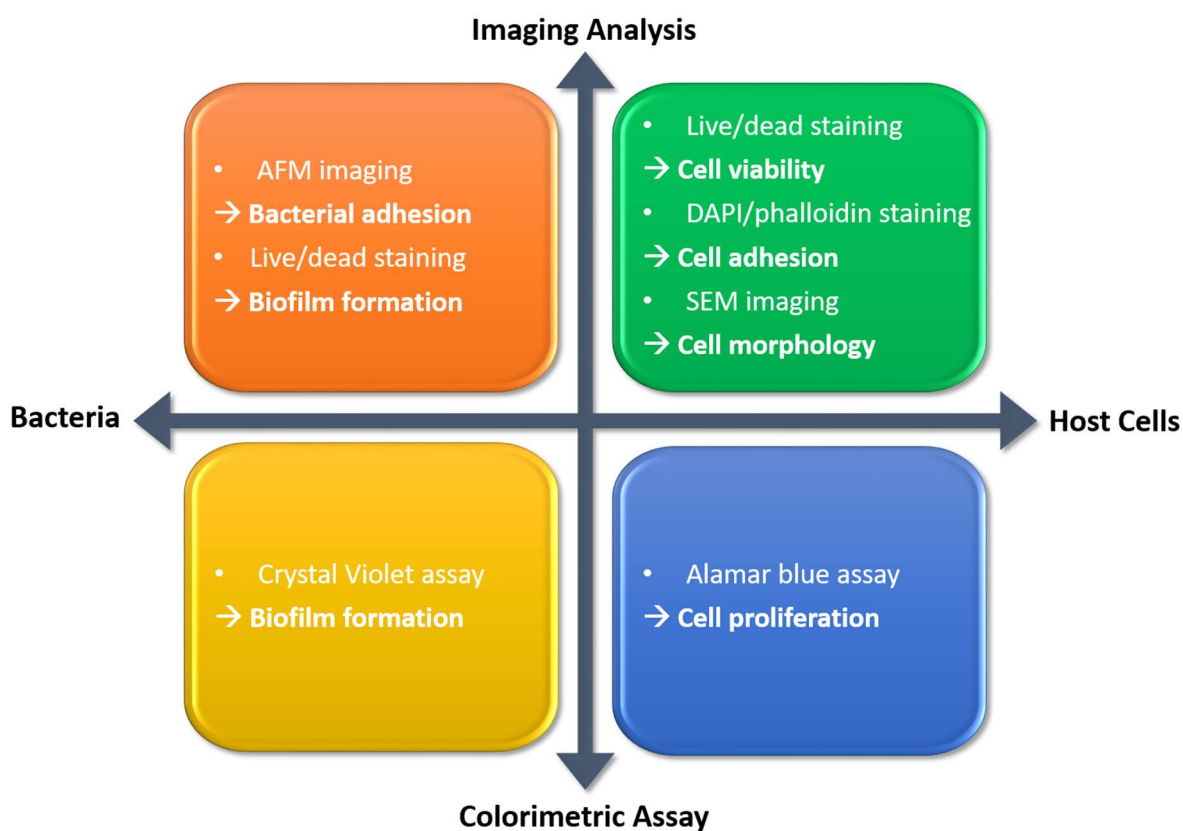


Figure 20: Summary of in-vitro studies used in this thesis to access biocompatibility and anti-biofilm properties.

The in-vitro tests for host cells are described in detail in Publication II. The antibacterial and anti-biofilm assessments shown in this thesis are only preliminary results due to insufficient experimental repetitions.

4.6 Materials and Methods of Unpublished Results

4.6.1 Spin Coating of Bioresorbable Polymers

The spin coating was carried out using a SPIN150i-NPP Single Substrate Spin Processor (SPS-International) with a vacuum chuck to fix the substrate. 0.3 mL of coating solution was dispensed to cover the whole substrate. The spin coating was performed at the rotation rate of 2k, 4k, 6k, 8k, and 10k rpm for 40 seconds with a 10k rpm/sec acceleration rate. After the coating procedure, the samples were air-dried and collected for further study.

The protocol for spin coating of biopolymers includes three main procedures: (i) substrate cleaning, (ii) biopolymer solution preparation, and (iii) spin coating. Firstly, the

mirror-polished Ti-BMG disks (substrates) were cleaned before spin coating. Ti-BMG disks were loaded into a homemade cleaning rack where the disks were placed vertically. The cleaning rack with Ti-BMG disks was immersed in dilute detergent solution (1% universal detergent solution), and ultrasonic cleaning was applied for 15 minutes. Afterward, the cleaning rack with Ti-BMG disks was rinsed with deionized water and then immersed in deionized water, and ultrasonic cleaning was applied for 5 minutes. The deionized water was changed, and then ultrasonic cleaning was applied for another 5 minutes, repeated thrice. Finally, the cleaning rack with Ti-BMG disks was immersed in acetone and 2-isopropanol for ultrasonic cleaning for 15 minutes each. The cleaned Ti-BMG disks were dried in air and collected for use.

For biopolymer solution preparation, PDLLA-PEG polymer granules were dissolved in chloroform to prepare PDLLA-PEG coating solution with 5% (w/v) and 7.5% (w/v). A final check occurred before the spin coating procedure to ensure that (i) substrates were clean without visible particles and (ii) polymers were fully dissolved into the solution.

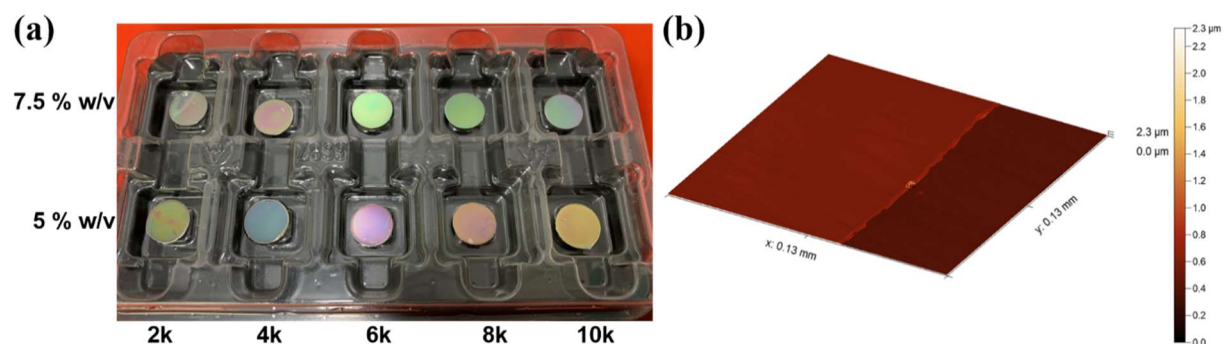


Figure 21: Spin coating of PDLLA-PEG on Ti-BMG disks: (a) A photo of coatings with different parameters. (B) Step height measurement from CLSM images for coating thickness.

The coated sample is shown in Figure 21(a). It is worth noting that the difference in the color of the coating implied the different coating thickness. The coating thickness was evaluated via step height measurements on CLSM images taken from the regions where part of the coating was scratched to the substrate, as displayed in Figure 21(b). The results for coating thickness are summarized in Table 4. A coating thickness between 100 nm and 250 nm is targeted for the hard tissue implant application. Hence, the coating parameter with 10000 rpm rotation speed and 7.5% w/v solution concentration was chosen for further examination.

Table 3: The thickness of PDLLA-PEG coating regarding rotation speed (rpm) and solution concentration (% w/v).

Conc.	Thickness (nm)				
	2000 rpm	4000 rpm	6000 rpm	8000 rpm	10000 rpm
7.5% w/v	≈ 300 ~ 400	≈ 300 ~ 360	≈ 180 ~ 300	≈ 150 ~ 300	≈ 130 ~ 200
5.0% w/v	≈ 130 ~ 220	≈ 150 ~ 230	≈ 70 ~ 220	≈ 60 ~ 160	≈ 20 ~ 100

5 Discussion and Summary of Scientific Contributions

5.1 Thermoplastic Forming of Ti-BMGs with Nanocrystallization

As mentioned in section 3.1, BMG communities believed that the processing window of TPF is defined by the TTT curves of the material, and it was crucial to avoid intersecting the nose-shaped crystallization curves during the whole TPF process. The main concerns about the crystallization during TPF are (i) loss of the deformability and (ii) loss of the mechanical properties of BMGs. **Publication I** and **Publication II** tackle both concerns step by step in the following sections.

5.1.1 TPF Can Shape and Pattern BMGs Even with Nanocrystallization

Publication I re-considered the belief that *BMGs can not be deformed and patterned once the materials are crystallized* and applied the proposed TPF strategy on $\text{Ti}_{40}\text{Zr}_{10}\text{Cu}_{34}\text{Pd}_{14}\text{Sn}_2$ BMG to shape a rod into a disk and create patterns from macro- to micro-scale.[21] Standing on the results of Publication I, **Publication II** advances the TPF technique to the nano-scale and a hierarchical structure integrating micro- and nano-patterns on the same surface, and this is the first time nano-patterns and hierarchical structures are achieved on Ni-free Ti-based BMGs.[35] The following are key contributions:

- Even when the $\text{Ti}_{40}\text{Zr}_{10}\text{Cu}_{34}\text{Pd}_{14}\text{Sn}_2$ BMG is annealed quite near to T_g , the first nanocrystalline phase tends to form within short periods of time.[21] For example, the isothermal DSC analysis proved that the first phase crystallization happens in less than 10 minutes, even at 23 °C above T_g (Figure 22(a)).[21]
- In this case, as illustrated in Figure 22(b), the conventional TPF process route (P2) would operate for a short time and slightly above the T_g to avoid intersecting the crystallization curve in the TTT diagram. **Publication I** proposed a strategy (P3) for TPF of $\text{Ti}_{40}\text{Zr}_{10}\text{Cu}_{34}\text{Pd}_{14}\text{Sn}_2$ BMG, accepting that nanocrystals will form but making use of the lower viscosity of the supercooled liquid when operating at higher temperatures above T_g . [21]
- Following this strategy, the $\text{Ti}_{40}\text{Zr}_{10}\text{Cu}_{34}\text{Pd}_{14}\text{Sn}_2$ BMG rod can be deformed to a thin disk with only 18% of its initial height. Moreover, surface patterns with scales from 300 μm down to 400 nm are successfully imprinted on BMG disks (Figure 22(c)).[21,35]
- In **Publication II**, the strategy of allowing nanocrystallization is developed into a two-step TPF process to create a hierarchical structure integrating 400 nm HCP protrusions on 2.5 μm square protuberances (Figure 22(c-d)).[35]
- The isochronous DSC analysis proved the nanocrystal formation in TPF-processed samples through a weaker or missing first exothermic peak.[35]

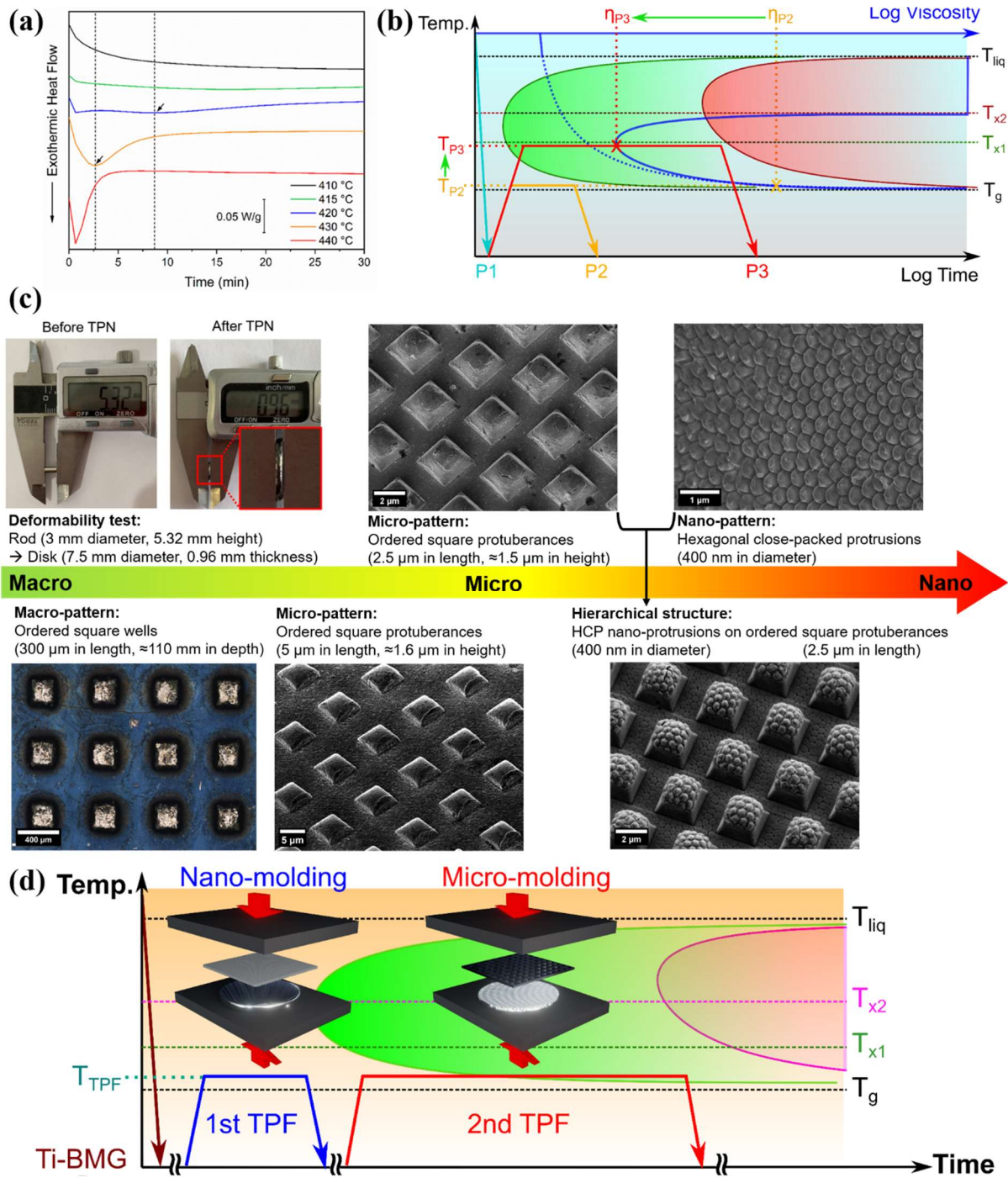


Figure 22: TPF of $Ti_{40}Zr_{10}Cu_{34}Pd_{14}Sn_2$ BMG with nanocrystallization: (a) Isothermal DSC curves at various temperatures.[21] (b) Schematic TTT diagram illustrating the conventional TPF process route (P2) and the proposed strategy (P3).[21] (c) TPF processed $Ti_{40}Zr_{10}Cu_{34}Pd_{14}Sn_2$ BMG from macro- to nano-scales. Adapted from [21,35]. (d) The two-step TPF process to create hierarchical structures.[35]

The results above indicate that BMGs can still be shaped and patterned via TPF, even with the formation of nanocrystals during the initial crystallization event.[21,35] Moreover, the processing temperature can be near to T_x to make use of the lower viscosity of the amorphous matrix to deform and pattern the material.[21] **Publication I** and **Publication II** reveal the

prospect of utilizing the TPF process for a wide range of mediocre glass forming systems and semi-crystalline composites into surface-enhanced functional materials.[21,35]

5.1.2 Crystallization Tolerance in $Ti_{40}Zr_{10}Cu_{34}Pd_{14}Sn_2$ BMG for Mechanical Properties

When BMGs are annealed at high temperatures like TPF, their amorphous structures tend to re-arrange in the manner of relaxation and crystallization. Both relaxation and crystallization are known to influence the mechanical properties of BMGs and can be quantified by DSC analysis.[35] In **Publication I**, it is discovered that after the TPF process with nanocrystallization to the degree that the first exothermic peak fully vanished in the DSC curve, the Vickers hardness (HV1) increases by 6% compared with the as-cast sample (621 HV vs. 584 HV).[21] Based on this outcome, the next questions are whether it is possible to control the degree of nanocrystallization during TPF and to which extent of crystallization BMGs start to lose their beneficial mechanical properties, such as low Young's modulus, for implant applications. Therefore, **Publication II** includes a detailed analysis of the relationships among mechanical properties, glassy states, and temperature histories from the TPF process, as displayed in Figure 23.[35]

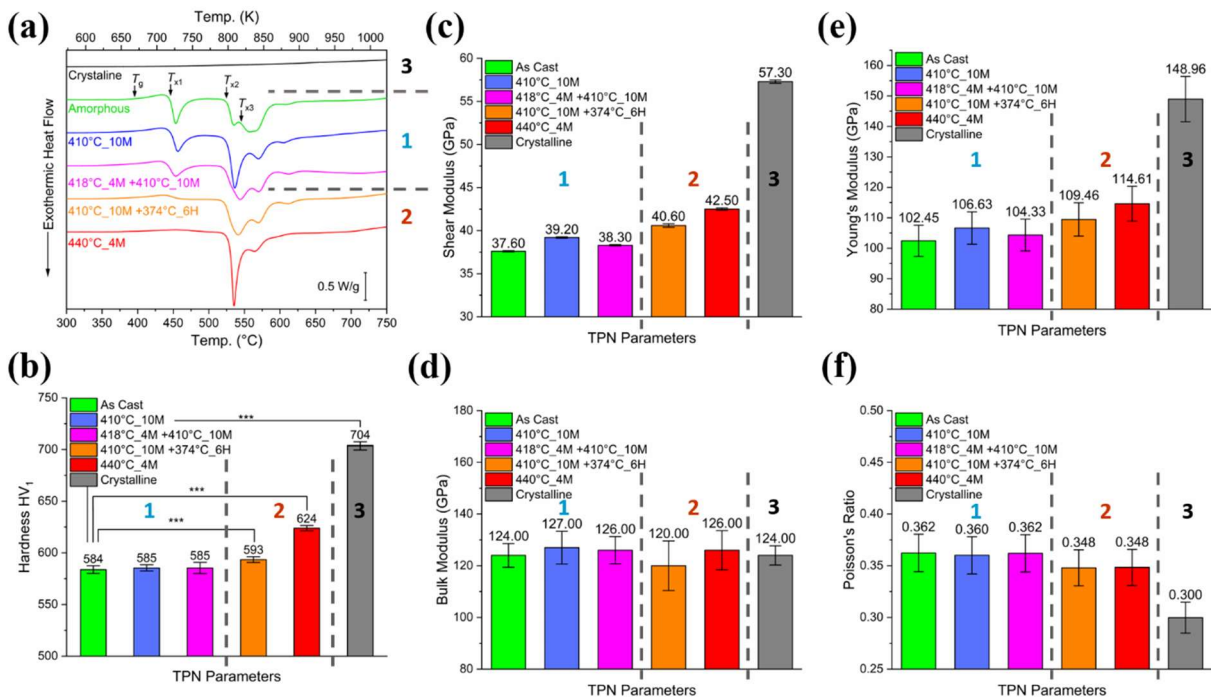


Figure 23: In-depth study for the correlation of $Ti_{40}Zr_{10}Cu_{34}Pd_{14}Sn_2$ BMG disks from thermal histories of the TPF process to their glassy states and mechanical properties: (a) DSC curves from constant-rate heating (20 °C/min) measurements. (b) Microhardness. (c) Shear modulus. (d) Bulk modulus. (e) Young's modulus. (f) Poisson's ratio. Note that the measured bulk and shear moduli were used to calculate Poisson's ratio and Young's modulus. Adapted from [35].

“As Cast” and “Crystalline” represent two extreme structural states, where “As Cast” has a fully amorphous state without thermo-processing, and “Crystalline” is the same material annealed to a fully crystallized structure.[35] “410°C_10M” refers to the TPF process at 410°C for 10 min, which is applied to imprint micro- or nano-patterns. “418 °C_4M +410 °C_10M” stands for the two-step TPF process to create a two-tier hierarchical structure. In the first step, the material is imprinted with a nano-pattern at 418 °C for 4 min, and in the second step, the micro-pattern is superposed at 410 °C for 10 min.[35] “410 °C_10M +374 °C_6H” is based on a diffusion-based nanomolding technique inspired by Liu et al. to produce nanorods smaller than 100 nm diameter on crystalline metals.[180] The concept is to imprint the nano-protrusion at 410 °C for 10 min via the TPF and then lower the temperature to 374 °C for 6 hr while maintaining constant pressure.[35] “440 °C_4M” is the TPF setting used in **Publication I**, allowing nanocrystal formation during the TPF.[21,35] The main findings are summarized below:

- (i) Depending on the exothermic peaks from DSC curves (Figure 23(a)), the studied TPF conditions can be split into three classes.[35]
 - **Class I** contains the samples (“As Cast”, “410°C_10M”, and “418 °C_4M +410 °C_10M”) that still show the first exothermic peaks around 450°C.[35]
 - **Class II** is for those (“410 °C_10M +374 °C_6H” and “440 °C_4M”) whose first exothermic peaks vanished.[35]
 - **Class III** is “Crystalline”, where all three peaks for crystallization events have disappeared.[35]
- (ii) According to the Vickers hardness (Figure 23(b)), elastic constants (shear and bulk moduli) determined via RUS (Figure 23(c-d)), and Young’s modulus and Poisson’s ratio calculated from elastic constants (Figure 23(e-f)), the changes in mechanical properties follow the three-class category introduced above for the DSC curves.[35]
 - **Class I:** The treated BMGs retain mechanical properties similar to their as-cast condition.[35]
 - **Class II:** Changes in mechanical properties are expected, including increased hardness, increased Young's modulus, and decreased Poisson's ratio.[35]
 - **Class III:** Once the BMGs are fully crystallized, the hardness and Young’s modulus increase substantially.[35]
- (iii) The micro-, nano-patterned, and even the hierarchically structured Ti₄₀Zr₁₀Cu₃₄Pd₁₄Sn₂ BMG disks fabricated in **Publication II** maintain favorable mechanical properties from as-cast materials.[35]

Based on DSC analysis, the relationship between structural and mechanical properties, including Young’s modulus and hardness, is categorized into three classes.[35] This categorization system from DSC analysis can be a valuable tool for determining the limitations of thermal processing in applications where mechanical properties are taken into account.[35]

Most importantly, earlier research on the TPF processed BMGs asserted that crystallization must be avoided to retain their mechanical properties.[3,19,130] Our discovery suggests $\text{Ti}_{40}\text{Zr}_{10}\text{Cu}_{34}\text{Pd}_{14}\text{Sn}_2$ BMGs possess crystallization tolerance to TPF, and slight crystallization is allowed before losing their mechanical properties.[35] The discovery opens the opportunity of implementing the TPF process for a wide range of mediocre glass forming systems and semi-crystalline composites into functional materials without sacrificing their favorable mechanical properties.

5.2 Patterned Ti-BMGs for Biomedical Applications

Two potential biomedical applications of TPF patterned $\text{Ti}_{40}\text{Zr}_{10}\text{Cu}_{34}\text{Pd}_{14}\text{Sn}_2$ BMG are suggested in **Publication II**: (i) Dental or orthopedic tissue implants and (ii) a toolbox for studying cell response on rigid and ordered surfaces.[35] Regarding these two applications, the following sections will summarize key findings from the in-vitro studies in Publication II. The in-vitro studies were conducted by culturing Saos-2 cell lines on four different surface topographies of $\text{Ti}_{40}\text{Zr}_{10}\text{Cu}_{34}\text{Pd}_{14}\text{Sn}_2$ BMGs. These four surface topographies include: (i) Flat (mirror-polished), (ii) Micro-pattern (2.5 μm square protuberances), (iii) Nano-pattern (400 nm HCP protrusions), (iv) Hierarchical-pattern (400 nm HCP protrusions on 2.5 μm square protuberances).

5.2.1 Biocompatibility of $\text{Ti}_{40}\text{Zr}_{10}\text{Cu}_{34}\text{Pd}_{14}\text{Sn}_2$ BMGs for Hard Tissue Implants

Cell proliferation and viability are reliable indicators of an implant material's biocompatibility. Saos-2 cell proliferation on four different surfaces of $\text{Ti}_{40}\text{Zr}_{10}\text{Cu}_{34}\text{Pd}_{14}\text{Sn}_2$ BMG was accessed via the Alamar Blue assay on days 1, 3, and 7, as shown in Figure 24(a).[35] On days 3 and 7, the metabolic activity data were compared across various surface topographies after being normalized with respect to the value of day 1.

- The four surface topographies do not appear to have any substantial effects at any time point.[35]

Cell viability was accessed based on the live/dead images of Saos-2 cells on day 3, and the representative images were chosen and displayed in Figure 24(b). Figure 24(c-d) shows the quantified results such as percentage and number of live cells.[35]

- All four surface topographies of Ti-BMG have a cell viability higher than 90%, and the cell viability is even above 96% on Ti-BMG.Flat.[35]
- The number of living cells does not significantly differ amongst the four surface topographies.[35]
- Regarding cell spatial distribution in the live/dead images, Saos-2 cells on a flat surface cluster together to form colonies in some regions and leave empty spaces in others, while Saos-2 cells on the hierarchical-patterned surface disperse throughout the entire surface with fewer cells in close contact.[35]

In this study, all four $\text{Ti}_{40}\text{Zr}_{10}\text{Cu}_{34}\text{Pd}_{14}\text{Sn}_2$ BMG disks have very high biocompatibility, and the surface patterns do not deteriorate their biocompatibility.[35] When it comes to implant applications, numerous studies show that micro- and nano-scale topographies can improve the antibiofilm properties of the material by reducing bacteria adhesion.[107,143] Therefore, more studies to investigate the antibiofilm properties of these patterned surfaces are essential for hard-tissue implant applications.

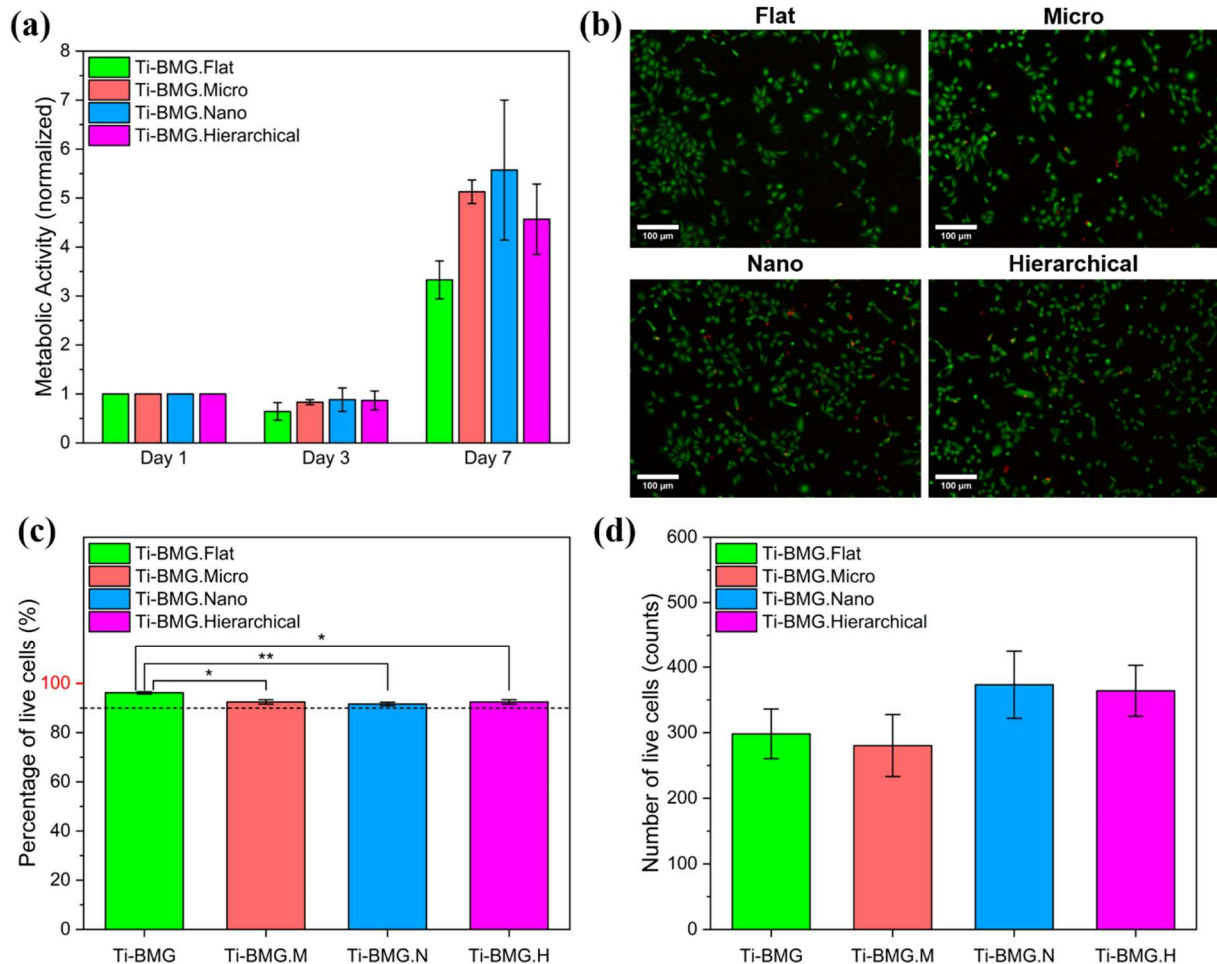


Figure 24: Biocompatibility of $\text{Ti}_{40}\text{Zr}_{10}\text{Cu}_{34}\text{Pd}_{14}\text{Sn}_2$ BMG with four different surface topographies: (a) Saos-2 cell proliferation at days 1, 3, and 7. (b) Fluorescence images of live/dead assay at day 3 (live cells stain green and dead cells stain red). (c) Cell viability and (d) number of live cells at day 3 by live/dead assay. Adapted from [35].

5.2.2 TPF-Patterned Ti-BMGs as a Toolbox for Studying Cell-Surface Interaction

From a biomedical science perspective, the surface morphology of the implants influences osseointegration and anti-biofilm properties.[35,40,132–134] Saos-2 cell morphology and cell adhesion on the four surface topographies were examined using SEM and CLSM after three days of culture, as shown in Figure 25.[35] The following are key findings from the observation of SEM (Figure 25(a)) and CLSM images (Figure 25(b)):

- Cells spread well on all tested surfaces, and several dividing cells were observed.[35]
- Filopodia connect multiple cells to each other, and filopodia longer than 20 μm are observed on the surface of Ti-BMG.Micro and Ti-BMG.Hierarchical.[35] These filopodia cross over the micro protuberances rather than going around them.[35]
- Some cells develop filopodia parallel to each other, matching the direction of the micro-pattern.[35]
- Compared to patterned surfaces, cells on flat surfaces are closer to one another and have polygonal shapes with larger areas.[35] Actin stress fibers are apparent on all four surfaces, while flat surfaces have the clearest and most prolonged ones.[35]
- On the three patterned surfaces, the cells are less homogeneously spread, with some having star-shaped or dendritic morphologies and others having rounded shapes.[35]

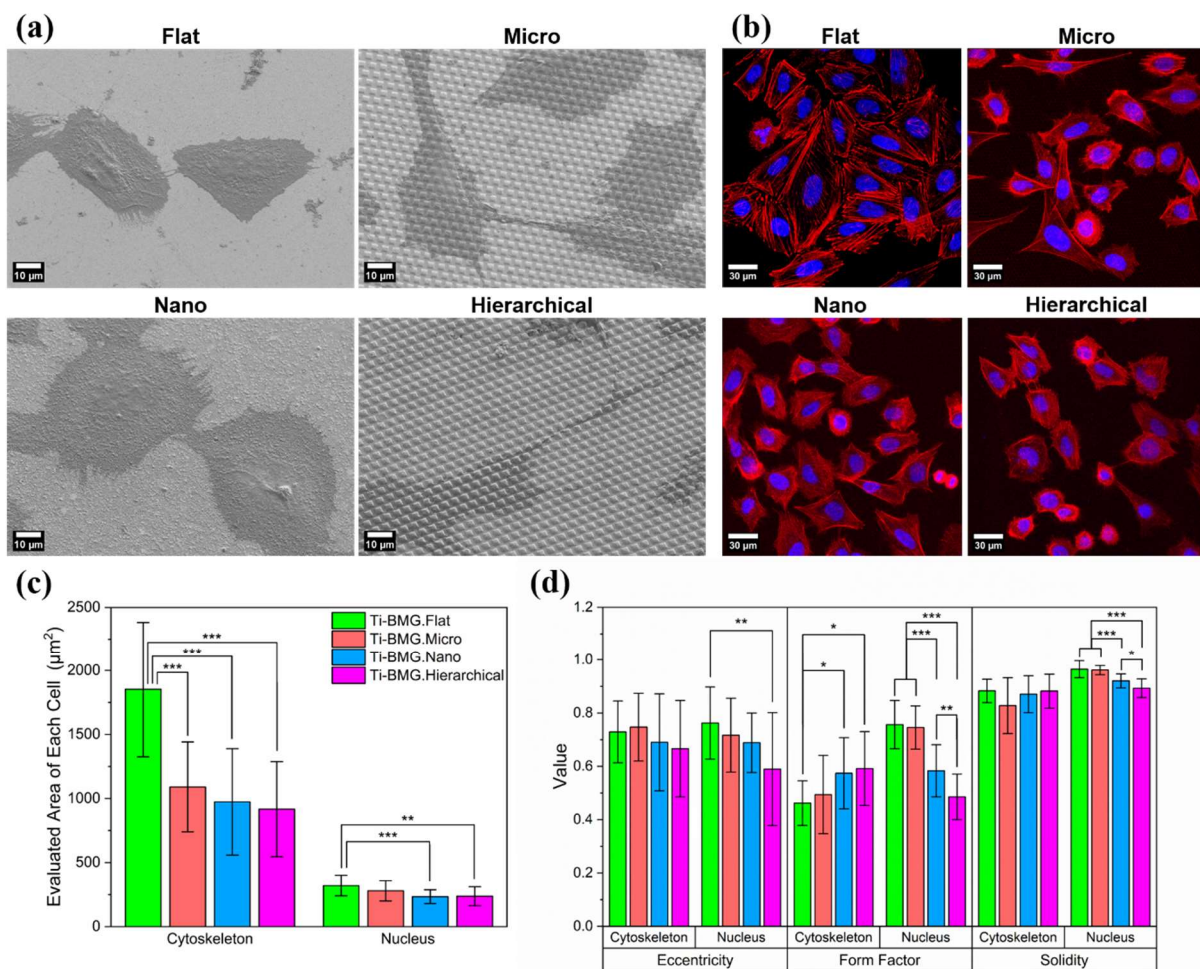


Figure 25: Morphological analysis of Saos-2 cells at day 3: (a) SEM images for cell morphology. (b) DAPI/phalloidin staining images for cell adhesion. (c-d) Quantitative morphometric analysis from DAPI/phalloidin staining images, where (c) area and (d) eccentricity, form factor, and solidity were analyzed from the nuclei and cytoskeleton of each cell. Adapted from [35].

A quantitative analysis was performed on the CLSM images from DAPI/phalloidin staining.[35] Figure 25(c) presents the areas of the cytoskeleton and nucleus of each cell on the surfaces. Figure 25(d) examines three morphometric parameters to describe cell morphologies: eccentricity, form factor, and solidity.[35] The values of these parameters range from 0 to 1.

- Patterned surfaces have much smaller cytoskeleton areas compared to the flat surface, while only nano- and hierarchical-patterned surfaces considerably reduce the nucleus area.[35]
- Nano- and hierarchical-patterned surfaces have significantly increased cytoskeleton form factors.[35] However, all surfaces have cytoskeleton form factors less than 0.6, indicating that cells spread with several protrusions.[35]
- The nuclear form factor has an inverted trend compared to the cytoskeleton form factor, where the flat surface has the highest value, and the hierarchically patterned one has the lowest.[35] This suggests that the nanofeatures give the nucleus a ridged shape, and the impact can be further enhanced when the micro-feature is present.[35]
- The nuclei are more elongated on the flat surface compared to the hierarchical-patterned surface, indicated by a significantly lower nuclear eccentricity on the hierarchical-patterned surface compared to the flat surface.[35]

Generally, patterned surfaces are observed to promote the formation of longer filopodia on the edge of the cytoskeleton, leading to star-shaped and dendritic cell morphologies.[35,140] The micro-pattern alone does not ridge the nucleus, but the nano-pattern does. However, when combined with the nano-pattern, the micro-pattern creates a more irregular nuclear shape on the hierarchical-patterned surface.[35] The role of surface topography on protein absorption and subsequent cell response needs to be further elucidated.[35]

Currently, most patterns with high degrees of order are created on polymeric substrates, with fewer studies investigating cell responses on rigid- and ordered-patterned surfaces.[134] Obtaining hierarchical topography on Ti-alloys is mainly hampered by uncontrollable roughness, as most investigations use chemical and laser-based methods. When the random roughness is compared to the well-defined dimensions of surface topography, it becomes easier to identify and measure the influence of a particular surface feature on a given cell response.[35,58] TPF-patterned Ti-BMGs provide a viable platform to research cell behavior on stiff and ordered surfaces because they permit a high degree of order and design freedom in the surface topography.[35]

5.3 Patterned Pt-BMGs as Catalysts for Hydrogen Evolution Reactions

Given the high surface area created during the TPF, the electrocatalytic performance of Pt_{57.5}Cu_{14.7}Ni_{5.3}P_{22.5} BMGs for HER (in 0.5 M H₂SO₄ electrolyte) is explored.[153]

Pt_{57.5}Cu_{14.7}Ni_{5.3}P_{22.5} BMGs with three surface topographies are created by TPF, as shown in Figure 26(a).[153] These three surface topographies include: (i) Flat (mirror-polished), (ii) Micro-pattern (micro-rods with 2.5 μm diameter, 4.2 μm inter-rod distance, and 1.7 μm gap between each rod), (iii) Nano-pattern (nano-rods with 90 nm diameter, 125 nm inter-rod distance, and 35 nm gap between each rod).[153]

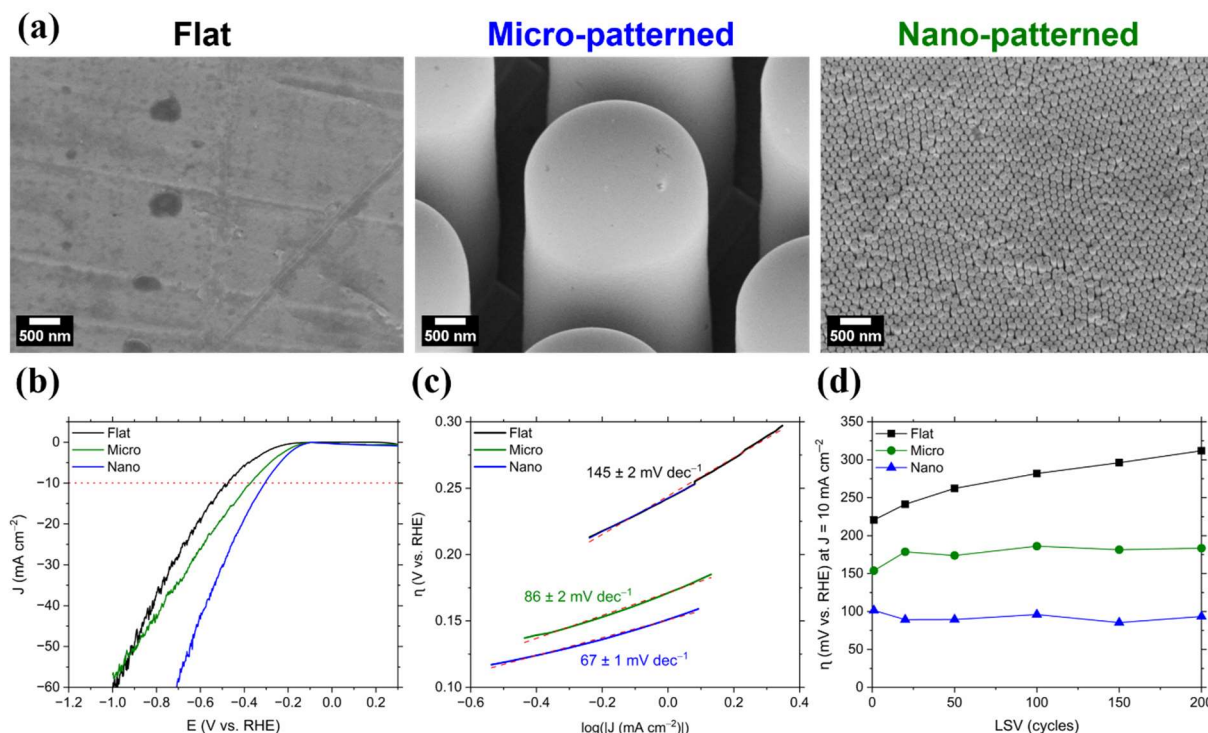


Figure 26: The HER performance (in 0.5 M H₂SO₄ electrolyte) of TPF processed Pt_{57.5}Cu_{14.7}Ni_{5.3}P_{22.5} BMGs with flat, micro-patterned, and nanopatterned surfaces: (a) SEM images at 50k magnification of samples before electrochemical measurements. (b-d) Results of electrochemical studies with (b) LSV curves of the 1st cycle and (c) their corresponding Tafel curves. (d) Additional stability tests up to 200 LSV cycles shows the trend of overpotential η at J = 10 mA cm⁻². Adapted from [153].

5.3.1 Influence of Surface Topographies on Electrocatalytic Performance

LSV cycles (with potentials starting from -1.2 V to 0.3 V at a scan rate of 0.005 V s⁻¹ with a shift in onset potential of 0.4 V until -0.2 V) were conducted to investigate the electrochemical hydrogen evolution kinetics of flat, micro-patterned, and nano-patterned Pt-BMG samples, as shown in Figure 26(b).[153] These LSV curves were then used to calculate the Tafel slope values, as Figure 26(c) revealed. In order to study the electrocatalytic stability and the self-improvement characteristics of flat, micro-patterned, and nano-patterned Pt-BMGs for HER, stability tests for 200 LSV cycles (with samples positioned horizontally) were performed, as displayed in Figure 26(d).[153]

Generally, the lower absolute overpotential $|E|$ and lower Tafel slope value are beneficial for HER electrocatalysts.[116,181] Achieving a high current density through a lower

absolute overpotential confirms an acceleration of the hydrogen evolution reaction.[182,183] The following are the main findings in terms of HER performance for Pt-BMG catalysts with three different topographies:[153]

- The absolute overpotential $|E|$ required to achieve a current density of $J = -10 \text{ mA cm}^{-2}$ (Figure 26(b)): Nano < Micro < Flat (0.30 V, 0.37 V, and 0.48 V, respectively) [153]
- The Tafel slopes determined from the relatively straight region of the cathodic region (Figure 26(c)): Nano < Micro < Flat ($67 \pm 1 \text{ mV dec}^{-1}$, $86 \pm 2 \text{ mV dec}^{-1}$, $145 \pm 2 \text{ mV dec}^{-1}$, respectively) [153]
- The electrocatalytic stability and the self-improvement behavior after 200 LSV cycles (Figure 26(d)): Nano > Micro > Flat (The absolute overpotential for $J = -10 \text{ mA cm}^{-2}$ was reduced by 8% in nano-patterned samples yet increased by 19% for the micro-patterned samples and 41% for the flat samples.) [153]

As a result, nano-patterned Pt-BMG demonstrates superior performance as HER electrocatalysts compared to their flat and micro-patterned counterparts, exhibiting lower absolute overpotential, smaller Tafel slope value, and self-improvement behavior in long-term operation.[153]

5.3.2 Stability Test of 1000 LSV Cycles for Nano-patterned Pt-BMG

In the previous section, the nano-patterned Pt-BMG shows better electrocatalytic performance for HER than the flat and micro-patterned Pt-BMGs.[153] Hence, a stability test for 1000 LSV cycles (with potentials between -0.8 V and 0.2 V at a scan rate of 0.02 V s^{-1}) was conducted with the nano-patterned Pt-BMG, as shown in Figure 27(a).[153] The LSV curves of the 1st and 1000th cycles were then used to calculate the Tafel slope values, as displayed in Figure 27(b). The key findings are the following:[153]

- A slight increase in absolute overpotential $|E|$ for $J = -10 \text{ mA cm}^{-2}$ until 50 LSV cycles are observed. After the 50th LSV cycle, the absolute overpotential $|E|$ for $J = -10 \text{ mA cm}^{-2}$ starts to decrease, and from the 500th cycle, the absolute overpotential $|E|$ for $J = -10 \text{ mA cm}^{-2}$ is even lower than 0.26 V of the 1st cycle (Figure 27(a)).[153]
- The absolute overpotential $|E|$ for $J = -10 \text{ mA cm}^{-2}$ decreases further to 0.15 V at the 1000th cycle (Figure 27(a)).[153]
- The Tafel slopes decrease from $67 \pm 1 \text{ mV dec}^{-1}$ at the 1st LSV cycle to $42 \pm 1 \text{ mV dec}^{-1}$ at the 1000th LSV cycles (Figure 27(b)).[153]

Therefore, the stability test highlights the self-improvement behavior of the nano-patterned Pt-BMG catalyst for electrocatalytic performance after 1000 LSV cycles.[153]

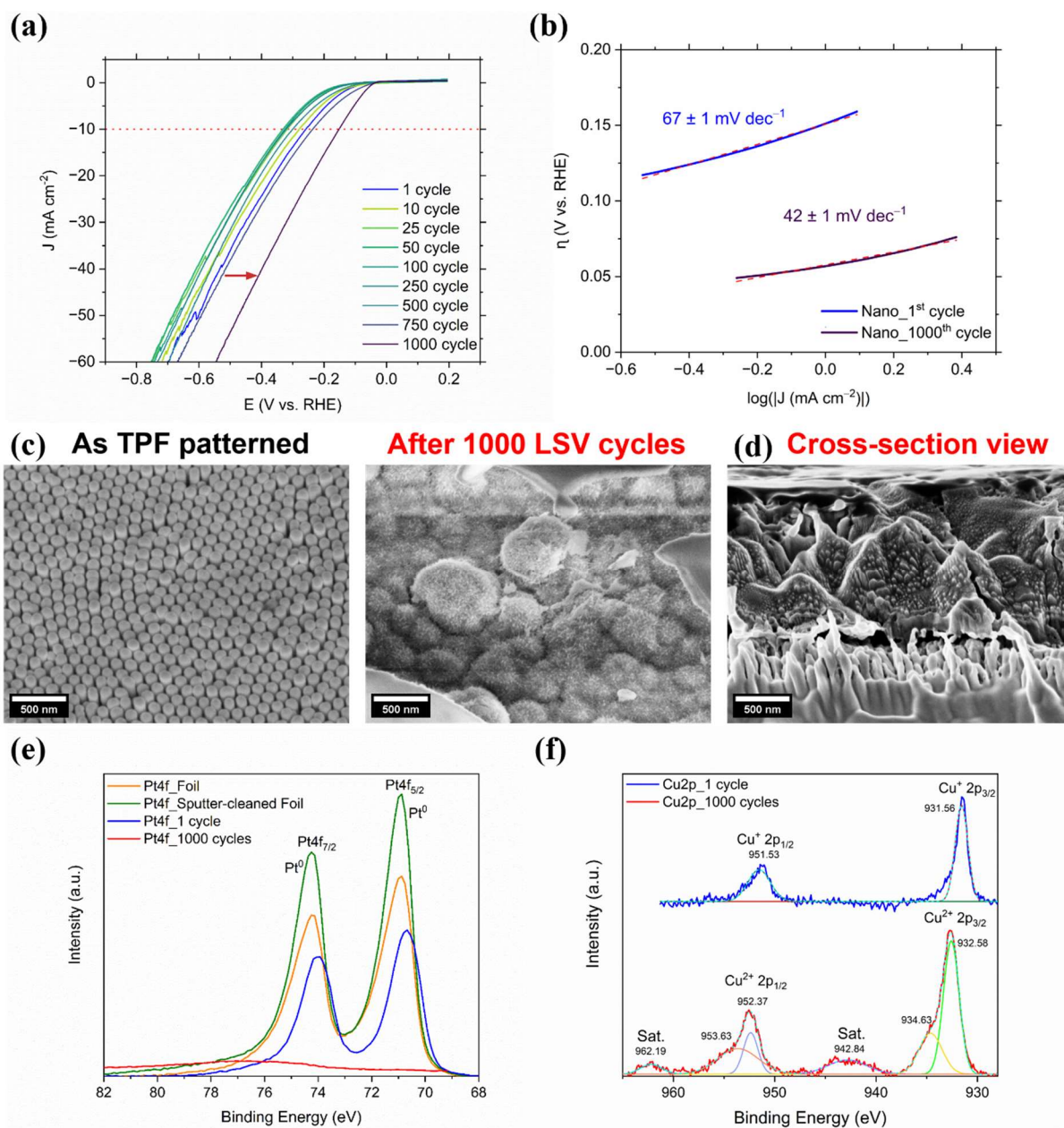


Figure 27: The stability test of the nano-patterned $\text{Pt}_{57.5}\text{Cu}_{14.7}\text{Ni}_{5.3}\text{P}_{22.5}$ BMG for 1000 LSV cycles (in 0.5 M H_2SO_4 electrolyte): (a-b) Results of electrochemical studies with (a) LSV curves and (b) Tafel curves. (c-d) SEM images at 100k magnification with (c) top views showing the alternation of surface topographies after the stability test and (d) the cross-section view revealing a new layer formed on top of the nano-pattern. (e-f) XPS analysis of (a) Pt4f and (b) Cu2p. Adapted from [153].

Multiple complementary methods were used to characterize the surfaces of the nano-patterned samples after 1 and 1000 LSV cycles to understand the reason for the improved electrocatalytic properties, as demonstrated in Figure 27(c-f).[153] SEM image analysis of the nano-patterned Pt-BMG shows that the surface topography changes dramatically after the stability test, as shown in Figure 27(c-d):[153]

- The top views of the SEM images (Figure 27(c)) reveal that the surface topography of Pt-BMG nanorods is replaced by a porous CuO/Cu₂O foam.[153]
- The cross-section view of the SEM image (Figure 27(d)) indicates that a layer of CuO/Cu₂O foam (about 1 μm thick) was deposited on top of the Pt-BMG nanorods.[153]
- Three topographies were observed for the deposited CuO/Cu₂O foam: (1) Smooth island-like CuO, (2) dandelion-like CuO, and (3) CuO nanosheets.[153]

X-ray photoelectron spectroscopy (XPS) is a technique that enables the analysis of the elemental chemical states on the material surface, as illustrated in Figure 27(e-f):[153]

- The Pt4f spectra (Figure 27(e)) indicate that the Pt in the Pt-BMG after 1 LSV cycle is in a metallic state, and almost no Pt signal can be detected for the Pt-BMG after 1000 LSV cycles.[153]
- The Cu2p spectra (Figure 27(f)) of both 1- and 1000-cycle samples show prominent signals that are associated with Cu-metal/Cu₂O (at ~932 and ~952 eV) and CuO (at ~934 and ~954 eV).[153] The sample after 1000 LSV cycles shows substantial satellite peaks in the Cu2p spectrum, indicating a mixture of CuO and Cu₂O.[153]
- No Ni and P signals are found on the surface of the Pt-BMGs after both 1 and 1000 LSV cycles.[153]

The results of the EIS, XPS, AES, SEM, and EDX analyses combined show that after 1000 LSV cycles, a new Cu_xO layer developed on top of the Pt-BMG nanorods.[153] A three-step mechanism has been proposed to explain the formation of a porous Cu_xO layer on the nano-patterned Pt-BMG during LSV cycles.[153] The steps are as follows:

1. In the low overpotential section of LSV scans, Cu electro-dissolution from the nano-patterned Pt_{57.5}Cu_{14.7}Ni_{5.3}P_{22.5} BMG occurs under cathodic polarization conditions, supplying a source of Cu ions at the surface–electrolyte contact.[153]
2. During the high overpotential part of LSV scans, the dissolved Cu²⁺_(aq) ions are re-deposited in metallic form on the electrode ($\text{Cu}^{2+}_{(\text{aq})} + 2e^{-} \rightarrow \text{Cu}_{(\text{s})}$), and the evolving hydrogen bubbles serve as a template for material deposition.[153]
3. Oxidation of the re-deposited Cu to Cu_xO during the low overpotential section of the LSV cycle.[153]

This work presents a method for fabricating Cu_xO foams using patterned BMGs, which could be employed in a variety of applications, such as gas sensing, supercapacitor, photocatalytic, and antibacterial applications.[184–187] Furthermore, the nano-patterning of BMGs with DHBT deposition provides a viable approach for the synthesis of metal or metal-oxide foams.[153] For instance, the proposed three-step process can be implemented to create Cu_xO foams from any nano-patternable BMG systems containing Cu and another element with a higher dissolution potential than Cu.[153] Therefore, future research could explore using more

cost-effective BMG systems with high fragility to replace noble-based BMGs and lower production costs.[153] Lastly, beyond HER, the synergy of metallic glasses, thermoplastic patterning, and dynamic bubble templating provides a feasible approach to fabricating metal/metal-oxide foams for various applications or as a strategy for self-improving catalysts.[153]

5.4 Unpublished Contributions

5.4.1 Cell Response on PDLLA-PEG Coated $\text{Ti}_{40}\text{Zr}_{10}\text{Cu}_{34}\text{Pd}_{14}\text{Sn}_2$ BMGs

Saos-2 cell morphology on hierarchical-patterned Ti-BMG disks with and without PDLLA-PEG coating were examined using SEM after three days of culture, as demonstrated in Figure 28. SEM images show that Saos-2 cells were rounded up and failed to express cellular extensions when cultured on the PDLLA-PEG coated sample, implying weak cell adhesion on the coating surface (Figure 28(a, c)). On the contrary, for the reference without PDLLA-PEG coating, Saos-2 cells on the hierarchical-patterned Ti-BMG surface were flattened, which appeared well spread and with long cellular extensions, indicating good cell adhesion.

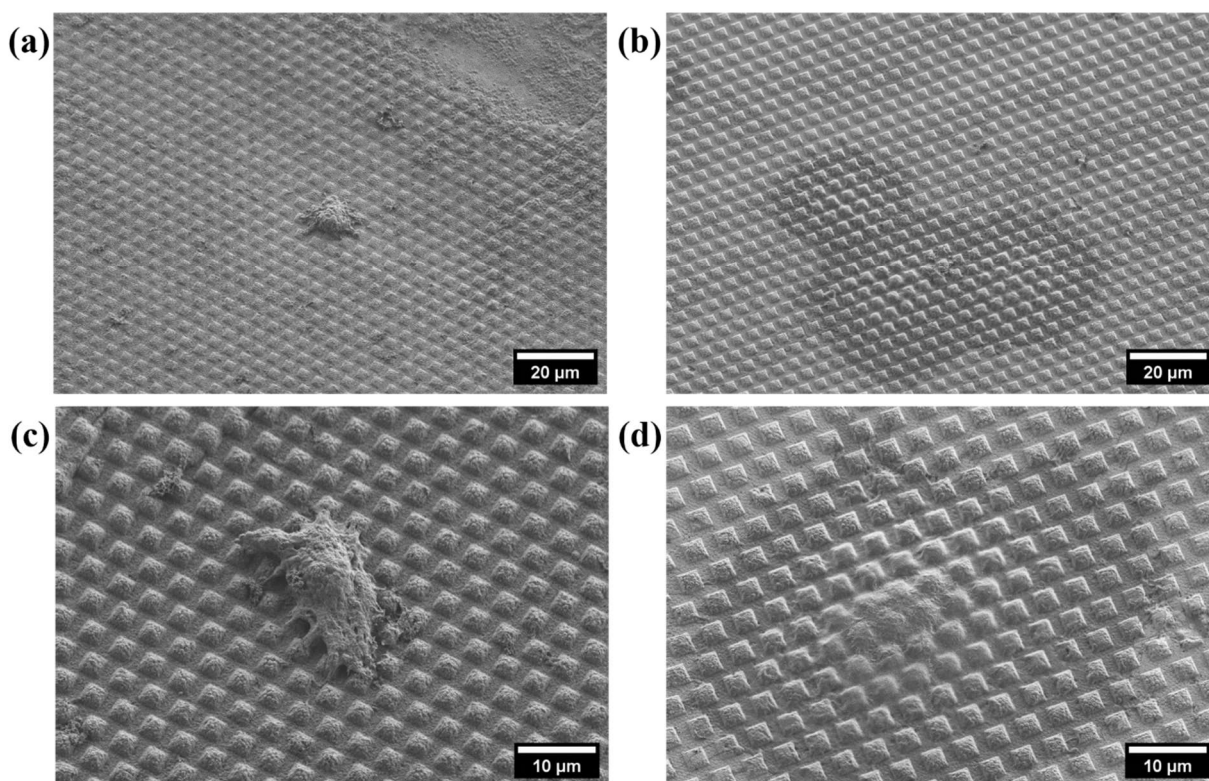


Figure 28: SEM imaging of cell morphology of Saos-2 cells at day 3 on hierarchical-patterned Ti-BMGs with (a, c) and without (b, d) PDLLA-PEG coating at a magnification of 4000 times (a, b) and 2000 times (c, d).

The concept behind applying PDLLA-PEG coatings on the implant surfaces is to enhance the antifouling properties by forming a hydration layer against bacteria adhesion. The SEM images suggest that the hydration layer from the PDLLA-PEG coating might also hinder cell adhesion. However, the hindering effect on cell adhesion can be controlled by the degradation rate of the coating. Hence, deeper investigations are required on PDLLA-PEG coated Ti-BMG samples, such as co-culture assays including both human and bacterial cells, as well as studies for a more extended culturing period. The current result implies that the PDLLA-PEG coating can be used in applications where cell adhesion should be avoided, like removable implants.

5.4.2 Staphylococcus Aureus on $\text{Ti}_{40}\text{Zr}_{10}\text{Cu}_{34}\text{Pd}_{14}\text{Sn}_2$ BMGs

Due to insufficient experimental repetitions, the antibacterial and anti-biofilm assessments shown in this section are preliminary results and may only be used as references. More in-depth investigations are required. Biofilm formation of *Staphylococcus aureus* (*S. aureus*) after 24 hours was evaluated via crystal violet assays to compare the antibacterial property of Cu disk (mirror-polished), Ti-6Al-4V disk (stock surface), and Ti-BMG disk ($\text{Ti}_{40}\text{Zr}_{10}\text{Cu}_{34}\text{Pd}_{14}\text{Sn}_2$, mirror-polished), as shown in Figure 29(a). The crystal violet assay was conducted with three biological replicates (the same type of organism treated or grown in the same conditions showing biological variation), and each has two technical replicates (repeated measurements of a sample showing variation of the measuring equipment and protocols). This protocol used Cu disks as a negative control because Cu and its alloys are well-known for their antimicrobial properties.[188] Ti-6Al-4V disks (stock surface) are positive control since they are considered one of the best biocompatible metallic materials for implant applications.[166]

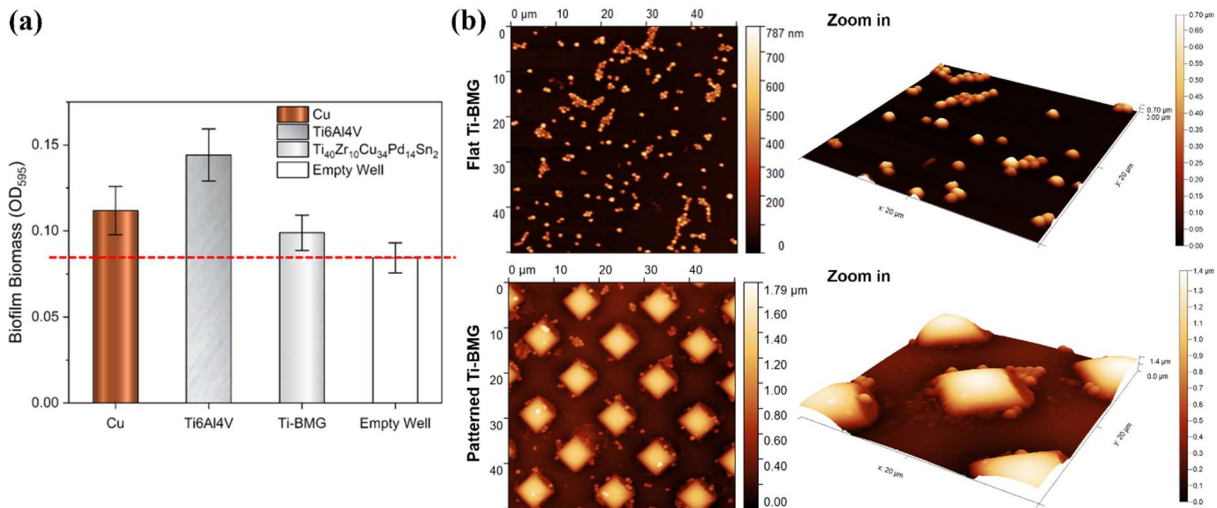


Figure 29: (a) Comparison of biofilm formation of *Staphylococcus aureus* (*S. aureus*) after 24 hours of incubation on Cu, Ti-6Al-4V, and Ti-BMG disks. (b) AFM scanning of *S. aureus* bacterial adhesion on Ti-BMGs with flat and patterned surfaces. The patterned Ti-BMG has ordered square protuberances with a height of $\approx 1.6 \mu\text{m}$ and $5 \mu\text{m}$ in length and width.

It was found that Ti-BMG had less biofilm formation than Ti-6Al-4V alloy after 24 hours (Figure 29(a)). However, Cu did not show good antimicrobial performance as the negative control in this protocol. The antimicrobial performance of Cu disks was compromised, presumably due to the high reactivity of Cu in the Lysogeny broth (culture medium), resulting in the heavy soiling on the disk surfaces, which substantially hindered bacterial-metal contact and reduced the contact killing of bacteria.[188,189] Therefore, in order to properly assess the antimicrobial of $\text{Ti}_{40}\text{Zr}_{10}\text{Cu}_{34}\text{Pd}_{14}\text{Sn}_2$ BMG in future work, it is suggested that: (i) All tested samples are polished to the same level of roughness to eliminate potential influence from the surface topography. (ii) The material selection for negative control should take into account the protocol and testing environments.

Figure 29(b) displays AFM images of *Staphylococcus aureus* (*S. aureus*) bacterial adhesion on $\text{Ti}_{40}\text{Zr}_{10}\text{Cu}_{34}\text{Pd}_{14}\text{Sn}_2$ BMGs with flat and patterned surfaces. In order to remove salt contents that might cause artifacts for AFM scanning from bacterial broth, the bacterial broth underwent a washing procedure in which it was mildly centrifuged, collected, and re-suspended in de-ionized water. This procedure was repeated five times to acquire a bacteria suspension before it was dispensed on the samples. The samples were then dried in air in the hood. Since the bacteria suspension was dried in the air without further incubation right after being dispensed on the samples, the presented AFM images represent the putative initial attachment of bacteria during biofilm formation. When seeded on the patterned Ti-BMG, *Staphylococcus aureus* (*S. aureus*) bacteria appear to adhere to the edges of the humps. However, the role played by evaporation in the location still needs to be further elucidated.

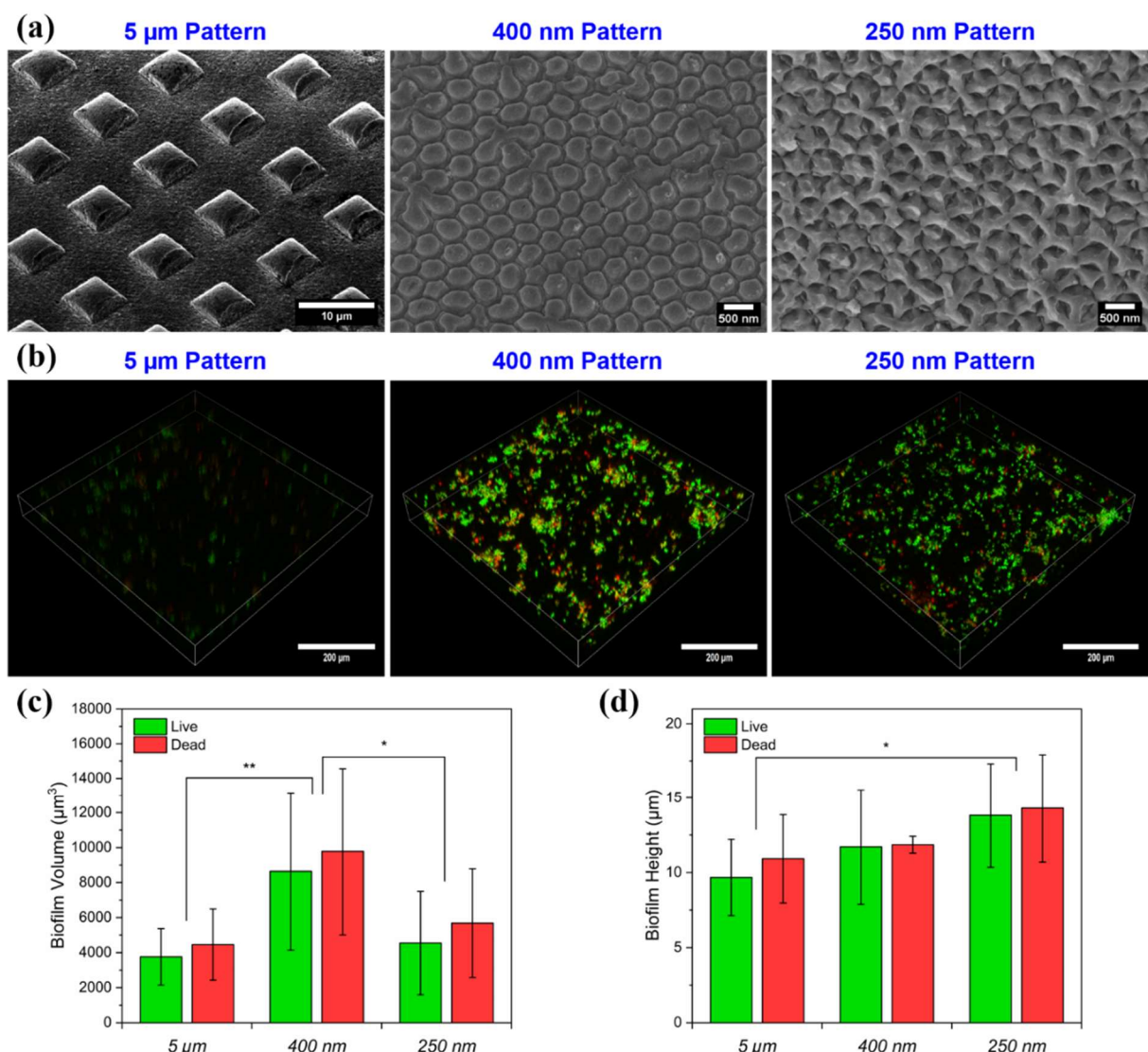


Figure 30: Biofilm formation of *S. aureus* on patterned Ti-BMGs after 24 hours of incubation: (a) SEM images of test samples. (b) Representative biofilm images from fluorescent CLSM. Viable bacteria are labeled in green, while dead bacteria are marked red. (c)(d) Results of quantitative image analysis of CLSM images (b) via BiofilmQ software. (c) Biofilm volume. (d) Biofilm height.

The biofilm formation of *S. aureus* after 24 hours of incubation on $\text{Ti}_{40}\text{Zr}_{10}\text{Cu}_{34}\text{Pd}_{14}\text{Sn}_2$ BMGs with three different pattern designs (5 μm square protuberance, 400 nm protrusions, and 250 nm ridges) is revealed in Figure 30. The SEM images of the three tested pattern designs are shown in Figure 30(a). After 24 hours of incubation, five fluorescent CLSM images are taken for each sample, and the representative images are shown in Figure 30(b). By simply observing these CLSM images (qualitative analysis), it is clear that the 400 nm pattern exhibits the most biofilm formation, followed by the 250 nm pattern, while the 5 nm pattern has the least biofilm formation. To further quantify the biofilm formation, the biofilm images are analyzed with BiofilmQ software via threshold-based 3D segmentation. The evaluated biofilm volume and biofilm height of viable and dead bacteria are illustrated in Figure 30 (c) and (d), respectively. Differences were considered as statistically significant for p-values <0.05 (denoted by: *p <0.05 ; **p <0.01 ; ***p <0.001). The results of biofilm volume are consistent with qualitative analysis. It is worth noting that even the 400 nm pattern has less biofilm formation than most metallic substrates. However, it is crucial to repeat these experiments with sufficient technical and biological replicas to conclude the antibiofilm properties of patterned Ti-BMGs.

5.4.3 Hedgehog-like Hierarchical Structure on Pd-BMGs

In order to explore the capability of the two-step TPF process, $\text{Pd}_{43}\text{Cu}_{27}\text{Ni}_{10}\text{P}_{20}$ BMG was chosen for the preliminary experiments. $\text{Pd}_{43}\text{Cu}_{27}\text{Ni}_{10}\text{P}_{20}$ BMG has a much lower viscosity, high fragility, and a larger supercooled liquid region (SCLR) than Ti-BMGs, as shown in Table 5. Furthermore, the $\text{Pd}_{43}\text{Cu}_{27}\text{Ni}_{10}\text{P}_{20}$ BMG has a significant noble metal content, conferring a higher intrinsic resistance to oxidation than Ti-BMGs. Hence, $\text{Pd}_{43}\text{Cu}_{27}\text{Ni}_{10}\text{P}_{20}$ BMG is much easier to process with TPF than the targeted Ti-BMG. The detailed TPF processing parameters are summarized in section 4.3.3.

Table 4: A comparison of both types of BMGs in terms of the formability criteria.[1]

Materials	SCLR: ΔT (K)	Liquid fragility index: m	Formability parameter $S = (T_x - T_g)/(T_l - T_g)$
$\text{Pd}_{43}\text{Cu}_{27}\text{Ni}_{10}\text{P}_{20}$	101	65.2	0.406
$\text{Ti}_{40}\text{Zr}_{10}\text{Cu}_{34}\text{Pd}_{14}\text{Ga}_2$	46	40.3	0.086

The results are demonstrated in Figure 31 with SEM images of nano-patterned, micro-patterned, and hierarchical-structured surfaces. The nano-pattern (Figure 31(a)) features nanorods with 40 nm in diameter and around 100 nm in height. The micro-pattern (Figure 31(b)) has ordered square protuberances with 1 μm in length and around 0.6 μm in height. The hierarchical structure (Figure 31(c-d)) puts together the topographies of micro-pattern and nano-pattern, which look like an array of hedgehogs.

A two-stage TPF technique is used to build the hierarchical structure. In the first step, the nano-pattern (Figure 31(a)) is imprinted, and in the second step, the micro-pattern (Figure

31(b)) is generated and superposed on the nano-pattern. Therefore, each “hedgehog” has 1 μm square protuberance as its body and 40 nm diameter nanorods as its spikes (or quills) on its body, leading to a total height of around 0.5 μm . For the hierarchical structure, the aspect ratio of the nanorods was controlled between 2 and 5 at the first TPF step to prevent the nanorods from forming bundles but still protruding enough after the second TPF step.

It is worth noting that nanorods are everywhere on the surface of the hierarchical structure, both on the square protuberances, which are the free spaces from the Si mold during the second step TPF, and flat regions where the Si mold presses them during the second step TPF. In order to further inspect if there is a difference in height for the nanorods on the square protuberances (free space) and flat regions (compressed by Si mold), an AFM image is taken, as demonstrated in Figure 31(e). A topography profile extracted from the AFM image (Figure 31(f)) reveals that the nanorods have heights around 100 nm on the square protuberances (free space) and around 50 nm on the flat region (compressed by Si mold). Artifacts from AFM, such as lateral broadening and edge rounding, need to be considered when getting the topography of nanorods, especially when nanorods are not aligned to the z-direction. Nevertheless, the AFM image demonstrates that in the area that came into contact with Si mold during the second TPF stage, the nanorods were compressed by around 50%.

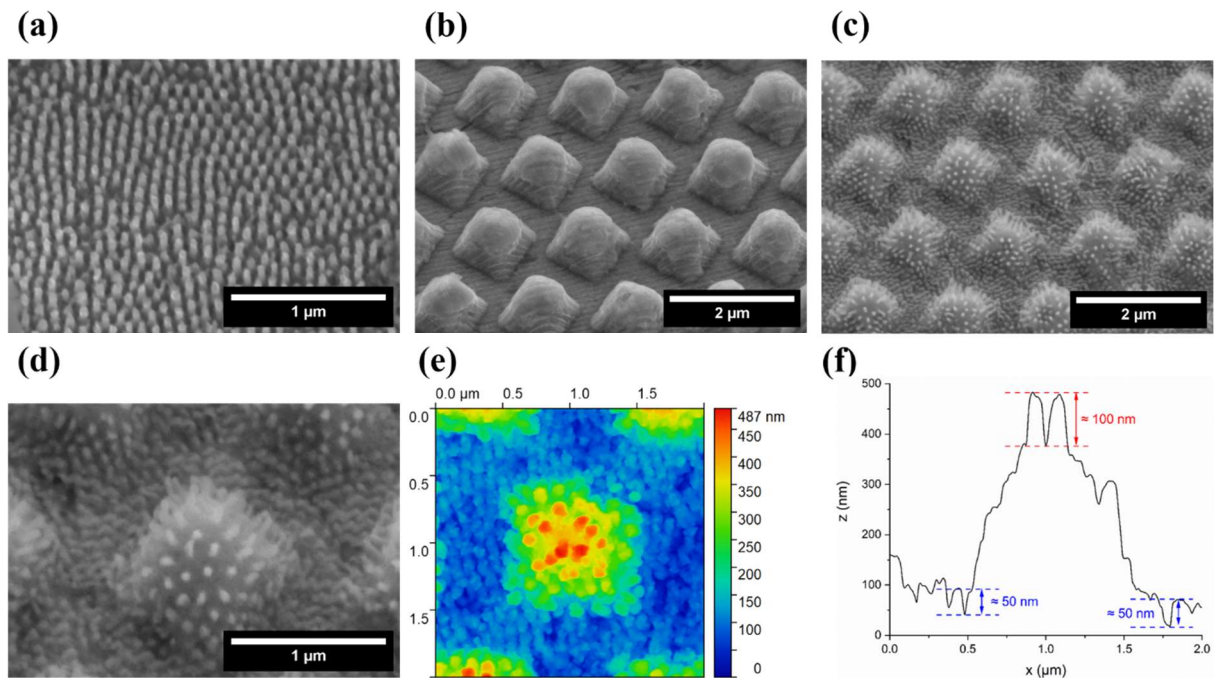


Figure 31: TPF patterned $\text{Pd}_{43}\text{Cu}_{27}\text{Ni}_{10}\text{P}_{20}$ BMGs: (a-d) SEM images of (a) nanopattern with 40 nm diameter nanorods, (b) Micropattern of square protuberances with 1 μm length, and (c-d) Hedgehog-like hierarchical structure integrating the nano- and micro-patterns on the same surface via a two-step TPF process. (e) AFM image of the hedgehog-like pattern. (f) Profile analysis from the AFM image (e).

The preliminary experiments of TPF with $\text{Pd}_{43}\text{Cu}_{27}\text{Ni}_{10}\text{P}_{20}$ BMGs are quite promising, and these experiences served as stepping stones for Publication II, in which the two-step TPF

process is further developed to successfully create the hierarchical structure on Ti-BMGs. Moreover, when dissolving the Si mold in the KOH, it was found that the dissolved Si floating in the KOH tends to precipitate selectively on the nanorods on the square protuberances. This phenomenon hints at the possibility of enhancing the activity of functional materials by creating hierarchical structures using TPF.

6 Conclusions and Outlook

The present thesis showcases that TPF is able to shape a $\text{Ti}_{40}\text{Zr}_{10}\text{Cu}_{34}\text{Pd}_{14}\text{Sn}_2$ BMG rod into a thin disk with only 18% of its initial height and imprint surface patterns from 300 μm to 400 nm.[21,35] A two-step TPF successfully created hierarchical structures integrating micro- and nano-patterns on $\text{Ti}_{40}\text{Zr}_{10}\text{Cu}_{34}\text{Pd}_{14}\text{Sn}_2$ BMG while preserving the advantageous mechanical properties of the as-cast materials.[35] The relationships among glassy states, mechanical properties, and thermal histories from TPF were investigated.[35] Our discovery suggests a crystallization tolerance in $\text{Ti}_{40}\text{Zr}_{10}\text{Cu}_{34}\text{Pd}_{14}\text{Sn}_2$ BMGs during TPF, allowing slight crystallization without losing the mechanical properties of BMGs.[35] This thesis demonstrates the opportunity to apply the TPF process for shaping and surface-patterning a wide range of mediocre glass-forming systems and semi-crystalline composites into functional materials without compromising their favorable mechanical properties.[21,35]

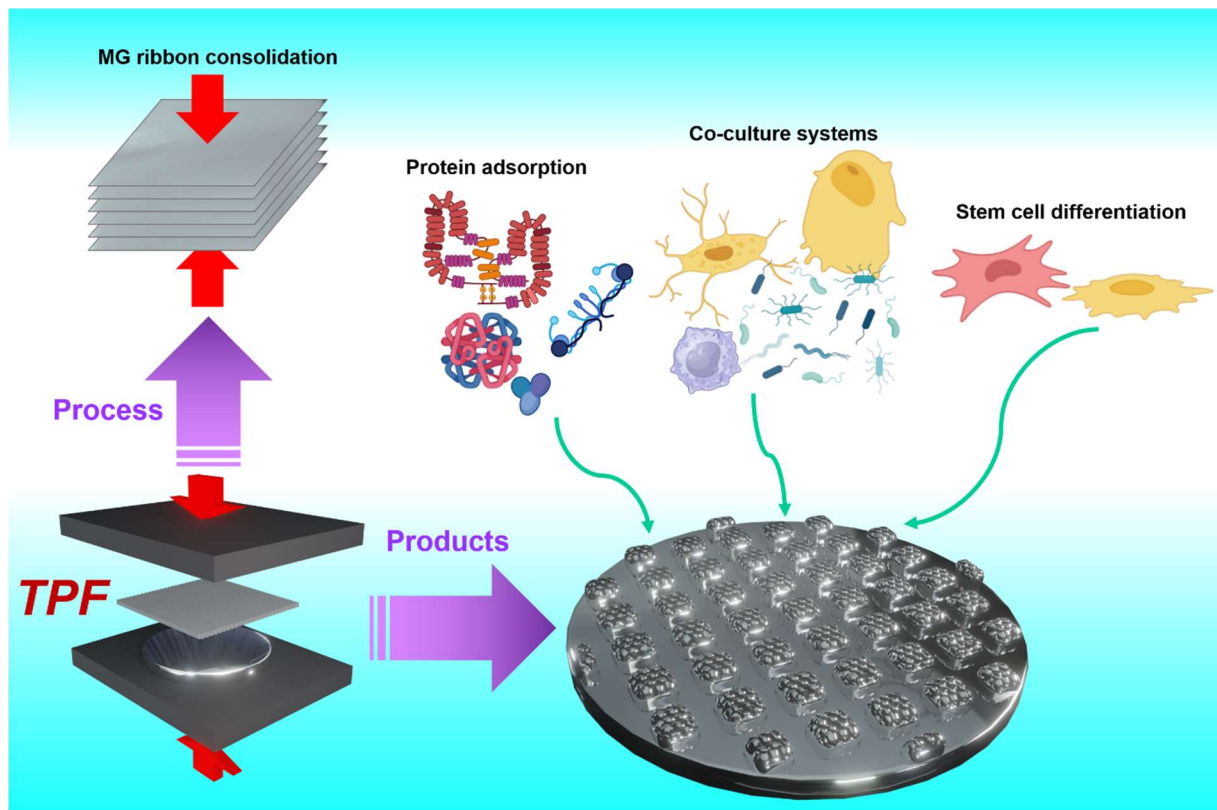


Figure 32: Outlooks for thermoplastic forming in amorphous metals from process and product aspects. Biological icons were created with BioRender.com.

One of the most prospective applications for Ti-BMGs is orthopedic and dental implants. The $\text{Ti}_{40}\text{Zr}_{10}\text{Cu}_{34}\text{Pd}_{14}\text{Sn}_2$ BMGs used in the present thesis have been reported to have a critical diameter of about 12 mm.[172] This size is sufficient for small-size components in most dental applications, such as fixtures, screws, and abutments. Combined with the TPF technique, the processability and functionality of Ti-BMGs are greatly improved. For instance, instead of subtractive machining, TPF can be utilized to form the desired final shapes, and the

pattern created via TPF can be optimized to improve implant grip and avoid loosening. Furthermore, most studies rely on chemical and laser-based approaches to achieve hierarchical topography on Ti-alloys, in which uncontrollable roughness is still a primary challenge. This thesis presents a feasible way to achieve Ti-alloys with well-defined hierarchical topography and limited roughness.[35] Most importantly, our TPF-patterned Ti-BMGs broaden the toolbox for researching cell responses on rigid and ordered surfaces.[35]

The present thesis demonstrates the designability and versatility of TPF in BMGs, shedding light on meeting the need for functional materials in interdisciplinary applications. In Figure 32, several outlooks are proposed from process and product aspects. From the process aspect, could TPF be applied to consolidate MG ribbons into “bulk” MGs? From the product aspect, the patterned BMGs with rigid and ordered surfaces can serve as platforms to study how surface topography influences protein adsorption, cell-bacteria competition (via in vitro co-culture systems), and stem cell differentiation. The above-mentioned outlook is merely a glimpse of potential works, and more possibilities have to be explored by scientists from multidisciplinary perspectives.

References

- [1] B. Sarac, J. Eckert, Thermoplasticity of metallic glasses: Processing and applications, *Progress in Materials Science* 127 (2022) 100941. <https://doi.org/10.1016/j.pmatsci.2022.100941>.
- [2] C. Suryanarayana, A. Inoue, Bulk Metallic Glasses (2nd ed.), *CRC Press* (2017). <https://doi.org/10.1201/9781315153483>.
- [3] J. Schroers, Bulk Metallic Glasses, *Physics Today* 66 (2013) 32–37. <https://doi.org/10.1063/PT.3.1885>.
- [4] K. Gao, X.G. Zhu, L. Chen, W.H. Li, X. Xu, B.T. Pan, W.R. Li, W.H. Zhou, L. Li, W. Huang, Y. Li, Recent development in the application of bulk metallic glasses, *Journal of Materials Science & Technology* 131 (2022) 115–121. <https://doi.org/10.1016/j.jmst.2022.05.028>.
- [5] W. Klement, R.H. Willens, P. Duwez, Non-crystalline Structure in Solidified Gold–Silicon Alloys, *Nature* 187 (1960) 869–870. <https://doi.org/10.1038/187869b0>.
- [6] Z. Savaedi, R. Motallebi, H. Mirzadeh, M. Malekan, Superplasticity of bulk metallic glasses (BMGs): A review, *Journal of Non-Crystalline Solids* 583 (2022) 121503. <https://doi.org/10.1016/j.jnoncrysol.2022.121503>.
- [7] M. Chen, A brief overview of bulk metallic glasses, *NPG Asia Materials* 3 (2011) 82–90. <https://doi.org/10.1038/asiamat.2011.30>.
- [8] J.F. Löffler, Recent progress in the area of bulk metallic glasses, *International Journal of Materials Research* 97 (2006) 225–233. <https://doi.org/10.3139/ijmr-2006-0039>.
- [9] A. Inoue, X.M. Wang, W. Zhang, Developments and Applications of Bulk Metallic Glasses, *Reviews on Advanced Materials Science* 18 (2008) 1-9.

- [10] A. Inoue, A. Takeuchi, Recent development and application products of bulk glassy alloys, *Acta Materialia* 59 (2011) 2243–2267. <https://doi.org/10.1016/j.actamat.2010.11.027>.
- [11] N. Li, W. Chen, L. Liu, Thermoplastic Micro-Forming of Bulk Metallic Glasses: A Review, *JOM* 68 (2016) 1246–1261. <https://doi.org/10.1007/s11837-016-1844-y>.
- [12] D.C. Hofmann, S.N. Roberts, Microgravity metal processing: from undercooled liquids to bulk metallic glasses, *Npj Microgravity* 1 (2015) 15003. <https://doi.org/10.1038/npjmgrav.2015.3>.
- [13] M. Davidson, S. Roberts, G. Castro, R.P. Dillon, A. Kunz, H. Kozachkov, M.D. Demetriou, W.L. Johnson, S. Nutt, D.C. Hofmann, Investigating Amorphous Metal Composite Architectures as Spacecraft Shielding, *Advanced Engineering Materials* 15 (2013) 27–33. <https://doi.org/10.1002/adem.201200313>.
- [14] A.G. Murphy, P. Meagher, A. Norman, D.J. Browne, Mechanical and thermal stability of Bulk Metallic Glass alloys identified as candidates for space mechanism applications, *Materials & Design* 224 (2022) 111350. <https://doi.org/10.1016/j.matdes.2022.111350>.
- [15] Q. Halim, N.A.N. Mohamed, M.R.M. Rejab, W.N.W.A. Naim, Q. Ma, Metallic glass properties, processing method and development perspective: a review, *The International Journal of Advanced Manufacturing Technology* 112 (2021) 1231–1258. <https://doi.org/10.1007/s00170-020-06515-z>.
- [16] A. Liens, A. Etiemble, P. Rivory, S. Balvay, J.-M. Pelletier, S. Cardinal, D. Fabrègue, H. Kato, P. Steyer, T. Munhoz, J. Adrien, N. Courtois, D. Hartmann, J. Chevalier, On the Potential of Bulk Metallic Glasses for Dental Implantology: Case Study on Ti₄₀Zr₁₀Cu₃₆Pd₁₄, *Materials* 11 (2018) 249. <https://doi.org/10.3390/ma11020249>.
- [17] Y.C. Hu, Y.Z. Wang, R. Su, C.R. Cao, F. Li, C.W. Sun, Y. Yang, P.F. Guan, D.W. Ding, Z.L. Wang, W.H. Wang, A Highly Efficient and Self-Stabilizing Metallic-Glass Catalyst for Electrochemical Hydrogen Generation, *Advanced Materials* 28 (2016) 10293–10297. <https://doi.org/10.1002/adma.201603880>.
- [18] M.M. Khan, A. Nemati, Z.U. Rahman, U.H. Shah, H. Asgar, W. Haider, Recent Advancements in Bulk Metallic Glasses and Their Applications: A Review, *Critical Reviews in Solid State and Materials Sciences* 43 (2018) 233–268. <https://doi.org/10.1080/10408436.2017.1358149>.
- [19] J. Schroers, Processing of Bulk Metallic Glass, *Advanced Materials* 22 (2010) 1566–1597. <https://doi.org/10.1002/adma.200902776>.
- [20] L. Liu, T. Zhang, Z. Liu, C. Yu, X. Dong, L. He, K. Gao, X. Zhu, W. Li, C. Wang, P. Li, L. Zhang, L. Li, Near-Net Forming Complex Shaped Zr-Based Bulk Metallic Glasses by High Pressure Die Casting, *Materials* 11 (2018) 2338. <https://doi.org/10.3390/ma11112338>.
- [21] F.-F. Cai, B. Sarac, Z. Chen, C. Czibula, F. Spieckermann, J. Eckert, Surmounting the thermal processing limits: Patterning TiZrCuPdSn bulk metallic glass even with nanocrystallization, *Materials Today Advances* 16 (2022) 100316. <https://doi.org/10.1016/j.mtadv.2022.100316>.
- [22] S. Kumar Patel, B. Kumar Swain, A. Behera, S. Sanjeeb Mohapatra, Metallic Glasses: A Revolution in Material Science, in: D. Minić, M. Vasić (Eds.), *Metallic Glasses*, *IntechOpen* (2020). <https://doi.org/10.5772/intechopen.90165>.

- [23] A.B. Behboud, Development of Nanostructured Metallic Glasses With High Toughness, Master's thesis, Middle East Technical University (2021). <https://doi.org/10.13140/RG.2.2.31305.26727>.
- [24] Q. Viel, Glass-to-crystal transition in a chiral pharmaceutical system, Doctoral dissertation, Normandie Université (2017).
- [25] M. Lai, X. Zhang, F. Fang, Crystal Orientation Effect on the Subsurface Deformation of Monocrystalline Germanium in Nanometric Cutting, *Nanoscale Research Letters* 12 (2017) 296. <https://doi.org/10.1186/s11671-017-2047-3>.
- [26] M.G. Abiad, M.T. Carvajal, O.H. Campanella, A Review on Methods and Theories to Describe the Glass Transition Phenomenon: Applications in Food and Pharmaceutical Products, *Food Engineering Reviews* 1 (2009) 105–132. <https://doi.org/10.1007/s12393-009-9009-1>.
- [27] A.R. Yavari, A.L. Moulec, A. Inoue, N. Nishiyama, N. Lupu, E. Matsubara, W.J. Botta, G. Vaughan, M.D. Michiel, Å. Kvik, Excess free volume in metallic glasses measured by X-ray diffraction, *Acta Materialia* 53 (2005) 1611–1619. <https://doi.org/10.1016/j.actamat.2004.12.011>.
- [28] H. Wang, Bulk metallic glass composites, *Journal of Materials Science and Technology* 21 (2005) 86–90.
- [29] E.A.A. Neel, J.C. Knowles, Biocompatibility and other properties of phosphate-based glasses for medical applications, in: *Cellular Response to Biomaterials*, Elsevier, 2009: pp. 156–182. <https://doi.org/10.1533/9781845695477.1.156>.
- [30] Y. Sun, A. Concustell, A.L. Greer, Thermomechanical processing of metallic glasses: extending the range of the glassy state, *Nature Reviews Materials* 1 (2016) 16039. <https://doi.org/10.1038/natrevmats.2016.39>.
- [31] C. Zhang, D. Ouyang, S. Pauly, L. Liu, 3D printing of bulk metallic glasses, *Materials Science and Engineering: R: Reports* 145 (2021) 100625. <https://doi.org/10.1016/j.mser.2021.100625>.
- [32] Metallic Glass Gears Make for Graceful Robots, NASA Jet Propulsion Laboratory (JPL). <https://www.jpl.nasa.gov/news/metallic-glass-gears-make-for-graceful-robots> (accessed February 2, 2024).
- [33] J.J. Kruzic, Bulk Metallic Glasses as Structural Materials: A Review, *Advanced Engineering Materials* 18 (2016) 1308–1331. <https://doi.org/10.1002/adem.201600066>.
- [34] Amorphous Metal, Liquidmetal. <https://liquidmetal.com/amorphous-metal/> (accessed February 2, 2024).
- [35] F.-F. Cai, A. Blanquer, M.B. Costa, L. Schweiger, B. Sarac, A.L. Greer, J. Schroers, C. Teichert, C. Nogués, F. Spieckermann, J. Eckert, Hierarchical Surface Pattern on Ni-Free Ti-Based Bulk Metallic Glass to Control Cell Interactions, *Small* 20 (2024) 2310364. <https://doi.org/10.1002/sml.202310364>.
- [36] H.F. Li, Y.F. Zheng, Recent advances in bulk metallic glasses for biomedical applications, *Acta Biomaterialia* 36 (2016) 1–20. <https://doi.org/10.1016/j.actbio.2016.03.047>.
- [37] J. Schroers, G. Kumar, T.M. Hodges, S. Chan, T.R. Kyriakides, Bulk metallic glasses for biomedical applications, *JOM* 61 (2009) 21–29. <https://doi.org/10.1007/s11837-009-0128-1>.

- [38] P. Meagher, E.D. O’Cearbhaill, J.H. Byrne, D.J. Browne, Bulk Metallic Glasses for Implantable Medical Devices and Surgical Tools, *Advanced Materials* 28 (2016) 5755–5762. <https://doi.org/10.1002/adma.201505347>.
- [39] M. Niinomi, M. Nakai, Titanium-Based Biomaterials for Preventing Stress Shielding between Implant Devices and Bone, *International Journal of Biomaterials* 2011 (2011) 836587. <https://doi.org/10.1155/2011/836587>.
- [40] L. Damiati, M.G. Eales, A.H. Nobbs, B. Su, P.M. Tsimbouri, M. Salmeron-Sanchez, M.J. Dalby, Impact of surface topography and coating on osteogenesis and bacterial attachment on titanium implants, *Journal of Tissue Engineering* 9 (2018) 204173141879069. <https://doi.org/10.1177/2041731418790694>.
- [41] S. Gravier, G. Kapelski, M. Suéry, J.-J. Blandin, Thermoplastic Forming of Bulk Metallic Glasses, *International Journal of Applied Glass Science* 3 (2012) 180–187. <https://doi.org/10.1111/j.2041-1294.2012.00083.x>.
- [42] E. Yüce, F. Spieckermann, A. Asci, S. Wurster, P. Ramasamy, L. Xi, B. Sarac, J. Eckert, Toxic element-free Ti-based metallic glass ribbons with precious metal additions, *Materials Today Advances* 19 (2023) 100392. <https://doi.org/10.1016/j.mtadv.2023.100392>.
- [43] J. Mi, R.A. Harding, J. Campbell, The tilt casting process, *International Journal of Cast Metals Research* 14 (2002) 325–334. <https://doi.org/10.1080/13640461.2002.11819450>.
- [44] R. Nowosielski, R. Babilas, Fabrication of bulk metallic glasses by centrifugal casting method, *Journal of Achievements in Materials and Manufacturing Engineering* 20 (2007) 487–490.
- [45] H.R. Lashgari, M. Ferry, S. Li, Additive manufacturing of bulk metallic glasses: Fundamental principle, current/future developments and applications, *Journal of Materials Science & Technology* 119 (2022) 131–149. <https://doi.org/10.1016/j.jmst.2021.09.068>.
- [46] M. Hasan, J. Schroers, G. Kumar, Functionalization of Metallic Glasses through Hierarchical Patterning, *Nano Letters* 15 (2015) 963–968. <https://doi.org/10.1021/nl504694s>.
- [47] J. Schroers, T.M. Hodges, G. Kumar, H. Raman, A.J. Barnes, Q. Pham, T.A. Waniuk, Thermoplastic blow molding of metals, *Materials Today* 14 (2011) 14–19. [https://doi.org/10.1016/S1369-7021\(11\)70018-9](https://doi.org/10.1016/S1369-7021(11)70018-9).
- [48] R.M. Ojeda Mota, N. Liu, S.A. Kube, J. Chay, H.D. McClintock, J. Schroers, Overcoming geometric limitations in metallic glasses through stretch blow molding, *Applied Materials Today* 19 (2020) 100567. <https://doi.org/10.1016/j.apmt.2020.100567>.
- [49] J. Schroers, On the formability of bulk metallic glass in its supercooled liquid state, *Acta Materialia* 56 (2008) 471–478. <https://doi.org/10.1016/j.actamat.2007.10.008>.
- [50] G. Kumar, H.X. Tang, J. Schroers, Nanomoulding with amorphous metals, *Nature* 457 (2009) 868–872. <https://doi.org/10.1038/nature07718>.
- [51] B. Sarac, G. Kumar, T. Hodges, S. Ding, A. Desai, J. Schroers, Three-Dimensional Shell Fabrication Using Blow Molding of Bulk Metallic Glass, *Journal of Microelectromechanical Systems* 20 (2011) 28–36. <https://doi.org/10.1109/JMEMS.2010.2090495>.

- [52] H.M. Chiu, G. Kumar, J. Blawdziewicz, J. Schroers, Thermoplastic extrusion of bulk metallic glass, *Scripta Materialia* 61 (2009) 28–31. <https://doi.org/10.1016/j.scriptamat.2009.02.052>.
- [53] G. Kumar, A. Desai, J. Schroers, Bulk Metallic Glass: The Smaller the Better, *Advanced Materials* 23 (2011) 461–476. <https://doi.org/10.1002/adma.201002148>.
- [54] M. Ishida, H. Takeda, N. Nishiyama, K. Kita, Y. Shimizu, Y. Saotome, A. Inoue, Wear resistivity of super-precision microgear made of Ni-based metallic glass, *Materials Science and Engineering: A* 449–451 (2007) 149–154. <https://doi.org/10.1016/j.msea.2006.02.300>.
- [55] J.A. Bardt, G.R. Bourne, T.L. Schmitz, J.C. Ziegert, W. Gregory Sawyer, Micromolding three-dimensional amorphous metal structures, *Journal of Materials Research* 22 (2007) 339–343. <https://doi.org/10.1557/jmr.2007.0035>.
- [56] B. Sarac, S. Bera, S. Balakin, M. Stoica, M. Calin, J. Eckert, Hierarchical surface patterning of Ni- and Be-free Ti- and Zr-based bulk metallic glasses by thermoplastic net-shaping, *Materials Science and Engineering: C* 73 (2017) 398–405. <https://doi.org/10.1016/j.msec.2016.12.059>.
- [57] F. Wang, H. Zhang, X. Liang, F. Gong, J. Ma, Fabrication of metallic glass micro grooves by thermoplastic forming, *Journal of Micromechanics and Microengineering* 27 (2017) 025009. <https://doi.org/10.1088/1361-6439/aa51b5>.
- [58] J. Padmanabhan, E.R. Kinser, M.A. Stalter, C. Duncan-Lewis, J.L. Balestrini, A.J. Sawyer, J. Schroers, T.R. Kyriakides, Engineering Cellular Response Using Nanopatterned Bulk Metallic Glass, *ACS Nano* 8 (2014) 4366–4375. <https://doi.org/10.1021/nn501874q>.
- [59] G. Kumar, P.A. Staffier, J. Blawdziewicz, U.D. Schwarz, J. Schroers, Atomically smooth surfaces through thermoplastic forming of metallic glass, *Applied Physics Letters* 97 (2010) 101907. <https://doi.org/10.1063/1.3485298>.
- [60] Z. Li, Z. Huang, F. Sun, X. Li, J. Ma, Forming of metallic glasses: mechanisms and processes, *Materials Today Advances* 7 (2020) 100077. <https://doi.org/10.1016/j.mtadv.2020.100077>.
- [61] W. Chen, Z. Liu, J. Schroers, Joining of bulk metallic glasses in air, *Acta Materialia* 62 (2014) 49–57. <https://doi.org/10.1016/j.actamat.2013.08.053>.
- [62] N. Li, J. Pan, Z. Liu, L. Liu, Metallic glass nanostructures: Forming strategies and functional applications, *Materials Today Advances* 15 (2022) 100253. <https://doi.org/10.1016/j.mtadv.2022.100253>.
- [63] J. Fu, J. Ma, Nanoengineering of Metallic Glasses, *Advanced Engineering Materials* 25 (2023) 2200659. <https://doi.org/10.1002/adem.202200659>.
- [64] E.R. Kinser, J. Padmanabhan, R. Yu, S.L. Corona, J. Li, S. Vaddiraju, A. Legasse, A. Loye, J. Balestrini, D.A. Solly, J. Schroers, A.D. Taylor, F. Papadimitrakopoulos, R.I. Herzog, T.R. Kyriakides, Nanopatterned Bulk Metallic Glass Biosensors, *ACS Sensors* 2 (2017) 1779–1787. <https://doi.org/10.1021/acssensors.7b00455>.
- [65] A.K. Jain, C.H. Lee, H.S. Gill, 5-Aminolevulinic acid coated microneedles for photodynamic therapy of skin tumors, *Journal of Controlled Release* 239 (2016) 72–81. <https://doi.org/10.1016/j.jconrel.2016.08.015>.

- [66] Z. Hu, C.S. Meduri, R.S.J. Ingle, H.S. Gill, G. Kumar, Solid and hollow metallic glass microneedles for transdermal drug-delivery, *Applied Physics Letters* 116 (2020) 203703. <https://doi.org/10.1063/5.0008983>.
- [67] A.L. Greer, Fine fibres with multifunctionality, *Nature Nanotechnology* 15 (2020) 1–2. <https://doi.org/10.1038/s41565-020-0725-2>.
- [68] W. Yan, I. Richard, G. Kurtuldu, N.D. James, G. Schiavone, J.W. Squir, T. Nguyen-Dang, T. Das Gupta, Y. Qu, J.D. Cao, R. Ignatans, S.P. Lacour, V. Tileli, G. Courtine, J.F. Löffler, F. Sorin, Structured nanoscale metallic glass fibres with extreme aspect ratios, *Nature Nanotechnology* 15 (2020) 875–882. <https://doi.org/10.1038/s41565-020-0747-9>.
- [69] S. Gao, J. Jia, S. Chen, H. Luan, Y. Shao, K. Yao, Oxide-derived nanostructured metallic-glass electrodes for efficient electrochemical hydrogen generation, *RSC Advances* 7 (2017) 27058–27064. <https://doi.org/10.1039/C7RA02954C>.
- [70] M. Carmo, R.C. Sekol, S. Ding, G. Kumar, J. Schroers, A.D. Taylor, Bulk Metallic Glass Nanowire Architecture for Electrochemical Applications, *ACS Nano* 5 (2011) 2979–2983. <https://doi.org/10.1021/nn200033c>.
- [71] B. Sarac, J. Ketkaew, D.O. Popnoe, J. Schroers, Honeycomb Structures of Bulk Metallic Glasses, *Advanced Functional Materials* 22 (2012) 3161–3169. <https://doi.org/10.1002/adfm.201200539>
- [72] X. Luo, M. Meng, R. Li, Z. Li, I.S. Cole, X.-B. Chen, T. Zhang, Honeycomb-like porous metallic glasses decorated by Cu nanoparticles formed by one-pot electrochemically galvanostatic etching, *Materials & Design* 196 (2020) 109109. <https://doi.org/10.1016/j.matdes.2020.109109>.
- [73] G. Kaltenboeck, T. Harris, K. Sun, T. Tran, G. Chang, J.P. Schramm, M.D. Demetriou, W.L. Johnson, Accessing thermoplastic processing windows in metallic glasses using rapid capacitive discharge, *Scientific Reports* 4 (2014) 6441. <https://doi.org/10.1038/srep06441>.
- [74] G. Wang, M.D. Demetriou, J.P. Schramm, P.K. Liaw, W.L. Johnson, Compression-compression fatigue of Pd₄₃Ni₁₀Cu₂₇P₂₀ metallic glass foam, *Journal of Applied Physics* 108 (2010) 023505. <https://doi.org/10.1063/1.3457221>.
- [75] J. Ma, X.Y. Zhang, D.P. Wang, D.Q. Zhao, D.W. Ding, K. Liu, W.H. Wang, Superhydrophobic metallic glass surface with superior mechanical stability and corrosion resistance, *Applied Physics Letters* 104 (2014) 173701. <https://doi.org/10.1063/1.4874275>.
- [76] N. Li, T. Xia, L. Heng, L. Liu, Superhydrophobic Zr-based metallic glass surface with high adhesive force, *Applied Physics Letters* 102 (2013) 251603. <https://doi.org/10.1063/1.4812480>.
- [77] C. Uzun, C. Meduri, N. Kahler, L.G. De Peralta, J.M. McCollum, M. Pantoya, G. Kumar, A.A. Bernussi, Photoinduced heat conversion enhancement of metallic glass nanowire arrays, *Journal of Applied Physics* 125 (2019) 015102. <https://doi.org/10.1063/1.5059423>.
- [78] M. Kanik, P. Bordeenithikasem, D. Kim, N. Selden, A. Desai, R. M'Closkey, J. Schroers, Metallic Glass Hemispherical Shell Resonators, *Journal of Microelectromechanical Systems* 24 (2015) 19–28. <https://doi.org/10.1109/JMEMS.2014.2363581>.

- [79] N.T. Panagiotopoulos, K. Georgarakis, A.M. Jorge Jr, M. Aljerf, W.J. Botta, A.L. Greer, A.R. Yavari, Advanced ultra-light multifunctional metallic-glass wave springs, *Materials & Design* 192 (2020) 108770. <https://doi.org/10.1016/j.matdes.2020.108770>.
- [80] K.W. Dong, J. Kong, Y. Peng, Q. Zhou, K.H. Wang, Thermoplastic bonding of TC4 and 316L stainless steel with a Ti-based bulk metallic glass as the filler metal, *Journal of Materials Research and Technology* 11 (2021) 487–497. <https://doi.org/10.1016/j.jmrt.2021.01.042>.
- [81] S. Soman, A.R. Ajitha, Life cycle assessment of metallic biomaterials, in: *Fundamental Biomaterials: Metals*, Elsevier (2018) 411–423. <https://doi.org/10.1016/B978-0-08-102205-4.00022-2>.
- [82] S. Scialla, G. Martuscelli, F. Nappi, S.S.A. Singh, A. Iervolino, D. Larobina, L. Ambrosio, M.G. Raucci, Trends in Managing Cardiac and Orthopaedic Device-Associated Infections by Using Therapeutic Biomaterials, *Polymers* 13 (2021) 1556. <https://doi.org/10.3390/polym13101556>.
- [83] M.E. Afari, W. Syed, L. Tsao, Implantable devices for heart failure monitoring and therapy, *Heart Fail Reviews* 23 (2018) 935–944. <https://doi.org/10.1007/s10741-018-9687-y>.
- [84] Global Orthopaedic Implants Market Report and Forecast 2024-2032. <https://www.expertmarketresearch.com/reports/orthopaedic-implants-market> (accessed February 7, 2024).
- [85] Cardiovascular Implants Market Report and Forecast 2024-2032 | IMARC Group. <https://www.imarcgroup.com/cardiovascular-implants-market> (accessed February 7, 2024).
- [86] S.F. DDS, Dental implant contamination: 3 reasons behind a late-stage failure, *Perio Implant Advisory* (2019). <https://www.perioimplantadvisory.com/clinical-tips/article/14071593/dental-implant-contamination-3-reasons-behind-a-latestage-failure> (accessed February 9, 2024).
- [87] T. Avril, Hip and knee-replacement infections: Doctors debate best solutions, *Https://Www.Inquirer.Com* (2018). <https://www.inquirer.com/philly/health/hip-knee-replacement-infections-rothman-jefferson-guidelines-20180727.html> (accessed February 9, 2024).
- [88] J.G.S. Souza, M.M. Bertolini, R.C. Costa, B.E. Nagay, A. Dongari-Bagtzoglou, V.A.R. Barão, Targeting implant-associated infections: titanium surface loaded with antimicrobial, *iScience* 24 (2021) 102008. <https://doi.org/10.1016/j.isci.2020.102008>.
- [89] A. Oliva, M.C. Miele, D. Al Ismail, F. Di Timoteo, M. De Angelis, L. Rosa, A. Cutone, M. Venditti, M.T. Mascellino, P. Valenti, C.M. Mastroianni, Challenges in the Microbiological Diagnosis of Implant-Associated Infections: A Summary of the Current Knowledge, *Frontiers in Microbiology* 12 (2021) 750460. <https://doi.org/10.3389/fmicb.2021.750460>.
- [90] H.J. Busscher, H.C. van der Mei, G. Subbiahdoss, P.C. Jutte, J.J.A.M. van den Dungen, S.A.J. Zaat, M.J. Schultz, D.W. Grainger, Biomaterial-Associated Infection: Locating the Finish Line in the Race for the Surface, *Science Translational Medicine* 4 (2012). <https://doi.org/10.1126/scitranslmed.3004528>.

- [91] S. Amin Yavari, S.M. Castenmiller, J.A.G. Van Strijp, M. Croes, Combating Implant Infections: Shifting Focus from Bacteria to Host, *Advanced Materials* 32 (2020) 2002962. <https://doi.org/10.1002/adma.202002962>.
- [92] J.S. VanEpps, J.G. Younger, Implantable Device-Related Infection, *Shock* 46 (2016) 597–608. <https://doi.org/10.1097/SHK.0000000000000692>.
- [93] S. Shiels, L. Mangum, J. Wenke, Revisiting the “race for the surface” in a pre-clinical model of implant infection, *European Cells and Materials* 39 (2020) 77–95. <https://doi.org/10.22203/eCM.v039a05>.
- [94] E.A. Masters, B.F. Ricciardi, K.L.D.M. Bentley, T.F. Moriarty, E.M. Schwarz, G. Muthukrishnan, Skeletal infections: microbial pathogenesis, immunity and clinical management, *Nature Reviews Microbiology* 20 (2022) 385–400. <https://doi.org/10.1038/s41579-022-00686-0>.
- [95] D.G. Kennedy, A.M. O’Mahony, E.P. Culligan, C.M. O’Driscoll, K.B. Ryan, Strategies to Mitigate and Treat Orthopaedic Device-Associated Infections, *Antibiotics* 11 (2022) 1822. <https://doi.org/10.3390/antibiotics11121822>.
- [96] C.W.K. Rosman, J.M. Van Dijn, J. Sjollem, Interactions between the foreign body reaction and *Staphylococcus aureus* biomaterial-associated infection. Winning strategies in the derby on biomaterial implant surfaces, *Critical Reviews in Microbiology* 48 (2022) 624–640. <https://doi.org/10.1080/1040841X.2021.2011132>.
- [97] J. Jiao, S. Zhang, X. Qu, B. Yue, Recent Advances in Research on Antibacterial Metals and Alloys as Implant Materials, *Frontiers in Cellular and Infection Microbiology* 11 (2021) 693939. <https://doi.org/10.3389/fcimb.2021.693939>.
- [98] D. Szymiski, N. Walter, K. Hierl, M. Rupp, V. Alt, Direct Hospital Costs per Case of Periprosthetic Hip and Knee Joint Infections in Europe – A Systematic Review, *The Journal of Arthroplasty* (2024) S0883540324000329. <https://doi.org/10.1016/j.arth.2024.01.032>.
- [99] A. Premkumar, D.A. Kolin, K.X. Farley, J.M. Wilson, A.S. McLawhorn, M.B. Cross, P.K. Sculco, Projected Economic Burden of Periprosthetic Joint Infection of the Hip and Knee in the United States, *The Journal of Arthroplasty* 36 (2021) 1484–1489.e3. <https://doi.org/10.1016/j.arth.2020.12.005>.
- [100] Giles, Sun Tzu On The Art Of War, 0 ed., *Routledge* (2013). <https://doi.org/10.4324/9781315030081>.
- [101] M.K. Pal, M. Lavanya, Microbial Influenced Corrosion: Understanding Bioadhesion and Biofilm Formation, *Journal of Bio- and Tribo-Corrosion* 8 (2022) 76. <https://doi.org/10.1007/s40735-022-00677-x>.
- [102] M.H. Muhammad, A.L. Idris, X. Fan, Y. Guo, Y. Yu, X. Jin, J. Qiu, X. Guan, T. Huang, Beyond Risk: Bacterial Biofilms and Their Regulating Approaches, *Frontiers in Microbiology* 11 (2020) 928. <https://doi.org/10.3389/fmicb.2020.00928>.
- [103] B. Li, T.J. Webster, Bacteria antibiotic resistance: New challenges and opportunities for implant-associated orthopedic infections, *Journal of Orthopaedic Research* (2017) 22–32. <https://doi.org/10.1002/jor.23656>.
- [104] Z. Wu, B. Chan, J. Low, J.J.H. Chu, H.W.D. Hey, A. Tay, Microbial resistance to nanotechnologies: An important but understudied consideration using antimicrobial nanotechnologies in orthopaedic implants, *Bioactive Materials* 16 (2022) 249–270. <https://doi.org/10.1016/j.bioactmat.2022.02.014>.

- [105] M. Goudarzi, M. Navidinia, N. Khadembashi, R. Rasouli, Biofilm Matrix Formation in Human: Clinical Significance, Diagnostic Techniques, and Therapeutic Drugs, *Archives of Clinical Infectious Diseases* 16 (2021). <https://doi.org/10.5812/archcid.107919>.
- [106] G. Shineh, M. Mobaraki, M.J. Perves Bappy, D.K. Mills, Biofilm Formation, and Related Impacts on Healthcare, Food Processing and Packaging, Industrial Manufacturing, Marine Industries, and Sanitation—A Review, *Applied Microbiology* 3 (2023) 629–665. <https://doi.org/10.3390/applmicrobiol3030044>.
- [107] W. Li, E.S. Thian, M. Wang, Z. Wang, L. Ren, Surface Design for Antibacterial Materials: From Fundamentals to Advanced Strategies, *Advanced Science* 8 (2021) 2100368. <https://doi.org/10.1002/advs.202100368>.
- [108] Z. Chen, Z. Wang, W. Qiu, F. Fang, Overview of Antibacterial Strategies of Dental Implant Materials for the Prevention of Peri-Implantitis, *Bioconjugate Chemistry* 32 (2021) 627–638. <https://doi.org/10.1021/acs.bioconjchem.1c00129>.
- [109] R. Kaur, S. Liu, Antibacterial surface design – Contact kill, *Progress in Surface Science* 91 (2016) 136–153. <https://doi.org/10.1016/j.progsurf.2016.09.001>.
- [110] D.P. Linklater, V.A. Baulin, S. Juodkazis, R.J. Crawford, P. Stoodley, E.P. Ivanova, Mechano-bactericidal actions of nanostructured surfaces, *Nature Reviews Microbiology* 19 (2021) 8–22. <https://doi.org/10.1038/s41579-020-0414-z>.
- [111] Q. Song, S.Y. Chan, Z. Xiao, R. Zhao, Y. Zhang, X. Chen, T. Liu, Y. Yan, B. Zhang, F. Han, P. Li, Contact-killing antibacterial mechanisms of polycationic coatings: A review, *Progress in Organic Coatings* 188 (2024) 108214. <https://doi.org/10.1016/j.porgcoat.2024.108214>.
- [112] S. Hawi, S. Goel, V. Kumar, O. Pearce, W.N. Ayre, E.P. Ivanova, Critical Review of Nanopillar-Based Mechanobactericidal Systems, *ACS Applied Nano Materials* 5 (2022) 1–17. <https://doi.org/10.1021/acsnm.1c03045>.
- [113] H.Y. Ahmadabadi, K. Yu, J.N. Kizhakkedathu, Surface modification approaches for prevention of implant associated infections, *Colloids and Surfaces B: Biointerfaces* 193 (2020) 111116. <https://doi.org/10.1016/j.colsurfb.2020.111116>.
- [114] J.J. Londoño, M.B. Costa, F.-F. Cai, F. Spieckermann, A. Levesque, S. Prades-Rödel, A.L. Greer, J. Eckert, A. Blatter, Microalloying as a strategy to modulate antibacterial ion release from metallic glasses, *Journal of Alloys and Compounds* 968 (2023) 172121. <https://doi.org/10.1016/j.jallcom.2023.172121>.
- [115] F. Liu, C. Shi, X. Guo, Z. He, L. Pan, Z. Huang, X. Zhang, J. Zou, Rational Design of Better Hydrogen Evolution Electrocatalysts for Water Splitting: A Review, *Advanced Science* 9 (2022) 2200307. <https://doi.org/10.1002/advs.202200307>.
- [116] W. Zhai, Y. Ma, D. Chen, J.C. Ho, Z. Dai, Y. Qu, Recent progress on the long-term stability of hydrogen evolution reaction electrocatalysts, *InfoMat* 4 (2022) e12357. <https://doi.org/10.1002/inf2.12357>.
- [117] Y. Xu, X. Zhang, Y. Liu, R. Wang, Y. Yang, J. Chen, A critical review of research progress for metal alloy materials in hydrogen evolution and oxygen evolution reaction, *Environmental Science and Pollution Research* 30 (2022) 11302–11320. <https://doi.org/10.1007/s11356-022-24728-5>.
- [118] C. Li, J.-B. Baek, Recent Advances in Noble Metal (Pt, Ru, and Ir)-Based Electrocatalysts for Efficient Hydrogen Evolution Reaction, *ACS Omega* 5 (2020) 31–40. <https://doi.org/10.1021/acsomega.9b03550>.

- [119] Md.N. Islam, J. Ahmed, M. Faisal, J.S. Algethami, K. Aoki, Y. Nagao, F.A. Harraz, M.A. Hasnat, Efficient Electrocatalytic Hydrogen Evolution Reaction on CuO Immobilized Stainless-Steel Electrode Prepared by the SILAR Method, *ChemistrySelect* 8 (2023) e202301077. <https://doi.org/10.1002/slct.202301077>.
- [120] L. Liu, Y. Wang, Y. Zhao, Y. Wang, Z. Zhang, T. Wu, W. Qin, S. Liu, B. Jia, H. Wu, D. Zhang, X. Qu, M. Chhowalla, M. Qin, Ultrahigh Pt-Mass-Activity Hydrogen Evolution Catalyst Electrodeposited from Bulk Pt, *Advanced Functional Materials* 32 (2022) 2112207. <https://doi.org/10.1002/adfm.202112207>.
- [121] Y. Tong, H. Ma, F. Xiao, S. Bohm, H. Fu, Y. Luo, Precision engineering of precious metal catalysts for enhanced hydrogen production efficiency, *Process Safety and Environmental Protection* 178 (2023) 559–579. <https://doi.org/10.1016/j.psep.2023.08.066>.
- [122] P. Yu, F. Wang, T.A. Shifa, X. Zhan, X. Lou, F. Xia, J. He, Earth abundant materials beyond transition metal dichalcogenides: A focus on electrocatalyzing hydrogen evolution reaction, *Nano Energy* 58 (2019) 244–276. <https://doi.org/10.1016/j.nanoen.2019.01.017>.
- [123] C. Hu, C. Lv, N. Zeng, A. Liu, Y. Liu, L. Hu, P. Li, Y. Yao, J. Cai, T. Tang, Recent Advances in Ni-Based Electrocatalysts for Hydrogen Evolution Reaction, *Energy Technology* 11 (2023) 2201048. <https://doi.org/10.1002/ente.202201048>.
- [124] A. Ali, P.K. Shen, Nonprecious metal's graphene-supported electrocatalysts for hydrogen evolution reaction: Fundamentals to applications, *Carbon Energy* 2 (2020) 99–121. <https://doi.org/10.1002/cey2.26>.
- [125] W.H. Ryu, K.J. Kim, M.K. Kwak, C.W. Ryu, E.S. Park, Development of Zr-based metallic glasses to utilize thermoplastic forming processes of engineering plastics, *Materials & Design* 232 (2023) 112100. <https://doi.org/10.1016/j.matdes.2023.112100>.
- [126] K. Kosiba, L. Deng, S. Scudino, Viscous Flow of Supercooled Liquid in a Zr-Based Bulk Metallic Glass Synthesized by Additive Manufacturing, *Materials* 13 (2020) 3803. <https://doi.org/10.3390/ma13173803>.
- [127] A. Monfared, W. Liu, L. Zhang, Metallic glass hardening after thermoplastic forming, *Materials Science and Engineering: A* 725 (2018) 181–186. <https://doi.org/10.1016/j.msea.2018.04.021>.
- [128] G. Kumar, D. Rector, R.D. Conner, J. Schroers, Embrittlement of Zr-based bulk metallic glasses, *Acta Materialia* 57 (2009) 3572–3583. <https://doi.org/10.1016/j.actamat.2009.04.016>.
- [129] J. Ketkaew, Z. Liu, W. Chen, J. Schroers, Critical Crystallization for Embrittlement in Metallic Glasses, *Physical Review Letters* 115 (2015) 265502. <https://doi.org/10.1103/PhysRevLett.115.265502>.
- [130] J. Ketkaew, W. Chen, H. Wang, A. Datye, M. Fan, G. Pereira, U.D. Schwarz, Z. Liu, R. Yamada, W. Dmowski, M.D. Shattuck, C.S. O'Hern, T. Egami, E. Bouchbinder, J. Schroers, Mechanical glass transition revealed by the fracture toughness of metallic glasses, *Nature Communications* 9 (2018) 3271. <https://doi.org/10.1038/s41467-018-05682-8>.
- [131] M.L. Lind, G. Duan, W.L. Johnson, Isoconfigurational Elastic Constants and Liquid Fragility of a Bulk Metallic Glass Forming Alloy, *Physical Review Letters* 97 (2006) 015501. <https://doi.org/10.1103/PhysRevLett.97.015501>.

- [132] M.B. Berger, P. Slosar, Z. Schwartz, D.J. Cohen, S.B. Goodman, P.A. Anderson, B.D. Boyan, A Review of Biomimetic Topographies and Their Role in Promoting Bone Formation and Osseointegration: Implications for Clinical Use, *Biomimetics* 7 (2022) 46. <https://doi.org/10.3390/biomimetics7020046>.
- [133] R. Rodriguez-González, L. Monsalve-Guil, A. Jimenez-Guerra, E. Velasco-Ortega, J. Moreno-Muñoz, E. Nuñez-Marquez, R.A. Pérez, J. Gil, I. Ortiz-Garcia, Relevant Aspects of Titanium Topography for Osteoblastic Adhesion and Inhibition of Bacterial Colonization, *Materials* 16 (2023) 3553. <https://doi.org/10.3390/ma16093553>.
- [134] N. Gui, W. Xu, D.E. Myers, R. Shukla, H.P. Tang, M. Qian, The effect of ordered and partially ordered surface topography on bone cell responses: a review, *Biomaterials Science* 6 (2018) 250–264. <https://doi.org/10.1039/C7BM01016H>.
- [135] J. Barberi, S. Spriano, Titanium and Protein Adsorption: An Overview of Mechanisms and Effects of Surface Features, *Materials* 14 (2021) 1590. <https://doi.org/10.3390/ma14071590>.
- [136] K. Kulangara, K.W. Leong, Substrate topography shapes cell function, *Soft Matter* 5 (2009) 4072. <https://doi.org/10.1039/b910132m>.
- [137] Y. Wang, Y. Yang, T. Yoshitomi, N. Kawazoe, Y. Yang, G. Chen, Regulation of gene transfection by cell size, shape and elongation on micropatterned surfaces, *Journal of Materials Chemistry B* 9 (2021) 4329–4339. <https://doi.org/10.1039/D1TB00815C>.
- [138] A.M. Loye, E.R. Kinser, S. Bensouda, M. Shayan, R. Davis, R. Wang, Z. Chen, U.D. Schwarz, J. Schroers, T.R. Kyriakides, Regulation of Mesenchymal Stem Cell Differentiation by Nanopatterning of Bulk Metallic Glass, *Scientific Reports* 8 (2018) 8758. <https://doi.org/10.1038/s41598-018-27098-6>.
- [139] M. d'Angelo, E. Benedetti, M.G. Tupone, M. Catanesi, V. Castelli, A. Antonosante, A. Cimini, The Role of Stiffness in Cell Reprogramming: A Potential Role for Biomaterials in Inducing Tissue Regeneration, *Cells* 8 (2019) 1036. <https://doi.org/10.3390/cells8091036>.
- [140] C. Matschegewski, S. Staehlke, R. Loeffler, R. Lange, F. Chai, D.P. Kern, U. Beck, B.J. Nebe, Cell architecture–cell function dependencies on titanium arrays with regular geometry, *Biomaterials* 31 (2010) 5729–5740. <https://doi.org/10.1016/j.biomaterials.2010.03.073>.
- [141] J. Rychly, B.J. Nebe, Cell-material interaction, *BioNanoMaterials* 14 (2013). <https://doi.org/10.1515/bnm-2013-0019>.
- [142] M.J. Dalby, Topographically induced direct cell mechanotransduction, *Medical Engineering & Physics* 27 (2005) 730–742. <https://doi.org/10.1016/j.medengphy.2005.04.005>.
- [143] A. Jaggessar, H. Shahali, A. Mathew, P.K.D.V. Yarlagaadda, Bio-mimicking nano and micro-structured surface fabrication for antibacterial properties in medical implants, *Journal of Nanobiotechnology* 15 (2017) 64. <https://doi.org/10.1186/s12951-017-0306-1>.
- [144] S.G. Higgins, M. Becce, A. Belessiotis-Richards, H. Seong, J.E. Sero, M.M. Stevens, High-Aspect-Ratio Nanostructured Surfaces as Biological Metamaterials, *Advanced Materials* 32 (2020) 1903862. <https://doi.org/10.1002/adma.201903862>.
- [145] H. Jeon, C.G. Simon Jr, G. Kim, A mini-review: Cell response to microscale, nanoscale, and hierarchical patterning of surface structure, *Journal of Biomedical Materials*

- Research Part B: Applied Biomaterials* 102 (2014) 1580–1594. <https://doi.org/10.1002/jbm.b.33158>.
- [146] K. Zhang, X. Xiao, X. Wang, Y. Fan, X. Li, Topographical patterning: characteristics of current processing techniques, controllable effects on material properties and co-cultured cell fate, updated applications in tissue engineering, and improvement strategies, *Journal of Materials Chemistry B* 7 (2019) 7090–7109. <https://doi.org/10.1039/C9TB01682A>.
- [147] S. Jafarkhani, E. Amiri, S. Moazzeni, T. Zohoorian-Abootorabi, M. Eftekhary, S. Aminnezhad, M. Khakbiz, Exploring the effects of micro-nano surface topography on MG63 osteoblast-like cell responses: An in vitro study, *Colloids and Surfaces A: Physicochemical and Engineering Aspects* 675 (2023) 131872. <https://doi.org/10.1016/j.colsurfa.2023.131872>.
- [148] J. Kim, W.-G. Bae, K.-T. Lim, K.-J. Jang, S. Oh, K.-J. Jang, N. Li Jeon, K.-Y. Suh, J. Hoon Chung, Density of nanopatterned surfaces for designing bone tissue engineering scaffolds, *Materials Letters* 130 (2014) 227–231. <https://doi.org/10.1016/j.matlet.2014.05.107>.
- [149] B.S. Kopf, S. Ruch, S. Berner, N.D. Spencer, K. Maniura-Weber, The role of nanostructures and hydrophilicity in osseointegration: In-vitro protein-adsorption and blood-interaction studies, *Journal of Biomedical Materials Research Part A* 103 (2015) 2661–2672. <https://doi.org/10.1002/jbm.a.35401>.
- [150] M. Kulkarni, A. Mazare, J. Park, E. Gongadze, M.S. Killian, S. Kralj, K. Von Der Mark, A. Iglič, P. Schmuki, Protein interactions with layers of TiO₂ nanotube and nanopore arrays: Morphology and surface charge influence, *Acta Biomaterialia* 45 (2016) 357–366. <https://doi.org/10.1016/j.actbio.2016.08.050>.
- [151] E. Jia, X. Zhao, Y. Lin, Z. Su, Protein adsorption on titanium substrates and its effects on platelet adhesion, *Applied Surface Science* 529 (2020) 146986. <https://doi.org/10.1016/j.apsusc.2020.146986>.
- [152] S. Astals, M. Romero-Güiza, J. Mata-Alvarez, Municipal Solid Waste, in: G. Ferreira (eds), *Alternative Energies. Advanced Structured Materials*, vol 34, Springer, Berlin, Heidelberg (2013) 1–26. https://doi.org/10.1007/978-3-642-40680-5_1.
- [153] F.-F. Cai, B. Sarac, A. Akman, J.J. Londoño, S. Gümürükcü, L. Schweiger, M. Hantusch, J. Schroers, A. Blatter, A. Gebert, F. Spieckermann, J. Eckert, Nano-Patterned Pt-Based Metallic Glass Electrocatalysts with In-Situ Copper Oxide Foam for Enhanced Hydrogen Evolution, (2024). <https://doi.org/10.48550/arXiv.2406.14079>.
- [154] D. Bhalothia, L. Krishnia, S.-S. Yang, C. Yan, W.-H. Hsiung, K.-W. Wang, T.-Y. Chen, Recent Advancements and Future Prospects of Noble Metal-Based Heterogeneous Nanocatalysts for Oxygen Reduction and Hydrogen Evolution Reactions, *Applied Sciences* 10 (2020) 7708. <https://doi.org/10.3390/app10217708>.
- [155] A.E. Hughes, N. Haque, S.A. Northey, S. Giddey, Platinum Group Metals: A Review of Resources, Production and Usage with a Focus on Catalysts, *Resources* 10 (2021) 93. <https://doi.org/10.3390/resources10090093>.
- [156] C. Sealy, The problem with platinum, *Materials Today* 11 (2008) 65–68. [https://doi.org/10.1016/S1369-7021\(08\)70254-2](https://doi.org/10.1016/S1369-7021(08)70254-2).
- [157] J.O. Bockris, A.K.N. Reddy, *Electrodics in Chemistry, Engineering, Biology, and Environmental Science*, Springer (2004).

- [158] Y. Yan, C. Wang, Z. Huang, J. Fu, Z. Lin, X. Zhang, J. Ma, J. Shen, Highly efficient and robust catalysts for the hydrogen evolution reaction by surface nano engineering of metallic glass, *Journal of Materials Chemistry A* 9 (2021) 5415–5424. <https://doi.org/10.1039/D0TA10235K>.
- [159] R.C. Sekol, G. Kumar, M. Carmo, F. Gittleson, N. Hardesty-Dyck, S. Mukherjee, J. Schroers, A.D. Taylor, Bulk Metallic Glass Micro Fuel Cell, *Small* 9 (2013) 2081–2085. <https://doi.org/10.1002/sml.201201647>.
- [160] G. Doubek, R.C. Sekol, J. Li, W. Ryu, F.S. Gittleson, S. Nejati, E. Moy, C. Reid, M. Carmo, M. Linardi, P. Bordeenithikasem, E. Kinser, Y. Liu, X. Tong, C.O. Osuji, J. Schroers, S. Mukherjee, A.D. Taylor, Guided Evolution of Bulk Metallic Glass Nanostructures: A Platform for Designing 3D Electrocatalytic Surfaces, *Advanced Materials* 28 (2016) 1940–1949. <https://doi.org/10.1002/adma.201504504>.
- [161] B. Sarac, Y.P. Ivanov, T. Karazehir, B. Putz, A.L. Greer, A.S. Sarac, J. Eckert, Metallic Glass Films with Nanostructured Periodic Density Fluctuations Supported on Si/SiO₂ as an Efficient Hydrogen Sorber, *Chemistry – A European Journal* 26 (2020) 8244–8253. <https://doi.org/10.1002/chem.202001596>.
- [162] W. Xu, S. Zhu, Y. Liang, Z. Cui, X. Yang, A. Inoue, H. Wang, A highly efficient electrocatalyst based on amorphous Pd–Cu–S material for hydrogen evolution reaction, *Journal of Materials Chemistry A* 5 (2017) 18793–18800. <https://doi.org/10.1039/C7TA05314B>.
- [163] J. Tian, W. Wu, Z. Tang, Y. Wu, R. Burns, B. Tichnell, Z. Liu, S. Chen, Oxygen Reduction Reaction and Hydrogen Evolution Reaction Catalyzed by Pd–Ru Nanoparticles Encapsulated in Porous Carbon Nanosheets, *Catalysts* 8 (2018) 329. <https://doi.org/10.3390/catal8080329>.
- [164] S. Wang, N. Li, L. Liu, Enhanced hydrogen generation performance of Pd-based micro/nano hierarchical porous structure, *Materials Letters* 228 (2018) 443–446. <https://doi.org/10.1016/j.matlet.2018.06.090>.
- [165] B. Sarac, T. Karazehir, M. Mühlbacher, A.S. Sarac, J. Eckert, Electrocatalytic Behavior of Hydrogenated Pd–Metallic Glass Nanofilms: Butler–Volmer, Tafel, and Impedance Analyses, *Electrocatalysis* 11 (2020) 94–109. <https://doi.org/10.1007/s12678-019-00572-z>.
- [166] C. Veiga, J.P. Davim, A.J.R. Loureiro, Properties and applications of titanium alloys: A brief review, *Reviews on Advanced Materials Science* 32.2 (2012): 133–148.
- [167] M. Niinomi, Mechanical properties of biomedical titanium alloys, *Materials Science and Engineering: A* 243 (1998) 231–236. [https://doi.org/10.1016/S0921-5093\(97\)00806-X](https://doi.org/10.1016/S0921-5093(97)00806-X).
- [168] D. Pressl, C. Teichert, G. Hlawacek, H. Clemens, P.P. Iliev, A. Schuster, F. Feyerabend, R. Willumeit, Characterization of Phospholipid Bilayers on Ti-6Al-4V and Ti-6Al-7Nb, *Advanced Engineering Materials* 10 (2008) 47–52. <https://doi.org/10.1002/adem.200800103>.
- [169] A. Sypien, M. Stoica, T. Czeppe, Properties of the Ti₄₀Zr₁₀Cu₃₆Pd₁₄ BMG Modified by Sn and Nb Additions, *Journal of Materials Engineering and Performance* 25 (2016) 800–808. <https://doi.org/10.1007/s11665-016-1898-6>.
- [170] S. Bera, B. Sarac, S. Balakin, P. Ramasamy, M. Stoica, M. Calin, J. Eckert, Micro-patterning by thermoplastic forming of Ni-free Ti-based bulk metallic glasses, *Materials & Design* 120 (2017) 204–211. <https://doi.org/10.1016/j.matdes.2017.01.080>.

- [171] M. Calin, M. Stoica, N. Zheng, X.R. Wang, S. Scudino, A. Gebert, J. Eckert, Thermal Stability and Crystallization Kinetics of $\text{Ti}_{40}\text{Zr}_{10}\text{Cu}_{34}\text{Pd}_{14}\text{Sn}_2$ Bulk Metallic Glass, *Solid State Phenomena* 188 (2012) 3–10. <https://doi.org/10.4028/www.scientific.net/SSP.188.3>.
- [172] S. Zhu, G. Xie, F. Qin, X. Wang, A. Inoue, Effect of Minor Sn Additions on the Formation and Properties of TiCuZrPd Bulk Glassy Alloy, *Materials Transactions* 53 (2012) 500–503. <https://doi.org/10.2320/matertrans.M2011281>.
- [173] N. Zheng, G. Wang, L.C. Zhang, M. Calin, M. Stoica, G. Vaughan, N. Mattern, J. Eckert, In situ high-energy x-ray diffraction observation of structural evolution in a Ti-based bulk metallic glass upon heating, *Journal of Materials Research* 25 (2010) 2271–2277. <https://doi.org/10.1557/jmr.2010.0298>.
- [174] F.X. Qin, X.M. Wang, A. Inoue, Effect of annealing on microstructure and mechanical property of a Ti–Zr–Cu–Pd bulk metallic glass, *Intermetallics* 15 (2007) 1337–1342. <https://doi.org/10.1016/j.intermet.2007.04.005>.
- [175] M. Onak, J. Pszczoła, An arc melting system with a non-contact ignition, *Physics for Economy* (2018). <https://doi.org/10.7862/rf.2018.pfe.3>.
- [176] Arc Melter AM 500 - Edmund Bühler GmbH. <https://www.edmund-buehler.de/en/materials-science/arc-melting/arc-melter-am-500> (accessed February 2, 2024).
- [177] Experimental Facilities & Sample Products | Materials Modeling and Development Group | Oregon State University, (n.d.). <https://research.engr.oregonstate.edu/mmdg/experimental-facilities-sample-products> (accessed February 2, 2024).
- [178] Z. Liu, J. Schroers, General nanomoulding with bulk metallic glasses, *Nanotechnology* 26 (2015) 145301. <https://doi.org/10.1088/0957-4484/26/14/145301>.
- [179] J.A. Cooper, B.R. Mintz, S.L. Palumbo, W.-J. Li, Assays for determining cell differentiation in biomaterials, in: Characterization of Biomaterials, *Elsevier*, (2013) 101–137. <https://doi.org/10.1533/9780857093684.101>.
- [180] N. Liu, G. Liu, A. Raj, S. Sohn, M.D. Morales-Acosta, J. Liu, J. Schroers, Unleashing nanofabrication through thermomechanical nanomolding, *Science Advances* 7 (2021) eabi4567. <https://doi.org/10.1126/sciadv.abi4567>.
- [181] S. Wang, A. Lu, C.-J. Zhong, Hydrogen production from water electrolysis: role of catalysts, *Nano Convergence* 8 (2021) 4. <https://doi.org/10.1186/s40580-021-00254-x>.
- [182] S.B. Adler, J.A. Lane, B.C.H. Steele, Electrode Kinetics of Porous Mixed-Conducting Oxygen Electrodes, *Journal of The Electrochemical Society* 143 (1996) 3554–3564. <https://doi.org/10.1149/1.1837252>.
- [183] M.E.G. Lyons, M.P. Brandon, The Oxygen Evolution Reaction on Passive Oxide Covered Transition Metal Electrodes in Aqueous Alkaline Solution. Part 1-Nickel, *International Journal of Electrochemical Science* 3 (2008) 1386–1424. [https://doi.org/10.1016/S1452-3981\(23\)15531-3](https://doi.org/10.1016/S1452-3981(23)15531-3).
- [184] X. Ju, X. Zhu, Z. Chang, L. Guo, C. Liao, Y. Zong, X. Li, X. Zheng, Controllable synthesis of porous CuO-Cu₂O/rGO microspheres composite as high-performance electrode material for supercapacitors, *Composite Interfaces* 27 (2020) 845–858. <https://doi.org/10.1080/09276440.2019.1707024>.

- [185] L.-J. Zhou, Y.-C. Zou, J. Zhao, P.-P. Wang, L.-L. Feng, L.-W. Sun, D.-J. Wang, G.-D. Li, Facile synthesis of highly stable and porous Cu₂O/CuO cubes with enhanced gas sensing properties, *Sensors and Actuators B: Chemical* 188 (2013) 533–539. <https://doi.org/10.1016/j.snb.2013.07.059>.
- [186] X. Li, W. Guo, H. Huang, T. Chen, M. Zhang, Y. Wang, Synthesis and Photocatalytic Properties of CuO Nanostructures, *Journal of Nanoscience and Nanotechnology* 14 (2014) 3428–3432. <https://doi.org/10.1166/jnn.2014.7965>.
- [187] P.C. Okoye, S.O. Azi, T.F. Qahtan, T.O. Owolabi, T.A. Saleh, Synthesis, properties, and applications of doped and undoped CuO and Cu₂O nanomaterials, *Materials Today Chemistry* 30 (2023) 101513. <https://doi.org/10.1016/j.mtchem.2023.101513>.
- [188] S. Mathews, M. Hans, F. Mücklich, M. Solioz, Contact Killing of Bacteria on Copper Is Suppressed if Bacterial-Metal Contact Is Prevented and Is Induced on Iron by Copper Ions, *Applied and Environmental Microbiology* 79 (2013) 2605–2611. <https://doi.org/10.1128/AEM.03608-12>.
- [189] P. Airey, J. Verran, Potential use of copper as a hygienic surface; problems associated with cumulative soiling and cleaning, *Journal of Hospital Infection* 67 (2007) 271–277. <https://doi.org/10.1016/j.jhin.2007.09.002>.

Publications and Appendix

A. List of Included Publications

- I. Surmounting the thermal processing limits: Patterning TiZrCuPdSn bulk metallic glass even with nanocrystallization
Fei-Fan Cai, Baran Sarac, Zhuo Chen, Caterina Czibula, Florian Spieckermann, Jürgen Eckert
Materials Today Advances, 16 (2022) 100316
DOI: doi.org/10.1016/j.mtadv.2022.100316

- II. Hierarchical Surface Pattern on Ni-free Ti-based Bulk Metallic Glass to Control Cell Interactions
Fei-Fan Cai, Andreu Blanquer, Miguel B. Costa, Lukas Schweiger, Baran Sarac, A. Lindsay Greer, Jan Schroers, Christian Teichert, Carme Nogués, Florian Spieckermann, Jürgen Eckert
Small, 20 (2023) 2310364
DOI: doi.org/10.1002/sml.202310364

- III. Nano-Patterned Pt-Based Bulk Metallic Glass Electrocatalysts with *In-Situ* Copper Oxide Foam for Enhanced Hydrogen Evolution
Fei-Fan Cai, Baran Sarac, Adnan Akman, Juan José Londoño, Selin Gümrükcü, Lukas Schweiger, Martin Hantusch, Jan Schroers, Andreas Blatter, Annett Gebert, Florian Spieckermann, Jürgen Eckert
Preprint available in *arXiv* (DOI: doi.org/10.48550/arXiv.2406.14079)
Manuscript submitted to *ACS Nano*

B. My Contribution to the Included Publications

	Conception and planning ¹	Experiments	Analysis and interpretation	Manuscript preparation ¹
Publication I	90	80	80	90
Publication II	90	80	80	90
Publication III	80	50	80	80

Fei-Fan Cai

¹ Supervision not included

C. Publication I

Materials Today Advances 16 (2022) 100316



Contents lists available at ScienceDirect

Materials Today Advances

journal homepage: www.journals.elsevier.com/materials-today-advances/



Surmounting the thermal processing limits: Patterning TiZrCuPdSn bulk metallic glass even with nanocrystallization



Fei-Fan Cai ^{a,*}, Baran Sarac ^b, Zhuo Chen ^b, Caterina Czibula ^{c,d}, Florian Spieckermann ^a, Jürgen Eckert ^{a,b}

^a Department of Materials Science, Chair of Materials Physics, Montanuniversität Leoben, Jahnstraße 12, A-8700 Leoben, Austria

^b Erich Schmid Institute of Materials Science, Austrian Academy of Sciences, Jahnstraße 12, A-8700 Leoben, Austria

^c Institute of Physics, Montanuniversität Leoben, Franz-Josef-Strasse 18, A-8700 Leoben, Austria

^d Institute of Bioproducts and Paper Technology, Graz University of Technology, Inffeldgasse 23, A-8010 Graz, Austria

ARTICLE INFO

Article history:

Received 25 August 2022

Received in revised form

18 October 2022

Accepted 26 October 2022

Available online 4 November 2022

Keywords:

Bulk metallic glass

Thermoplastic net-shaping

Titanium alloys

Patterning

Nanocrystals

Biomaterials

ABSTRACT

Ni-free Ti-based bulk metallic glasses (BMGs) are promising for biomedical applications, thanks to their excellent biocompatibility and high corrosion resistance. BMGs can be shaped and patterned by viscous flow deformation using thermoplastic net-shaping. This work presents a novel strategy for thermoplastic net-shaping of $\text{Ti}_{40}\text{Zr}_{10}\text{Cu}_{34}\text{Pd}_{14}\text{Sn}_2$ BMG. Instead of operating for a short time slightly above the glass transition temperature to avoid crystallization, the proposed method accepts the formation of nanocrystals and makes use of the lower viscosity of the supercooled liquid when processing above the glass transition temperature. Following this approach, $\text{Ti}_{40}\text{Zr}_{10}\text{Cu}_{34}\text{Pd}_{14}\text{Sn}_2$ BMG is deformed from a rod to a thin disk, and patterns scaling from $5\ \mu\text{m}$ to $300\ \mu\text{m}$ are successfully created on the Ti-BMG surfaces, demonstrating the potential to create complex features for functional materials. Furthermore, after the thermoplastic net-shaping treatment, the Vickers hardness increases by 6% while the corrosion and passivation current density decrease by an order of magnitude. This work reveals that the BMGs can still be deformed and patterned via the thermoplastic net-shaping technique if the first crystallization event of the BMG systems is the formation of nanocrystals. Most importantly, this work reveals the possibility of processing a broad family of mediocre glass-forming systems and semi-crystalline composites via thermoplastic net-shaping.

© 2022 The Authors. Published by Elsevier Ltd. This is an open access article under the CC BY license (<http://creativecommons.org/licenses/by/4.0/>).

Corresponding author

Fei-Fan Cai, fei-fan.cai@unileoben.ac.at, Department of Materials Science, Chair of Materials Physics, Montanuniversität Leoben, Jahnstraße 12, A-8700 Leoben, Austria

1. Introduction

Ti-based bulk metallic glasses (Ti-BMGs) have recently become a popular research topic for biomedical applications. Since Ti-BMGs have an amorphous structure without grain boundaries like in crystalline materials, they exhibit favorable properties such as high corrosion resistance [1–3] and good biocompatibility [4–7]. Moreover, their high strength and low Young's modulus are helpful for hard-tissue implant applications by alleviating the stress-shielding effect when contacting bone tissues [1–3,8,9]. In addition to the advantages mentioned above, Ti-BMGs can be post-processed by thermoplastic net-shaping (TPN) thanks to their amorphous structure [8,10–13]. During the TPN process, Ti-BMGs are heated up into their supercooled liquid region (SCLR), while the process temperature T_p is kept between the glass transition temperature T_g and the onset of the (first) crystallization step T_x [8,10–13]. When heating up into the SCLR, the deformation behavior of BMGs changes from inhomogeneous deformation to homogenous (Newtonian) flow, and this kind of temperature-dependent viscosity leading to viscous flow deformation can be utilized to deform the whole feedstock or create surface features [8,10–16].

Currently, Ni is often used in Ti-BMGs to improve the glass-forming ability (GFA) [3,17]. However, Ni is a toxic and carcinogenic element that would be detrimental to medical applications [18,19]. Hence, Ni-free Ti-based BMGs have gained interest due to their superior biocompatibility [1,2,8,9,20]. The $\text{Ti}_{40}\text{Zr}_{10}\text{Cu}_{36}\text{Pd}_{14}$ alloy has been highly explored recently since it shows good corrosion resistance in simulated body fluids, relatively higher strength and lower Young's modulus than the Ti-6Al-4V alloy, thus showing big advantages for use as dental implant material [1,9,21,22]. However, the $\text{Ti}_{40}\text{Zr}_{10}\text{Cu}_{36}\text{Pd}_{14}$ BMG has a rather narrow SCLR and low fragility, which means that the viscosity reduction is too low (only roughly one order of magnitude) [8,14], and the material is very hard to deform. Furthermore, the time before crystallization sets in is quite short, leading to a short processing window because the BMG cannot be deformed once it is crystallized. Derived from the $\text{Ti}_{40}\text{Zr}_{10}\text{Cu}_{36}\text{Pd}_{14}$ alloy, the $\text{Ti}_{40}\text{Zr}_{10}\text{Cu}_{34}\text{Pd}_{14}\text{Sn}_2$ alloy substitutes Cu with 2 at.% Sn [9,21,23,24]. By effectively controlling the nucleation of crystalline phases [9,21,24,25], Sn improves the GFA and enlarges the range of the SCLR before crystallization. Therefore, the $\text{Ti}_{40}\text{Zr}_{10}\text{Cu}_{34}\text{Pd}_{14}\text{Sn}_2$ BMG has more potential for processing by the TPN technique than $\text{Ti}_{40}\text{Zr}_{10}\text{Cu}_{36}\text{Pd}_{14}$ [14].

The conventional thermoplastic net-shaping process is operated between T_g and T_x for a short time to avoid crystallization. Reports in the literature rely on the restrictive belief that bulk metallic glasses cannot be deformed and patterned once the materials are crystallized [10,13,14,26,27]. However, in this study, we demonstrate that if the first crystallization event is the formation of nanocrystals, the BMGs can still be deformed and patterned. Hence, this work explored the processing potential of $\text{Ti}_{40}\text{Zr}_{10}\text{Cu}_{34}\text{Pd}_{14}\text{Sn}_2$ (at.%) BMG via compression-based TPN. The first part of this study reports on its very large possible deformability from a 3 mm diameter and 5.3 mm height rod shape to a 1 mm thin disk shape without crystallization,

proving the formability of $\text{Ti}_{40}\text{Zr}_{10}\text{Cu}_{34}\text{Pd}_{14}\text{Sn}_2$ BMG by TPN processing. The second part reports on the successful macro-patterning of a 300 μm square-well array and micro-patterning of a 5 μm square-hump array on the $\text{Ti}_{40}\text{Zr}_{10}\text{Cu}_{34}\text{Pd}_{14}\text{Sn}_2$ BMG surfaces. We found that micro-patterning is still achievable even if the first crystallization occurs and nanocrystals are formed during the TPN process. This opens the possibility of applying TPN processing for the vast group of mediocre glass-forming systems into surface enhanced functional materials.

2. Experimental methods

2.1. Casting of Ti-BMG

Master ingots with nominal composition $\text{Ti}_{40}\text{Zr}_{10}\text{Cu}_{34}\text{Pd}_{14}\text{Sn}_2$ (at.%) were prepared from pure elements (purities: Ti: 99.995 %; Zr: 99.95 %; Cu 99.999 %; Pd 99.9 %; Sn: 99.99 %) by arc-melting (Edmund Bühler GmbH). These ingots were heated five times above the liquidus temperature to ensure homogeneity. The master ingot was cast into a 3 mm diameter rod or a disk with 12 mm diameter and 2.5 mm thickness by copper mold suction casting. Both master ingot preparation and suction casting were conducted under a Ti-gettered Ar atmosphere in the same arc-melting machine. The as-cast disks were further cut to half the thickness using a Struers Accutom 50 device and then mirror-polished down to a thickness of about 1 mm to not only eliminate influences of possible surface crystallization and oxidation but also create parallel surfaces for further TPN processing. The amorphous structure was examined by X-ray diffraction (XRD) using a Bruker D2 Phaser with $\text{Co K}\alpha$ radiation. In order to study the process window for the TPN process, BMG pieces of about 20 mg were characterized by differential scanning calorimetry (DSC) under an argon atmosphere in constant-rate heating and isothermal modes. The constant-rate heating mode experiments were done in a NETZSCH DSC 404C device using alumina crucibles and a heating rate of 20 $^{\circ}\text{C}/\text{min}$. The isothermal mode experiments were performed in a Mettler Toledo DSC 3+ calorimeter with platinum crucibles at a 10 $^{\circ}\text{C}/\text{min}$ heating rate for the pre-heating step to eliminate possible overshooting of the signal.

2.2. Thermoplastic Net-Shaping of Ti-BMG

The basic setup of the TPN process in this work consisted of a compression test machine (Zwick Type 1382) with a homemade vacuum chamber, a vacuum pump, and a resistance heating sheath surrounding the chamber (Heraeus Type 19.519.000). The TPN process was carried out in the enclosed chamber under vacuum (4×10^{-4} mbar) conditions to minimize the influence of oxidation during the material flow (see Figure S1). The vacuum chamber was heated by the heating sheath to the desired processing temperature between 430 and 450 $^{\circ}\text{C}$ (average heating rate around 6.8 $^{\circ}\text{C}/\text{min}$). Meanwhile, a preload of 1 kN was applied to the sample before the sample reached the processing temperature to avoid unwanted dynamic impact. Once the sample reached the processing temperature, the load was slowly increased to the maximum load of 10 kN (loading rate between 4.5 and 7.5 N/sec) and held for a specific

time. The process was monitored and recorded on a computer using the LabVIEW system design software with respect to force, temperature and displacement (see Figure S2).

The deformability test was executed by compressing a 3 mm diameter and 5.3 mm height BMG rod under a constant load of 10 kN between 440 °C and 450 °C for 40 min. A 300 μm square-well array (macro-patterning) and a 5 μm square-hump array (micro-patterning) were demonstrated with 12 mm diameter BMG disks with 1 mm thickness. The macro-patterns were created by compressing BMG disks with a W720 tool steel template (an array of 300 μm cubes). The micro-patterns were created by compressing BMG disks with a silicon template (5 μm edge-sized square pores with 12 μm interpore distance, SmartMembranes GmbH).

2.3. Characterization of Ti-BMG after TPN

After the TPN process, the amorphous structure of samples was examined by XRD using a Bruker D2 Phaser with Co-K_α radiation ($\lambda = 1.7902 \text{ \AA}$). The three-dimensional topography of the generated patterns was observed via scanning electron microscopy (SEM–TESCAN MAGNA) and confocal laser scanning microscopy (CLSM–Olympus LEXT OLS4100). From the CLSM images, the dimension of the patterns was evaluated by analyzing the profile line to extract the step heights. Three-dimensional topographic maps were reproduced using the Gwyddion 2.58 software. In order to study the influence of the TPN process on the atomic structure of the material, the samples were inspected by high-resolution transmission electron microscopy (HRTEM) and selected area electron diffraction (SAED) using a 200 kV field emission TEM (JEOL2100F). The static water contact angles were recorded and analyzed via the sessile drop method with a contact angle goniometer (Ossila L2004A1). The volume of water droplets was 2 μl, and the measurements were repeated at least four times.

2.4. Hardness

In order to compare the hardness of Ti₄₀Zr₁₀Cu₃₄Pd₁₄Sn₂ BMG, disks from the as-cast state and after-TPN process were prepared. Vickers hardness tests were performed on a mirror-polished as-cast BMG disk and the flat region of the micro-pattered BMG disk without polishing. The tests were conducted using a 9.8 N load (HV₁) on a DuraScan 70 G5 universal laboratory hardness tester (EMCO-TEST Prüfmaschinen GmbH, Austria) following ISO 6507 standard. Each measurement was repeated 25 times in a five-by-five array with 300 μm distance.

2.5. Corrosion Resistance

0.9 wt.% aqueous phosphate-buffered saline (PBS) solution with a pH of 7.4 was used for this study. The electrochemical measurements were conducted in a three-electrode glass cell at 37 °C using a Pt counter electrode (0.5 mm diameter) and a reference electrode of Ag(s)/AgCl(s) with 3 M NaCl electrolyte and ion permeable porous glass junction that has a redox

potential of +0.195 V (at room temperature) vs. standard hydrogen electrode. The submerged areas are 0.120 cm² and 0.133 cm² for the as-cast and after-TPN states, respectively. The electrochemical measurements were conducted with a Gamry Interface 1010 Potentiostat/Galvanostat/ZRA. Before the electrochemical tests, open circuit potential was applied for 600 s to confirm the stabilization of the working electrode/electrolyte interface. Linear sweep voltammetry was implemented at a scan rate of 1 mV s⁻¹ in the forward direction (from minus to plus). The scan started from -0.3 V vs. OCP and stopped at +1.5 V vs. Ag/AgCl or when the current density reached 0.01 A cm⁻². Several scans were performed for each composition and electrolyte, and the best curves were selected.

3. Results and discussion

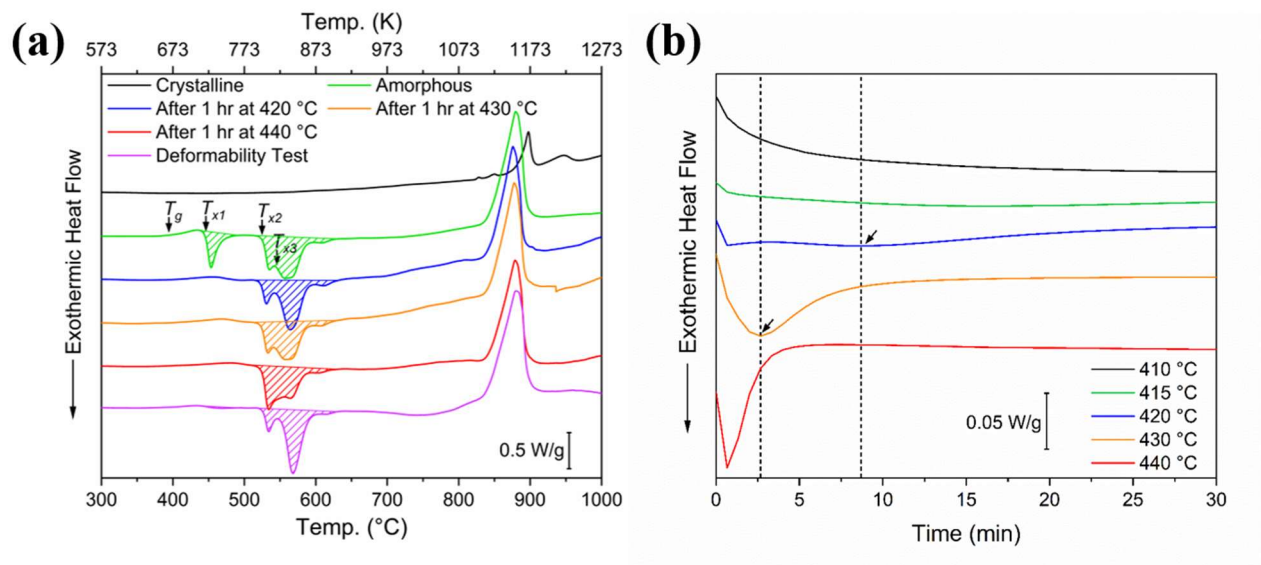


Figure 1: (a) Constant-rate heating (20 °C/min) and (b) isothermal DSC curves at different temperatures of Ti₄₀Zr₁₀Cu₃₄Pd₁₄Sn₂ BMG.

Table 1: Characteristic temperatures of Ti₄₀Zr₁₀Cu₃₄Pd₁₄Sn₂ BMG characterized from isochronous measurement:

Composition	T_g	T_{x1}	T_{x2}	T_{x3}	ΔT	T_m
Ti ₄₀ Zr ₁₀ Cu ₃₄ Pd ₁₄ Sn ₂	394 ± 2	446 ± 2	525 ± 2	545 ± 2	49 ± 4	840 ± 2

The processing window of the TPN technique was investigated by constant-rate heating and isothermal modes. The DSC curves from the isochronous measurements of the Ti₄₀Zr₁₀Cu₃₄Pd₁₄Sn₂ BMG are shown in Fig. 1(a), and the characteristic temperatures are listed in Table 1. Above all, the green line proves the amorphous state of the as-cast samples, and the black line is the reference curve for the crystalline state. Notably, there are three exothermic peaks in the amorphous curves. These exothermic peaks represent the formation of crystalline phases. The evaluated onset T_g and crystallization enthalpy from constant-rate heating DSC curves is shown in Table S1. According to Zheng et al. [23], the first exothermic peak is due to

the formation of α -(Ti/Zr), Pd₃Ti, CuTi₂, and Pd₂Ti phases. The second one corresponds to the formation of the CuTi phase, and the third one is mainly for the Pd₅Ti₃ and CuTi₂ phases. Furthermore, Calin et al. [9] suggested that the first crystallization event is related to the formation of a nanocrystalline α -(Ti/Zr) phase. Therefore, in Fig. 1(a), the DSC curves for 1 hour of annealing at 430 °C (orange line) and 440 °C (red line) show that the first exothermic peak (at 446 °C) disappears. However, the second exothermic peak (at 525 °C) and the third exothermic peak (at 545 °C) are preserved. This result indicates that after 1-hour of annealing at 430 °C and 440 °C, only the first nanocrystalline phase α -(Ti/Zr) forms. The crystalline phases corresponding to the second and third crystallization peaks in the isochronous DSC curves, such as Cu-Ti, Cu-Zr, and Pd-Ti phases, do not occur. Likewise, the DSC curves from isothermal measurements of Ti₄₀Zr₁₀Cu₃₄Pd₁₄Sn₂ BMG are displayed in Fig. 1(b), revealing that the first crystallization occurs within 10 min at 420 °C. Most importantly, even when annealed at 415 °C, i.e., about 21 °C above its T_g (394 ± 2 °C), the BMG still goes through the first crystallization process. Hence, the conclusion from the DSC measurements in both modes is that the first nanocrystalline phase is prone to form within short time windows, even when annealing very close to T_g .

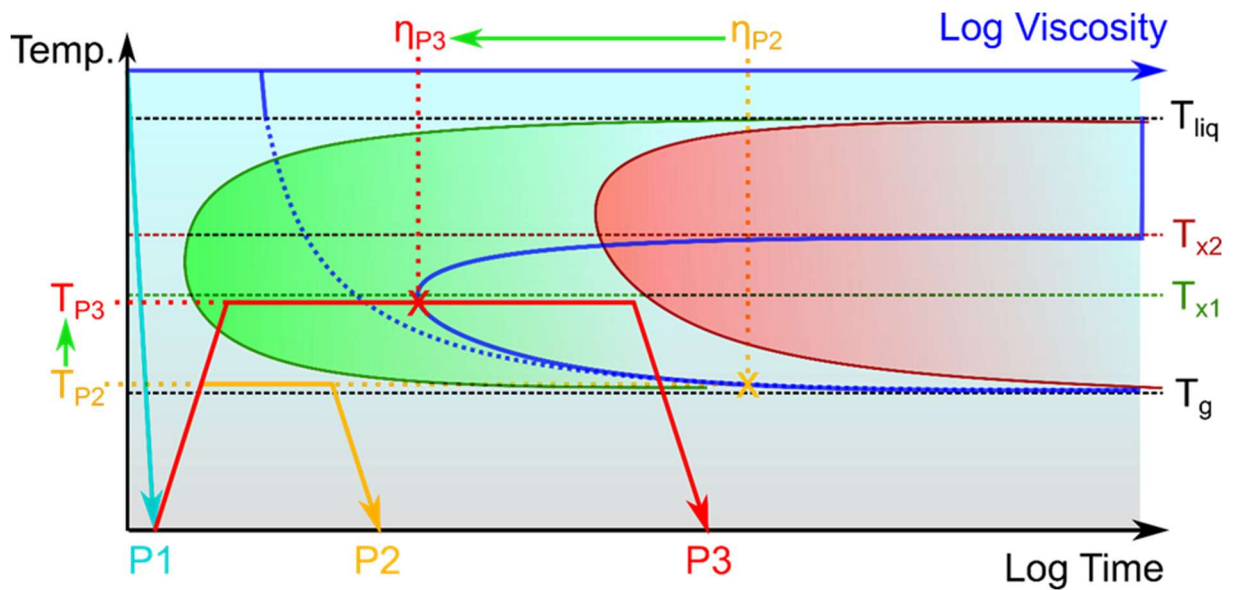


Figure 2: Schematic time-temperature-transformation (TTT) diagram combined with viscosity-temperature curve: (P1) Fast cooling to cast BMGs, (P2) Conventional TPN process path that avoids the first crystallization, (P3) The proposed TPN process path that goes through the first nanocrystalline formation. It is worth noting that (P3) has a longer processing time and lower viscosity than (P2).

A schematic time-temperature-transformation (TTT) diagram illustrating the phase transformation is plotted in Fig. 2 to help develop feasible processing paths for TPN of the Ti₄₀Zr₁₀Cu₃₄Pd₁₄Sn₂ BMG. In Fig. 2, the green crystallization nose represents the first nanocrystalline phase formation at $T_{x1} = 446 \pm 2$ °C (heating rate: 20 °C/min), and the red crystallization nose represents the second crystallization at $T_{x2} = 525 \pm 2$ °C (heating rate: 20 °C/min). The viscosity-temperature relation is integrated into this TTT diagram as a blue axis

and lines, referred to the characterization from Bera et al. [14] as in Figure S3. The blue-dashed line is the viscosity for an ideal amorphous structure where the viscosity decreases as temperature increases [12,27,28]. However, in the case of $\text{Ti}_{40}\text{Zr}_{10}\text{Cu}_{34}\text{Pd}_{14}\text{Sn}_2$ BMG, the material forms nanocrystals in an amorphous matrix. The nanocrystals might facilitate further crystallization at higher temperatures by acting as heterogeneous nucleation sites. Thus, the actual viscosity should increase at higher temperatures, as schematically indicated by the solid blue line [29–32]. Path 1 (light blue) denotes fast cooling upon casting to bypass the first crystallization nose to form BMG. The conventional TPN process, labeled as path 2 (yellow), would be operated slightly above T_g and keeping the temperature only for a short time window (< 10 min) to avoid crystallization. This path leads to the high viscosity of the supercooled liquid and necessitates a very short processing time. This is impractical for shaping and patterning $\text{Ti}_{40}\text{Zr}_{10}\text{Cu}_{34}\text{Pd}_{14}\text{Sn}_2$ BMG. However, there is a turning point. From the DSC analysis, the second crystalline phase (CuTi) does not form within 1 hr at 440°C . Hence, we propose another strategy by passing through the first nano-crystallization nose and preventing touching of the second crystallization nose. This strategy is labeled as path 3 (red) in Fig. 2. By this strategy, the processing time window is extended to 1 hr. Furthermore, T_{x2} ($525 \pm 2^\circ\text{C}$) is about 80°C higher than T_{x1} ($446 \pm 2^\circ\text{C}$), providing a wider temperature window for processing. If the processing temperature is increased from 415°C (T_{p2}) to 440°C (T_{p3}), the viscosity will drop from η_{P2} to η_{P3} , as indicated by green arrows. The lower viscosity makes viscous flow deformation easier, and less force is required for the process. Considering the viscosity-temperature dependence and the incubation time of isothermal crystallization, the possible TPN process window of $\text{Ti}_{40}\text{Zr}_{10}\text{Cu}_{34}\text{Pd}_{14}\text{Sn}_2$ BMG is proposed as 1 hour annealing between 440°C and 450°C .

To examine if the new strategy is feasible, a deformability test was conducted to demonstrate to which degree $\text{Ti}_{40}\text{Zr}_{10}\text{Cu}_{34}\text{Pd}_{14}\text{Sn}_2$ BMG can be shaped in the supercooled liquid regime (SCLR). In this test, a 3 mm diameter rod with 5.32 mm height was shaped into a 7.5 mm diameter disk with 0.96 mm thickness, as depicted in Fig. 3(a). The final thickness was only 18% of its original height. An indication of the viscous flow deformation is the barrel-shaped edge in the inset photo of Fig. 3(a). It is noteworthy that the constant load of 10 kN corresponds to stress of 1.35 GPa for the 3 mm diameter rod in the beginning. However, as the rod was deformed into a disk shape, the effective stress at the end of the process was reduced to 215 MPa because of the increase in the loading area. Hence, even though the deformability test took place for 40 min, the displacement was observed to barely change after 35 min, which can be attributed to the insufficient stress to drive the deformation. The disk from the deformability test was analyzed by the isochronous measurement of DSC, as shown in Fig. 1(a). As expected, the first exothermic peak disappears, yet the second and third exothermic peaks are preserved. This finding reveals that only the first nanocrystalline phase α -(Ti/Zr) forms after the TPN process. The crystal phase for the second and third exothermic peaks in the isochronous

DSC curves, such as Cu-Ti, Cu-Zr, and Pd-Ti phases, do not form. The disk from the deformability test was further inspected by XRD analysis to characterize its microstructure. The result is represented in Fig. 3(b). The XRD patterns for the TPN disk and the as-cast rod are quite similar: there are no obvious crystalline peaks in the XRD patterns in both cases. However, small-volume fractions of nanocrystals and crystalline spherulites cannot be detected by XRD [2,33]. Therefore, the XRD pattern of the deformability test can only confirm that the amorphous structure was mainly retained and the overall crystallinity was low in the whole sample. The results of the deformability test show that $\text{Ti}_{40}\text{Zr}_{10}\text{Cu}_{34}\text{Pd}_{14}\text{Sn}_2$ BMG can be formed into desired shapes for practical applications. Moreover, the low or almost negligible crystallinity of the samples after the TPN process reveals the potential to create patterns on the Ti-BMG in the following experiments.

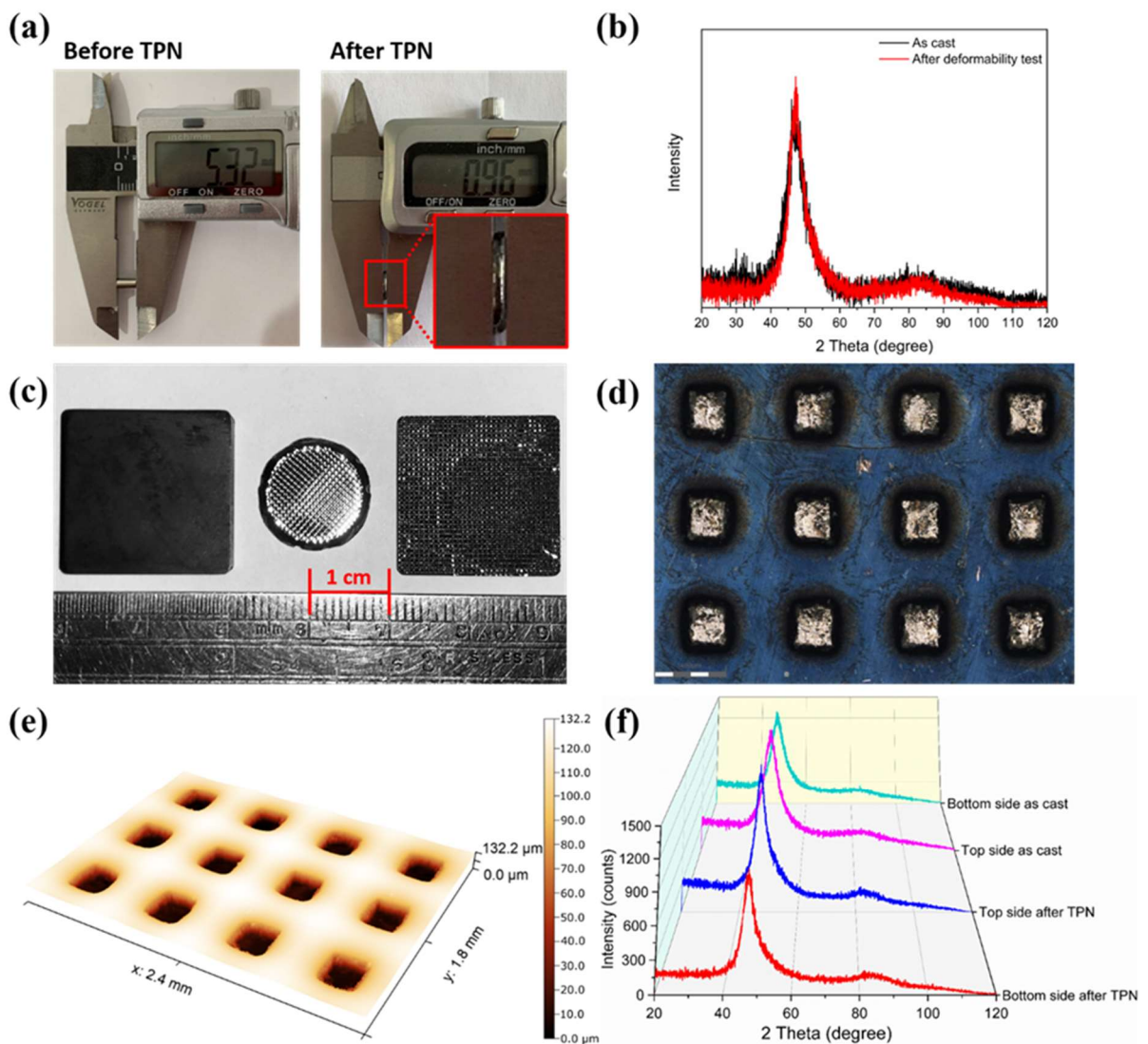


Figure 3: Deformability test (a-b) and macro-patterning (c-f) of $\text{Ti}_{40}\text{Zr}_{10}\text{Cu}_{34}\text{Pd}_{14}\text{Sn}_2$ BMG: (a) Photos showing the dimensional change of the sample in the deformability test. (b) XRD analysis. (c) Photo of the patterned BMG disk (middle) and W720 tool steel template (right). (d) A close look at the patterned surface. Scale bar: 400 μm . (e) Remapped topography of the patterned surface. (f) XRD analysis.

To investigate whether the new strategy of intentional first-phase nano-crystallization for a wider processing window is also applicable to produce patterns of surface features, we compressed a $\text{Ti}_{40}\text{Zr}_{10}\text{Cu}_{34}\text{Pd}_{14}\text{Sn}_2$ BMG disk together with a template with an array of $300\ \mu\text{m}$ cubes during the TPN process (Fig. 3(c)). Macro-patterning of square wells was successfully realized on the surface of $\text{Ti}_{40}\text{Zr}_{10}\text{Cu}_{34}\text{Pd}_{14}\text{Sn}_2$ BMG disks, as shown in Fig. 3(d). The 3-dimensional topography of the pattern surface was re-mapped via CLSM characterization, as shown in Fig. 3(e). The profile lines of the topographic map confirm that the square wells have dimensions around $110\ \mu\text{m}$ in depth and $300\ \mu\text{m}$ in length. Hence, the aspect ratio is around 0.37. The processing parameters for macro-molding were constant for loading 10 kN for 30 min at a temperature between 440°C and $450\ ^\circ\text{C}$. The initial diameter of the disk was around 12 mm, and the changes in the disk dimension were negligible. Therefore, the applied stress was evaluated to be constant $\approx 88\ \text{MPa}$. It is expected that if higher stress is applied, the processing time can be shortened, or the aspect ratio can be increased.

Taking a closer look at Fig. 3(d) reveals that the color of convex grids turned blue while the color of the square wells was unchanged. The reason is that the square wells are the regions compressed by the template during the TPN process, thus, less prone to oxidization. In contrast, the convex grids are the free spaces during the process, forming a thicker passive oxide layer at the processing temperature ($440 \sim 450\ ^\circ\text{C}$). Furthermore, the choice of molding material is critical because if an interfacial reaction occurs, it would make demolding without damaging the patterns more difficult. For instance, the patterned surfaces of BMG flaked off during demolding when the template was made of S255 steel. W720 tool steel proved to be a potential molding material for macro-patterning of $\text{Ti}_{40}\text{Zr}_{10}\text{Cu}_{34}\text{Pd}_{14}\text{Sn}_2$ BMG since there were no signs of interfacial reaction between the mold and BMG surfaces (Fig. 3(c)). With respect to structural analysis, the XRD patterns of the sample after the TPN process are similar to those before TPN processing (Fig. 3(f)). None of the XRD patterns reveal obvious crystalline peaks. This indicates that the amorphous structure was largely retained after the TPN process since nanocrystals and low crystallinity may not be detected by XRD. The promising results from the macro-molding of $\text{Ti}_{40}\text{Zr}_{10}\text{Cu}_{34}\text{Pd}_{14}\text{Sn}_2$ BMG triggered further attempts with micro-molding.

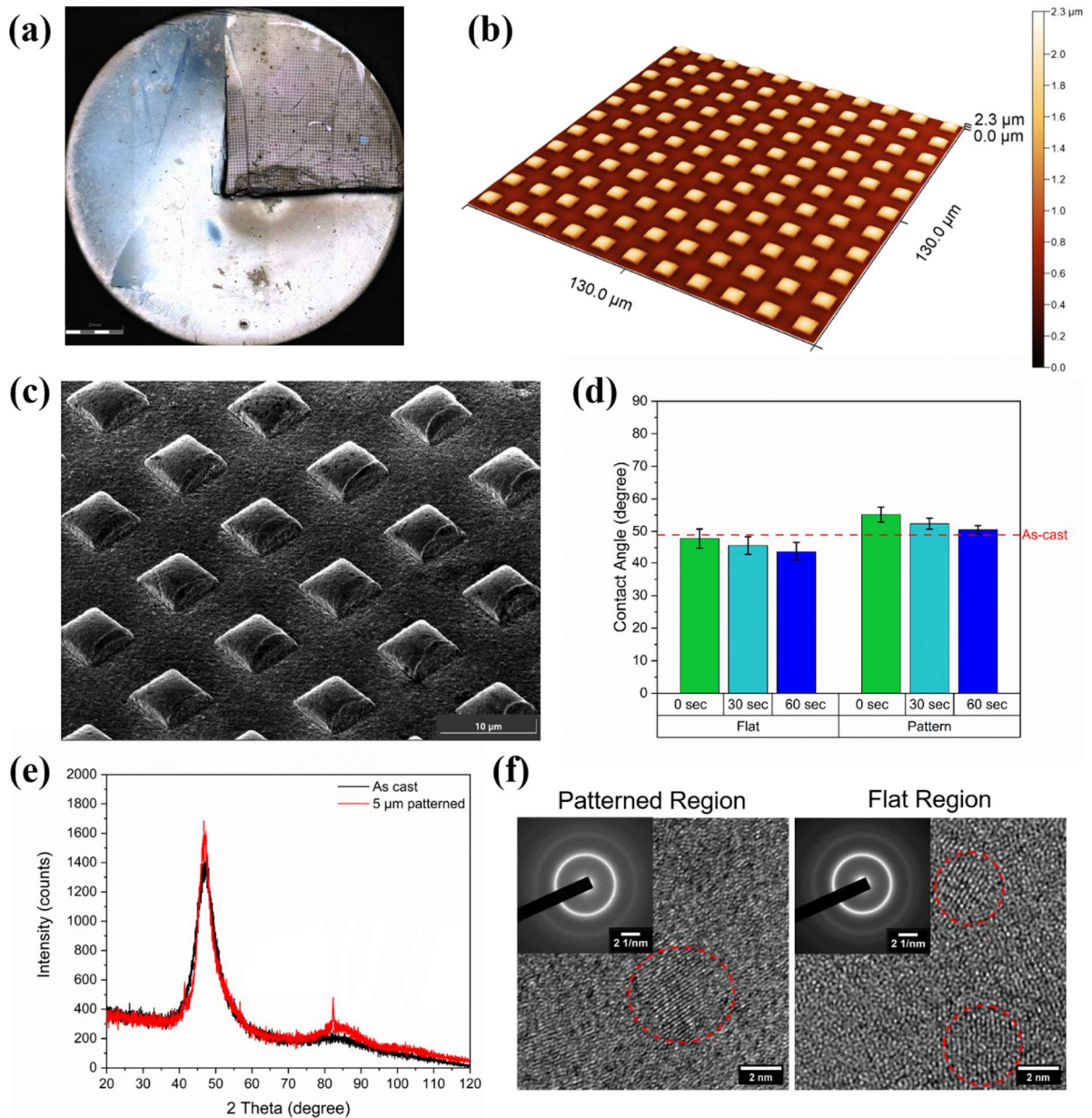


Figure 4: Micro-patterning of $\text{Ti}_{40}\text{Zr}_{10}\text{Cu}_{34}\text{Pd}_{14}\text{Sn}_2$ BMG: (a) Photo of the BMG disk, including the patterned region at the upper-right corner and the flat region in the remaining area. (b) Remapped topography and (c) SEM image of the patterned region. (d) Contact angle analysis of both patterned and flat regions. (e) XRD analysis. (f) HRTEM images and SAED patterns of both patterned and flat regions. The nanocrystals are marked with red-dash circles in HRTEM images.

For the micro-patterning experiments, an array of 5 μm square humps was created on the surface of $\text{Ti}_{40}\text{Zr}_{10}\text{Cu}_{34}\text{Pd}_{14}\text{Sn}_2$ BMG disks. A photo of the sample disk after micro-patterning is shown in Fig. 4(a). The patterned region is at the right-up corner of the BMG disk where the silicon mold was located, and the flat region is the remaining area of the surface, which was free space and did not come into contact with the mold. This allows investigation of the influence of viscous flow deformation since both the patterned and flat regions had the same thermal history. In Figs. 4(b) and (c), both CLSM and SEM display the micro-pattern of square

humps on the patterned region, which is the negative pattern from the silicon template with square pores. CLSM was utilized to measure the dimensions of the square humps with a height of around 1.6 μm and about 5 μm in length, as depicted in Fig. 4(b). SEM offers a good overview of the morphology of the humps in the patterned region, as displayed in Fig. 4(c). Especially the smooth curvatures on top of the humps indicates viscous flow deformation in the free spaces. The interaction between the supercooled liquid and the silicon mold leads to flat grids on the whole patterned region and clean right angles on the sides of the humps. As shown in Fig. 4(d), the contact angles of the patterned surface are slightly larger than the flat surfaces due to the increased roughness. The decreasing trends of contact angles after 30 and 60 seconds are similar on both surfaces. This indicates that the chemistry on the patterned surface did not change after contact with the silicon templates. XRD analysis shows slight crystallization after the TPN process after micro-molding (Fig. 4(e)). Therefore, HRTEM and SAED were applied to get more information on the origin of crystallization, as illustrated in Fig. 4(f). Because both regions underwent the same heating and cooling steps during the TPN process, the only difference is that the patterned regions were deformed through molding. Hence, the result that both regions show similar SAED patterns and HRTEM images means that the formation of nanocrystals is more related to the thermal history than to deformation-induced crystallization. The HRTEM images of both regions display nanocrystals (marked with red-dash circles) in the amorphous matrix. It is worth noticing that the SAED patterns on both regions have sharp rings representing the existence of nanocrystals instead of typical halo rings found in amorphous materials. Therefore, the DSC, XRD, and TEM characterizations indicate that the proposed process window goes through the first nano-crystallization event and prevents the second crystallization event. Furthermore, it is possible to shape and pattern the materials even through the formation of nanocrystals during the TPN process.

The properties such as hardness and corrosion resistance are improved after the TPN process. The result of Vickers hardness and the observations of indent are displayed in Fig. 5(a). After the TPN process, the Vickers hardness (HV_1) increases by 6% compared with the as-cast sample (621 HV vs. 584 HV). It is worth noticing that the indent observation of the after TPN sample has a shining cross that the beneath BMG material exposes after the thick oxide layer cracks. With respect to corrosion resistance, Fig. 5(b) shows the polarization behavior of $\text{Ti}_{40}\text{Zr}_{10}\text{Cu}_{34}\text{Pd}_{14}\text{Sn}_2$ BMG disks before and after the TPN process. After the TPN process, the new oxide layer built up significantly decreases the corrosion current by an order of magnitude down to $1.11 \times 10^{-7} \text{ A cm}^{-2}$ (see Table S2). Secondly, the TPN sample passivates at relatively lower passivation currents (cf. 3.46×10^{-7} vs. 6.90×10^{-6}). The third improvement is observed in the extent of the passive region η_{pit} ; although some serrations are visible above 0.2 V in the TPN sample, this value remains similar after TPN. These results corroborate the better corrosion resistance of the TPN deformed sample in PBS solution under 37 °C compared to the as-cast state.

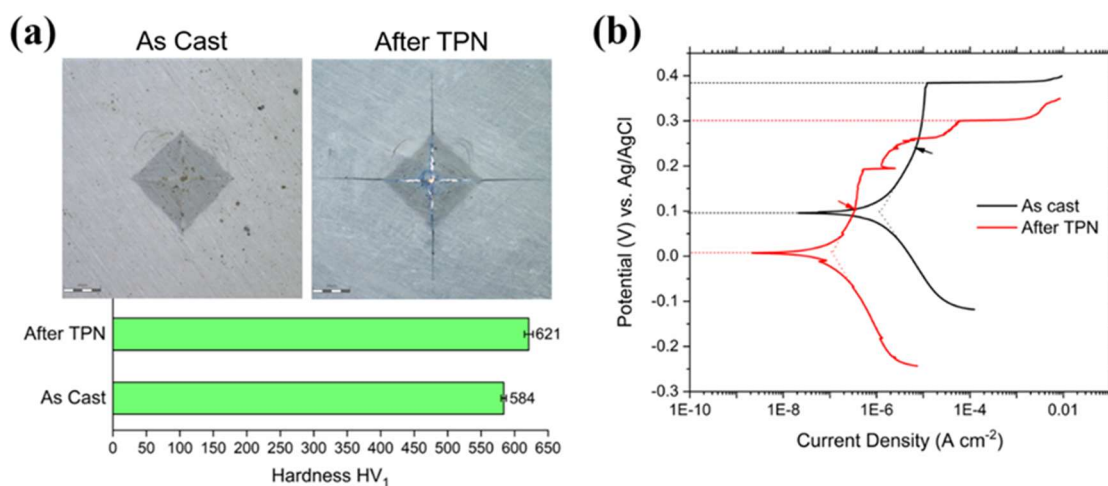


Figure 5: Comparison of (a) hardness and (b) corrosion resistance for $\text{Ti}_{40}\text{Zr}_{10}\text{Cu}_{34}\text{Pd}_{14}\text{Sn}_2$ BMG before and after the TPN process. (a) Optical microscopy observations and the HV_1 hardness histogram after Vickers indentation (b) Forward potentiodynamic polarization scans of the selected $\text{Ti}_{40}\text{Zr}_{10}\text{Cu}_{34}\text{Pd}_{14}\text{Sn}_2$ BMG disks at a scan rate of 1 mV s^{-1} in PBS solution at 37°C . The potential is given vs. the Ag/AgCl reference electrode. i_{corr} and E_{corr} are determined by extrapolation and intersection of the cathodic and anodic regions (dashed lines). The i_{pass} values are indicated by arrows. E_{pit} is given by the short dashed lines.

The conventional process route of the TPN technique is to avoid intersecting the crystallization curve in the TTT diagram since it was believed that BMGs can not be deformed and patterned once the materials are crystallized. However, this work finds that if the first crystallization event is the formation of nanocrystals, the BMGs can still be deformed and patterned even with the nanocrystallization. Furthermore, the processing temperature can be very close to T_x to make use of the lower viscosity of the amorphous matrix to deform and pattern the material. Therefore, for the BMG systems that have nanocrystal formation during the first crystallization step, the definition of SCLR, $\Delta T_x = (T_g - T_x)$, might lead to an underestimated process temperature, and the deformability of the material might be underestimated. For most applications, it is necessary to compensate for other properties such as biocompatibility, hydrogen production, etc. Therefore, the BMG systems with narrow SCLR still have the potential to be processed via TPN for vast applications.

4. Conclusions

This contribution investigated the processing window of thermoplastic net-shaping for $\text{Ti}_{40}\text{Zr}_{10}\text{Cu}_{34}\text{Pd}_{14}\text{Sn}_2$ BMG. It was found that the first nanocrystalline phase is prone to form within short periods even when the BMG is annealed very close to T_g . Isothermal DSC analysis proved that even at 23°C above T_g , the first phase crystallization occurs within 10 min. Instead of avoiding intersecting the crystallization curve in the TTT diagram, the newly proposed strategy for thermoplastic net-shaping of $\text{Ti}_{40}\text{Zr}_{10}\text{Cu}_{34}\text{Pd}_{14}\text{Sn}_2$ BMG is to accept that nanocrystals will form but make use of the lower viscosity of the supercooled liquid when processing at higher temperatures above T_g . $\text{Ti}_{40}\text{Zr}_{10}\text{Cu}_{34}\text{Pd}_{14}\text{Sn}_2$ BMG rods could be deformed

into a disk with only 18% of its original height via the TPN process, revealing large deformability within the SCLR. Furthermore, patterns with scales from 300 μm to 5 μm were successfully imprinted on $\text{Ti}_{40}\text{Zr}_{10}\text{Cu}_{34}\text{Pd}_{14}\text{Sn}_2$ BMG surfaces, demonstrating the potential to create more complex features such as hierarchical structures combining micro-patterns and macro-patterns. SAED and HRTEM analysis revealed that the formation of nanocrystals is more related to the thermal history during the TPN process than deformation-induced crystallization. After the TPN process, the Vickers hardness increases by 6%, and the corrosion current decreases by an order of magnitude. Hence, the TPN process improves the properties such as hardness and corrosion resistance. Furthermore, this work reveals that if the first crystallization event of the BMG systems is the formation of nanocrystals, the BMGs can still be deformed and patterned via the TPN technique, even with nanocrystallization. Altogether, this work provides a feasible approach for processing a broad family of mediocre glass-forming systems using TPN with extensive application potential.

Acknowledgements

The authors thank Prof. Zaoli Zhang and Prof. Christian Teichert for their insightful scientific discussions. Further thanks to Lukas Schweiger for help with scanning electron microscopic imaging, and Atacan Asci for his assistance in electrochemical tests.

Funding

This work was supported by the European Union's Horizon 2020 research and innovation programme under the Marie Skłodowska-Curie grant agreement No. 861046 (BIOREMIA-ETN). B.S. J.E. and F.S. acknowledge support from the Austrian Science Fund (FWF), Grant/Award Number: I3937-N36. C.C. acknowledges the support of the Hertha Firnberg Programme by the Austrian Science fund (FWF) Grant Number: T 1314-N.

Data availability

The raw/processed data required to reproduce these findings cannot be shared at this time as the data also forms part of an ongoing study.

Appendix A. Supplementary data

Supplementary data to this article can be found online at <https://doi.org/10.1016/j.mtadv.2022.100316>.

References

- [1] A. Liens, A. Etiemble, P. Rivory, S. Balvay, J.-M. Pelletier, S. Cardinal, D. Fabrègue, H. Kato, P. Steyer, T. Munhoz, J. Adrien, N. Courtois, D. Hartmann, J. Chevalier, On the Potential of Bulk Metallic Glasses for Dental Implantology: Case Study on $\text{Ti}_{40}\text{Zr}_{10}\text{Cu}_{36}\text{Pd}_{14}$, *Materials*. 11 (2018) 249. <https://doi.org/10.3390/ma11020249>.
- [2] A. Liens, B. Ter-Ovanesian, N. Courtois, D. Fabregue, T. Wada, H. Kato, J. Chevalier, Effect of alloying elements on the microstructure and corrosion behavior of TiZr-based

- bulk metallic glasses, *Corrosion Science*. 177 (2020) 108854. <https://doi.org/10.1016/j.corsci.2020.108854>.
- [3] P. Gong, L. Deng, J. Jin, S. Wang, X. Wang, K. Yao, Review on the Research and Development of Ti-Based Bulk Metallic Glasses, *Metals*. 6 (2016) 264. <https://doi.org/10.3390/met6110264>.
- [4] T.H. Li, P.C. Wong, S.F. Chang, P.H. Tsai, J.S.C. Jang, J.C. Huang, Biocompatibility study on Ni-free Ti-based and Zr-based bulk metallic glasses, *Materials Science and Engineering: C*. 75 (2017) 1–6. <https://doi.org/10.1016/j.msec.2017.02.006>.
- [5] A. Blanquer, A. Hynowska, C. Nogués, E. Ibáñez, J. Sort, M.D. Baró, B. Özkale, S. Pané, E. Pellicer, L. Barrios, Effect of Surface Modifications of Ti₄₀Zr₁₀Cu₃₈Pd₁₂ Bulk Metallic Glass and Ti-6Al-4V Alloy on Human Osteoblasts In Vitro Biocompatibility, *PLOS ONE*. 11 (2016) e0156644. <https://doi.org/10.1371/journal.pone.0156644>.
- [6] G. Xie, H. Kanetaka, H. Kato, F. Qin, W. Wang, Porous Ti-based bulk metallic glass with excellent mechanical properties and good biocompatibility, *Intermetallics*. 105 (2019) 153–162. <https://doi.org/10.1016/j.intermet.2018.12.002>.
- [7] W. Yang, Y. Liu, N. Hua, S. Pang, Y. Li, P.K. Liaw, T. Zhang, Formation and properties of biocompatible Ti-based bulk metallic glasses in the Ti–Cu–Zr–Fe–Sn–Si–Ag system, *Journal of Non-Crystalline Solids*. 571 (2021) 121060. <https://doi.org/10.1016/j.jnoncrysol.2021.121060>.
- [8] B. Sarac, S. Bera, S. Balakin, M. Stoica, M. Calin, J. Eckert, Hierarchical surface patterning of Ni- and Be-free Ti- and Zr-based bulk metallic glasses by thermoplastic net-shaping, *Materials Science and Engineering: C*. 73 (2017) 398–405. <https://doi.org/10.1016/j.msec.2016.12.059>.
- [9] M. Calin, M. Stoica, N. Zheng, X.R. Wang, S. Scudino, A. Gebert, J. Eckert, Thermal Stability and Crystallization Kinetics of Ti₄₀Zr₁₀Cu₃₄Pd₁₄Sn₂ Bulk Metallic Glass, *Solid State Phenomena*. 188 (2012) 3–10. <https://doi.org/10.4028/www.scientific.net/SSP.188.3>.
- [10] B. Sarac, S. Bera, F. Spieckermann, S. Balakin, M. Stoica, M. Calin, J. Eckert, Micropatterning kinetics of different glass-forming systems investigated by thermoplastic net-shaping, *Scripta Materialia*. 137 (2017) 127–131. <https://doi.org/10.1016/j.scriptamat.2017.02.038>.
- [11] J. Schroers, Bulk Metallic Glasses, *Physics Today*. 66 (2013) 32–37. <https://doi.org/10.1063/PT.3.1885>.
- [12] E. Bryn Pitt, G. Kumar, J. Schroers, Temperature dependence of the thermoplastic formability in bulk metallic glasses, *Journal of Applied Physics*. 110 (2011) 043518. <https://doi.org/10.1063/1.3624666>.
- [13] B. Sarac, J. Eckert, Thermoplasticity of metallic glasses: Processing and applications, *Progress in Materials Science*. (2022) 100941. <https://doi.org/10.1016/j.pmatsci.2022.100941>.
- [14] S. Bera, B. Sarac, S. Balakin, P. Ramasamy, M. Stoica, M. Calin, J. Eckert, Micropatterning by thermoplastic forming of Ni-free Ti-based bulk metallic glasses, *Materials & Design*. 120 (2017) 204–211. <https://doi.org/10.1016/j.matdes.2017.01.080>.
- [15] Z. Liu, N. Liu, J. Schroers, Nanofabrication through molding, *Progress in Materials Science*. 125 (2022) 100891. <https://doi.org/10.1016/j.pmatsci.2021.100891>.

- [16] M. Frey, J. Wegner, N. Neuber, B. Reiplinger, B. Bochtler, B. Adam, L. Ruschel, S.S. Riegler, H.-R. Jiang, S. Kleszczynski, G. Witt, R. Busch, Thermoplastic forming of additively manufactured Zr-based bulk metallic glass: A processing route for surface finishing of complex structures, *Materials & Design*. 198 (2021) 109368. <https://doi.org/10.1016/j.matdes.2020.109368>.
- [17] A. Kuball, O. Gross, B. Bochtler, B. Adam, L. Ruschel, M. Zamanzade, R. Busch, Development and characterization of titanium-based bulk metallic glasses, *Journal of Alloys and Compounds*. 790 (2019) 337–346. <https://doi.org/10.1016/j.jallcom.2019.03.001>.
- [18] C.A. Baumann, B.D. Crist, Nickel allergy to orthopaedic implants: A review and case series, *Journal of Clinical Orthopaedics and Trauma*. 11 (2020) S596–S603. <https://doi.org/10.1016/j.jcot.2020.02.008>.
- [19] A. Kanaji, V. Orhue, M.S. Caicedo, A.S. Viridi, D.R. Sumner, N.J. Hallab, T. Yoshiaki, K. Sena, Cytotoxic effects of cobalt and nickel ions on osteocytes in vitro, *Journal of Orthopaedic Surgery and Research*. 9 (2014) 91. <https://doi.org/10.1186/s13018-014-0091-6>.
- [20] S. Yamaura, S. Zhu, K. Abe, G. Xie, Ultrasonic Fatigue of Ti₄₀Zr₁₀Cu₃₄Pd₁₄Sn₂ Glassy Alloy, *Open Journal of Metal*. 04 (2014) 56–64. <https://doi.org/10.4236/ojmetal.2014.43007>.
- [21] S. Zhu, G. Xie, F. Qin, X. Wang, A. Inoue, Effect of Minor Sn Additions on the Formation and Properties of TiCuZrPd Bulk Glassy Alloy, *Materials Transactions*. 53 (2012) 500–503. <https://doi.org/10.2320/matertrans.M2011281>.
- [22] A. Rezvan, E. Sharifikolouei, A. Lassnig, V. Soprunyuk, C. Gammer, F. Spieckermann, W. Schranz, Z. Najmi, A. Cochis, A.C. Scalia, L. Rimondini, M. Manfredi, J. Eckert, B. Sarac, Antibacterial activity, cytocompatibility, and thermomechanical stability of Ti₄₀Zr₁₀Cu₃₆Pd₁₄ bulk metallic glass, *Materials Today Bio*. 16 (2022) 100378. <https://doi.org/10.1016/j.mtbio.2022.100378>.
- [23] N. Zheng, G. Wang, L.C. Zhang, M. Calin, M. Stoica, G. Vaughan, N. Mattern, J. Eckert, In situ high-energy x-ray diffraction observation of structural evolution in a Ti-based bulk metallic glass upon heating, *Journal of Materials Research*. 25 (2010) 2271–2277. <https://doi.org/10.1557/jmr.2010.0298>.
- [24] A. Sypien, M. Stoica, T. Czeppe, Properties of the Ti₄₀Zr₁₀Cu₃₆Pd₁₄ BMG Modified by Sn and Nb Additions, *Journal of Materials Engineering and Performance*. 25 (2016) 800–808. <https://doi.org/10.1007/s11665-016-1898-6>.
- [25] F.X. Qin, X.M. Wang, A. Inoue, Effect of annealing on microstructure and mechanical property of a Ti–Zr–Cu–Pd bulk metallic glass, *Intermetallics*. 15 (2007) 1337–1342. <https://doi.org/10.1016/j.intermet.2007.04.005>.
- [26] B. Sarac, G. Kumar, T. Hodges, S. Ding, A. Desai, J. Schroers, Three-Dimensional Shell Fabrication Using Blow Molding of Bulk Metallic Glass, *Journal of Microelectromechanical Systems*. 20 (2011) 28–36. <https://doi.org/10.1109/JMEMS.2010.2090495>.
- [27] J. Schroers, Processing of Bulk Metallic Glass, *Advanced Materials*. 22 (2010) 1566–1597. <https://doi.org/10.1002/adma.200902776>.
- [28] C. Suryanarayana, A. Inoue, *Bulk Metallic Glasses*, Second Edition, 2018.

- [29] E. Bakke, R. Busch, W.L. Johnson, The viscosity of the $Zr_{46.75}Ti_{8.25}Cu_{7.5}Ni_{10}Be_{27.5}$ bulk metallic glass forming alloy in the supercooled liquid, *Applied Physics Letters*. 67 (1995) 3260–3262. <https://doi.org/10.1063/1.114891>.
- [30] B. Deng, Y. Shi, The embrittlement and toughening of metallic glasses from nanocrystallization, *Journal of Applied Physics*. 125 (2019) 145101. <https://doi.org/10.1063/1.5089547>.
- [31] K. Kosiba, L. Deng, S. Scudino, Viscous Flow of Supercooled Liquid in a Zr-Based Bulk Metallic Glass Synthesized by Additive Manufacturing, *Materials*. 13 (2020) 3803. <https://doi.org/10.3390/ma13173803>.
- [32] J.B. Li, H.Z. Zhang, J.S.C. Jang, S.R. Jian, C. Li, J.C. Huang, T.G. Nieh, Viscous flow and thermoplastic forming ability of a Zr-based bulk metallic glass composite with Ta dispersoids, *Journal of Alloys and Compounds*. 536 (2012) S165–S170. <https://doi.org/10.1016/j.jallcom.2012.01.020>.
- [33] L. Gautier, A. Liens, B. Ter-Ovanesian, S. Marcelin, T. Douillard, H. Richard, N. Courtois, J. Chevalier, D. Fabrègue, Impact of spherulite-type crystalline defects on the mechanical and electrochemical properties of $Ti_{40}Cu_{36}Zr_{10}Pd_{14}$ metallic glasses, *Materialia*. 21 (2022) 101353. <https://doi.org/10.1016/j.mtla.2022.101353>.

Publication I – Supporting Information

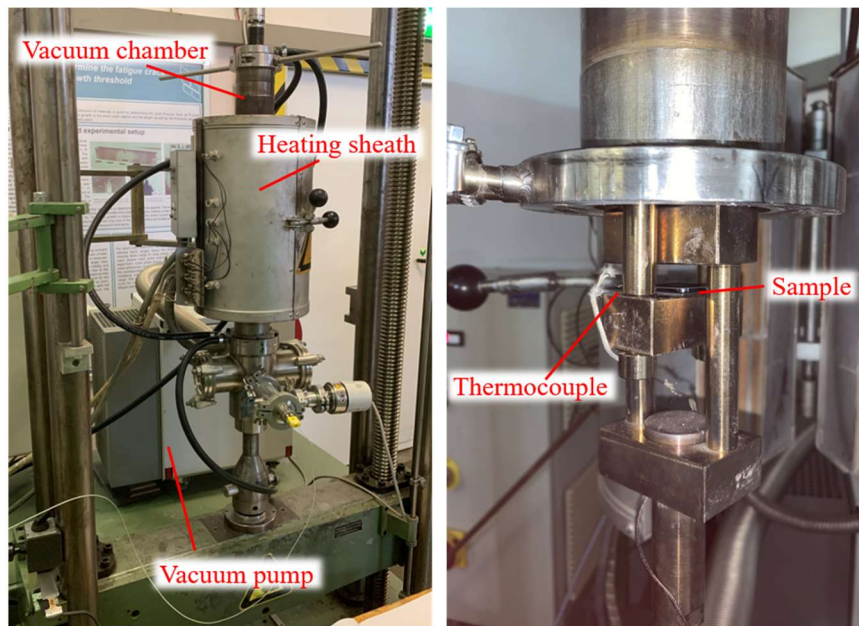


Figure S33: Setup of thermoplastic net-shaping (TPN) process. Due to the design of the shaft components, the compression test machine moves in a tensile direction to apply compressive stress on the sample.

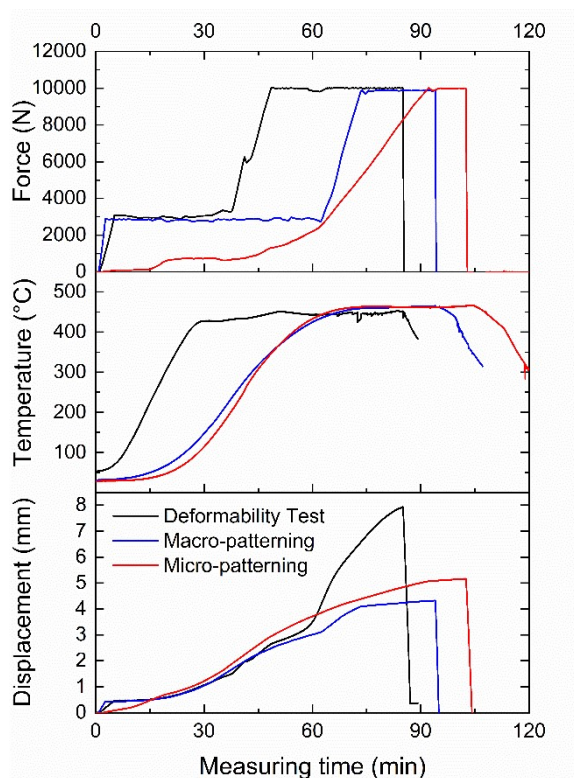


Figure S34: Record of the process parameters (applied force, temperature, and displacement) for the thermoplastic net-shaping (TPN) process. For micro-patterning, the force was applied

gently to avoid scattering the silicon template. The displacement includes the thermal expansion of the compression test machine.

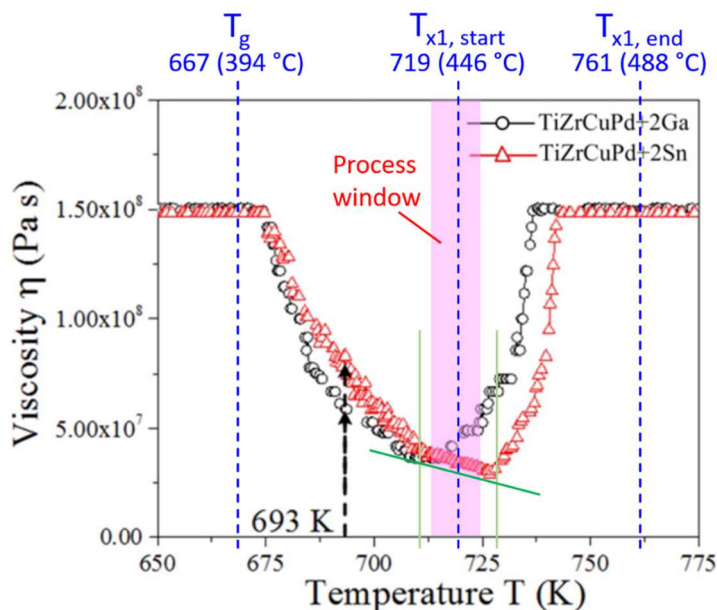


Figure S35: Temperature-dependent viscosity with the characteristic temperatures and process window in this work. Reproduced with permission from Bera et al. [1].

Table S5: Onset glass transitions (Onset T_g) and crystallization enthalpies from constant-rate heating DSC curves:

	Onset T_g (°C)	Enthalpy for peak 1 (J/g)	Enthalpy for the sum of peaks 2 and 3 (J/g)
Amorphous	394.4	7.844	27.705
After 1 hr at 420 °C	398.5	NA	26.554
After 1 hr at 430 °C	400.3	NA	26.421
After 1 hr at 440 °C	NA	NA	25.555
Deformability Test	397.0	0.630	26.625

Table S2: Passivation and pitting corrosion of the investigated Ti-based BMG before and after TPN. i_{corr} : corrosion current density, E_{corr} : corrosion potential, i_{pass} : passivation current density, E_{pit} : pitting potential, η_{pit} : passivation region.

State	i_{corr} (A cm ⁻²)	E_{corr} (V vs Ag/AgCl)	i_{pass} (A cm ⁻²)	E_{pit} (V vs Ag/AgCl)	η_{pit} (V) [$E_{\text{pit}} - E_{\text{corr}}$]
As-cast	1.28×10^{-6}	0.097	6.90×10^{-6}	0.384	0.287
TPN	1.11×10^{-7}	0.006	3.46×10^{-7}	0.300	0.294

References

- [1] S. Bera, B. Sarac, S. Balakin, P. Ramasamy, M. Stoica, M. Calin, J. Eckert, Micro-patterning by thermoplastic forming of Ni-free Ti-based bulk metallic glasses, *Materials & Design*. 120 (2017) 204–211. <https://doi.org/10.1016/j.matdes.2017.01.080>.

D. Publication II

Small, 20 (2023) 2310364



Research Article | Open Access |

Hierarchical Surface Pattern on Ni-Free Ti-Based Bulk Metallic Glass to Control Cell Interactions

Fei-Fan Cai , Andreu Blanquer, Miguel B. Costa, Lukas Schweiger, Baran Sarac, A. Lindsay Greer, Jan Schroers, Christian Teichert, Carme Nogués ... [See all authors](#)

First published: 18 December 2023 | <https://doi.org/10.1002/smll.202310364>

SECTIONS

PDF

TOOLS

SHARE

Abstract

Ni-free Ti-based bulk metallic glasses (BMGs) are exciting materials for biomedical applications because of their outstanding biocompatibility and advantageous mechanical properties. The glassy nature of BMGs allows them to be shaped and patterned via thermoplastic forming (TPF). This work demonstrates the versatility of the TPF technique to create micro- and nano-patterns and hierarchical structures on $\text{Ti}_{40}\text{Zr}_{10}\text{Cu}_{34}\text{Pd}_{14}\text{Sn}_2$ BMG. Particularly, a hierarchical structure fabricated by a two-step TPF process integrates 400 nm hexagonal close-packed protrusions on 2.5 μm square protuberances while preserving the advantageous mechanical properties from the as-cast material state. The correlations between thermal history, structure, and mechanical properties are explored. Regarding biocompatibility, $\text{Ti}_{40}\text{Zr}_{10}\text{Cu}_{34}\text{Pd}_{14}\text{Sn}_2$ BMGs with four surface topographies (flat, micro-patterned, nano-patterned, and hierarchical-structured surfaces) are investigated using Saos-2 cell lines. Alamar Blue assay and live/dead analysis show that all tested surfaces have good cell proliferation and viability. Patterned surfaces are observed to promote the formation of longer filopodia on the edge of the cytoskeleton, leading to star-shaped and dendritic cell morphologies compared with the flat surface. In addition to potential implant applications, TPF-patterned Ti-BMGs enable a high level of order and design flexibility on the surface topography, expanding the available toolbox for studying cell behavior on rigid and ordered surfaces.

Fei-Fan Cai^{1,2}, Andreu Blanquer³, Miguel B. Costa⁴, Lukas Schweiger¹, Baran Sarac²,
A. Lindsay Greer⁴, Jan Schroers⁵, Christian Teichert⁶, Carme Nogués³, Florian
Spieckermann¹, Jürgen Eckert^{1,2}

¹ Department of Materials Science, Chair of Materials Physics, Montanuniversität Leoben

² Erich Schmid Institute of Materials Science, Austrian Academy of Sciences

³ Departament de Biologia Cel·lular, Fisiologia i Immunologia, Universitat Autònoma de
Barcelona

⁴ Department of Materials Science & Metallurgy, University of Cambridge

⁵ Department of Mechanical Engineering and Materials Science, Yale University

⁶ Department Physics, Mechanics and Electrical Engineering, Chair of Physics,
Montanuniversität Leoben

Keywords: biocompatibility, biomaterials, bulk metallic glass, patterning, thermoplastic forming, titanium alloys, topography

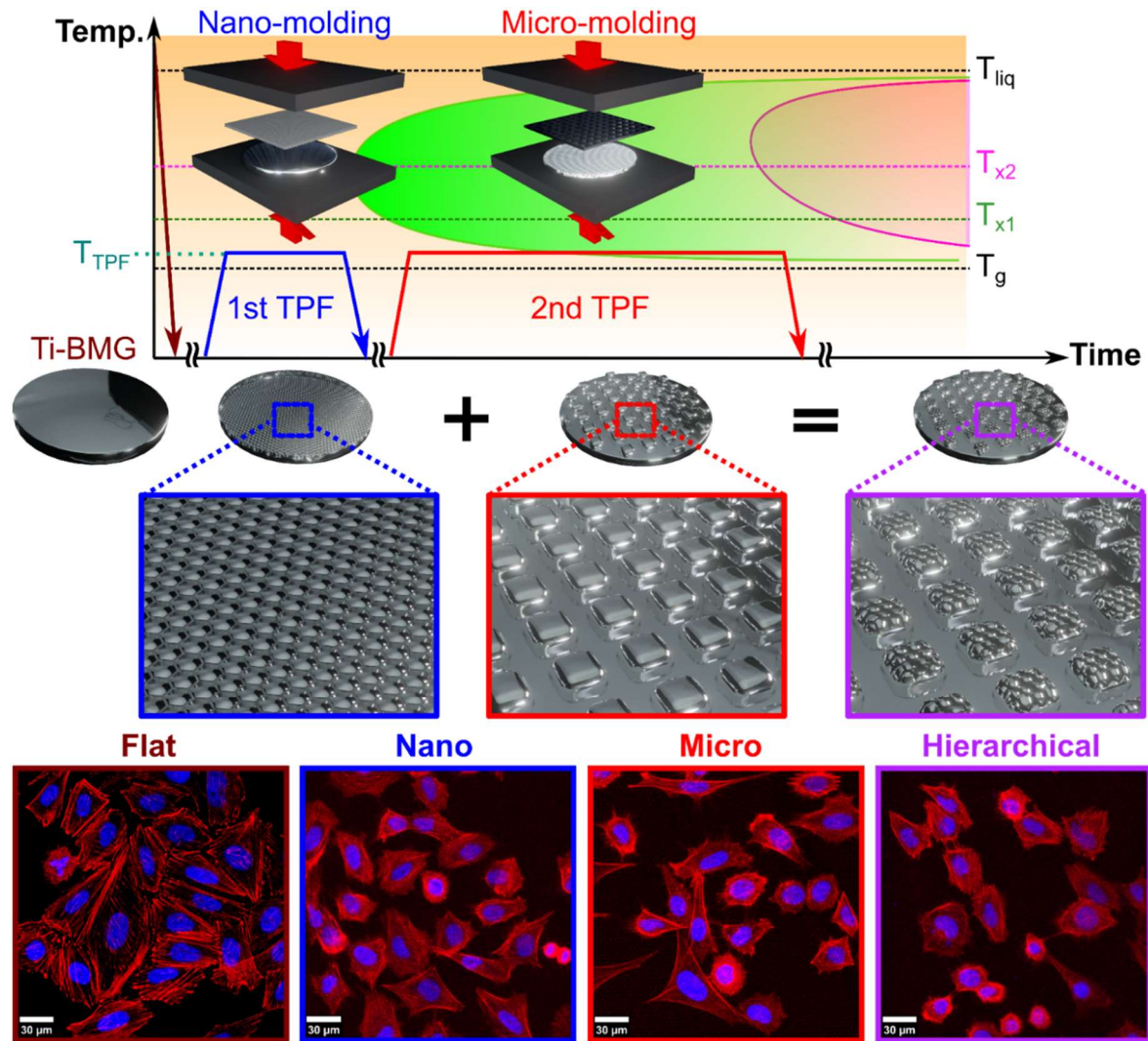
Corresponding author

Fei-Fan Cai, fei-fan.cai@oeaw.ac.at, Department of Materials Science, Chair of Materials Physics, Montanuniversität Leoben, Jahnstraße 12, A-8700 Leoben, Austria

Florian Spieckermann, florian.spieckermann@unileoben.ac.at, Department of Materials Science, Chair of Materials Physics, Montanuniversität Leoben, Jahnstraße 12, A-8700 Leoben, Austria

Table of Contents

A hierarchical structure integrating nano-scale protrusions on micro-scale protuberances is achieved on Ni-free Ti-based bulk metallic glasses via a two-step thermoplastic forming technique. The patterned materials preserve advantageous mechanical properties and biocompatibility from the as-cast materials. However, the surface features change the cell morphology. Besides implant applications, this work realizes a strategy for studying cell behavior on rigid ordered surfaces.



1. Introduction

Titanium-based bulk metallic glasses (Ti-BMGs) have recently attracted substantial interest in biomedical applications. The high titanium content of these alloys gives them intrinsic biocompatibility.^[1–3] In addition, owing to their amorphous nature, Ti-BMGs have attractive properties such as high corrosion resistance, wear resistance, lower Young's modulus, higher elasticity, and higher specific strength than traditional crystalline Ti-alloys, making them potential biomaterials for dental and orthopedic applications.^[2–7] The reduced Young's modulus and enhanced elastic behavior are expected to alleviate stress-shielding effects when contacting bone tissues.^[8,9] Indeed, many efforts have been devoted to the development of β -type titanium alloys achieving low Young's modulus below 80 GPa for crystalline materials.^[10–13] In amorphous materials, many Ti-BMGs, such as Ti–Ni–Cu and Ti–Zr–Cu–Ni alloy systems, rely on nickel to improve their glass-forming ability (GFA).^[6,14] Several studies have shown that nickel ions can induce harmful effects on the human body, such as cutaneous inflammations and carcinogenicity.^[15,16] Ion release is a by-product of corrosion, which in turn is generally facilitated by contact with body fluid.^[6,15] Without Ni, Ti–Zr–Cu–Pd BMG systems have improved biocompatibility and sufficient GFA for real-life applications.^[14,17,18]

BMGs can be processed by the thermoplastic forming (TPF) technique, another advantage for amorphous structures.^[19,20] When BMGs are heated to their supercooled liquid region (SCLR), the region between glass transition temperature (T_g) and crystallization temperature (T_x), the material can be deformed by viscous flow.^[17,19–21] Viscous flow deformation can be used to shape the entire feedstock and/or fabricate surface features on BMGs.^[19,20,22–24] Thus, TPF techniques can be used to, for example, manufacture screws from BMG rods. As an improved variant of Ti–Zr–Cu–Pd BMGs, $\text{Ti}_{40}\text{Zr}_{10}\text{Cu}_{34}\text{Pd}_{14}\text{Sn}_2$ (at%) BMG has more potential to be processed with TPF compared to the base composition $\text{Ti}_{40}\text{Zr}_{10}\text{Cu}_{36}\text{Pd}_{14}$ BMG.^[17,20] Replacing 2 at% of Cu with Sn in $\text{Ti}_{40}\text{Zr}_{10}\text{Cu}_{36}\text{Pd}_{14}$ BMG effectively slows the kinetics of crystallization in the $\text{Ti}_{40}\text{Zr}_{10}\text{Cu}_{34}\text{Pd}_{14}\text{Sn}_2$ BMG, resulting in an enhanced GFA and SCLR range.^[17,25,26] $\text{Ti}_{40}\text{Zr}_{10}\text{Cu}_{34}\text{Pd}_{14}\text{Sn}_2$ BMG has a critical diameter of 12 mm, which is sufficient for most dental and orthodontic applications, such as fixtures, screws, abutments, brackets, hooks, and ligatures.^[2,14,26]

In terms of biomedical science, the surface morphology of the implants affects osseointegration and anti-biofilm properties.^[9,27–29] Several studies prove that cells can sense their environment and convert mechanical stimuli such as stiffness and topography into biochemical signals to regulate cell response and function; this process is known as mechanotransduction.^[29–35] Hence, the surface topography of the implant can induce changes in cell morphology and further impact cell fate.^[1,6,9,27,35–37] It was demonstrated how the density of nano-protrusion controls responses of human mesenchymal stem cells, in which the dense pattern (1.2 μm spacing) inhibited cell spreading and directed cells to become adipocyte-like while the sparse pattern (5.6 μm spacing) induced cells to become osteoblast-like cells.^[38,39] Moreover, different cell types might respond differently to the same topography. Padmanabhan et al. showed that fibroblasts could detect as small as 55 nm nano-patterns.^[40] In comparison, macrophages failed to detect nano-patterns of smaller 150 nm and responded to a feature size of 200 nm.^[40] Finally, engineering the surface topography can improve implant grip and avoid loosening to save patients from pain.^[41,42]

Surface patterned Ni-free Ti-BMGs bridge the gap between materials science and biomedical engineering, but literature reports are limited. Regarding hierarchical structures on metallic glasses, Hasan et al. implemented hierarchical patterning on $\text{Pt}_{57.5}\text{Cu}_{14.7}\text{Ni}_{5.3}\text{P}_{22.5}$ BMG.^[43] For Ti-BMGs, Gong et al. have decorated surfaces with 400 nm-diameter nanorods on $\text{Ti}_{45}\text{Zr}_{20}\text{Be}_{30}\text{Fe}_5$ BMG.^[44] However, beryllium which is part of the latter alloy has high cytotoxicity and should be avoided in implants.^[45,46] Sarac et al. generated hierarchical square bumps with a maximum height of 5 μm , where the micro-forming kinetics were compared with $\text{Zr}_{48}\text{Cu}_{36}\text{Al}_8\text{Ag}_8$.^[47,48] For the above-mentioned $\text{Ti}_{40}\text{Zr}_{10}\text{Cu}_{34}\text{Pd}_{14}\text{Sn}_2$ BMG, Bera et al. demonstrated a circular bump pattern with roughly 500 μm diameter and 24 μm height.^[17] Cai et al. managed to micro-patterned square protuberances with 5 μm in length and around 1.6 μm

in height.^[20] However, hierarchical structures integrating micro- and nano-patterns at the same surface have not been achieved on Ti-based BMGs yet.

Here, for the first time, nano-patterns and hierarchical structures are created on the surface of Ni-free Ti-based BMGs. On $\text{Ti}_{40}\text{Zr}_{10}\text{Cu}_{34}\text{Pd}_{14}\text{Sn}_2$ BMG, we demonstrate the nano-pattern with a dragonfly-eye-like microstructure featuring 400 nm protrusions and a raspberry-shaped hierarchical structure by superimposing 400 nm diameter nano-protrusions on 2.5 μm square protuberances. The influences of various TPF conditions on structures and mechanical properties are studied. Biocompatibility of $\text{Ti}_{40}\text{Zr}_{10}\text{Cu}_{34}\text{Pd}_{14}\text{Sn}_2$ BMG is investigated using Saos-2 cell lines on four different surface topographies: flat, micro-patterned, nano-patterned, and hierarchical-structured surfaces. The influence of surface patterns on cell morphology is inspected by scanning electron microscopy (SEM) and confocal laser scanning microscopy (CLSM) and determined by quantitative morphometric analysis. Our work demonstrates that the hierarchical-patterned $\text{Ti}_{40}\text{Zr}_{10}\text{Cu}_{34}\text{Pd}_{14}\text{Sn}_2$ BMG maintains favorable mechanical properties from as-cast materials, such as Young's modulus and hardness. In addition to hard-tissue implant applications, TPF-patterned Ti-BMGs have highly ordered features and design flexibility on the surface, which can be a prospective platform for studying cell behavior on stiff and ordered surface topographies.

2. Results

2.1. Surface Topography of TPF-Patterned Ti-BMGs

Ni-free Ti-BMG systems have been patterned into nano-scale, and the two-tier hierarchical structure integrating micro- and nano-patterns is achieved (**Figure 1**). A demonstration of the two-step TPF process combined with a schematic time-temperature-transformation (TTT) diagram is exhibited in Figure 1a. The glass transition temperature is at T_g (394 ± 2 °C), and the processing temperature is represented as T_{TPF} . The green crystallization nose represents the first crystallization event at T_{x1} (446 ± 2 °C), and the pink crystallization nose represents the second crystallization at T_{x2} (525 ± 2 °C). The thermoformed patterns were inspected by SEM (Figure 1). The micro-pattern (Figure 1b) has ordered square protuberances with 2.5 μm in length and around 1.5 μm in height. The nano-pattern (Figure 1c) features 400 nm hexagonal close-packed protrusions, similar to the corneal surface structures of insect eyes.^[49] The hierarchical pattern (Figure 1d) combines the topographies of micro-pattern and nano-pattern, giving ordered raspberry-like hierarchical structures. The hierarchical structure is created by a two-step TPF process in which the nano-pattern (Figure 1c) is imprinted during the first step, followed by the generation of the micro-pattern (Figure 1b), which is superposed on the nano-pattern. Therefore, each “raspberry” is based on 2.5 μm square protuberances and possesses 400 nm diameter, hexagonal close-packed protrusions on the top, leading to a total height of around 2 μm . In the hierarchical structure, each 2.5 μm square protuberance has an average of 25 pieces of 400 nm diameter nano-protrusions, as is illustrated in Figure S1.

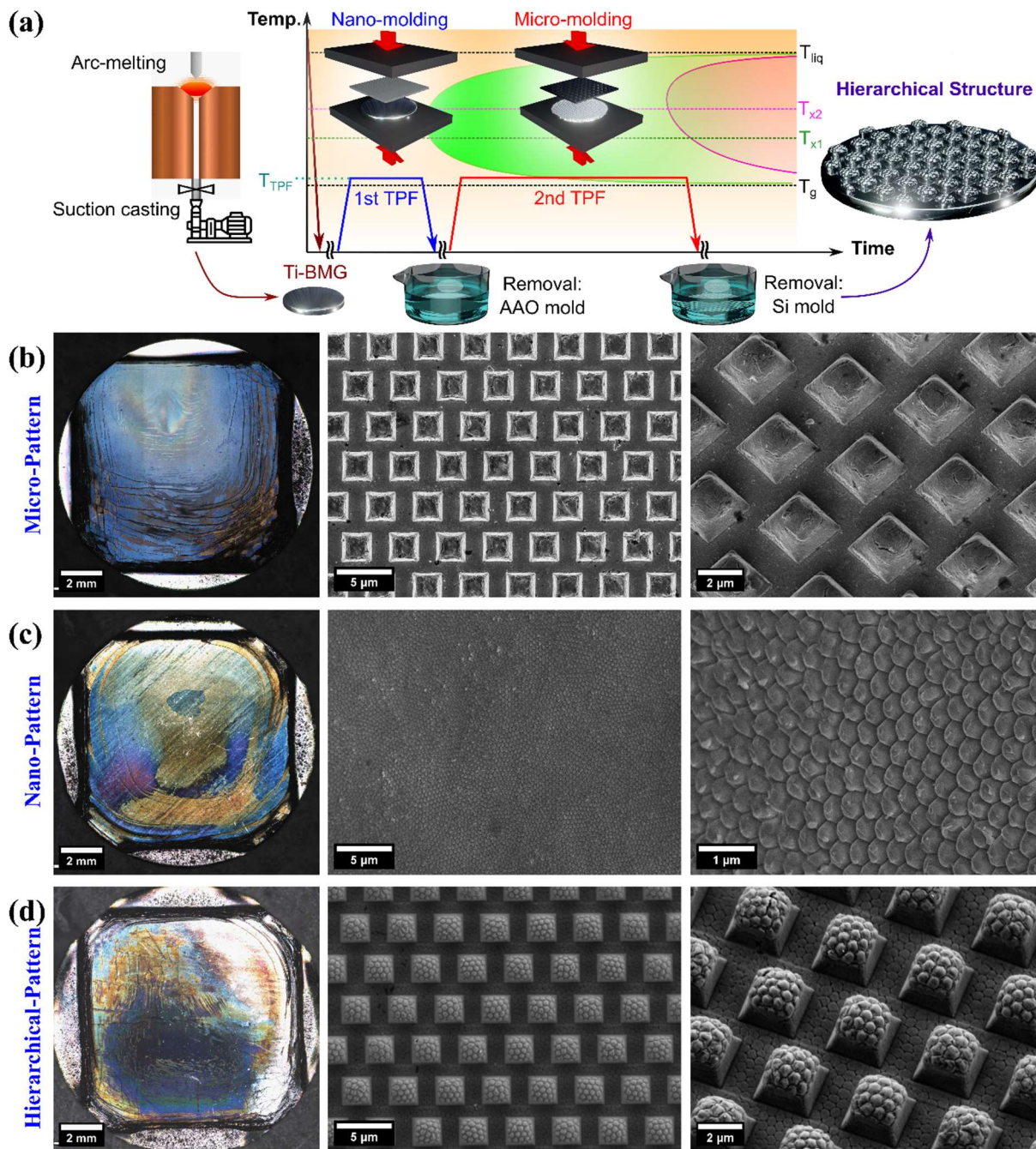


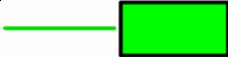





Figure 1: Thermoplastic forming of $\text{Ti}_{40}\text{Zr}_{10}\text{Cu}_{34}\text{Pd}_{14}\text{Sn}_2$ BMG: (a) Demonstration of two-step TPF process combined with a schematic time-temperature-transformation (TTT) diagram. Actual samples of (b) micro-pattern, (c) nano-pattern, and (d) hierarchical-pattern with raspberry-like appearance. The photos of the whole BMG disk are on the left, while SEM images are on the middle and right.

2.2. Structural and Mechanical Properties in Terms of Thermal History

The states of BMGs depend on their thermal history.^[50,51] The differences in states after the various TPF processing techniques were evaluated. **Table 1** describes the terminologies, color codes, intended applications used in the following figures, and the corresponding thermal histories of the TPF conditions. “As Cast” and “Crystalline” are references in which “As Cast” represents a fully amorphous state without thermo-processing, and “Crystalline”

represents the same material annealed to a fully crystallized structure. “410°C_10M” stands for the TPF process at 410°C for 10 min. This condition is used to generate micro- or nano-patterns in this work. “418°C_4M+410°C_10M” means the two-step TPF process to fabricate a 2-tier hierarchical structure in which the material is held at 418°C for 4 min to imprint the nano-pattern in the first step, and then at 410°C for 10 min to superpose the micro-pattern in the second step. “410°C_10M+374°C_6H” is the thermal history of a diffusion-based nano-molding technique inspired by Liu et al. to create nanorods with less than 100 nm diameter on crystalline metals.^[52] The idea is to create the nano-protrusion at 410°C for 10 min via the TPF process and then drop the temperature to 374°C for 6 h while holding the same pressure all the time. “440°C_4M” is based on the previous work from Cai et al. using the same BMG system that allows the nanocrystallization during the TPF process.^[20]

Table 1: Thermal history, color code, and intended application for various TPF processing techniques. (Format for thermal history: Temperature°C_Time, M = minute; H = hour)

Thermal History	Color	Intended Application
As Cast		Reference (fully amorphous)
410°C_10M		Micro- / Nano- pattern
418°C_4M+410°C_10M		2-tier hierarchical structure
410°C_10M+374°C_6H		TPF + Diffusion-based Nano-molding
440°C_4M		TPF with nano-crystallization
Crystalline		Reference (fully crystallized)

TPF-processed samples were characterized by XRD analysis to determine their microstructures. The XRD patterns of all TPF-processed samples are similar to the as-cast sample (**Figure 2a**), with the only feature being the characteristic broad halo around 48°. None of the XRD patterns reveal obvious crystalline peaks, suggesting the amorphous structure was retained. However, it should be noted that XRD may not detect nanocrystalline phases or small volume fractions of crystals.^[6,53] Nevertheless, the results of XRD analysis suggest that thermal processing in all conditions tested here does not induce significant crystallization. Figure 2b shows the results of the isochronous DSC analysis. For the references of the two extreme cases, the green line represents the amorphous state of the as-cast sample, and the black line represents the crystalline state. Three exothermic peaks are observed in the amorphous curves, indicating the formation of crystalline phases. It has been reported that the first exothermic peak is due to the formation of α -(Ti/Zr), Pd₃Ti, CuTi₂, and Pd₂Ti crystalline phases; the second peak to the formation of the CuTi crystalline phase; the third peak has been associated with the formation of the Pd₅Ti₃ and CuTi₂ crystalline phases.^[54] Notably, the curves for 410°C_10M (blue) and 418°C_4M+410°C_10M (purple) show the occurrence of the first exothermic peak. However,

the first exothermic peak in these samples is less intense than in the as-cast sample. In the DSC curve of 440°C_4M (red), the first exothermic peak disappeared. According to Calin et al.^[25], the first crystallization event involves forming a nanocrystalline α -(Ti/Zr) phase. Hence, nanocrystallization occurred after the thermal processing of 410°C_10M +374°C_6H and 440°C_4M.

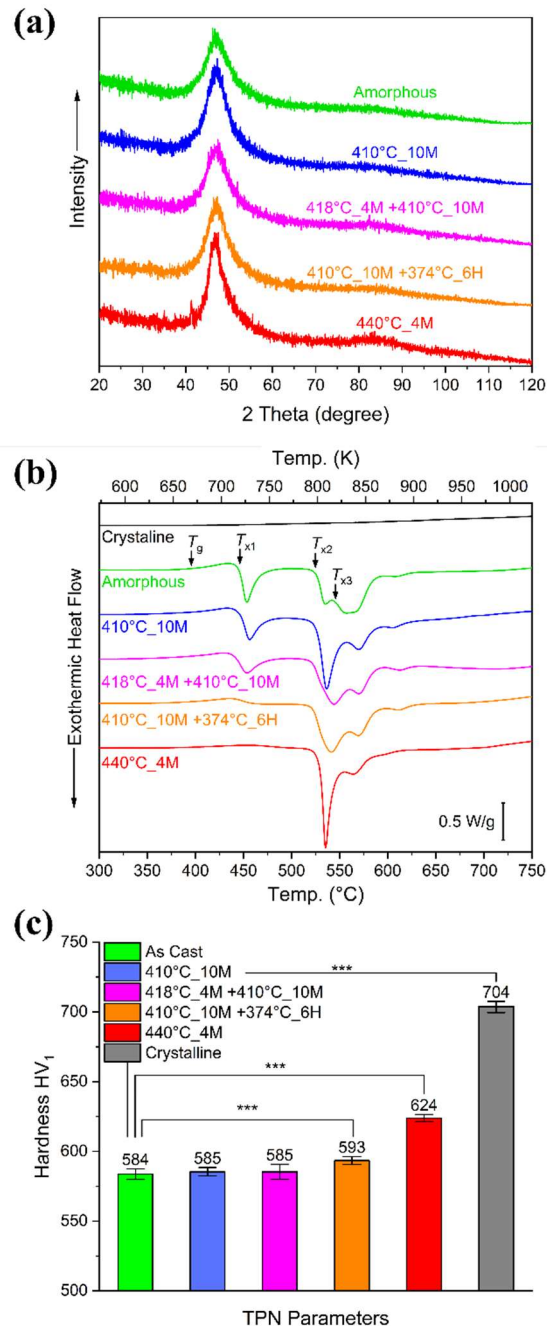


Figure 2: Characterization of $\text{Ti}_{40}\text{Zr}_{10}\text{Cu}_{34}\text{Pd}_{14}\text{Sn}_2$ BMG disks with various thermal histories during the TPF process: (a) XRD analysis (b) DSC curves from constant-rate heating (20 °C/min) measurements (c) Microhardness.

One of the main interests in BMGs for biomedical applications are their mechanical properties.^[55] The effects of the TPF processes on the mechanical properties have been

evaluated here by microhardness and RUS. The Vickers hardness (HV1) results are shown in Figure 2c. The hardness of the as-cast sample (584 HV) is similar to those found in 410°C_10M and 418°C_4M +410°C_10M samples (585 HV). The hardness of 410°C_10M +374°C_6H increases slightly to 593 HV. The hardness of 440°C_4M rises to 624 HV, 7% higher than the as-cast, an increase consistent with typical values associated with relaxation in BMGs. The hardness of the fully crystallized sample (704 HV) is 21% higher than the as-cast.

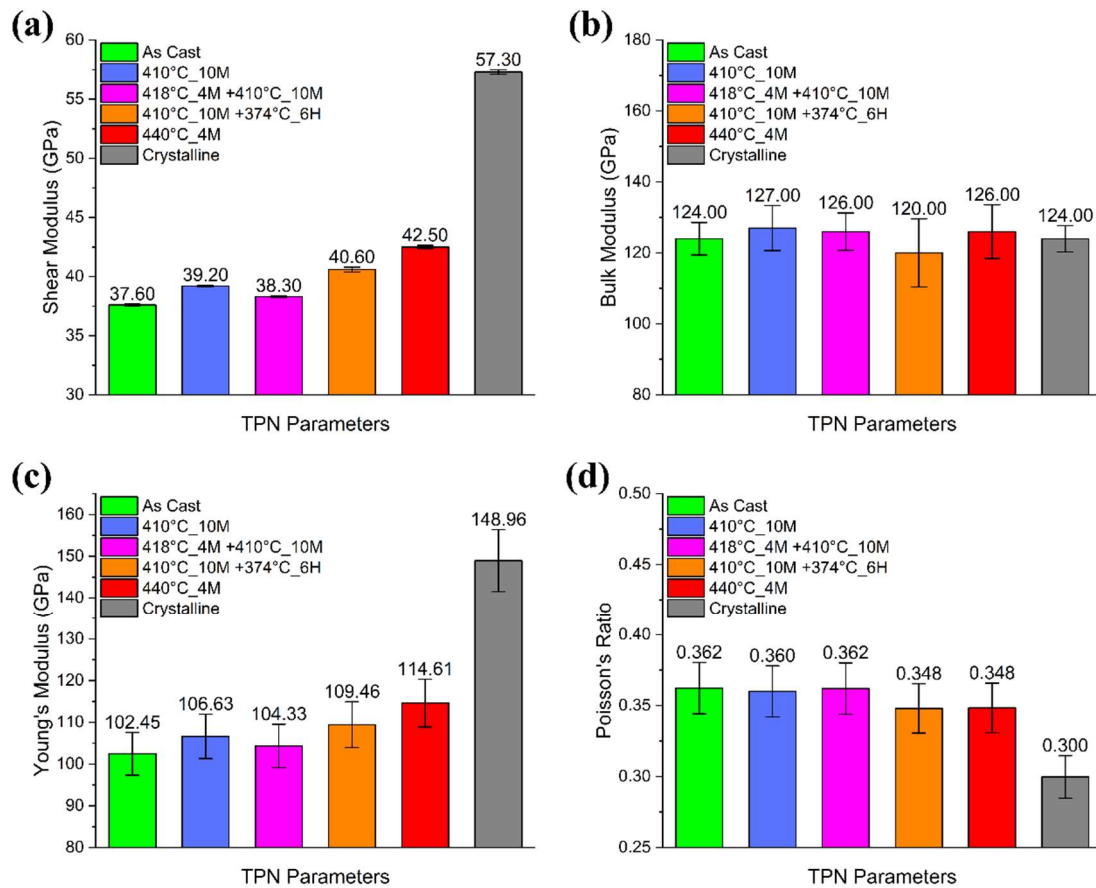


Figure 3: Mechanical properties determined via RUS: (a) Shear modulus. (b) Bulk modulus. (c) Young's modulus. (d) Poisson's ratio. It is worth noting that Young's modulus and Poisson's ratio were calculated from measured shear modulus and bulk modulus.

The shear and bulk modulus measured by RUS are shown in Figure 3a,b. Young's modulus and Poisson's ratio were calculated from the known relationships between elastic constants in isotropic materials (section 2.3., Figure 3c,d). The resonant modes in RUS were dominated by contributions from shear waves, and therefore, the experimental uncertainty is significantly lower for the shear modulus G ($\pm 0.2\%$) than for the bulk modulus K ($\pm 5\%$).^[56] The shear modulus increases gradually with harsher thermal processing conditions (longer time and higher temperature). Compared to the as-cast sample, an apparent increase in shear modulus is observed in the processing condition of 410°C_10M +374°C_6H (8%), 440°C_4M (13%), and Crystalline (52%). The bulk modulus does not change within the uncertainty following

thermal processing, and thus, Young's modulus follows the same trend as the shear modulus. Compared to the as-cast, a noticeable rise of Young's modulus is shown in 410°C_10M +374°C_6H (7%), 440°C_4M (12%), and Crystalline (45%). The Poisson's ratio shows an opposite trend to Young's modulus.

2.3. Wettability and Biocompatibility Regarding Surface Topography

The micro-, nano-, and hierarchical-patterned Ti-BMG disks, as illustrated in Figure 1, are further investigated for their surface properties, such as wettability and biocompatibility. The original mirror-polished Ti₄₀Zr₁₀Cu₃₄Pd₁₄Sn₂ BMG disk was provided as a reference (Ti-BMG.Flat). The result of contact angle measures is shown in **Figure 4a**. All patterns result in similar wettability. The flat reference surface exhibits the largest contact angle of 74°. All patterned surfaces have contact angles slightly smaller than that. The micro-pattern exhibits a contact angle of 71°, the hierarchical pattern a contact angle of 70°, while the nano-patterned surface has the smallest among the four tested surfaces with 68°.

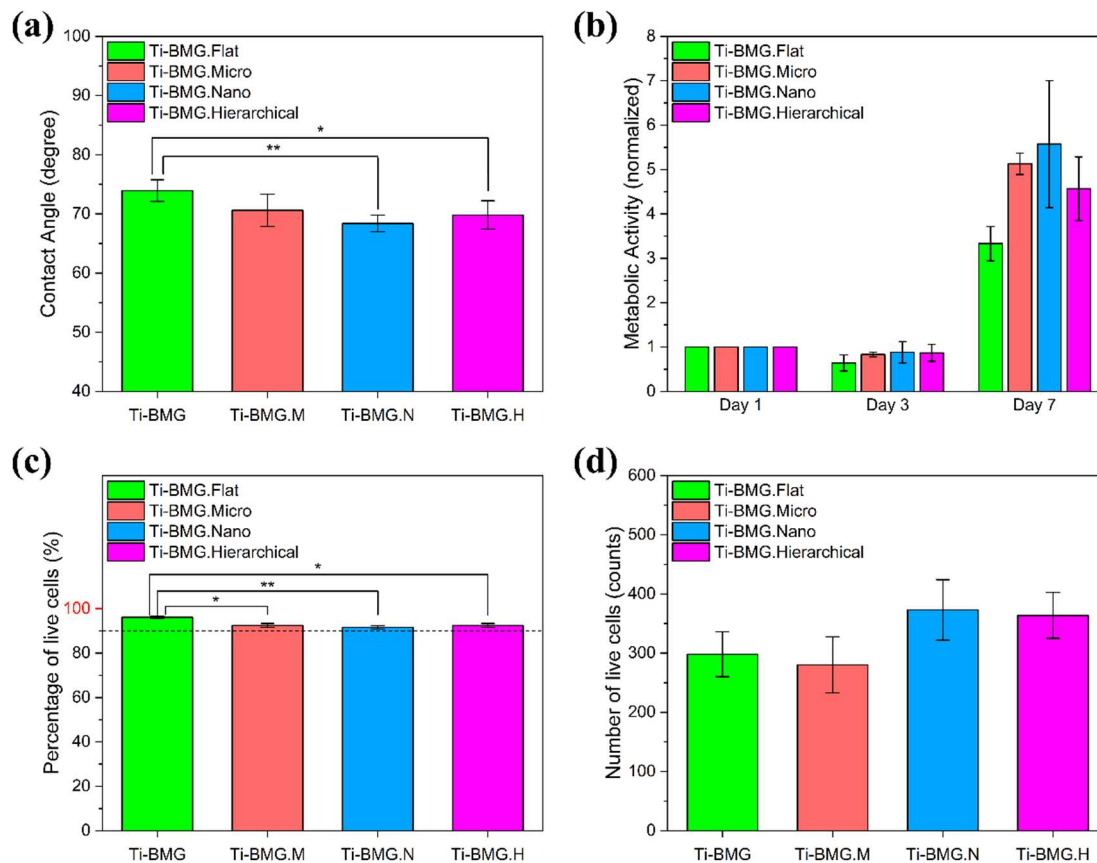


Figure 4: Wettability and biocompatibility of Ti₄₀Zr₁₀Cu₃₄Pd₁₄Sn₂ BMG with flat, micro-pattern, nano-pattern, hierarchical-pattern: (a) Water contact angles. (b) Saos-2 cell proliferation at day 1, 3, and 7 by Alamar Blue assay. (c) Percentage and (d) number of live cells at day 3 by live/dead cell viability kit.

Biocompatibilities of patterned Ti₄₀Zr₁₀Cu₃₄Pd₁₄Sn₂ BMG disks were investigated from several aspects, such as cell viability, cell proliferation, cell morphology, and cell adhesion.

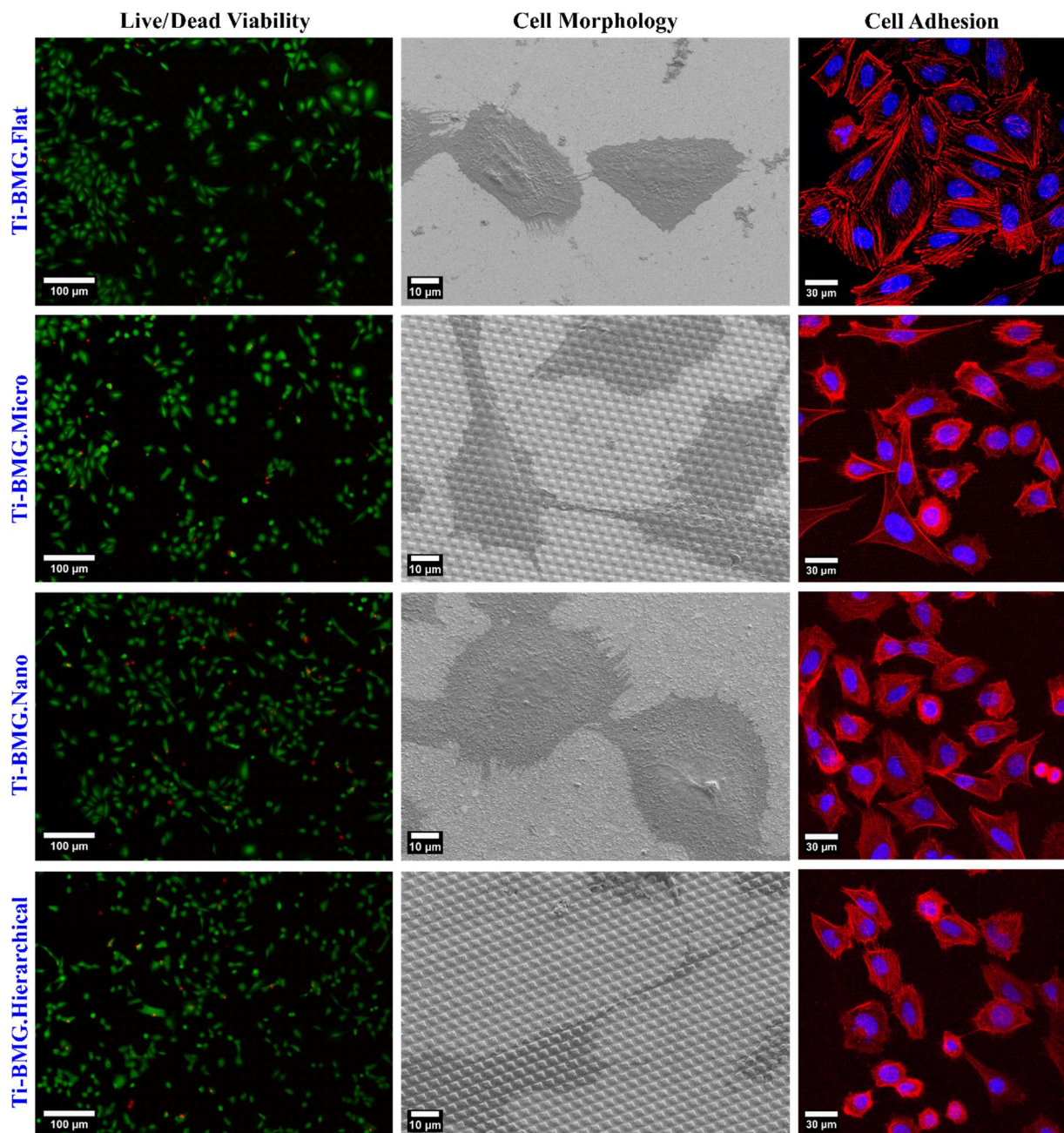


Figure 5: Cell viability, morphology, and adhesion of Saos-2 cells at day 3. In the live/dead viability, live cells are stained in green, while dead cells are stained in red. In the cell adhesion, actin cytoskeleton (red) and nuclei (blue) can be observed.

Saos-2 cell proliferation from Alamar Blue assay on four different surface topographies of Ti-BMG was analyzed on days 1, 3, and 7. The results are displayed in Figure 4b. The metabolic activity results were normalized regarding the value of day 1 and then compared among different surface topographies on days 3 and 7. No significant differences due to the four surface topographies were observed at any time point. Cell viability was evaluated from live/dead images by analyzing Saos-2 cells grown on the surfaces for 3 days after seeding. The quantified results, such as the percentage and number of live cells, are presented in Figure 4c,d correspondingly. All four surface topographies of Ti-BMG have cell viability higher than 90%

and the Ti-BMG.Flat has viability even above 96%. There are no significant differences between the four surface topographies regarding the number of live cells. Representative images from the live/dead assay of each surface topography are displayed in **Figure 5** Live/dead images, while live cells were dyed in green and dead cells in red.

Saos-2 cell morphology and cell adhesion on the four surface topographies were investigated after 3 days of culture via SEM and CLSM, as demonstrated in Figure 5. According to SEM images, Saos-2 cells spread well on all tested surfaces. Multiple cells are connected to each other by filopodia. Especially, filopodia longer than 20 μm are observed on the Ti-BMG.Micro and Ti-BMG.Hierarchical. Furthermore, these filopodia crossover the micro protuberances instead of going around them.

Regarding CLSM images from DAPI/phalloidin staining, cells on the flat surface have polygonal morphology with larger areas and are closer to each other than on patterned surfaces. Actin stress fibers were observed on all four surfaces, even though the flat surface has the most well-defined and prolonged actin stress fibers. The cells on the three patterned surfaces have less homogenously spread cells, with some of them stretched and elongated morphology and other cells in a rounded shape. It is worth noticing that some cells on all patterned surfaces have star-shaped or dendritic morphologies. Several dividing cells are observed on all tested surfaces.

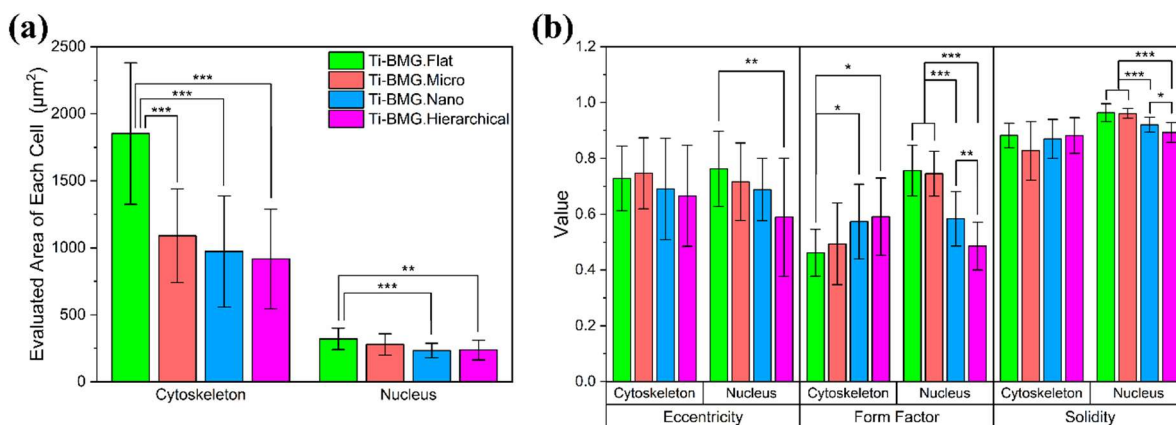


Figure 6: Quantitative morphometric analysis from DAPI/phalloidin staining images (Cell Adhesion in Figure 5) of Saos-2 cells after 3 days in culture on the four surface topographies of Ti-BMG: (a) Area, (b) eccentricity, form factor, and solidity of nuclei and cytoskeleton of each cell.

The CLSM images from DAPI/phalloidin staining were quantitatively analyzed. **Figure 6a** displays the areas of the cytoskeleton and nucleus of each cell on the surfaces. Briefly, all three patterned surfaces have significantly smaller cytoskeleton areas than the flat surface, while only nano- and hierarchical-patterned surfaces significantly reduce the nucleus area. In **Figure 6b**, three morphometric parameters: eccentricity, form factor, and solidity, are evaluated to describe cell morphologies. Each of these parameters has values ranging from 0 to 1. Tendencies were observed in the form factor. Nano- and hierarchical-patterned surfaces have significantly increased values in the cytoskeleton. However, the nuclear form factor exhibits an

inverse tendency, with the flat surface having the highest value and the hierarchically patterned surface having the lowest value. More interpretation about morphologic analysis is revealed in the discussion section.

3. Discussion

3.1. Influence of Thermal History on the Amorphous Structure and Mechanical Property

The correlations between the thermal histories from the TPF process, the glassy states, and mechanical properties were studied. Thermal processing of MGs at high temperatures typically induces two effects: relaxation and/or crystallization. Both relaxation and crystallization can be quantified by DSC analysis. According to crystallization enthalpies from DSC analysis, the studied TPF conditions can be divided into three categories, as listed in **Table 2**. Category I contains the samples that still show the first exothermic peaks around 450°C in the DSC curves, for instance, As Cast, 410°C_10M, and 418°C_4M +410°C_10M. Category II is for those whose first exothermic peaks disappeared, including 410°C_10M +374°C_6H and 440°C_4M. Category III is Crystalline, with all three peaks and the glass transition event having vanished.

Table 2: Three categories according to crystallization enthalpy analysis from DSC curves in Figure 2b.

Category	Thermal History	Crystallization Enthalpy 1 [J/g] \pm 5%	Crystallization Enthalpy 2+3 [J/g] \pm 5%
I	As Cast	8.0	28.1
I	410°C_10M	7.0	29.6
I	418°C_4M +410°C_10M	5.2	26.4
II	410°C_10M +374°C_6H	NA	28.3
II	440°C_4M	NA	26.9
III	Crystalline	NA	NA

It is clear that if the first exothermic peak in the DSC curves is retained after the thermal processing, as for Category I, then the mechanical properties also do not change significantly. The Vickers hardness results (Figure 2c) show no significant difference between the as-cast sample and the sample 410°C_10M and 418°C_4M +410°C_10M. However, the hardness increases dramatically if the thermal processing takes longer and is harsher so that the first exothermic peaks vanish, as for Category II. Once the material is fully crystallized, as for Category III, an even higher hardness is reached.

The assessment of elastic constants is consistent with the observed hardness and state changes. Typically, the shear modulus does not change by more than a few percent in the

amorphous state.^[57] The shear modulus in Category I is raised by less than 5%, suggesting the amorphous state is maintained. The shear modulus increases with relaxation in the glassy state have been reported in the range of 0–7%.^[57] Upon crystallization, the shear modulus has been reported to increase by 15–50%, with a typically cited value of 30%.^[58–60] Here, the samples assigned to Category II show shear modulus increases of 8% and 13% compared to the as-cast sample; these values are high, suggesting a potential mixture of relaxation and some nanocrystal formation. The crystalline sample (Category III) has a massive increase in shear modulus ($\approx 50\%$). The estimated Young's modulus and Poisson's ratio are influenced mainly by shear modulus since the bulk modulus weakly depends on thermal history.^[61]

Former studies about the TPF-based processing of BMGs claimed that crystallization must be avoided to preserve their mechanical properties.^[21,51,62] Our study suggests a crystallization tolerance for TPF processing, and slight crystallization is allowed before the $\text{Ti}_{40}\text{Zr}_{10}\text{Cu}_{34}\text{Pd}_{14}\text{Sn}_2$ BMGs lose their mechanical properties. For applications where mechanical properties are considered, the system of three categories from DSC analysis can be a practical tool to find the limits of thermal processing: (i) for Category I the processed BMGs maintain the mechanical properties as in the as-cast state, (ii) in Category II changes in mechanical properties are expected, such as higher hardness, Young's modulus, and lower Poisson's ratio, and (iii) Once the BMGs are fully crystallized as in Category III, the hardness and Young's modulus increase substantially. It is worth noting that the Crystalline sample exhibited brittle behavior during RUS sample preparation. Regarding orthopedic and dental implant applications, $\text{Ti}_{40}\text{Zr}_{10}\text{Cu}_{34}\text{Pd}_{14}\text{Sn}_2$ BMGs in Category I still show relatively lower Young's modulus (104 GPa) and higher Vickers hardness (585 HV) than the Ti-6Al-4V alloy, where the Ti-6Al-4V alloy is reported Young's modulus of 110–120 GPa and Vickers hardness 340–350 HV.^[1,14,63]

3.2. Interpretation of Wettability and Cell Response from Surface Topography

Wettability influences biocompatibility and can be modified through surface chemistry and topography.^[29,37,64] Generally, a surface is considered hydrophilic if the contact angle is smaller than 90° and hydrophobic if the contact angle is larger than 90° .^[9,30,65] According to the literature, hydrophilic surfaces have the advantages of upregulating bone cell attachment, spreading, differentiation, and later-stage mineralization.^[29,66–68] All tested surfaces of $\text{Ti}_{40}\text{Zr}_{10}\text{Cu}_{34}\text{Pd}_{14}\text{Sn}_2$ BMG disks are hydrophilic since they have contact angles smaller than 75° . It is worth noting that the passive oxide layer formed on the patterned surfaces is thicker than on the flat surface due to the TPF processing temperature above 400°C . The passive oxide layer has been reported to have the composition of 64–69% TiO_2 , 15–20% ZrO_2 , 10–18% Cu_2O , and 1–2% SnO_2 on $\text{Ti}_{40}\text{Zr}_{10}\text{Cu}_{34}\text{Pd}_{14}\text{Sn}_2$ BMG.^[6] Both surface topography and surface chemistry have effects on wettability.^[69–72] Hence, nano- and hierarchical-patterned surfaces are more hydrophilic than the flat surface due to the synergetic effect of the passive oxide layer formed during the TPF process and the patterned topographies after the TPF process. Further

studies are required to determine the independent influence of surface topography and surface chemistry on wettability.

In this study, all $\text{Ti}_{40}\text{Zr}_{10}\text{Cu}_{34}\text{Pd}_{14}\text{Sn}_2$ BMG disks have very high biocompatibility. Although there is no dramatic difference in cell viability and proliferation according to the Alamar Blue assay and Live/Dead Cytotoxicity, the topographical patterns have significantly changed the cell morphology and spatial distribution.

In the CLSM and SEM images (Figure 5), cells adhered to all patterned surfaces have many membrane extensions on the edge of the cell leading to star-shaped and dendritic cell morphologies. Especially on the micro- and hierarchical-patterned surfaces, these membrane extensions can expand longer than $20\ \mu\text{m}$ and climb over the micro protuberances instead of going around the protuberances. These extensions are filopodia filled with bundled actin filaments and work as topographical sensors in the microenvironment.^[38,69–71] Filopodia play important roles in driving fundamental cell functions such as cell adhesion, spreading, migration, and even division.^[38,69] Many works^[30,38,72,73] report that patterned surfaces promote the formation of longer filopodia, as observed in the CLSM and SEM images. Moreover, some cells develop filopodia parallel to each other to align with the direction of the micro-pattern, and several nuclear signals have black spots (spots with weak fluorescence signal) ordered in the nucleus, as shown in Figure S2. The black spots observed in the nucleus were deformations of the nucleus due to the micro-pattern. Generally, Saos-2 cells spread well on all tested surfaces in the CLSM images (Figure 5). The quantitative morphometric analysis provides a clear view of the influence of surface topography on cell morphology (Figure 6). From the area of the cytoskeleton and nucleus (Figure 6a), a ratio of cytoskeleton area to nucleus area can be calculated, which simply indicates how well cells spread on the surface. The flat surface has the highest ratio of 5.86, while the hierarchical-patterned surface has the lowest ratio of 3.80. The cell spreading results revealed that cells growing on the flat surface had the largest spreading area. For micro- and hierarchical-patterned surfaces, the area was $1090.45\ \mu\text{m}^2$ versus $916.97\ \mu\text{m}^2$, respectively. These numbers indicate that each cell covered approximately 62 pieces of square protuberances for micro-patterned surfaces and 52 pieces for hierarchical-patterned surfaces, taking into account the protuberance size of $2.5 \times 2.5\ \mu\text{m}^2$. Several studies have shown that a limited spreading area of cells is beneficial to maintain the undifferentiated state of embryonic stem cells.^[74,75]

The morphologies of the cytoskeleton and nucleus are described using three morphometric parameters: eccentricity, form factor, and solidity. Firstly, eccentricity measures how much the cell deviates from being circular using the bounding ellipse.^[76,77] A perfect circle has an eccentricity of 0, and a more elongated shape has a higher eccentricity.^[76,77] It is worth noticing that the nuclear eccentricity on the hierarchical-patterned surface is significantly lower than on the flat surface, which implies that the nuclei are more elongated on the flat surface than on the hierarchical-patterned surface. Rangamani et al. showed that increasing nucleus

eccentricity enhances mitogen-activated protein kinase (MAPK) 1,2 level in the COS-7 cell nucleus for growth factor receptor pathways.^[78] Form factor, also known as circularity, represents how starfish-like the shape (i.e., more protrusions and lobulations) compared with a circle.^[77,79] A perfect circle has a form factor of 1, and the ratio decreases with more cell protrusions or deconvoluted shapes.^[77,79] The cytoskeleton form factor of all four surfaces is smaller than 0.6, indicating that cells spread with several protrusions. Furthermore, the cytoskeleton form factor significantly increases on nano- and hierarchical-patterned surfaces. However, the nuclear form factor decreases in nano- and hierarchical-patterned surfaces (0.58 versus 0.49) compared with the flat surface (0.76). This decreasing trend indicates the nano-feature ridging the nucleus, and this effect can be amplified when the micro-feature is present, as shown in the hierarchical-patterned surface. Lastly, solidity is the ratio of the measured area to the area of a convex hull drawn around the object.^[77,80] This convex hull around the object can be imagined as a rubber band stretched around the perimeter so that the convex hull gaps away from the actual perimeter in undulating cells.^[77,80] Solidity is 1 if the actual perimeter is the same as the convex hull, and solidity is smaller if there are more retracted gaps of the actual perimeter than the convex hull. Nuclear solidity has a similar trend as the nuclear form factor, with no differences between flat and micro-patterned surfaces (0.96). Nevertheless, the nuclear solidity decreases to 0.92 for nanopatterned surfaces and 0.89 for the hierarchical-patterned surface. Again, it is interesting that the micro-pattern alone does not crumple the nucleus, while the nano-pattern does. Nevertheless, when combined with the nano-pattern, the micro-pattern creates a more irregular nuclear shape.

Regarding cell spatial distribution, in the CLSM images, it is apparent that Saos-2 cells are packed closer to each other on the flat surface than on three patterned surfaces. When comparing multiple live/dead images, Saos-2 cells on the flat surface tend to form colonies in some regions and leave empty spaces in other regions. On the contrary, especially on the hierarchical-patterned surface, Saos-2 cells tend to disperse on the whole region with lesser cells tightly contact with each other than on the flat surface. The role of surface topography on protein absorption and subsequent cell response needs to be further elucidated. Studies showed that micro-roughness increases protein adsorption by providing a larger specific surface area due to more active sites and features, while the aspect ratio of nano-roughness can affect protein conformation and orientation.^[81-84] A possible hypothesis is that the topography of patterned surfaces hinders cell migration. Therefore, cells develop long filopodia to sense each other instead of moving to the neighbor cells. Dallas et al. proposed that changes in cell motility may be critical in the transition from osteoblast to osteocyte, as reflected in the altered expression of many molecules involved in cytoskeletal function.^[85] Hence, combining cell culture on patterned surfaces with dynamic imaging approaches could be used to study the role of cell motility in bone cell function.

This work suggests potential applications of thermoplastic-formed $\text{Ti}_{40}\text{Zr}_{10}\text{Cu}_{34}\text{Pd}_{14}\text{Sn}_2$ BMG in two aspects: (1) Hard-tissue implants and (2) a toolbox for studying cell response. Regarding implant applications, the two-step TPF process successfully creates hierarchical structures on $\text{Ti}_{40}\text{Zr}_{10}\text{Cu}_{34}\text{Pd}_{14}\text{Sn}_2$ BMGs, and most importantly, the mechanical properties, such as Young's modulus and hardness, are retained. This work confirms that the surface patterns on the $\text{Ti}_{40}\text{Zr}_{10}\text{Cu}_{34}\text{Pd}_{14}\text{Sn}_2$ BMG disks do not deteriorate their biocompatibility. Furthermore, several studies demonstrate that micro- and nano-scale topographies can reduce bacteria adhesion, thereby improving the antibiofilm properties of the material.^[86,87] Therefore, further research to investigate the antibacterial properties of these patterned surfaces is crucial for hard-tissue implant applications. The patterned BMG surfaces created by the TPF process show a high degree of order (instead of random roughness) and design flexibility, which are beneficial to study cell behavior such as spreading, adhesion, proliferation, migration, and differentiation. Currently, most patterns with high degree of order are created on polymeric substrates, and fewer studies investigated cell responses on rigid- and ordered-patterned surfaces.^[29] Compared with random roughness, surface topography with well-defined dimensions can easily qualify and quantify the effect of a specific cell response from a particular surface feature.^[40] Several reviews have discussed how pattern parameters - such as the aspect ratio, repeat space, and shape of a patterned surface - can significantly affect cell proliferation, adhesion, migration, and differentiation with different cell types.^[29,36,88-91] In general, micro-structured substrates can affect cell morphology and cytoskeletal structure, while nano-structured surfaces can influence cell functions, including proliferation, differentiation, and alignment.^[90] The surface features of the hierarchical structures can be adjusted by implementing molds with different pore sizes and interpore distances. The prominence of a particular feature can be tuned through the applied pressure and holding time during the TPF. This design flexibility allows optimizing the particular surface feature to strengthen the desired response and combining multiple functions using a hierarchical structure.

4. Conclusions

Nano-patterns and multitier hierarchical structures have been fabricated with Ni-free Ti-based BMGs. The versatility of the TPF technique is exhibited on $\text{Ti}_{40}\text{Zr}_{10}\text{Cu}_{34}\text{Pd}_{14}\text{Sn}_2$ BMG. With 400 nm hexagonal close-packed nano-protrusions, the nano-pattern mimics the microstructure of a dragonfly's eye. A two-step TPF process takes the surface patterning to the next level by creating a hierarchical structure integrating 400 nm nano-protrusions on 2.5 μm square protuberances. The hierarchical-patterned Ti-BMG preserves advantageous mechanical properties after the two-step TPF process. Moreover, the connection between structural and mechanical properties, such as Young's modulus and hardness, is classified into three categories based on DSC analysis. The preserved low Young's modulus is essential to alleviate stress-shielding effects for hard-tissue implants.

Most importantly, for biomedical applications, the biocompatibilities of flat, micro-patterned, nano-patterned, and hierarchical-structured $\text{Ti}_{40}\text{Zr}_{10}\text{Cu}_{34}\text{Pd}_{14}\text{Sn}_2$ BMG are investigated using Saos-2 cell line. In-vitro assays confirm good cell viability and cell proliferation. Despite the changes in wettability being minor, surface patterns indeed change cell behaviors such as cell morphology and adhesion. Compared with the flat surface, patterned surfaces promote the formation of longer filopodia, leading to star-shaped and dendritic cell morphologies. Regarding cell spatial distribution, Saos-2 cells on a flat surface pack more closely to form colonies in some areas and leave empty spaces in others. However, Saos-2 cells scatter across the entire surface on the hierarchical-patterned surface, with fewer cells in close contact. Beyond hard-tissue implant applications, TPF-patterned Ti-BMGs provide a high degree of order and design flexibility on the surface topography, which can be a prospective toolbox for exploring cell behavior on stiff and ordered surfaces.

5. Experimental Section

Fabrication of Ti-BMG Disks: $\text{Ti}_{40}\text{Zr}_{10}\text{Cu}_{34}\text{Pd}_{14}\text{Sn}_2$ specimens were produced via arc-melting and suction casting. Master ingots with nominal composition $\text{Ti}_{40}\text{Zr}_{10}\text{Cu}_{34}\text{Pd}_{14}\text{Sn}_2$ (at%) were prepared from pure elements (purities above 99.9%). The ingots were melted five times to ensure homogeneity. The master ingot was cast into a disk with a 12 mm diameter and 2.5 mm thickness by copper mold suction casting. Both master ingot preparation and suction casting were carried out under a Ti-gettered Ar atmosphere in the same arc-melting machine (Edmund Bühler GmbH). The as-cast Ti-BMGs disks were cut to half the thickness using a wire-cut electrical discharge machining (EDM MV1200S, Mitsubishi Electric Europe B.V.). The disks were ground and mirror-polished to a thickness of around 1 mm and roughness of less than 1 μm to eliminate potential surface crystallization and oxidation, and to ensure the surfaces were parallel for the TPF processing.

Thermoplastic Forming of Ti-BMG: The apparatus used for TPF in this work is inspired by the previous works by J. Schroers and collaborators at Yale University.^[92,93] The setup is based on a compression machine (Zwick Z100, ZwickRoell GmbH & Co. KG) with ad-hoc components, including upper and lower anvils fitted with heating cartridge, a PID controller for process control, and water-cooling circulation to protect the loading cells from the heat. Various patterns from micro-scale to nano-scale, and hierarchical structures containing both, were manufactured on the $\text{Ti}_{40}\text{Zr}_{10}\text{Cu}_{34}\text{Pd}_{14}\text{Sn}_2$ BMG disks. Micro-patterns were imprinted using macro-porous silicon templates (Si mold) with 2.5 μm pore diameter and 4.2 μm interpore distance (SmartMembranes GmbH). Nano-patterns were imprinted from nano-porous alumina templates (AAO mold) with 400 nm pore diameter and 480 nm interpore distance (SmartMembranes GmbH). Silicon templates were dissolved with a KOH solution (1.5 M), while alumina templates were dissolved with a phosphoric acid solution (5% w/w). Hierarchical structures were fabricated via a two-step TPF process which created the nano-pattern first, and

then imprinted the micro-pattern on top of the nano-pattern as a second step (Figure S3). **Table 3** provides a summary of the processing parameters.

Table 3: Parameters of TPF processes to create patterns.

	Step	Max. Pressure [MPa]	Load Rate [MPa min ⁻¹]	Load Time [Minute]	Hold Time [Minute]
Micro-pattern	-	900 ± 10	150	6	4
Nano-pattern	-	900 ± 10	900	1	9
Hierarchical structure	1	900 ± 10	900	1	9
	2	900 ± 10	150	6	4

Characterization of Physical Properties and Wettability: The material properties of Ti-BMG disks were characterized after the suction casting and the TPF process. Several structural analyses were conducted to confirm the amorphous nature of as-cast states and the influence of thermal processing. The Ti-BMG disks were characterized by X-ray diffraction (XRD) using Bruker D2 Phaser with Co K α radiation. To inspect the formation of nanocrystals, samples of ≈ 20 mg mass were characterized by differential scanning calorimetry (DSC) using a NETZSCH DSC 404 F1 instrument under an argon atmosphere at a heating rate of 20 K min⁻¹ (constant-rate heating mode) using alumina crucibles. Overview images of the sample disk were recorded with confocal laser scanning microscopy (CLSM-Olympus LEXT OLS4100). The topographies of patterned surfaces were imaged with scanning electron microscopy (SEM-Zeiss LEO type 1525) using an in-lens detector. Microhardness was assessed with standard microindentation with a Vickers indenter, and the elastic constants with resonant ultrasound spectroscopy (RUS). Following ISO 6507 standard, Vickers hardness tests were performed using a 9.8 N load (HV1) on a DuraScan 70 G5 universal laboratory hardness tester (EMCO-TEST Prüfmaschinen GmbH, Austria). RUS was carried out at room temperature (RT) on cuboid samples in the as-cast state and after the various TPF conditions. The methodologies employed to determine the values of the elastic moduli were identical to those of McKnight et al.^[88] A lapping fixture was used to ensure the parallelism and perpendicularity of the faces. The root mean square (RMS) error of the fitting to the resonance spectra were <0.85%. The given Young's moduli and Poisson's ratios were computed from the measured bulk modulus and shear modulus using conversion formulae (1) and (2), respectively:

$$E = \frac{9KG}{3K + G} \quad (1)$$

$$\nu = \frac{3K - 2G}{2(3K + G)} \quad (2)$$

where K is the bulk modulus, G is the shear modulus, E is Young's modulus, and ν is Poisson's ratio. Static water contact angles were recorded and analyzed via the sessile drop method with a contact angle goniometer (Krüss DSA100). The measurements were performed and averaged for at least five locations, with water droplets of 2 μL volume.

Cell Culture and Cell Seeding: In vitro experiments were used to examine the four different surface topographies of $\text{Ti}_{40}\text{Zr}_{10}\text{Cu}_{34}\text{Pd}_{14}\text{Sn}_2$ BMG disks: (1) Flat (mirror-polished), (2) Micro-pattern, (3) Nano-pattern, (4) Hierarchical-pattern. Osteoblast-like Saos-2 cell line (ATCC HTB-85), derived from primary human osteosarcoma, were cultured in the fresh medium composed by Dulbecco's modified Eagle medium (DMEM) with 10% fetal bovine serum (Gibco) and 2% Penicillin-Streptomycin (P/S; Biowest, Riverside, MO, USA), under standard conditions (37°C and 5% CO_2). All Ti-BMG disks were sterilized with absolute ethanol for 30 min and air dried. The sterilized disks were placed into a 24-well plate individually. Then, 20,000 Saos-2 cells were seeded on top of the disks in each well and cultured under standard conditions.

Cell Viability and Cell Proliferation Assays: Cell viability on the Ti-BMG disks was assessed using the Live/Dead Viability/Cytotoxicity kit for mammalian cells (Invitrogen, Waltham, MA, USA). Saos-2 cells were seeded on the Ti-BMG disks as described in section 2.4.1. After 3 days of incubation, the assay was performed following the manufacturer's protocol. Live/dead images of 8 random regions within the whole Ti-BMG disk were captured by an Olympus IX71 inverted microscope with epifluorescence. Live/dead images were analyzed using CellProfiler (4.2.5) software to systematically count the number of live and dead cells. Saos-2 cell proliferation was evaluated by performing an Alamar Blue cell viability test (Thermo Fisher Scientific, USA) at incubation days 1, 3, and 7. After 24 h of cell seeding, Ti-BMG disks with adhered cells were transferred to a new well to discard the cells growing on the bottom of the well. Fresh medium with 10% Alamar Blue was added into each well, and cells were incubated under standard conditions in the dark for another 4 h. The supernatant was then collected, and fresh medium was added to the well plate to keep the culture going. 200 μL of the supernatant was transferred to a black-bottom Greiner CELLSTAR® 96-well plate (Sigma-Aldrich, Saint Louis, MO, USA), and the fluorescence was determined at 590 nm wavelength after excitation at 560 nm on a Spark multimode microplate reader (Tecan, Männedorf, Switzerland). The assay was repeated after 3 and 7 days. Fluorescence values on days 3 and 7 were normalized to values obtained from day 1. Experiments were performed in triplicate, and each has two technical replicas.

Cell Morphology and Cell Adhesion Analysis: The same samples from the cell viability assay were prepared for SEM imaging (Zeiss Merlin) with SE2 detector to study the influence of pattern designs on cell morphology. Ti-BMG disks with adhered cells were rinsed twice in phosphate-buffered saline (PBS), fixed in 4% paraformaldehyde (Sigma) in PBS for 45 min at RT, and washed twice in PBS. Cell dehydration was performed by increasing ethanol

concentrations (50, 70, 90, and twice 100%) for 5 min each. Lastly, samples were dried using hexamethyldisilazane (Electron Microscope Science) for 15 min and were ready for SEM imaging. Cell adhesion was inspected through the actin filaments distribution. Saos-2 cells were seeded on the Ti-BMG disks as described in section 2.4.1. After 3 days of incubation, the actin cytoskeleton was labeled with phalloidin (Invitrogen), while nuclei were stained with DAPI (Invitrogen). The staining was performed following the manufacturer's protocol. Fluorescence images were taken using a confocal laser scanning microscope (CLSM, Confocal Leica SP5, Leica Microsystems GmbH). One disk was analyzed for each surface topography. Quantitative morphometric analysis from the confocal images was performed using CellProfiler (4.2.5) software to evaluate the area, eccentricity, form factor, and solidity of cytoskeleton and nucleus.

Statistical Analysis: Vickers hardness and contact angle are presented as a mean \pm standard deviation (SD). Shear and bulk modulus from resonant ultrasound spectroscopy are presented as a mean \pm uncertainty. Results from the Alamar Blue assay and live/dead cell viability kit are presented as a mean \pm standard error (SE). Quantitative morphometric analysis from DAPI/phalloidin staining images is presented as a mean \pm standard deviation (SD). All statistical analyses were evaluated by one-way analysis of variance (ANOVA) and Tukey post hoc comparison using the software OriginPro 2019b (9.6.5). Differences were considered statistically significant for p-values < 0.05 . (denoted by: *p < 0.05 ; **p < 0.01 ; ***p < 0.001)

Supporting Information

Supporting Information is available from the Wiley Online Library or from the author.

Acknowledgements

This work was supported by the European Union's Horizon 2020 research and innovation program under the Marie Skłodowska-Curie grant agreement No. 861046 (BIOREMIA-ETN). B.S. J.E. and F.S. acknowledge support from the Austrian Science Fund (FWF), Grant/Award Number: I3937N36, and A.B. and C.N. acknowledge support from the Spanish Government grant PID2020-116844RB-C21 and the Generalitat de Catalunya (2021-SGR-00122). J.S. was supported by the National Science Foundation through the Advanced Manufacturing Program (CMMI 2311311). The authors thank Dr. Sungwoo Sohn, Naijia Liu, and Arindam Raj for their insightful scientific discussions regarding thermomechanical molding techniques. Further thanks to Robin Neubauer and Michael Pegritz for their practical opinions on the TPF design, and Dr. Michael Burtscher for his recommendations on cell analysis software. A.B. and C.N. would like to thank the staff from the Servei de Microscòpia of Universitat Autònoma de Barcelona.

Conflict of Interest

The authors declare no conflict of interest.

Data Availability Statement

The data that support the findings of this study are available from the corresponding author upon reasonable request.

References

- [1] C. Veiga, J. P. Davim, A. J. R. Loureiro, *Rev. Adv. Mater. Sci* **32.2** (2012): 133-148.
- [2] K. Imai, X. Zhou, X. Liu, *Metals* **2020**, *10*, 203.
- [3] P. Gong, L. Deng, J. Jin, S. Wang, X. Wang, K. Yao, *Metals* **2016**, *6*, 264.
- [4] M. Zhang, Y. Q. Song, H. J. Lin, Z. Li, W. Li, *Front. Mater.* **2022**, *8*, 814629.
- [5] A. Rezvan, E. Sharifikolouei, A. Lassnig, V. Soprunyuk, C. Gammer, F. Spieckermann, W. Schranz, Z. Najmi, A. Cochis, A. C. Scalia, L. Rimondini, M. Manfredi, J. Eckert, B. Sarac, *Materials Today Bio* **2022**, 100378.
- [6] A. Liens, B. Ter-Ovanessian, N. Courtois, D. Fabregue, T. Wada, H. Kato, J. Chevalier, *Corrosion Science* **2020**, *177*, 108854.
- [7] E. Yüce, F. Spieckermann, A. Ascı, S. Wurster, P. Ramasamy, L. Xi, B. Sarac, J. Eckert, *Materials Today Advances* **2023**, *19*, 100392.
- [8] M. Niinomi, M. Nakai, *International Journal of Biomaterials* **2011**, *2011*, 1.
- [9] L. Damiati, M. G. Eales, A. H. Nobbs, B. Su, P. M. Tsimbouri, M. Salmeron-Sanchez, M. J. Dalby, *J Tissue Eng* **2018**, *9*, 204173141879069.
- [10] M. Surmeneva, I. Grubova, N. Glukhova, D. Khrapov, A. Koptug, A. Volkova, Y. Ivanov, C. M. Cotrut, A. Vladescu, A. Teresov, N. Koval, A. Tyurin, R. Surmenev, *Metals* **2021**, *11*, 1066.
- [11] I. Y. Grubova, M. Kozadaeva, A. P. Volkova, D. Khrapov, R. A. Surmenev, A. V. Koptug, A. Vladescu (Dragomir), A. Tyurin, M. A. Surmeneva, *Journal of Materials Research and Technology* **2023**, *25*, 4457.
- [12] L. A. Alberta, J. Vishnu, A. Hariharan, S. Pilz, A. Gebert, M. Calin, *Journal of Materials Research and Technology* **2022**, *20*, 3306.
- [13] A. Akman, L. A. Alberta, P. M. Giraldo-Osorno, A. B. Turner, M. Hantusch, A. Palmquist, M. Trobos, M. Calin, A. Gebert, *Journal of Materials Research and Technology* **2023**, *25*, 4110.
- [14] A. Liens, A. Etiemble, P. Rivory, S. Balvay, J.-M. Pelletier, S. Cardinal, D. Fabrègue, H. Kato, P. Steyer, T. Munhoz, J. Adrien, N. Courtois, D. Hartmann, J. Chevalier, *Materials* **2018**, *11*, 249.
- [15] C. A. Baumann, B. D. Crist, *Journal of Clinical Orthopaedics and Trauma* **2020**, *11*, S596.
- [16] A. Kanaji, V. Orhue, M. S. Caicedo, A. S. Viridi, D. R. Sumner, N. J. Hallab, T. Yoshiaki, K. Sena, *J Orthop Surg Res* **2014**, *9*, 91.
- [17] S. Bera, B. Sarac, S. Balakin, P. Ramasamy, M. Stoica, M. Calin, J. Eckert, *Materials & Design* **2017**, *120*, 204.
- [18] A. Blanquer, A. Hynowska, C. Nogués, E. Ibáñez, J. Sort, M. D. Baró, B. Özkale, S. Pané, E. Pellicer, L. Barrios, *PLoS ONE* **2016**, *11*, e0156644.
- [19] B. Sarac, J. Eckert, *Progress in Materials Science* **2022**, *127*, 100941.

- [20] F.-F. Cai, B. Sarac, Z. Chen, C. Czibula, F. Spieckermann, J. Eckert, *Materials Today Advances* **2022**, *16*, 100316.
- [21] J. Schroers, *Adv. Mater.* **2010**, *22*, 1566.
- [22] Y. Saotome, K. Itoh, T. Zhang, A. Inoue, *Scripta Materialia* **2001**, *44*, 1541.
- [23] W. Chen, Z. Liu, H. M. Robinson, J. Schroers, *Acta Materialia* **2014**, *73*, 259.
- [24] R. M. Ojeda Mota, N. Liu, S. A. Kube, J. Chay, H. D. McClintock, J. Schroers, *Applied Materials Today* **2020**, *19*, 100567.
- [25] M. Calin, M. Stoica, N. Zheng, X. R. Wang, S. Scudino, A. Gebert, J. Eckert, *SSP* **2012**, *188*, 3.
- [26] S. Zhu, G. Xie, F. Qin, X. Wang, A. Inoue, *Mater. Trans.* **2012**, *53*, 500.
- [27] M. B. Berger, P. Slosar, Z. Schwartz, D. J. Cohen, S. B. Goodman, P. A. Anderson, B. D. Boyan, *Biomimetics* **2022**, *7*, 46.
- [28] R. Rodríguez-González, L. Monsalve-Guil, A. Jimenez-Guerra, E. Velasco-Ortega, J. Moreno-Muñoz, E. Nuñez-Marquez, R. A. Pérez, J. Gil, I. Ortiz-Garcia, *Materials* **2023**, *16*, 3553.
- [29] N. Gui, W. Xu, D. E. Myers, R. Shukla, H. P. Tang, M. Qian, *Biomater. Sci.* **2018**, *6*, 250.
- [30] C. Matschegewski, S. Staehlke, R. Loeffler, R. Lange, F. Chai, D. P. Kern, U. Beck, B. J. Nebe, *Biomaterials* **2010**, *31*, 5729.
- [31] M. d'Angelo, E. Benedetti, M. G. Tupone, M. Catanesi, V. Castelli, A. Antonosante, A. Cimini, *Cells* **2019**, *8*, 1036.
- [32] J. Rychly, B. J. Nebe, *BioNanoMaterials* **2013**, *14*.
- [33] Y. Wang, Y. Yang, T. Yoshitomi, N. Kawazoe, Y. Yang, G. Chen, *J. Mater. Chem. B* **2021**, *9*, 4329.
- [34] A. M. Loye, E. R. Kinser, S. Bensouda, M. Shayan, R. Davis, R. Wang, Z. Chen, U. D. Schwarz, J. Schroers, T. R. Kyriakides, *Sci Rep* **2018**, *8*, 8758.
- [35] M. J. Dalby, *Medical Engineering & Physics* **2005**, *27*, 730.
- [36] K. Zhang, X. Xiao, X. Wang, Y. Fan, X. Li, *J. Mater. Chem. B* **2019**, *7*, 7090.
- [37] M. Martínez-Calderon, R. J. Martín-Palma, A. Rodríguez, M. Gómez-Aranzadi, J. P. García-Ruiz, S. M. Olaizola, M. Manso-Silván, *Phys. Rev. Materials* **2020**, *4*, 056008.
- [38] J. Albuschies, V. Vogel, *Sci Rep* **2013**, *3*, 1658.
- [39] E. H. Ahn, Y. Kim, Kshitiz, S. S. An, J. Afzal, S. Lee, M. Kwak, K.-Y. Suh, D.-H. Kim, A. Levchenko, *Biomaterials* **2014**, *35*, 2401.
- [40] J. Padmanabhan, E. R. Kinser, M. A. Stalter, C. Duncan-Lewis, J. L. Balestrini, A. J. Sawyer, J. Schroers, T. R. Kyriakides, *ACS Nano* **2014**, *8*, 4366.
- [41] Z. M. Jin, J. Zheng, W. Li, Z. R. Zhou, *Biosurface and Biotribology* **2016**, *2*, 173.
- [42] A. J. Rahyussalim, A. F. Marsetio, I. Saleh, T. Kurniawati, Y. Whulanza, *Journal of Nanomaterials* **2016**, *2016*, 1.
- [43] M. Hasan, J. Schroers, G. Kumar, *Nano Letters* **2015**, *15*, 963.

- [44] P. Gong, H. Kou, S. Wang, L. Deng, X. Wang, J. Jin, *Journal of Alloys and Compounds* **2019**, *801*, 267.
- [45] T. P. Taylor, M. Ding, D. S. Ehler, T. M. Foreman, J. P. Kaszuba, N. N. Sauer, *Journal of Environmental Science and Health, Part A* **2003**, *38*, 439.
- [46] B. Priyadarshini, M. Rama, Chetan, U. Vijayalakshmi, *Journal of Asian Ceramic Societies* **2019**, *7*, 397.
- [47] B. Sarac, S. Bera, S. Balakin, M. Stoica, M. Calin, J. Eckert, *Materials Science and Engineering: C* **2017**, *73*, 398.
- [48] B. Sarac, S. Bera, F. Spieckermann, S. Balakin, M. Stoica, M. Calin, J. Eckert, *Scripta Materialia* **2017**, *137*, 127.
- [49] T. B. H. Schroeder, J. Houghtaling, B. D. Wilts, M. Mayer, *Adv. Mater.* **2018**, *30*, 1705322.
- [50] Y. Sun, A. Concustell, A. L. Greer, *Nat Rev Mater* **2016**, *1*, 16039.
- [51] J. Ketkaew, W. Chen, H. Wang, A. Datye, M. Fan, G. Pereira, U. D. Schwarz, Z. Liu, R. Yamada, W. Dmowski, M. D. Shattuck, C. S. O'Hern, T. Egami, E. Bouchbinder, J. Schroers, *Nat Commun* **2018**, *9*, 3271.
- [52] N. Liu, G. Liu, A. Raj, S. Sohn, M. D. Morales-Acosta, J. Liu, J. Schroers, *Sci. Adv.* **2021**, *7*, eabi4567.
- [53] L. Gautier, A. Liens, B. Ter-Ovanessian, S. Marcelin, T. Douillard, H. Richard, N. Courtois, J. Chevalier, D. Fabrègue, *Materialia* **2022**, *21*, 101353.
- [54] N. Zheng, G. Wang, L. C. Zhang, M. Calin, M. Stoica, G. Vaughan, N. Mattern, J. Eckert, *J. Mater. Res.* **2010**, *25*, 2271.
- [55] J. Schroers, G. Kumar, T. M. Hodges, S. Chan, T. R. Kyriakides, *JOM* **2009**, *61*, 21.
- [56] M. B. Costa, J. J. Londoño, A. Blatter, A. Hariharan, A. Gebert, M. A. Carpenter, A. L. Greer, *Acta Materialia* **2023**, *244*, 118551.
- [57] G. R. Garrett, M. D. Demetriou, M. E. Launey, W. L. Johnson, *Proc. Natl. Acad. Sci. U.S.A.* **2016**, *113*, 10257.
- [58] D. Weaire, M. F. Ashby, J. Logan, M. J. Weins, *On the use of pair potentials to calculate the properties of amorphous metals*, *Acta Metallurgica*, **1971**.
- [59] W. H. Wang, *Progress in Materials Science* **2012**, *57*, 487.
- [60] L. S. Huo, J. F. Zeng, W. H. Wang, C. T. Liu, Y. Yang, *Acta Materialia* **2013**, *61*, 4329.
- [61] Y. Q. Cheng, A. J. Cao, E. Ma, *Acta Materialia* **2009**, *57*, 3253.
- [62] J. Schroers, *Physics Today* **2013**, *66*, 32.
- [63] M. Niinomi, *Materials Science and Engineering: A* **1998**, *243*, 231.
- [64] K. L. Menzies, L. Jones, *Optometry and Vision Science* **2010**, *87*, 387.
- [65] F. S. M. Ismail, R. Rohanzadeh, S. Atwa, R. S. Mason, A. J. Ruys, P. J. Martin, A. Bendavid, *J Mater Sci: Mater Med* **2007**, *18*, 705.
- [66] J. Y. Lim, M. C. Shaughnessy, Z. Zhou, H. Noh, E. A. Vogler, H. J. Donahue, *Biomaterials* **2008**, *29*, 1776.

- [67] M.-H. Lee, N. Oh, S.-W. Lee, R. Leesungbok, S.-E. Kim, Y.-P. Yun, J.-H. Kang, *Biomaterials* **2010**, *31*, 3804.
- [68] J. Wei, T. Igarashi, N. Okumori, T. Igarashi, T. Maetani, B. Liu, M. Yoshinari, *Biomed. Mater.* **2009**, *4*, 045002.
- [69] J. L. Gallop, *Seminars in Cell & Developmental Biology* **2020**, *102*, 81.
- [70] C. A. Heckman, H. K. Plummer, *Cellular Signalling* **2013**, *25*, 2298.
- [71] M. J. P. Biggs, R. G. Richards, M. J. Dalby, *Nanomedicine: Nanotechnology, Biology and Medicine* **2010**, *6*, 619.
- [72] J.-W. Lee, K.-B. Lee, H. Jeon, H.-K. Park, *ANAL. SCI.* **2011**, *27*, 369.
- [73] F. M. Refaaq, X. Chen, S. W. Pang, *Sci Rep* **2020**, *10*, 20003.
- [74] P.-Y. Wang, H. Thissen, P. Kingshott, *Acta Biomaterialia* **2016**, *45*, 31.
- [75] X. Wang, T. Nakamoto, I. Dulińska-Molak, N. Kawazoe, G. Chen, *J. Mater. Chem. B* **2016**, *4*, 37.
- [76] S. Baar, M. Kuragano, K. Tokuraku, S. Watanabe, *Sci Rep* **2022**, *12*, 16884.
- [77] A. F. J. Janssen, S. Y. Breusegem, D. Larrieu, *Cells* **2022**, *11*, 347.
- [78] P. Rangamani, A. Lipshtat, E. U. Azeloglu, R. C. Calizo, M. Hu, S. Ghassemi, J. Hone, S. Scarlata, S. R. Neves, R. Iyengar, *Cell* **2013**, *154*, 1356.
- [79] K. Rabel, R.-J. Kohal, T. Steinberg, P. Tomakidi, B. Rolauffs, E. Adolfsson, P. Palmero, T. Fürderer, B. Altmann, *Sci Rep* **2020**, *10*, 12810.
- [80] R. V. Vöföly, J. Gallagher, G. D. Pisano, M. Bartlett, S. A. Braybrook, *New Phytol* **2019**, *221*, 540.
- [81] J. Barberi, S. Spriano, *Materials* **2021**, *14*, 1590.
- [82] B. S. Kopf, S. Ruch, S. Berner, N. D. Spencer, K. Maniura-Weber, *Journal of Biomedical Materials Research Part A* **2015**, *103*, 2661.
- [83] M. Kulkarni, A. Mazare, J. Park, E. Gongadze, M. S. Killian, S. Kralj, K. Von Der Mark, A. Iglíč, P. Schmuki, *Acta Biomaterialia* **2016**, *45*, 357.
- [84] E. Jia, X. Zhao, Y. Lin, Z. Su, *Applied Surface Science* **2020**, *529*, 146986.
- [85] S. L. Dallas, L. F. Bonewald, *Annals of the New York Academy of Sciences* **2010**, *1192*, 437.
- [86] A. Jaggessar, H. Shahali, A. Mathew, P. K. D. V. Yarlagadda, *J Nanobiotechnol* **2017**, *15*, 64.
- [87] W. Li, E. S. Thian, M. Wang, Z. Wang, L. Ren, *Adv. Sci.* **2021**, *8*, 2100368.
- [88] R. E. A. McKnight, M. A. Carpenter, T. W. Darling, A. Buckley, P. A. Taylor, *American Mineralogist* **2007**, *92*, 1665.
- [89] S. Jafarkhani, E. Amiri, S. Moazzeni, T. Zohoorian-Abootorabi, M. Eftekhary, S. Aminnezhad, M. Khakbiz, *Colloids and Surfaces A: Physicochemical and Engineering Aspects* **2023**, *675*, 131872.
- [90] H. Jeon, C. G. Simon Jr, G. Kim, *Journal of Biomedical Materials Research Part B: Applied Biomaterials* **2014**, *102*, 1580.

- [91] J. Kim, W.-G. Bae, K.-T. Lim, K.-J. Jang, S. Oh, K.-J. Jang, N. Li Jeon, K.-Y. Suh, J. Hoon Chung, *Materials Letters* **2014**, *130*, 227.
- [92] Z. Liu, J. Schroers, *Nanotechnology* **2015**, *26*, 145301.
- [93] G. Kumar, H. X. Tang, J. Schroers, *Nature* **2009**, *457*, 868.

Publication II – Supporting Information

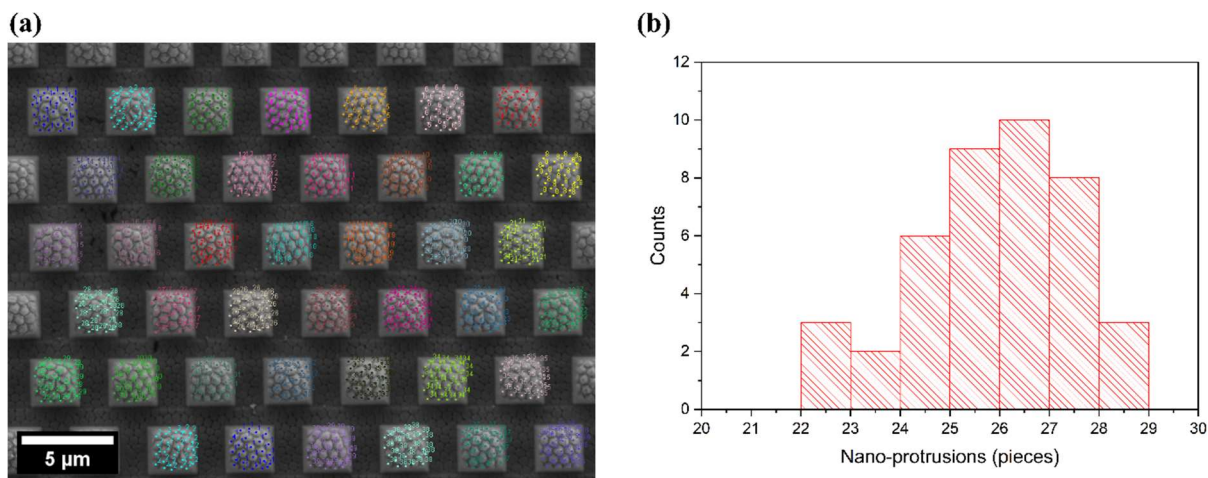


Figure S1: Nano-protrusions on square micro-protuberances for the hierarchical structure: (a) Counts via ImageJ (Fiji 1.54d). (b) Histogram of counting results.

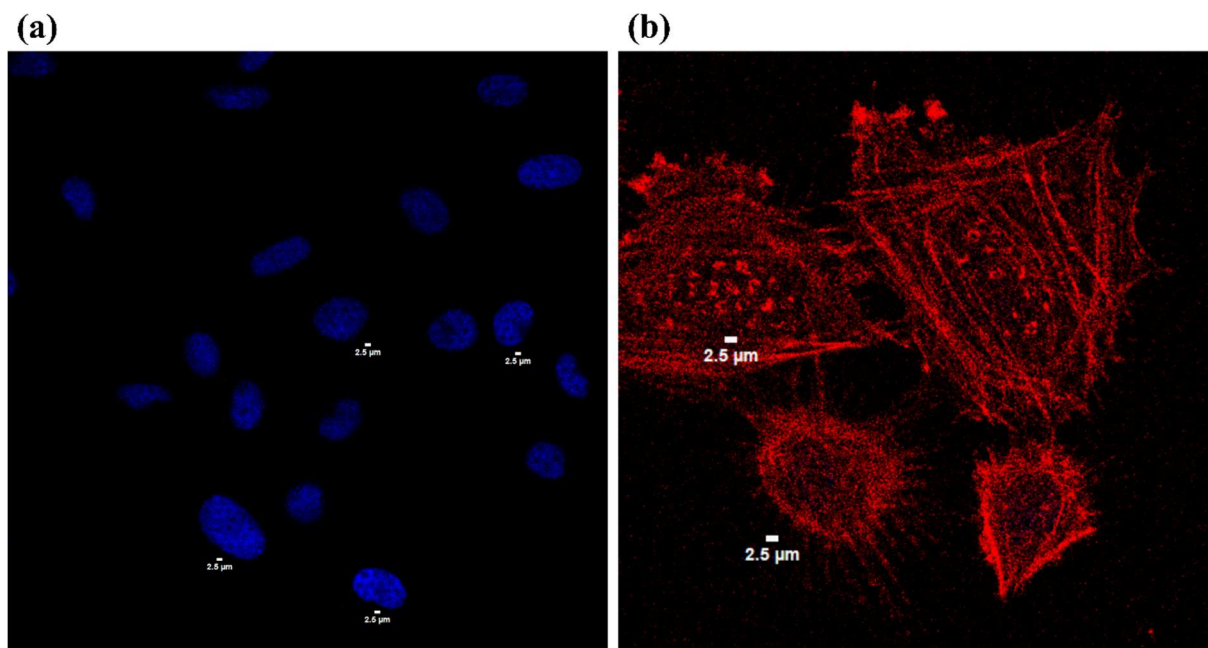


Figure S2: CLSM images of Saos-2 cells on the micro-patterned sample: (a) Spots with weak fluorescence signal (black spots) were deformations of the nucleus due to the micro-pattern. (b) Some cells develop filopodia parallel to each other to align with the direction of the micro-pattern.

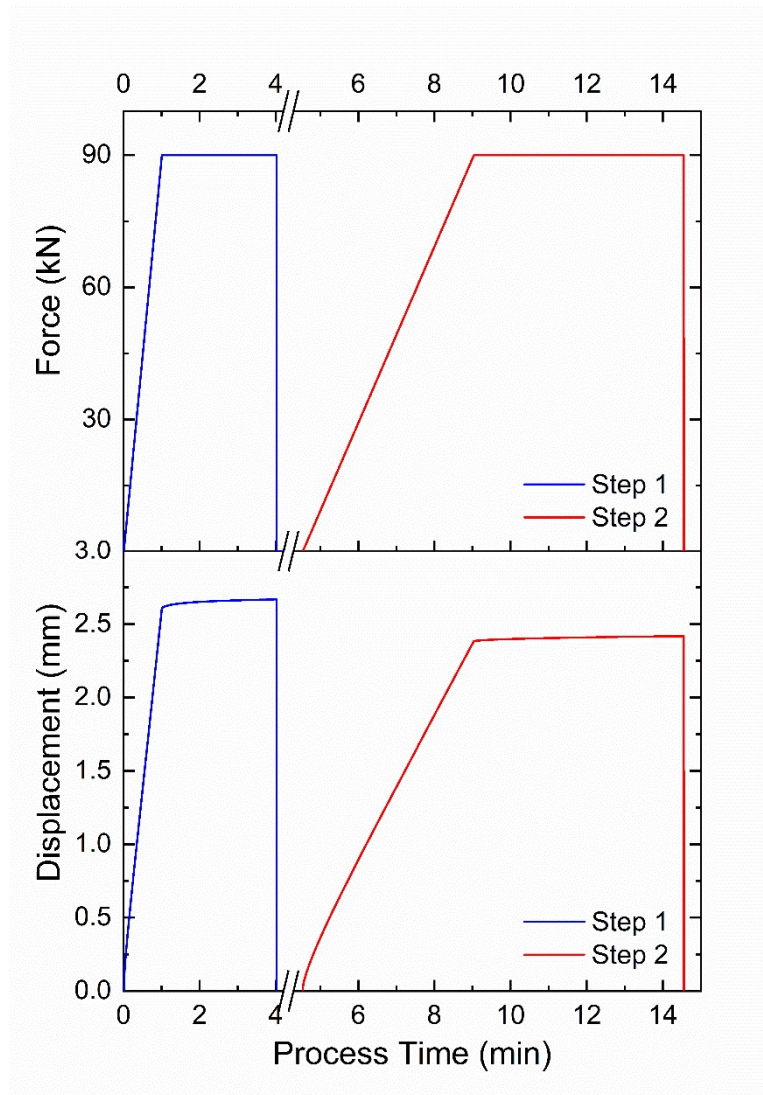


Figure S3: Record of the process parameters (applied force and displacement) for the thermoplastic forming (TPF) process of the hierarchical structures. The displacement includes the thermal expansion of the compression test machine.

E. Publication III

Nano-Patterned Pt-Based Bulk Metallic Glass Electrocatalysts with *In-Situ* Copper Oxide Foam for Enhanced Hydrogen Evolution

Fei-Fan Cai^{1,2}, Baran Sarac², Adnan Akman³, Juan José Londoño^{1,4}, Selin Gümrükcü^{2,5},
Lukas Schweiger¹, Martin Hantusch³, Jan Schroers⁶, Andreas Blatter⁴, Annett Gebert³,
Florian Spieckermann¹, Jürgen Eckert^{1,2}

¹ Department of Materials Science, Chair of Materials Physics, Montanuniversität Leoben

² Erich Schmid Institute of Materials Science, Austrian Academy of Sciences

³ Leibniz Institute for Solid State and Materials Research

⁴ Research and Development Department, PX Services

⁵ Department of Chemistry, Istanbul Technical University

⁶ Department of Mechanical Engineering and Materials Science, Yale University

Preprint available in *arXiv* (<https://doi.org/10.48550/arXiv.2406.14079>)

Manuscript submitted to *ACS Nano*

Keywords

Metallic glass, Thermoplastic forming, Platinum alloys, Electrocatalysts, Hydrogen evolution reaction, Dynamic bubble templating

Corresponding author

Florian Spieckermann, florian.spieckermann@unileoben.ac.at, Department of Materials Science, Chair of Materials Physics, Montanuniversität Leoben, Jahnstraße 12, A-8700 Leoben, Austria

Fei-Fan Cai, f.cai@stud.unileoben.ac.at, Erich Schmid Institute of Materials Science, Austrian Academy of Sciences, Jahnstraße 12, A-8700 Leoben, Austria

Abstract

Hydrogen is a promising energy carrier for replacing fossil fuels, and hydrogen production via hydrogen evolution reaction (HER) is an environmentally friendly option if electrocatalysts with low overpotentials and long-term stability are used. In this work, the electrocatalytic performance of Pt_{57.5}Cu_{14.7}Ni_{5.3}P_{22.5} bulk metallic glass (BMG) with flat, micro-patterned, and nano-patterned surfaces for HER in 0.5 M H₂SO₄ is studied. The nano-patterned Pt-BMG demonstrates outstanding long-term stability and self-improving behavior with a final overpotential of 150 mV and a Tafel slope of 42 mV dec⁻¹ after 1000 linear sweep voltammetry (LSV) cycles, which is respectively 42% and 37% lower than in the first LSV cycle. X-ray photoelectron spectroscopy (XPS) and Auger electron spectroscopy (AES) indicate the formation of a layer of CuO/Cu₂O foam deposited on top of the nano-patterned surface during the stability test of 1000 LSV cycles. A three-step process is proposed to explain the formation of Cu_xO foam via dynamic hydrogen bubble templating (DHBT) electrodeposition from Cu dissolution of the Pt-BMG without using copper salt. This work provides a method to create Cu_xO foams that could be used for various applications. Moreover, nano-patterned BMGs with DHBT deposition offer a feasible strategy to synthesize metal or metal-oxide foams.

1. Introduction

Energy is an inseparable part of modern life, and it is required to perform virtually all human activities, from personal devices to the socio-economic development of a country.¹⁻³ Hydrogen (H₂) emerges as a viable energy carrier for both storage and transportation due to its notable benefits, including high energy density (140 MJ/kg), versatile applicability, and zero carbon emissions if produced by renewable energy sources.^{1,3-6} For efficient and sustainable hydrogen production, the hydrogen evolution reaction (HER) from water electrolysis is the most feasible option.⁷⁻¹¹ However, a highly active and long-lasting catalyst is essential to accelerate the production of hydrogen gas by HER.¹² Pt-based materials have been proven to be the most efficient catalysts for HER in acidic electrolytes, yet their high cost, poor stability, and scarcity severely limit their wide spread utilization.^{8,13-15}

Dynamic hydrogen bubble templating (DHBT) electrodeposition is a technique that uses the evolving hydrogen bubbles in HER as a dynamic template to synthesize porous metal foams.^{16,17} During DHBT electrodeposition, metal electrodeposition and hydrogen evolution happen simultaneously at a cathode with a high overpotential. Consequently, hydrogen bubbles

act as a dynamic template, obstructing metal ion–cathode contact, so that metal ions can only be deposited between bubbles, creating porous metal structures.^{16,17}

Bulk metallic glasses (BMGs) have unique mechanical, physical, and chemical properties compared to crystalline alloys, thanks to their disordered atomic structure.^{12,18–20} BMGs can be shaped and patterned via thermoplastic forming (TPF) which is based on viscous flow in their supercool liquid region (SCLR).^{21–25} Noble metal-based BMGs, such as Pt- and Pd-based BMGs, have been used in jewelry and implant applications.^{18,21} For HER applications, BMGs could be a strategy to alleviate the cost issues of noble elements in the catalysts by forming alloys with other inexpensive metals.^{8,25} Previous studies have revealed that Pd-based BMG catalysts, such as nano-structured Pd_{40.5}Ni_{40.5}Si_{4.5}P_{14.5} BMG and Pd₄₀Ni₁₀Cu₃₀P₂₀ MG ribbons, have two unusual characteristics: (i) a self-stabilizing behavior under long-term static overpotentials and (ii) an improved activity as the number of cyclic voltammetry (CV) cycles increases due to selective dealloying.^{9,26–28} These characteristics of Pd-based BMG catalysts are beneficial compared to the deteriorating activity found for polycrystalline Pd-alloys.^{9,12,26,28–32} Most electrocatalytic research on Pt-based BMGs focuses on hydrogen oxidation reactions for fuel cells.^{12,23,24,33} The puzzle of Pt-based BMGs for HER in hydrogen production is still unexplored.

This work explores the electrocatalytic performance of Pt_{57.5}Cu_{14.7}Ni_{5.3}P_{22.5} BMG for hydrogen production upon HER. Pt_{57.5}Cu_{14.7}Ni_{5.3}P_{22.5} BMG specimens with flat, micro-patterned, and nano-patterned surfaces were created through TPF. Superior electrocatalytic properties of nanorod-patterned Pt-BMG were observed in linear sweep voltammetry (LSV), Tafel plots, electrochemical impedance spectroscopy (EIS), and cyclic voltammograms. Furthermore, nanorod-patterned Pt-BMG shows a remarkable improvement as the number of LSV cycles increases in the stability tests. Scanning electron microscopic (SEM) images, X-ray photoelectron spectroscopy (XPS), and Auger electron spectroscopy (AES) reveal that a layer of CuO/Cu₂O (Cu_xO) foam forms after 1000 cycles, covering the Pt_{57.5}Cu_{14.7}Ni_{5.3}P_{22.5} nano-patterns. A three-step process is proposed to explain the formation of the Cu_xO foam without using copper salt via DHBT electrodeposition from the Cu dissolution of Pt-BMG. Overall, our results reveal that nano-structured Pt-based BMG opens a new possibility of creating high-efficiency and long-term stability electrocatalysts for hydrogen generation.

2. Materials and Methods

2.1. Casting of Pt_{57.5}Cu_{14.7}Ni_{5.3}P_{22.5} BMG

Pt_{57.5}Cu_{14.7}Ni_{5.3}P_{22.5} BMG was produced via induction-melting and tilt-casting. High-purity elements (> 99.95%) were used to alloy a feedstock of Pt_{57.5}Cu_{14.7}Ni_{5.3}P_{22.5} (Pt-BMG) in an induction furnace, where the phosphorus losses due to evaporation were minimal. The feedstock was cast into a Pt-BMG rod with 6 mm diameter and 100 mm length by tilt-casting into a copper mold. No fluxing chemicals were added, and all melting and casting processes were carried out in a high-purity argon protective environment. The as-cast rod was cut into disks with 0.8 mm thickness. The disks from the bottom, middle, and top sections of the as-cast rod were characterized by X-ray diffraction (XRD) using a Bruker D2 Phaser diffractometer with Co K α radiation ($\lambda = 0.17889$ nm) to prove the amorphous structure of the whole as-cast rod. No crystallinity was detected in any of the Pt-BMG disks. The disks were ground and mirror-polished to a thickness of roughly 0.7 mm to eliminate potential surface oxidation and to guarantee parallel surfaces for TPF processing.

2.2. Thermoplastic Forming of Pt_{57.5}Cu_{14.7}Ni_{5.3}P_{22.5} BMG

The TPF apparatus utilized in this study was inspired by previous work by Schroers et al.^{34,35} The setup is based on a compression machine (Zwick Z100, ZwickRoell GmbH & Co. KG) with ad-hoc components, featuring upper and lower anvils fitted with heating cartridges, a PID controller for process control, and water-cooling circulation to protect the load cells from the heat. A polished Pt_{57.5}Cu_{14.7}Ni_{5.3}P_{22.5} BMG disk with a diameter of 6 mm and a thickness of around 0.7 mm was placed on a template. The Pt-BMG disk was then heated to the SCLR (253 \pm 2°C) and imprinted from the template. Table 1 shows the TPF processing parameters. Pt-BMG samples with different surface topographies of flat, micro-rods, and nano-rods were fabricated using different templates. Flat surfaces served as references and were imprinted using a mirror-polished (roughness less than 1 μ m) stainless steel sheet foil as template. Micro-rods were imprinted using macro-porous silicon templates (Si mold) with 2.5 μ m pore diameter and 4.2 μ m interpore distance (SmartMembranes GmbH). Nano-rods were imprinted from nanoporous alumina templates (AAO mold) with 90 nm pore diameter and 125 nm interpore distance (SmartMembranes GmbH). Silicon templates were dissolved in KOH solution (1.5 M), while alumina templates were dissolved in phosphoric acid solution (5% w/w).

Table 6: TPF processing parameters.

Nomenclature	Topography	Max. Force [kN]	Loading Rate [kN min ⁻¹]	Loading Time [Minute]	Holding Time [Minute]
Flat	Flat	5.6 ± 0.2	5.6	1	10
Micropattern (Micro)	Micro-rods	1.4 ± 0.2	0.7	2	4
Nanopattern (Nano)	Nano-rods	5.6 ± 0.2	5.6	1	6

2.3. Electrochemical Measurements

The electrochemical measurements were conducted in a three-electrode glass cell at room temperature. A RE-1BP type Ag/AgCl reference electrode with a ceramic junction filled with 3 M KCl electrolyte (+0.195 V vs. reference hydrogen electrode (RHE)) and a 0.5 mm diameter 23 cm long Pt wire ring were used as reference and counter electrodes, respectively. The samples for the electrochemical measurements were subsequently sonicated in acetone, isopropyl alcohol, and water for 5 minutes each, then dried by hot air. For the micro- and nano-patterned samples, in order to eliminate the signal of the back side, the back side of the samples was painted with varnish. The electrochemical measurements were carried out with a Gamry Interface 1010E Potentiostat/Galvanostat/ZRA. Samples were submerged into 0.5 M H₂SO₄ solution. Once the open circuit potential (OCP) became steady (i.e., maximum of 5 mV change with 1 h), and electrochemical impedance spectroscopy (EIS) was performed at OCP (−0.356 V for flat, −0.428 V for micro-patterned, and −0.306 V for nano-patterned samples, respectively) at an AC amplitude of 0.01 V recorded from 100000 to 0.1 Hz. Electrochemically active surface area (ECSA) of flat, micro, and nanostructured samples were measured by cyclic voltammetry (CV) before and after HER measurements. Subsequently, linear sweep voltammetry (LSV) was conducted with the same electrodes at a scan rate of 0.005 V s⁻¹ with potentials starting from −1.2 V to 0.3 V with a shift in the onset potential of 0.4 V at every cycle until −0.2 V. Among these measurements, LSV from −1.0 V to 0.3 V was displayed, and Tafel slope values were calculated from these curves, which were drawn with respect to the ECSA calculations. The change in ECSA after 1 LSV cycle is extremely small (within error limits of %5) and hence can be ignored. After LSV was finished at the 1st and 1000th cycle, EIS was performed again under the same conditions. Suitable electrochemical circuit models (ECMs) were built and simulated in ZSimpWin V 3.10 (AC Impedance data analysis software). In order to measure the electrochemically active surface area (ECSA), the cyclic voltammetry (CV) scan was done with

the TPF-prepared samples between -0.1 V and 1.2 V (negative to positive) at a scan rate of 0.02 V s^{-1} . Stability measurements were performed on a fresh nano-patterned sample between -0.8 V and 0.2 V at 0.02 V s^{-1} for 1000 LSV cycles. The last measurement was done with 0.005 V s^{-1} to measure the Tafel slope.

2.4. Surface Characterization

Overview images of the sample disks were recorded with confocal laser scanning microscopy (CLSM-Olympus LEXT OLS4100). The surface topographies of Pt-BMG specimens were imaged with 30° tilt via scanning electron microscopy (SEM- Zeiss LEO type 1525) using an In-Lens detector. The cross-section for SEM imaging was prepared using an Ion Milling System (E-3500, Hitachi) at an acceleration voltage of 6 kV and a discharge voltage of 4 kV for 8 hours. The ion-polished cross-sections were investigated by SEM (SEM Magna, Tescan) and energy dispersive X-ray spectroscopy (EDX; XFlash 6-60, Bruker corporation). X-ray photoelectron spectroscopy (XPS) analysis was carried out to investigate the chemical composition of the passive films formed on nano-patterned samples after 1 and 1000 LSV cycles (a flat sample was used as reference). To capture XPS spectra, a PHI 5600 spectrometer (Physical Electronics) with an Al $K\alpha$ monochromatic X-ray source (200 W) was used. For high-resolution scans, a pass energy of 29 eV was applied. A neutralizer was engaged to avoid charging effects. The binding energy is referenced to C1s 284.8 eV. The collected XPS data was fitted using the Unifit software. Auger electron spectroscopy (AES) analysis was implemented on the nano-patterned sample after 1000 LSV cycles for chemical analysis of the surface. The spectrometer (JEOL JAMP 9500F, Tokyo, Japan) is equipped with a hemispherical analyzer and operated with 10 kV and 10 nA electron beam conditions. The samples were sputter-cleaned for 30 seconds prior to the AES measurements to eliminate possible contamination. The argon ions were accelerated with 2.1 keV, leading to an estimated sputter rate of 6 nm/min (calibrated to 100 nm SiO_2 from Si).

3. Results

3.1. Surface Topography of the Pt-BMG Electro-catalysts

The Pt_{57.5}Cu_{14.7}Ni_{5.3}P_{22.5} BMG electro-catalysts with flat, micro-patterned, and nano-patterned surfaces were fabricated via the TPF technique. The resulting samples are shown in Figure 1. The flat samples (Figures 1(a-c)) have a diameter of around 11 ± 0.1 mm and a thickness of 0.16 ± 0.1 mm and a smooth surface topography. The micro-patterned samples (Figures 1(d-f)) have a diameter of about 7.6 ± 0.1 mm and a thickness of 0.20 ± 0.1 mm, with a micro-rod array surface feature. The micro-rods are $2.5 \mu\text{m}$ in diameter with a $4.2 \mu\text{m}$ inter-rod distance, and a $1.7 \mu\text{m}$ gap between each other. The nano-patterned samples (Figures 1(g-i)) have a diameter of around 10.5 ± 0.1 mm and a thickness of 0.17 ± 0.1 mm, and exhibit a nano-rod array surface features. The nano-rods have a diameter of 90 nm, a 125 nm inter-rod distance, and a 35 nm gap between each other.

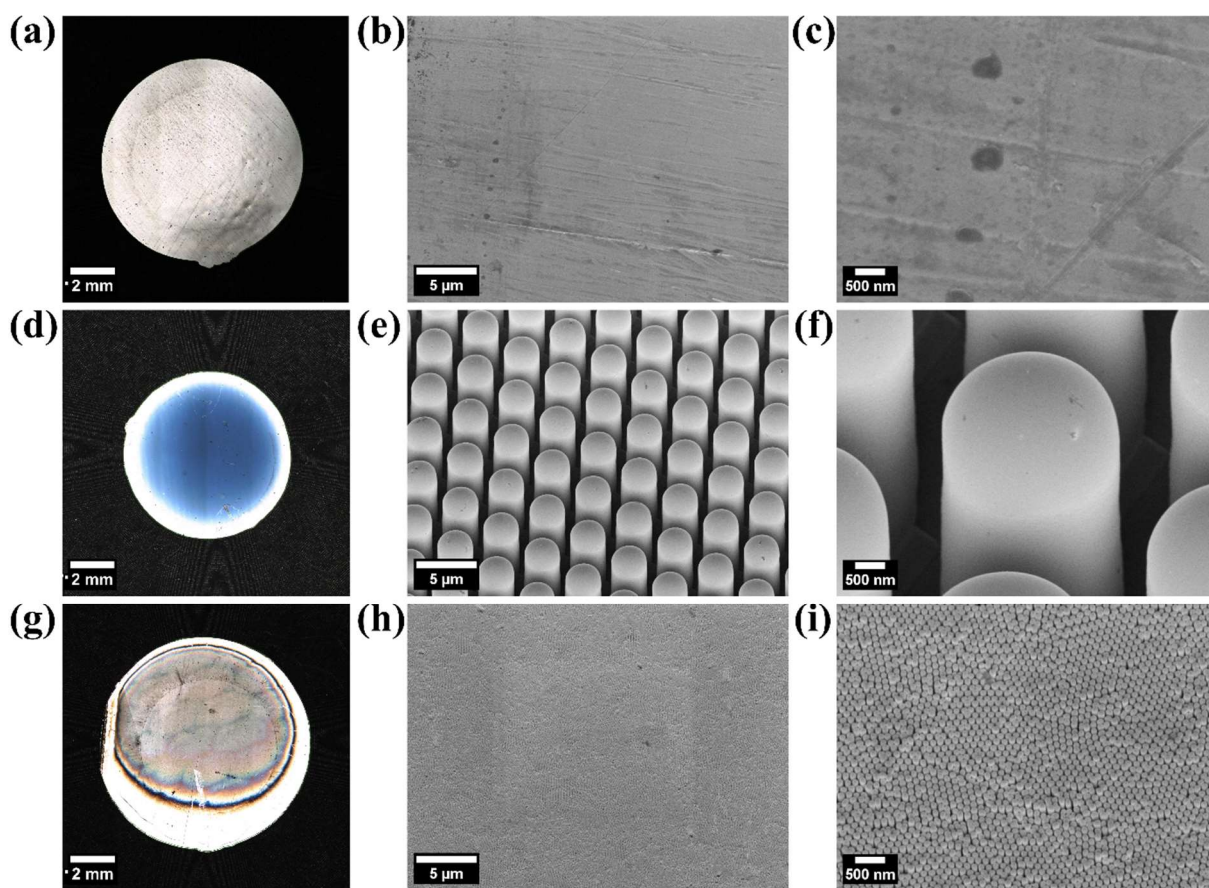


Figure 36: Thermoplastic formed Pt_{57.5}Cu_{14.7}Ni_{5.3}P_{22.5} BMG with (a-c) a flat surface, (d-f) a micro-rod surface, and (g-i) a nano-rod surface. (a)(d)(g) show overview images of the entire BMG disk from CLSM, while (b)(e)(h) and (c)(f)(i) exhibit SEM images at 10k and 50k magnification, respectively.

3.2. Electrochemical Hydrogen Evolution Kinetics

In order to reveal the electrochemical hydrogen evolution kinetics of flat, micro-patterned, and nano-patterned samples, LSV cycles were performed (Figure 2(a)). The ECSA values of flat, micro-patterned, and nano-patterned samples are 1.936 mm^2 , 2.886 mm^2 , and 2.598 mm^2 , respectively. Based on the ECSA calculations, the overpotential E (V vs. RHE) required to deliver a current density of $J = -10 \text{ mA cm}^{-2}$ for the flat, micro-patterned, and nano-patterned samples is -0.48 V , -0.37 V , and -0.30 V , respectively. All samples reached chemical equilibrium close to 0 mA cm^{-2} at $\sim -0.1 \text{ V}$. Compared to the flat samples ($145 \pm 2 \text{ mV dec}^{-1}$), the Tafel slopes determined from the relatively straight region of the cathodic region evidence a decrease for the micro-patterned samples ($86 \pm 2 \text{ mV dec}^{-1}$), as shown in Figure 2(b). The Tafel slope further decreases to $67 \pm 1 \text{ mV dec}^{-1}$ for the nano-patterned samples. This reveals that a smaller overpotential range is needed to change the current density by one order of magnitude (decade), confirming an acceleration of the hydrogen evolution reaction.^{36,37}

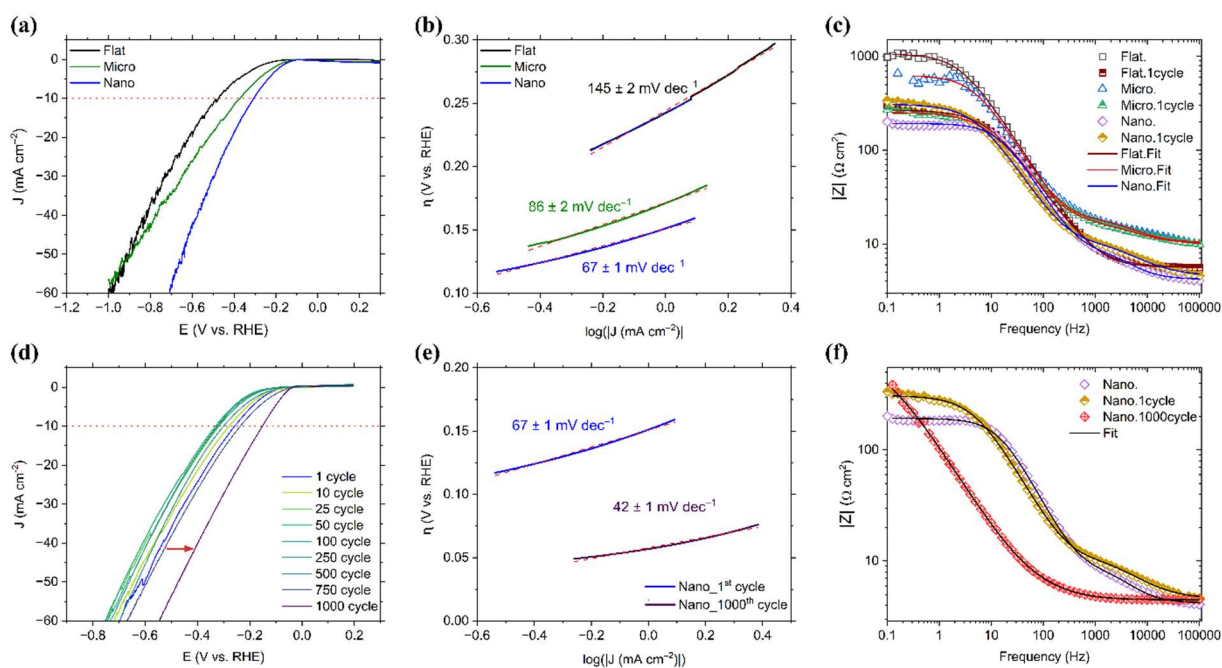


Figure 37: Results of electrochemical studies of $\text{Pt}_{57.5}\text{Cu}_{14.7}\text{Ni}_{15.3}\text{P}_{22.5}$ BMG electrocatalysts in $0.5 \text{ M H}_2\text{SO}_4$ electrolyte: (a) LSV of the flat, micro-patterned and nano-patterned samples, and (b) their corresponding Tafel curves. (c) The Bode magnitude plot of the samples before and after 1 cycle LSV. (d) Electrochemical cycling performance tests for 1000 cycles. (e) The Tafel curves of the nano-patterned sample in the 1st and 1000th cycle. (f) The Bode magnitude plot of nano-patterned samples between fresh (Nano.), one cycle (Nano.1cycle) and 1000th cycle (Nano.1000cycle) states.

The stability of the electrodes can be measured using electrochemical cycling performance tests. The nano-patterned samples were selected due to their lowest Tafel slope and smallest absolute overpotential for HER. Figure 2(d) depicts the evolution of the LSV curves of the nano-patterned samples under 1000 cycles. Up to 50 cycles, the absolute overpotential $|E|$ increases slightly. However, after this point, the absolute overpotential $|E|$ decreases significantly for 1000 cycles, corresponding to the overpotential required to achieve a current density of $J = -10 \text{ mA cm}^{-2}$ shifts from -0.26 V at the 1st cycle to -0.15 V at the 1000th cycle. The ECSA values increased from 1.984 mm^2 to 3.247 mm^2 after 1000 LSV cycles. The decrease in the absolute overpotential also affects the Tafel slopes (Figure 2(e)), which vary from $67 \pm 1 \text{ mV dec}^{-1}$ to $42 \pm 1 \text{ mV dec}^{-1}$. These remarkable small values are comparable to the benchmark materials in HER electrocatalysis (Table S1).³⁸⁻⁴⁰

The nano-patterned Pt-BMG shows a self-improvement behavior in electrocatalytic performance after 1000 LSV cycles. Additional stability tests for 200 LSV cycles (with samples positioned horizontally) were conducted to compare the self-improvement behavior of flat, micro-patterned, and nano-patterned Pt-BMGs. Figure S1 shows that after 200 LSV cycles, only the nano-patterned sample has the absolute overpotential $|E|$ decreased by 8% for $J = -10 \text{ mA cm}^{-2}$. In contrast, the absolute overpotential $|E|$ of the flat and micro-patterned samples increases by 41% and 19%, respectively. Therefore, nano-patterned Pt-BMGs outperform their flat and micro-patterned counterparts regarding lower absolute overpotential, smaller Tafel slope value, and long-term stability for HER applications.

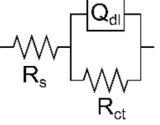
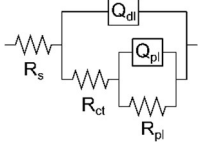
The Bode magnitude plot in Figure 2(c) shows distinct differences before and after the first LSV cycle. For flat and micro-patterned samples, decreases in the magnitude $|Z|$ at the mid-to-low frequency range ($<1000\text{Hz}$) are observed. Interestingly, for the nano-patterned samples, the magnitude $|Z|$ at the near-DC range ($<10 \text{ Hz}$) increases after the first LSV cycle. However, in Figure 2(f), the magnitude $|Z|$ of the 1000th cycle (Nano.1 cycle) is lower than fresh (Nano.) and one cycle (Nano.1 cycle) states, which is the case for almost the entire overall frequency range, yet approaching the one cycle state at the lowest frequency.

3.3. Analysis of an Equivalent Circuit Model (ECM) from EIS Measurements

The EIS data from Figure 2(c, f) were further fitted by a R(QR) equivalent circuit model (ECM) for the flat samples and by a R(Q(R(QR))) ECM for the micro- and nano-patterned samples (Table 2). The R(QR) model for the flat samples includes a solution resistance R_s , a charge

transfer resistance R_{ct} , and a constant phase element (CPE) Q_{dl} for the double-layer capacitance. Besides R_s , R_{ct} , and Q_{dl} , the R(Q(R(QR))) model for the micro- and nano-patterned samples adds a patterned layer CPE Q_{pl} and a patterned layer resistance R_{pl} to enhance the fit quality as well as to analyze the influence of surface modifications due to patterning. It is worth noting that CPE is used to account for the non-ideal behavior of the charged interface.^{41,42} The impedance of CPE is defined as $Z_{CPE} = 1/Y_0(j\omega)^n$, where Y_0 is CPE parameter and n is CPE exponent.⁴³ Hence, $Q_{dl}-Y_0$ and $Q_{dl}-n$ are the CPE parameter and the CPE exponent of the double-layer, respectively. $Q_{pl}-Y_0$ and $Q_{pl}-n$ are the CPE parameter and the CPE exponent of the patterned layer, respectively.

Table 7: ECM of the samples before and after LSV cycles. R_s : solution resistance, $Q_{dl}-Y_0$: constant phase element (CPE) parameter of the double-layer, $Q_{dl}-n$: CPE exponent of the double-layer, R_{ct} : charge transfer resistance, $Q_{pl}-Y_0$: CPE parameter of the patterned layer, $Q_{pl}-n$: CPE exponent of the patterned layer, R_{pl} : resistance of the patterned layer, χ^2 : chi-squared.

Sample	Circuit Model	R_s ($\Omega \text{ cm}^2$)	$Q_{dl}-Y_0$ ($\text{S s}^n \text{ cm}^{-2}$)	$Q_{dl}-n$ (-)	R_{ct} ($\Omega \text{ cm}^2$)	$Q_{pl}-Y_0$ ($\text{S s}^n \text{ cm}^{-2}$)	$Q_{pl}-n$ (-)	R_{pl} ($\Omega \text{ cm}^2$)	χ^2
Flat.		5.6	2.2×10^{-5}	0.87	1064	-	-	-	2.1×10^{-3}
Flat. 1cycle		5.7	3.8×10^{-5}	0.81	263	-	-	-	1.3×10^{-3}
Micro.		10.3	7.0×10^{-6}	0.91	808	2.9×10^{-6}	0.83	10.4	9.2×10^{-3}
Micro. 1cycle		9.9	1.4×10^{-5}	0.82	236	6.8×10^{-6}	0.76	9.0	1.1×10^{-3}
Nano.		4.2	8.5×10^{-6}	0.92	182	5.0×10^{-6}	0.88	6.6	1.8×10^{-3}
Nano. 1cycle	4.5	1.5×10^{-5}	0.89	299	1.4×10^{-5}	0.73	8.1	9.5×10^{-4}	
Nano. 1000 cycle	4.8	1.0×10^{-3}	0.71	649	1.3×10^{-3}	0.79	7.5	1.4×10^{-3}	

As illustrated in Figure 2(c, f), the fitting curves exhibit a high degree of correlation with the Bode magnitude plots derived from the EIS data within the measured frequency range. The solution resistance R_s deviates very slightly, and the values are negligible, confirming that the system is mainly influenced by the electrochemical reactions. For the double-layer capacitance Q_{dl} , there is an increase in the CPE parameter $Q_{dl}-Y_0$ for all the samples, whereas the CPE exponent $Q_{dl}-n$ decreases slightly after HER. The significant decreases in the charge transfer

resistance R_{ct} for the flat and micro-patterned samples dominate their decreases in the magnitude of the impedance in Figure 2(c).

The patterned layer CPE Q_{pl} in the circuit reflects the response of the micro- and nano-patterns. The CPE parameter $Q_{pl}-Y_0$ of the micro-patterns increases significantly with a dramatic decrease in the relevant CPE exponent $Q_{pl}-n$. R_{pl} varies slightly, but the values are generally quite low, revealing that electron transfer happens extremely fast on such patterned surfaces.

Regarding the nano-patterned samples, especially after 1000 cycles, $Q_{dl}-Y_0$ and $Q_{pl}-Y_0$ increase by two orders of magnitude after 1000 LSV cycles, which could be attributed to the ion accumulation. The notable decrease in $Q_{dl}-n$ implies a substantial deviation from ideal capacitive behavior. R_{ct} increases by more than twofold, suggesting increased difficulty for ions to cross the electrode-electrolyte interface. These observations provide support for the subsequent conclusion that a porous layer has formed on top of the Pt-BMG nanorods after 1000 LSV cycles.

3.4. Surface Characterization After 1000 Cycles

As shown in Figure 3, the surfaces of the nano-patterned samples were characterized after 1 and 1000 LSV cycles by multiple complementary methods to find the reason for the improved electrocatalytic performance. X-ray photoelectron spectroscopy (XPS) allows for the analysis of the elemental chemical states on the material surface. The Pt4f spectrums are revealed in Figure 3(a), where sputter-cleaned and untreated Pt foils are provided as references for the Pt-metal and Pt-oxide, respectively. The Pt-metal has a characteristic doublet at ~ 71 and ~ 74 eV, while Pt-oxide has a second doublet at ~ 72 and ~ 75 eV.^{23,44} Hence, the Pt in the Pt-BMG after 1 LSV cycle is in a metallic state, similar to the sputter-cleaned Pt foil, and the slightly different FWHMs are due to the more heterogeneous environment in the BMG compared to the pure metal. Interestingly, no Pt signal is detected on the BMG surface after 1000 LSV cycles.

Regarding the Cu2p spectra, it has been reported that Cu-metal and Cu^+ have signals at ~ 932 and ~ 952 eV, whereas Cu^{2+} has signals at ~ 934 and ~ 954 eV.^{17,45-47} As shown in Figure 3(b), the BMG surfaces after both 1 LSV cycle and 1000 LSV cycles show prominent signals associated with Cu-metal/ Cu_2O (at ~ 932 and ~ 952 eV) and CuO (at ~ 934 and ~ 954 eV) while more substantial satellite peaks indicating a mixture of CuO and $Cu(OH)_2$ are found for the sample after 1000 cycles. It is worth noting that the Cu2p signals for Cu_2O or Cu-metal are

challenging to distinguish in this case. Generally, the Cu content is higher after 1000 cycles than after 1 cycle, and no Pt is detected after 1000 cycles. Even after 1 LSV cycle, Ni and P signals were not detected from XPS on the surface of the flat and the nano-patterned Pt-BMGs. AES was used to clarify the composition of the surface of the nano-patterned Pt-BMG after 1000 LSV cycles. Figure S2(a) provides a representative SEM image with markers of the local AES probing areas, and Figure S2(b) displays the spectra of Pt, Cu, C, and O. The forming surface foam on the nano-patterned Pt-BMG after 1000 LSV cycles contains CuO rather than Pt-BMG, supporting the XPS findings.

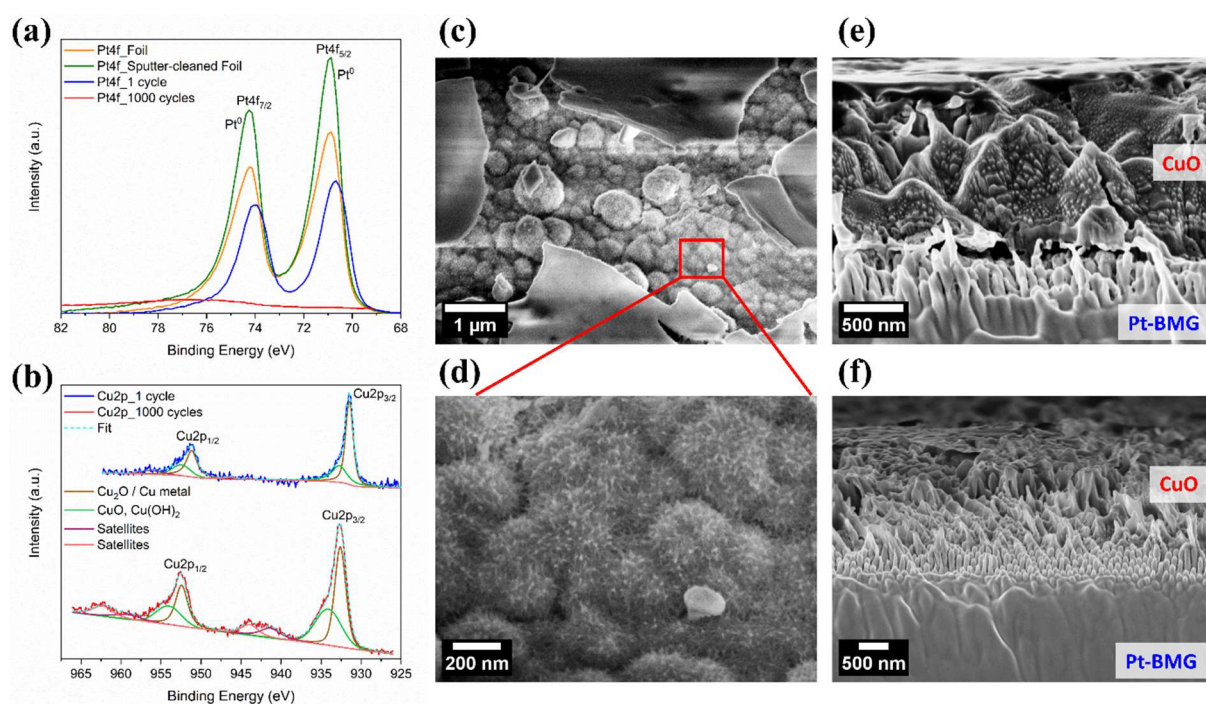


Figure 38: Surface characterization of nano-patterned $\text{Pt}_{57.5}\text{Cu}_{14.7}\text{Ni}_{15.3}\text{P}_{22.5}$ BMG after 1000 cycles: (a)(b) XPS spectra of (a) Pt4f and (b) Cu2p. (c)(d) SEM images of the top view where (d) is the zoomed-in view of the dandelion-like CuO in (c). (e)(f) SEM images of the cross-section view showing dandelion-like CuO and smooth islands like CuO in (d) and CuO nanosheets in (e).

The surface topography of nano-patterned Pt-BMG changes dramatically after 1000 LSV cycles, as displayed in Figure 3(c). The Pt-BMG nanorods shown in Figure 1(i) are covered by CuO/Cu₂O with smooth island-like and dandelion-like topographies. The dandelion-like topography is composed of CuO/Cu₂O with fur-like structures, leading to a porous structure, as revealed in Figure 3(d). Due to the high corrosion resistance of Pt in the electrolyte used, it is unlikely that the Pt-BMG nanorods dissolved in the electrolyte during the stability test. Hence, the ion-polished cross-section of the sample was inspected by SEM (illustrated in Figures 3(d-e)), revealing that an about 1 μm thick layer of CuO/Cu₂O foam forms on top of the Pt-BMG

nanorods. Several agglomerated CuO particles with only a few microns in size form above the deposited layer (Figure S3). The following topographies were found for the deposited CuO/Cu₂O foam: (1) Smooth island-like CuO in Figure 3(c), (2) dandelion-like CuO in Figure 3(d), and (3) CuO nanosheets in Figure 3(e).

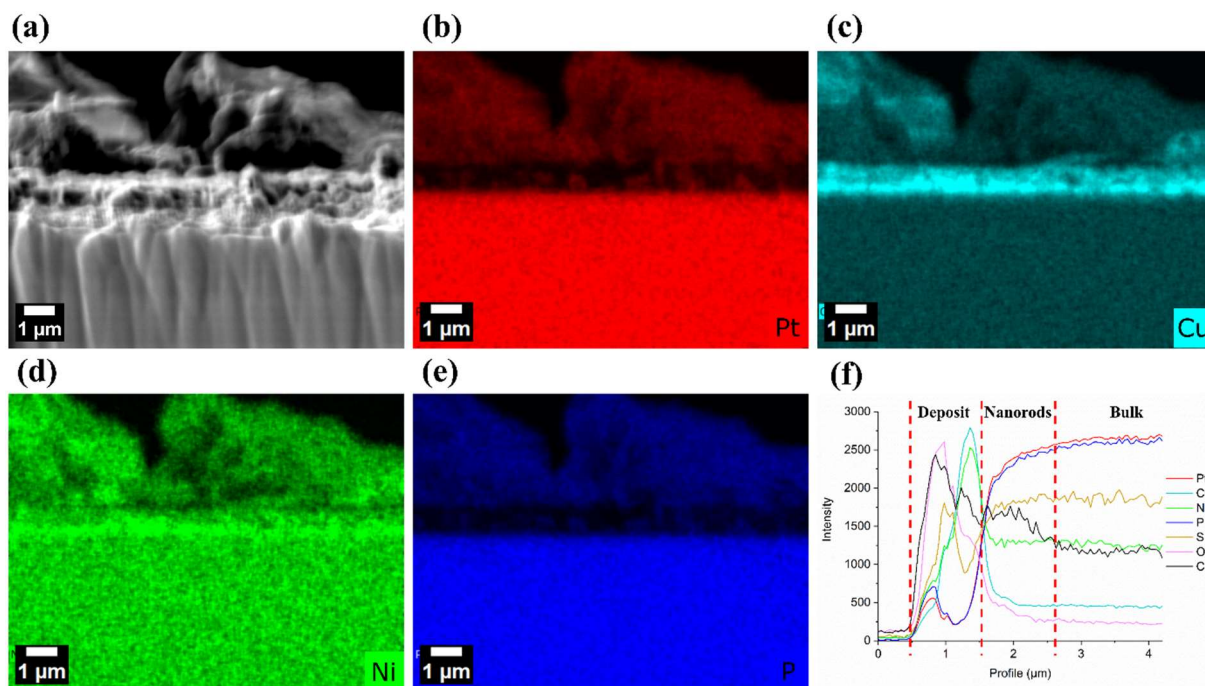


Figure 39: EDX elemental mapping of the cross-section of the nano-patterned Pt-BMG after 1000 LSV cycles. (a) The representative SEM image. (b-e) Elemental mapping of (b) Pt, (c) Cu, (d) Ni, and (e) P. (f) EDX line scan profile of (a).

The cross-section and the related EDX elemental distributions of the nano-patterned Pt-BMG after 1000 LSV cycles are shown in Figure 4. The EDX mapping confirms that the newly deposited layer mainly comprises Cu, as illustrated in Figure 4(c). It is worth noting that the elemental distribution also shows high Ni contents in the deposited layer, which is an artifact of the overlapping spectrum with Cu (Figure 4(d)). In Figure 4(f), the line scan profile of the cross-section reveals that the newly deposited layer has a thickness of around 1 μm. The upper deposit layer is mainly composed of C and O, which can be attributed to carbon contamination from hydrocarbon adsorption of the atmosphere. In contrast, the lower deposit layer mainly consists of Cu, which belongs to the CuO/Cu₂O layer identified by XPS and AES analysis.

4. Discussion

The efficiency of HER is higher in an acidic electrolyte because of an abundance of protons accessible for instantaneous charge and discharge in the acidic medium compared to an alkaline medium.³⁸ However, weak stability and insufficient corrosion resistance of electrocatalysts are usually the main challenges for commercial-scale applications with long-term operation times.^{38,39,48} Therefore, an ideal electrocatalyst for water splitting should have a low overpotential, a low Tafel slope value, a large exchange current density, and long-term stability.^{38,48} The nano-patterned Pt-BMGs have lower overpotential and smaller Tafel slopes than their flat and micro-patterned counterparts. Moreover, in the stability test, the nano-patterned Pt-BMGs demonstrate self-improvement characteristics in electrocatalytic performance after 1000 LSV cycles. Combining the findings of the EIS, XPS, AES, SEM, and EDX analyses indicates that a Cu_xO layer forms on the top of Pt-BMG nanorods after 1000 LSV cycles.

Firstly, the EIS data and ECM fitting of the nano-patterned Pt-BMG show that after 1000 LSV cycles compared to 1 LSV cycle, (1) the CPE parameters of the double-layer ($Q_{dl}-Y_0$) and the patterned layer ($Q_{pt}-Y_0$) increase by two orders of magnitude, and (2) the charge transfer resistance (R_{ct}) increases more than twice, implying the deposition of a porous layer on the surface (Table 2). XPS and AES analyses further show that this extra surface layer mainly consists of Cu_xO from HER. Since the Cu_xO layer is deposited on top of the Pt-BMG and covers the entire surface, surface-sensitive methods like XPS can not detect the Pt signal from the nano-patterned Pt-BMG after 1000 LSV cycles. Finally, the SEM images from the top view and the cross-section reveal that a Cu_xO layer was deposited on top of the Pt-BMG nanorods. The formed Cu_xO layer has a thickness of about 1 μm , and three types of topographies are observed: (1) Smooth islands, (2) dandelion-like structure, and (3) nanosheets. The EDX elemental distribution further confirms carbon contamination (from hydrocarbon adsorption of the atmosphere) of the upper deposition layer and a Cu-rich layer on the lower deposition side. The following sections discuss how the Cu_xO layer was deposited and how it improves the HER.

4.1. How Is Cu_xO Deposited on the Nano-patterned Pt-BMG During LSV Scans?

A three-step mechanism is proposed to explain the formation of a porous Cu_xO layer on the nano-patterned Pt-BMG during LSV cycles (Figure 5): (i) dissolution of Cu from Pt-BMG in the low overpotential section, (ii) re-deposition of Cu foam via dynamic hydrogen bubbles

templating (DHBT) electrochemical deposition in the high overpotential section, (iii) oxidation of the deposited Cu to Cu_xO during the low overpotential section of the LSV cycle.

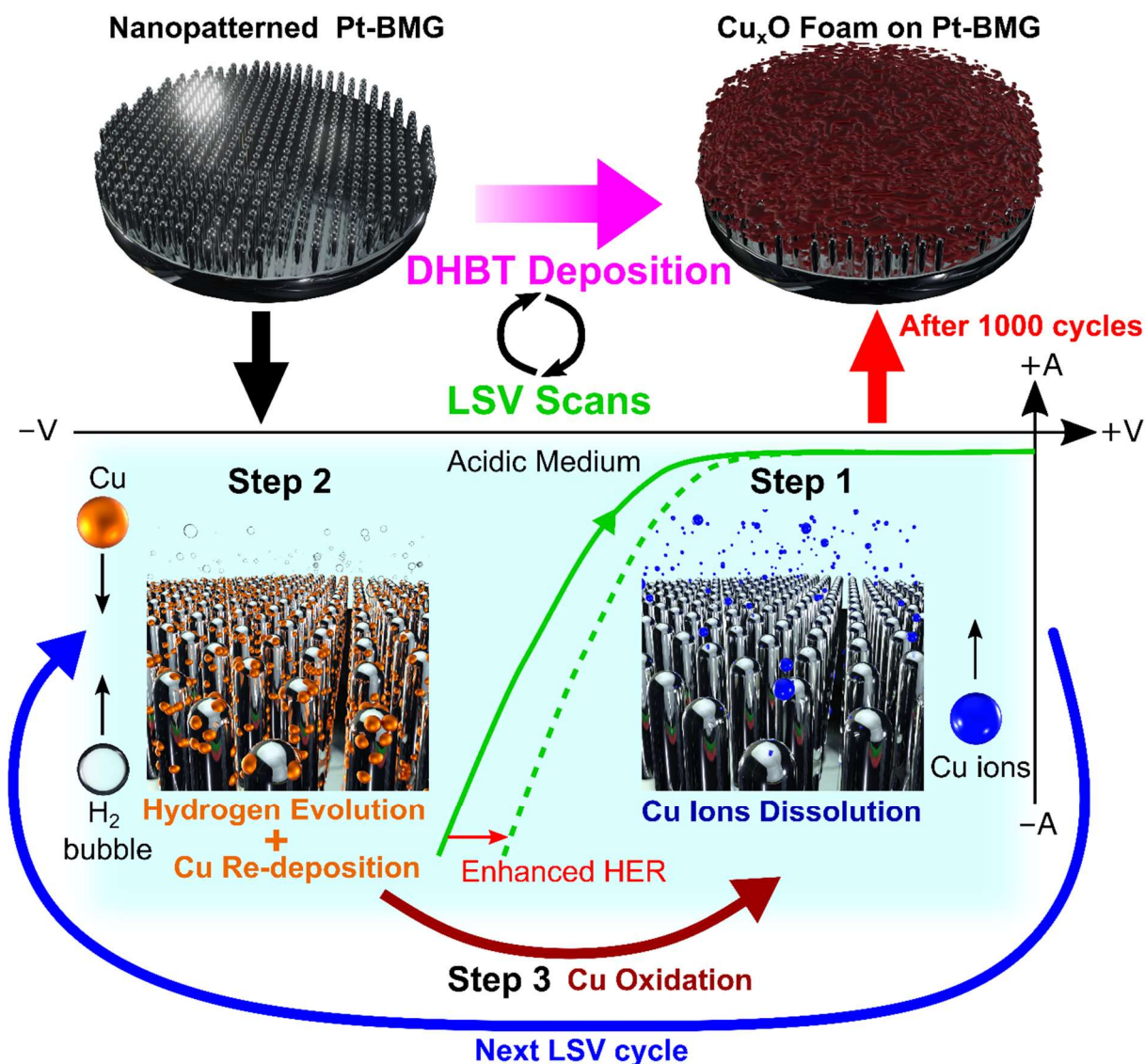


Figure 40: Proposed mechanism of Cu dissolution and $\text{CuO/Cu}_2\text{O}$ foam formation on the nano-patterned Pt-BMG.

In the first step, Cu electro-dissolution occurs from the nano-patterned $\text{Pt}_{57.5}\text{Cu}_{14.7}\text{Ni}_{5.3}\text{P}_{22.5}$ BMG under cathodic polarization conditions during the low overpotential part of LSV scans, providing a source of Cu ions at the surface–electrolyte contact.⁴⁷ According to the conventional Pourbaix diagram of Cu, it is unlikely that Cu will dissolve under our experimental conditions (potential: -0.8 to 0.2 V vs. RHE; electrolyte: 0.5 M H_2SO_4). However, conventional Pourbaix diagrams are restricted to the bulk form of pure metals and have limitations in determining dissolution rates.⁴⁹ For instance, Taylor et al. illustrated a drastically negative shift of the dissolution balance potential in the Pourbaix diagram for Cu nanomaterials because a large number of surface atoms with low coordination in nanomaterials have strong adsorption with

water, oxygen, hydrogen, and hydroxyl ions, which could decrease the ionization potentials of the surface Cu atoms, as shown in Figure S4(a).^{50,51} Therefore, the surface morphology of the nano-patterned samples with 90 nm diameter nano-rods has a higher tendency to dissolve Cu from Pt-BMG into the surrounding electrolyte than the flat and micro-patterned (2.5 μm diameter micro-rods) samples. Moreover, Kreizer et al. reported that in acidic solutions with trace oxygen, Cu dissolution occurs under even milder cathodic polarization conditions (−0.40 to −0.70 V vs. the standard hydrogen electrode (SHE)).^{47,52,53} Because the evolving hydrogen bubbles stir the electrode/interface layer and make the electrode more accessible to oxygen, the Cu dissolution rate is increased by the formation/dissolution of adsorption-complex $\text{Cu}_x\text{O}_{x/2}$.^{47,52,53} Their studies also showed that oxygen exposure is critical for Cu dissolution because of the required intermediate products ($\text{Cu}_x\text{O}_{x/2}$), and Cu dissolution could not occur in deaerated media.⁵³ The synergy effect incorporating (a) the negative shift of the dissolution balance potential from the nano-pattern and (b) the oxygen exposure due to the perturbed electrode/electrolyte layer from the evolved hydrogen bubbles, facilitates the nano-patterned Pt-BMG to leach $\text{Cu}^{2+}_{(\text{aq})}$ ions, providing the source for re-deposition in the next step.

In the re-deposition step, during the high overpotential section of LSV scans, the dissolved $\text{Cu}^{2+}_{(\text{aq})}$ ions are reduced to the metallic form on the electrode ($\text{Cu}^{2+}_{(\text{aq})} + 2e^- \rightarrow \text{Cu}_{(\text{s})}$) while the evolving hydrogen bubbles act as a depositing template. The concept of applying the evolving hydrogen bubbles during HER as a dynamic template to obtain 3D metal foams is known as the dynamic hydrogen bubble template (DHBT) method.^{16,17} When the HER occurs at a cathode with a high overpotential, metal electrodeposition and hydrogen evolution operate simultaneously; thus, hydrogen bubbles interfere with the contact between metal ions and the cathode, and metal ions can only be electrodeposited between bubbles, leading to porous metal structures.^{16,17} It has been reported that the surface topography of electrocatalysts influences the evolution of hydrogen bubbles via its hydrophilicity to water molecules and its aerophobicity to gas bubbles, respectively.^{25,54,55} It is observed during LSV cycles that the nano-patterned Pt-BMG evolves smaller and faster hydrogen bubbles than the flat Pt-BMG (watch supplementary videos). Therefore, the surface pattern of Pt-BMG could be utilized to control the bubble formation rate and the bubble size during HER, thereby allowing further tuning of the pore size and density of the deposited Cu upon DHBT electrodeposition.

Finally, there are two possible reasons why the deposited Cu is oxidized to Cu_xO ($\text{Cu}_2\text{O}/\text{CuO}$). Firstly, during the vigorous HER, proton consumption at the electrode/electrolyte interface is substantial, leading to an increase in local pH.^{47,56} Since copper oxides are stable in alkaline

and neutral solutions, such an electro-dissolution mechanism would encourage the formation of copper oxides on the deposit.⁴⁷ The other reason can be illustrated by a Pourbaix diagram of copper with the dashed line “a”, as shown in Figure S4(b).⁵⁷ At potentials above this dashed line “a” in hydrogen evolution, Cu oxidation could occur ($2\text{Cu} + \text{H}_2\text{O} \rightarrow \text{Cu}_2\text{O} + 2\text{H}^+ + 2\text{e}^-$).⁵⁷ With this Pourbaix diagram, the re-deposited Cu foam can further oxidize when the LSV scan proceeds to the low overpotential section in the stability test.

This three-step process provides a strategy to achieve a porous Cu_xO layer without using copper salt in the plating bath, opening another potential application for BMGs. In principle, any nano-patternable BMG alloy that contains Cu and another element with a higher dissolution potential than Cu can form Cu_xO foams using the proposed three-step process. Hence, future research could focus on investigating more cost-effective BMG systems with high fragility to reduce production costs. Beyond hydrogen evolution applications, it would be interesting to further investigate the porous Cu_xO layer created in this work for other potential applications, such as gas sensing, supercapacitor, photocatalytic, and antibacterial applications.^{46,58–60}

4.2. How Does the Newly Deposited Cu_xO foam Enhance the HER Performance?

The nano-patterned Pt-BMG already shows superior electrocatalytic performance to the flat and micro-patterned Pt-BMGs during the initial LSV scans, as revealed in Figures 1 and S2. It is expected that the Cu_xO layer has not formed yet during the initial LSV scans. Therefore, the superior electrocatalytic performance can be attributed to the surface topography of nano-rods. Nano-topographies have been reported to promote HER via hydrophilicity and aerophobicity.^{25,61,62} Consequently, the nano-patterned surface renders the Pt-BMG more hydrophilic and aerophobic compared with flat and micro-patterned specimens. The hydrophilic and aerophobic surfaces reduce the adhesion between hydrogen bubbles and the material surface, allowing bubbles to escape from the surface with a smaller bubble size.⁶³ This enables rapid departure of the evolved hydrogen bubbles from the catalyst while preventing the bursting of large hydrogen bubbles (watch supplementary videos), which could deteriorate the structural integrity and stability of the catalyst.⁶³ Moreover, hydrophilic surfaces generally possess higher mass transfer efficiency, increasing the possibility of collisions between water molecules and catalytic active sites.⁶³ The zigzag nature of the LSV curves indicates hydrogen bubble formation, growth, and detachment. In Figure 2(a), the flat Pt-BMG displays more prominent zigzags in the LSV curve, indicating significant coalescence of hydrogen bubbles. On the contrary, the nano-patterned Pt-BMG has a smoother LSV curve than the flat Pt-BMG,

implying the evolution of small hydrogen bubbles on the nano-patterned surface. Thus, the nano-patterned surface has improved hydrophilicity and aerophobicity, elevating the turnover frequency of catalytic active sites that contribute to the HER. Further studies regarding bubble formation, growth, and detachment are required.

As the LSV cycles progress during the stability test, the newly deposited Cu_xO foam builds on the nano-pattern of the Pt-BMG, further improving the HER performance. The impressive HER performance is attributed to the porous structures deposited, as discovered by SEM. These structures can strongly improve the ionic diffusion and electron transfer kinetics by increasing the surface area to volume ratio. As a result, the overpotential required to achieve a current density of $J = -10 \text{ mA cm}^{-2}$ decreases by 42%, and the Tafel slope value is reduced by 37%.

Several studies have reported that CuO- and Cu_2O -derived materials exhibit respectable electrocatalytic and photocatalytic properties for HER.^{59,64-69} Other studies based on Pd-based MGs, amorphous TiCuRu alloys for HER, and Pt-BMGs for ethanol oxidation reaction (EOR) show self-stabilizing or self-improvement characteristics in catalytic performance via selective dealloying of Cu.^{23,25,27,70,71} Present work demonstrates that the dissolution of Cu and re-deposition of Cu_xO foam on nano-patterned Pt-BMGs can be a strategy to enhance the catalytic activity and long-term stability for HER, uncovering a new mechanism for improving the durability of catalysts. As shown in Figure 2(d), the electrocatalytic performance improved significantly from 750 to 1000 cycles. The deposited Cu_xO foam exhibits significant self-improvement with increasing LSV cycles. This indicates a potential for hydrogen evolution reaction (HER) applications, necessitating further in-depth studies on the long-term performance of nano-patterned Cu-containing BMGs.

5. Conclusion

This study focuses on the HER activity of flat and patterned $\text{Pt}_{57.5}\text{Cu}_{14.7}\text{Ni}_{5.3}\text{P}_{22.5}$ BMGs in an acidic environment. The results confirm a minimum Tafel slope of $67 \pm 1 \text{ mV dec}^{-1}$ for the nano-patterned BMG. After 1000 LSV cycles of the same sample, the Tafel slope decreases by 37%, with an overpotential reduction of 42%. The HER performance is attributed to a Cu_xO foam which forms on the nano-patterned surface, as confirmed by SEM, XPS, and EDX. This foam increases the surface area-to-volume ratio and provides more active sites, thereby enhancing the ionic diffusion and electron transfer kinetics significantly

A three-step process involving (i) dissolution of Cu from Pt-BMG in the low overpotential section, (ii) re-deposition of Cu foam via dynamic hydrogen bubbles templating (DHBT) deposition in the high overpotential section, and (iii) oxidation of the deposited Cu to Cu_xO , is proposed to explain how the Cu_xO foam forms on the nano-patterned Pt-BMG during the stability test. Metallic glass is utilized in DHBT electrodeposition with the help of nano-patterning to fabricate porous metal-oxide foam without the need for metal salt. The resulting nanostructured catalyst exhibits high HER performance. More possibilities combining metallic glasses, thermoplastic patterning, and dynamic bubble templating as a new strategy for fabricating porous metal-oxide foams and self-improving catalysts still remain to be explored.

Supporting Information

The Supporting Information is available free of charge at XXX.

The Tafel slope and overpotential η at 10 mA cm^{-2} of some reported electrocatalysts for HER; additional stability tests comparing the overpotential η (mV vs. RHE) at $J = 10\text{ mA cm}^{-2}$ of flat, micro-patterned and nano-patterned samples up to 200 LSV cycles; AES analysis of the Nano.1000cycle sample; SEM images of agglomerated CuO particles on top of the deposited CuO layer; modified Pourbaix diagrams for Cu with green arrows marking the experimental condition (PDF)

Acknowledgements

This work was supported by the European Union's Horizon 2020 research and innovation program under the Marie Skłodowska-Curie grant agreement No. 861046 (BIOREMIA-ETN). B.S. J.E. and F.S. acknowledge support from the Austrian Science Fund (FWF), Grant/Award Number: I3937-N36.

References

- (1) Pareek, A.; Dom, R.; Gupta, J.; Chandran, J.; Adepu, V.; Borse, P. H. Insights into Renewable Hydrogen Energy: Recent Advances and Prospects. *Materials Science for Energy Technologies* **2020**, *3*, 319–327. <https://doi.org/10.1016/j.mset.2019.12.002>.
- (2) Filippov, S. P.; Yaroslavl'tsev, A. B. Hydrogen Energy: Development Prospects and Materials. *Russ. Chem. Rev.* **2021**, *90* (6), 627–643. <https://doi.org/10.1070/RCR5014>.
- (3) Abe, J. O.; Popoola, A. P. I.; Ajenifuja, E.; Popoola, O. M. Hydrogen Energy, Economy and Storage: Review and Recommendation. *International Journal of Hydrogen Energy* **2019**, *44* (29), 15072–15086. <https://doi.org/10.1016/j.ijhydene.2019.04.068>.
- (4) Yue, M.; Lambert, H.; Pahon, E.; Roche, R.; Jemei, S.; Hissel, D. Hydrogen Energy Systems: A Critical Review of Technologies, Applications, Trends and Challenges.

- Renewable and Sustainable Energy Reviews* **2021**, *146*, 111180. <https://doi.org/10.1016/j.rser.2021.111180>.
- (5) Zhao, G.; Rui, K.; Dou, S. X.; Sun, W. Heterostructures for Electrochemical Hydrogen Evolution Reaction: A Review. *Adv Funct Materials* **2018**, *28* (43), 1803291. <https://doi.org/10.1002/adfm.201803291>.
- (6) Wang, S.; Lu, A.; Zhong, C.-J. Hydrogen Production from Water Electrolysis: Role of Catalysts. *Nano Convergence* **2021**, *8* (1), 4. <https://doi.org/10.1186/s40580-021-00254-x>.
- (7) Dubouis, N.; Grimaud, A. The Hydrogen Evolution Reaction: From Material to Interfacial Descriptors. *Chem. Sci.* **2019**, *10* (40), 9165–9181. <https://doi.org/10.1039/C9SC03831K>.
- (8) Li, C.; Baek, J.-B. Recent Advances in Noble Metal (Pt, Ru, and Ir)-Based Electrocatalysts for Efficient Hydrogen Evolution Reaction. *ACS Omega* **2020**, *5* (1), 31–40. <https://doi.org/10.1021/acsomega.9b03550>.
- (9) Hu, Y. C.; Wang, Y. Z.; Su, R.; Cao, C. R.; Li, F.; Sun, C. W.; Yang, Y.; Guan, P. F.; Ding, D. W.; Wang, Z. L.; Wang, W. H. A Highly Efficient and Self-Stabilizing Metallic-Glass Catalyst for Electrochemical Hydrogen Generation. *Advanced Materials* **2016**, *28* (46), 10293–10297. <https://doi.org/10.1002/adma.201603880>.
- (10) Lasia, A. Mechanism and Kinetics of the Hydrogen Evolution Reaction. *International Journal of Hydrogen Energy* **2019**, *44* (36), 19484–19518. <https://doi.org/10.1016/j.ijhydene.2019.05.183>.
- (11) Liu, F.; Shi, C.; Guo, X.; He, Z.; Pan, L.; Huang, Z.; Zhang, X.; Zou, J. Rational Design of Better Hydrogen Evolution Electrocatalysts for Water Splitting: A Review. *Advanced Science* **2022**, *9* (18), 2200307. <https://doi.org/10.1002/advs.202200307>.
- (12) Hu, Y.; Sun, C.; Sun, C. Functional Applications of Metallic Glasses in Electrocatalysis. *ChemCatChem* **2019**, *11* (10), 2401–2414. <https://doi.org/10.1002/cctc.201900293>.
- (13) Bhalothia, D.; Krishnia, L.; Yang, S.-S.; Yan, C.; Hsiung, W.-H.; Wang, K.-W.; Chen, T.-Y. Recent Advancements and Future Prospects of Noble Metal-Based Heterogeneous Nanocatalysts for Oxygen Reduction and Hydrogen Evolution Reactions. *Applied Sciences* **2020**, *10* (21), 7708. <https://doi.org/10.3390/app10217708>.
- (14) Hughes, A. E.; Haque, N.; Northey, S. A.; Giddey, S. Platinum Group Metals: A Review of Resources, Production and Usage with a Focus on Catalysts. *Resources* **2021**, *10* (9), 93. <https://doi.org/10.3390/resources10090093>.
- (15) Sealy, C. The Problem with Platinum. *Materials Today* **2008**, *11* (12), 65–68. [https://doi.org/10.1016/S1369-7021\(08\)70254-2](https://doi.org/10.1016/S1369-7021(08)70254-2).
- (16) Arshad, F.; Tahir, A.; Haq, T. U.; Munir, A.; Hussain, I.; Sher, F. Bubbles Templated Interconnected Porous Metallic Materials: Synthesis, Surface Modification, and Their Electrocatalytic Applications for Water Splitting and Alcohols Oxidation. *ChemistrySelect* **2022**, *7* (41), e202202774. <https://doi.org/10.1002/slct.202202774>.
- (17) Gu, Y.; Li, J.; Wang, L.; Xie, M.; Wu, X.; Xie, F.; Ryan, M. P. Template-Free Cu Electrodeposition to Prepare Cu–Micro-Brush Electrodes for Electrochemical CO₂ Reduction. *ChemistrySelect* **2019**, *4* (37), 10995–11001. <https://doi.org/10.1002/slct.201903097>.
- (18) Suryanarayana, C.; Inoue, A. *Bulk Metallic Glasses, Second Edition*; 2018.

- (19) Jiang, R.; Da, Y.; Chen, Z.; Cui, X.; Han, X.; Ke, H.; Liu, Y.; Chen, Y.; Deng, Y.; Hu, W. Progress and Perspective of Metallic Glasses for Energy Conversion and Storage. *Advanced Energy Materials* **2022**, *12* (8), 2101092. <https://doi.org/10.1002/aenm.202101092>.
- (20) Chen, M. A Brief Overview of Bulk Metallic Glasses. *NPG Asia Mater* **2011**, *3* (9), 82–90. <https://doi.org/10.1038/asiamat.2011.30>.
- (21) Londoño, J. J.; Costa, M. B.; Cai, F.-F.; Spieckermann, F.; Levesque, A.; Prades-Rödel, S.; Greer, A. L.; Eckert, J.; Blatter, A. Microalloying as a Strategy to Modulate Antibacterial Ion Release from Metallic Glasses. *Journal of Alloys and Compounds* **2023**, *968*, 172121. <https://doi.org/10.1016/j.jallcom.2023.172121>.
- (22) Sarac, B.; Eckert, J. Thermoplasticity of Metallic Glasses: Processing and Applications. *Progress in Materials Science* **2022**, *127*, 100941. <https://doi.org/10.1016/j.pmatsci.2022.100941>.
- (23) Carmo, M.; Sekol, R. C.; Ding, S.; Kumar, G.; Schroers, J.; Taylor, A. D. Bulk Metallic Glass Nanowire Architecture for Electrochemical Applications. *ACS Nano* **2011**, *5* (4), 2979–2983. <https://doi.org/10.1021/nn200033c>.
- (24) Sekol, R. C.; Kumar, G.; Carmo, M.; Gittleson, F.; Hardesty-Dyck, N.; Mukherjee, S.; Schroers, J.; Taylor, A. D. Bulk Metallic Glass Micro Fuel Cell. *Small* **2013**, *9* (12), 2081–2085. <https://doi.org/10.1002/sml.201201647>.
- (25) Yan, Y.; Wang, C.; Huang, Z.; Fu, J.; Lin, Z.; Zhang, X.; Ma, J.; Shen, J. Highly Efficient and Robust Catalysts for the Hydrogen Evolution Reaction by Surface Nano Engineering of Metallic Glass. *J. Mater. Chem. A* **2021**, *9* (9), 5415–5424. <https://doi.org/10.1039/D0TA10235K>.
- (26) Sarac, B.; Ivanov, Y. P.; Karazehir, T.; Putz, B.; Greer, A. L.; Sarac, A. S.; Eckert, J. Metallic Glass Films with Nanostructured Periodic Density Fluctuations Supported on Si/SiO₂ as an Efficient Hydrogen Sorber. *Chemistry A European J* **2020**, *26* (37), 8244–8253. <https://doi.org/10.1002/chem.202001596>.
- (27) Gao, S.; Jia, J.; Chen, S.; Luan, H.; Shao, Y.; Yao, K. Oxide-Derived Nanostructured Metallic-Glass Electrodes for Efficient Electrochemical Hydrogen Generation. *RSC Adv.* **2017**, *7* (43), 27058–27064. <https://doi.org/10.1039/C7RA02954C>.
- (28) Xu, W.; Zhu, S.; Liang, Y.; Cui, Z.; Yang, X.; Inoue, A.; Wang, H. A Highly Efficient Electrocatalyst Based on Amorphous Pd–Cu–S Material for Hydrogen Evolution Reaction. *J. Mater. Chem. A* **2017**, *5* (35), 18793–18800. <https://doi.org/10.1039/C7TA05314B>.
- (29) Tian, J.; Wu, W.; Tang, Z.; Wu, Y.; Burns, R.; Tichnell, B.; Liu, Z.; Chen, S. Oxygen Reduction Reaction and Hydrogen Evolution Reaction Catalyzed by Pd–Ru Nanoparticles Encapsulated in Porous Carbon Nanosheets. *Catalysts* **2018**, *8* (8), 329. <https://doi.org/10.3390/catal8080329>.
- (30) Wang, S.; Li, N.; Liu, L. Enhanced Hydrogen Generation Performance of Pd-Based Micro/Nano Hierarchical Porous Structure. *Materials Letters* **2018**, *228*, 443–446. <https://doi.org/10.1016/j.matlet.2018.06.090>.
- (31) Sarac, B.; Karazehir, T.; Mühlbacher, M.; Sarac, A. S.; Eckert, J. Electrocatalytic Behavior of Hydrogenated Pd-Metallic Glass Nanofilms: Butler-Volmer, Tafel, and Impedance Analyses. *Electrocatalysis* **2020**, *11* (1), 94–109. <https://doi.org/10.1007/s12678-019-00572-z>.

- (32) Sarac, B.; Karazehir, T.; Yüce, E.; Mühlbacher, M.; Sarac, A. S.; Eckert, J. Porosity and Thickness Effect of Pd–Cu–Si Metallic Glasses on Electrocatalytic Hydrogen Production and Storage. *Materials & Design* **2021**, *210*, 110099. <https://doi.org/10.1016/j.matdes.2021.110099>.
- (33) Hasannaemi, V.; Mukherjee, S. Noble-Metal Based Metallic Glasses as Highly Catalytic Materials for Hydrogen Oxidation Reaction in Fuel Cells. *Sci Rep* **2019**, *9* (1), 12136. <https://doi.org/10.1038/s41598-019-48582-7>.
- (34) Kumar, G.; Tang, H. X.; Schroers, J. Nanomoulding with Amorphous Metals. *Nature* **2009**, *457* (7231), 868–872. <https://doi.org/10.1038/nature07718>.
- (35) Liu, Z.; Schroers, J. General Nanomoulding with Bulk Metallic Glasses. *Nanotechnology* **2015**, *26* (14), 145301. <https://doi.org/10.1088/0957-4484/26/14/145301>.
- (36) Adler, S. B.; Lane, J. A.; Steele, B. C. H. Electrode Kinetics of Porous Mixed-Conducting Oxygen Electrodes. *J. Electrochem. Soc.* **1996**, *143* (11), 3554–3564. <https://doi.org/10.1149/1.1837252>.
- (37) Lyons, M. E. G.; Brandon, M. P. The Oxygen Evolution Reaction on Passive Oxide Covered Transition Metal Electrodes in Aqueous Alkaline Solution. Part 1-Nickel. *International Journal of Electrochemical Science* **2008**, *3* (12), 1386–1424. [https://doi.org/10.1016/S1452-3981\(23\)15531-3](https://doi.org/10.1016/S1452-3981(23)15531-3).
- (38) Raveendran, A.; Chandran, M.; Dhanusuraman, R. A Comprehensive Review on the Electrochemical Parameters and Recent Material Development of Electrochemical Water Splitting Electrocatalysts. *RSC Adv.* **2023**, *13* (6), 3843–3876. <https://doi.org/10.1039/D2RA07642J>.
- (39) Ferriday, T. B.; Middleton, P. H.; Kolhe, M. L. Review of the Hydrogen Evolution Reaction—A Basic Approach. *Energies* **2021**, *14* (24), 8535. <https://doi.org/10.3390/en14248535>.
- (40) Āurovič, M.; Hnát, J.; Bouzek, K. Electrocatalysts for the Hydrogen Evolution Reaction in Alkaline and Neutral Media. A Comparative Review. *Journal of Power Sources* **2021**, *493*, 229708. <https://doi.org/10.1016/j.jpowsour.2021.229708>.
- (41) He, X.-D.; Xu, F.; Li, F.; Liu, L.; Wang, Y.; Deng, N.; Zhu, Y.-W.; He, J.-B. Composition-Performance Relationship of Ni_xCu_y Nanoalloys as Hydrogen Evolution Electrocatalyst. *Journal of Electroanalytical Chemistry* **2017**, *799*, 235–241. <https://doi.org/10.1016/j.jelechem.2017.05.050>.
- (42) Ran, J.; Girardi, L.; Dražić, G.; Wang, Z.; Agnoli, S.; Xia, H.; Granozzi, G. The Effect of the 3D Nanoarchitecture and Ni-Promotion on the Hydrogen Evolution Reaction in MoS₂/Reduced GO Aerogel Hybrid Microspheres Produced by a Simple One-Pot Electrospraying Procedure. *Small* **2022**, *18* (14), 2105694. <https://doi.org/10.1002/sml.202105694>.
- (43) Li, X.-R.; Zhang, Q.-H.; Meng, X.-Z.; Wu, L.-K.; Cao, F.-H. Effect of Pretreatments on the Hydrogen Evolution Kinetics of Pure Titanium Using Impedance and SECM Technologies. *Corrosion Science* **2021**, *191*, 109726. <https://doi.org/10.1016/j.corsci.2021.109726>.
- (44) Wang, J.; Song, Z.; Xu, K.; Liu, M. Rectifying Switching Characteristics of Pt/ZnO/Pt Structure Based Resistive Memory. *J. Nanosci. Nanotech.* **2010**, *10* (11), 7088–7091. <https://doi.org/10.1166/jnn.2010.2758>.

- (45) Ma, X.-X.; Chen, L.; Zhang, Z.; Tang, J.-L. Electrochemical Performance Evaluation of CuO@Cu₂O Nanowires Array on Cu Foam as Bifunctional Electrocatalyst for Efficient Water Splitting. *Chinese Journal of Analytical Chemistry* **2020**, *48* (1), e20001–e20012. [https://doi.org/10.1016/S1872-2040\(19\)61211-9](https://doi.org/10.1016/S1872-2040(19)61211-9).
- (46) Zhou, L.-J.; Zou, Y.-C.; Zhao, J.; Wang, P.-P.; Feng, L.-L.; Sun, L.-W.; Wang, D.-J.; Li, G.-D. Facile Synthesis of Highly Stable and Porous Cu₂O/CuO Cubes with Enhanced Gas Sensing Properties. *Sensors and Actuators B: Chemical* **2013**, *188*, 533–539. <https://doi.org/10.1016/j.snb.2013.07.059>.
- (47) Najdovski, I.; Selvakannan, P.; O’Mullane, A. P. Cathodic Corrosion of Cu Substrates as a Route to Nanostructured Cu/M (M=Ag, Au, Pd) Surfaces. *ChemElectroChem* **2015**, *2* (1), 106–111. <https://doi.org/10.1002/celec.201402259>.
- (48) Zhai, W.; Ma, Y.; Chen, D.; Ho, J. C.; Dai, Z.; Qu, Y. Recent Progress on the Long-Term Stability of Hydrogen Evolution Reaction Electrocatalysts. *InfoMat* **2022**, *4* (9), e12357. <https://doi.org/10.1002/inf2.12357>.
- (49) *Electrochemical and Corrosion Behavior of Metallic Glasses*; MDPI, 2021. <https://doi.org/10.3390/books978-3-03943-723-8>.
- (50) Zhang, B. Electrochemical Behaviors and Applications of Copper-Based Nanostructures, Nanyang Technological University, 2018. <https://doi.org/10.32657/10220/46336>.
- (51) Taylor, C. D.; Neurock, M.; Scully, J. R. First-Principles Investigation of the Fundamental Corrosion Properties of a Model Cu₃₈ Nanoparticle and the (111), (113) Surfaces. *Journal of The Electrochemical Society* **2008**, *155* (8). <https://doi.org/10.1149/1.2926598>.
- (52) Kreizer, V.; Marshakov, I. K.; Tutukina, N. M.; Zartsyn, I. D. The Effect of Oxygen on Copper Dissolution during Cathodic Polarization. **2003**, *39* (1).
- (53) Kreizer, I. V.; Marshakov, I. K.; Tutukina, N. M.; Zartsyn, I. D. Partial Reactions of Copper Dissolution under Cathodic Polarization in Acidic Media. *Protection of Metals* **2004**, *40* (1), 23–25. <https://doi.org/10.1023/B:PROM.0000013107.65745.b0>.
- (54) Cheng, X.; Du, Z.; Ding, Y.; Li, F.; Hua, Z.; Liu, H. Bubble Management for Electrolytic Water Splitting by Surface Engineering: A Review. *Langmuir* **2023**, *39* (48), 16994–17008. <https://doi.org/10.1021/acs.langmuir.3c02477>.
- (55) Andaveh, R.; Darband, G. B.; Maleki, M.; Rouhaghdam, A. S. Superaerophobic/Superhydrophilic Surfaces as Advanced Electrocatalysts for the Hydrogen Evolution Reaction: A Comprehensive Review. *J. Mater. Chem. A* **2022**, *10* (10), 5147–5173. <https://doi.org/10.1039/D1TA10519A>.
- (56) Yokoyama, Y.; Miyazaki, K.; Miyahara, Y.; Fukutsuka, T.; Abe, T. In Situ Measurement of Local pH at Working Electrodes in Neutral pH Solutions by the Rotating Ring-Disk Electrode Technique. *ChemElectroChem* **2019**, *6* (18), 4750–4756. <https://doi.org/10.1002/celec.201900759>.
- (57) McCafferty, E. Thermodynamics of Corrosion: Pourbaix Diagrams. In *Introduction to Corrosion Science*; Springer New York: New York, NY, 2010; pp 95–117. https://doi.org/10.1007/978-1-4419-0455-3_6.
- (58) Ju, X.; Zhu, X.; Chang, Z.; Guo, L.; Liao, C.; Zong, Y.; Li, X.; Zheng, X. Controllable Synthesis of Porous CuO-Cu₂O/rGO Microspheres Composite as High-Performance Electrode Material for Supercapacitors. *Composite Interfaces* **2020**, *27* (9), 845–858. <https://doi.org/10.1080/09276440.2019.1707024>.

- (59) Li, X.; Guo, W.; Huang, H.; Chen, T.; Zhang, M.; Wang, Y. Synthesis and Photocatalytic Properties of CuO Nanostructures. *J. Nanosci. Nanotech.* **2014**, *14* (5), 3428–3432. <https://doi.org/10.1166/jnn.2014.7965>.
- (60) Okoye, P. C.; Azi, S. O.; Qahtan, T. F.; Owolabi, T. O.; Saleh, T. A. Synthesis, Properties, and Applications of Doped and Undoped CuO and Cu₂O Nanomaterials. *Materials Today Chemistry* **2023**, *30*, 101513. <https://doi.org/10.1016/j.mtchem.2023.101513>.
- (61) Li, A.; Zhang, P.; Kan, E.; Gong, J. Wettability Adjustment to Enhance Mass Transfer for Heterogeneous Electrocatalysis and Photocatalysis. *eScience* **2024**, *4* (1), 100157. <https://doi.org/10.1016/j.esci.2023.100157>.
- (62) Darband, G. B.; Aliofkhaezrai, M.; Shanmugam, S. Recent Advances in Methods and Technologies for Enhancing Bubble Detachment during Electrochemical Water Splitting. *Renewable and Sustainable Energy Reviews* **2019**, *114*, 109300. <https://doi.org/10.1016/j.rser.2019.109300>.
- (63) Li, L.; Tian, F.; Qiu, L.; Wu, F.; Yang, W.; Yu, Y. Recent Progress on Ruthenium-Based Electrocatalysts towards the Hydrogen Evolution Reaction. *Catalysts* **2023**, *13* (12), 1497. <https://doi.org/10.3390/catal13121497>.
- (64) Islam, Md. N.; Ahmed, J.; Faisal, M.; Algethami, J. S.; Aoki, K.; Nagao, Y.; Harraz, F. A.; Hasnat, M. A. Efficient Electrocatalytic Hydrogen Evolution Reaction on CuO Immobilized Stainless-Steel Electrode Prepared by the SILAR Method. *ChemistrySelect* **2023**, *8* (28), e202301077. <https://doi.org/10.1002/slct.202301077>.
- (65) Naaz, F.; Sharma, A.; Shahazad, M.; Ahmad, T. Hydrothermally Derived Hierarchical CuO Nanoflowers as an Efficient Photocatalyst and Electrocatalyst for Hydrogen Evolution. *ChemistrySelect* **2022**, *7* (33), e202201800. <https://doi.org/10.1002/slct.202201800>.
- (66) Cai, Z.; Li, A.; Zhang, W.; Zhang, Y.; Cui, L.; Liu, J. Hierarchical Cu@Co-Decorated CuO@Co₃O₄ Nanostructure on Cu Foam as Efficient Self-Supported Catalyst for Hydrogen Evolution Reaction. *Journal of Alloys and Compounds* **2021**, *882*, 160749. <https://doi.org/10.1016/j.jallcom.2021.160749>.
- (67) Wang, X.; Yang, J.; Shi, L.; Gao, M. Surfactant-Free Synthesis of CuO with Controllable Morphologies and Enhanced Photocatalytic Property. *Nanoscale Res Lett* **2016**, *11* (1), 125. <https://doi.org/10.1186/s11671-016-1278-z>.
- (68) Farahbakhsh, N.; Sanjabi, S. Activated Cu/Cu₂O Foam with Ni Nanoparticles for Electrocatalytic Activity Enhancement of Hydrogen Evolution Reaction (HER) in Acidic Media. *Journal of Industrial and Engineering Chemistry* **2019**, *70*, 211–225. <https://doi.org/10.1016/j.jiec.2018.10.018>.
- (69) Wang, M.; Cheng, X.; Ni, Y. Simple Vapor–Solid-Reaction Route for Porous Cu₂O Nanorods with Good HER Catalytic Activity. *Dalton Trans.* **2019**, *48* (3), 823–832. <https://doi.org/10.1039/C8DT03572E>.
- (70) Tian, J.; Hu, Y.; Lu, W.; Zhu, J.; Liu, X.; Shen, J.; Wang, G.; Schroers, J. Dealloying of an Amorphous TiCuRu Alloy Results in a Nanostructured Electrocatalyst for Hydrogen Evolution Reaction. *Carbon Energy* **2023**, *5* (8), e322. <https://doi.org/10.1002/cey2.322>.
- (71) Jia, Z.; Nomoto, K.; Wang, Q.; Kong, C.; Sun, L.; Zhang, L.-C.; Liang, S.-X.; Lu, J.; Kruzic, J. J. A Self-Supported High-Entropy Metallic Glass with a Nanosponge Architecture for Efficient Hydrogen Evolution under Alkaline and Acidic Conditions.

Advanced Functional Materials **2021**, *31* (38), 2101586.
<https://doi.org/10.1002/adfm.202101586>.

Publication III – Supporting Information

Table S1: The Tafel slope and overpotential η at 10 mA cm^{-2} of some reported electrocatalysts for HER.

Catalysts	Tafel slope (mV dec^{-1})	η (mV vs. RHE) at $J = 10 \text{ mA cm}^{-2}$	Stability	Electrolyte	Ref.
Nanorods patterned $\text{Pt}_{57.5}\text{Cu}_{14.7}\text{Ni}_{5.3}\text{P}_{22.5}$ BMG	42	150	1000 cycles	0.5 M H_2SO_4	This work
Nanowires patterned $\text{Pd}_{40}\text{Ni}_{10}\text{Cu}_{30}\text{P}_{20}$ MG	90.7	113	-	0.5 M H_2SO_4	1
Pristine Pt_3Te_4	49	46	-	0.5 M H_2SO_4	2
200 nm-thick Pt film	44.6	64.7	-	0.5 M H_2SO_4	3
Polycrystalline Pt electrode	31	73	-	0.5 M H_2SO_4	4
Pt/C	30	84	-	0.5 M H_2SO_4	4
Pt sheet	30	59	-	0.5 M H_2SO_4	5
Pure Pt	38	-	-	0.5 M H_2SO_4	6
$\text{Ir}_{25}\text{Ni}_{33}\text{Ta}_{42}$ MG film	35	99	1000 cycles	0.5 M H_2SO_4	7
Oxide-derived nanorods $\text{Pd}_{40.5}\text{Ni}_{40.5}\text{Si}_{4.5}\text{P}_{14.5}$ MG	42.6	36	40000 sec	0.5 M H_2SO_4	8
$\text{Pd}_{40.5}\text{Ni}_{40.5}\text{Si}_{4.5}\text{P}_{14.5}$ MG plate	73.6	138	-	0.5 M H_2SO_4	8
$\text{Ni}_{20}\text{Fe}_{20}\text{Mo}_{10}\text{Co}_{35}\text{Cr}_{15}$ high entropy alloy	41	107	8 hr	0.5 M H_2SO_4	9
$\text{Pd}_{20}\text{Pt}_{20}\text{Cu}_{20}\text{Ni}_{20}\text{P}_{20}$ high entropy MG	44.6	62	100 hr	0.5 M H_2SO_4	10
$\text{Ni}_{4.5}\text{Fe}_{4.5}\text{S}_8$ in bulk	72	280	1000 cycles	0.5 M H_2SO_4	11
PtCu/ WO_3 @CF	45.9	41	2000 cycles	0.5 M H_2SO_4	12
CuO-modified stainless steel	52	154	500 cycles	0.01 M H_2SO_4	13
Cu/ Cu_2O foam with Ni nanoparticles	50	290	100 cycles	0.1 M H_2SO_4	14
Hierarchical CuO nanoflowers	67.4	1020	50 cycles	0.5 M H_2SO_4	15

Porous Cu ₂ O nanorods	106	184	20 hr	1.0M KOH	16
-----------------------------------	-----	-----	-------	----------	----

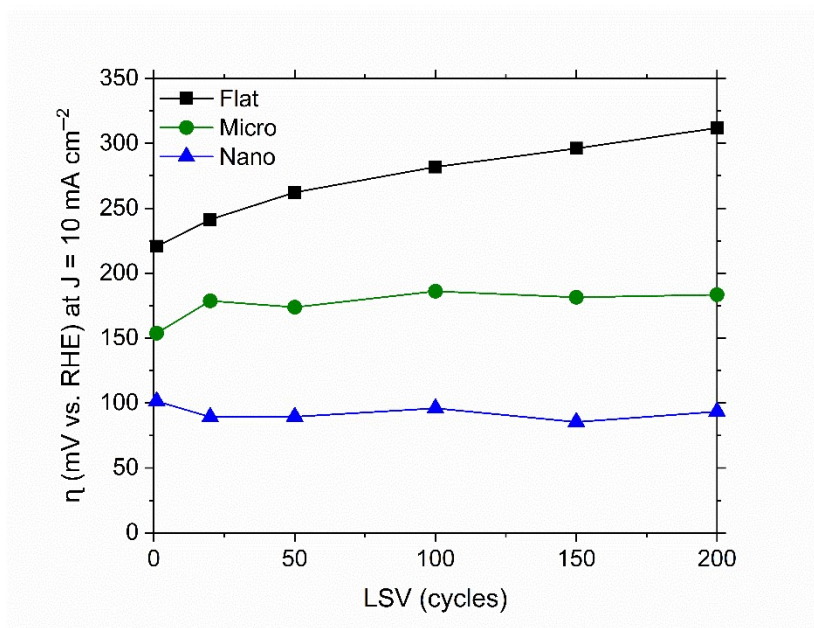


Figure S1: Additional stability tests comparing the overpotential η (mV vs. RHE) at $J = 10 \text{ mA cm}^{-2}$ of flat, micro-patterned and nano-patterned samples up to 200 LSV cycles.

Additional stability test (experimental method):

For additional electrochemical measurements, a Solartron XM ModuLab potentiostat was used in combination with a three-electrode cell. The samples were used as working electrode, and silver chloride (Ag|AgCl ($E(\text{Ag}|\text{AgCl}) = 0.197 \text{ V vs. SHE}$)) was used as reference electrode. Pt wire was used as counter electrode to complete the three-electrode cell setup. The samples were submerged in 0.5 M H₂SO₄ solution, and the open circuit potential (OCP) was monitored until it reached a steady state. Subsequently, linear sweep voltammetry (LSV) was performed from -1 V (vs. Ag|AgCl) to 0 V (vs. Ag|AgCl) with a scan rate of 0.02 V/s for 200 cycles on fresh flat, micro-patterned, and nano-patterned samples.

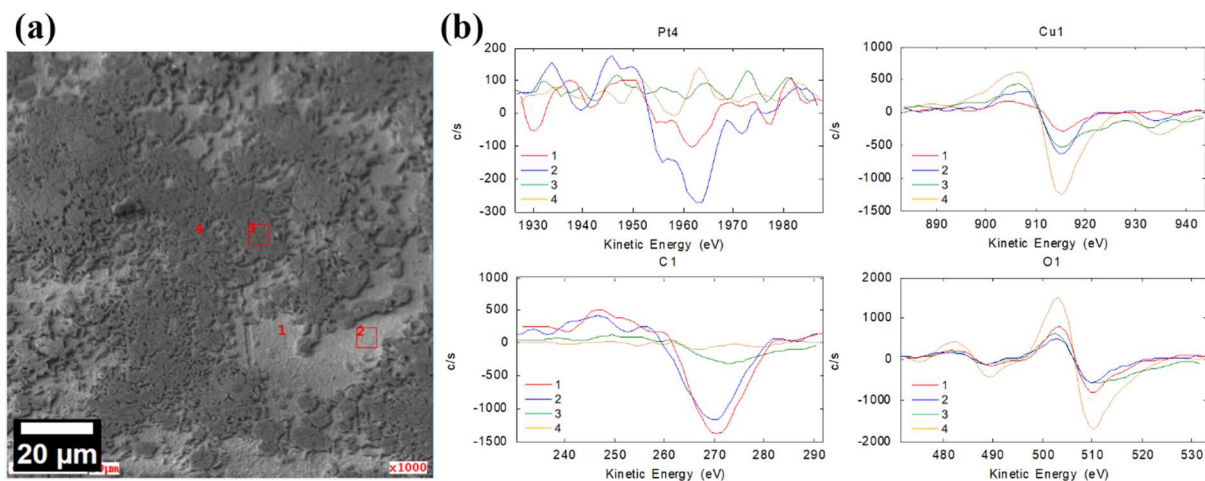


Figure S2: AES analysis of the Nano.1000cycle sample. (a) The representative SEM image with markers of selected area and (b) AES spectra of Pt, Cu, C, and O.

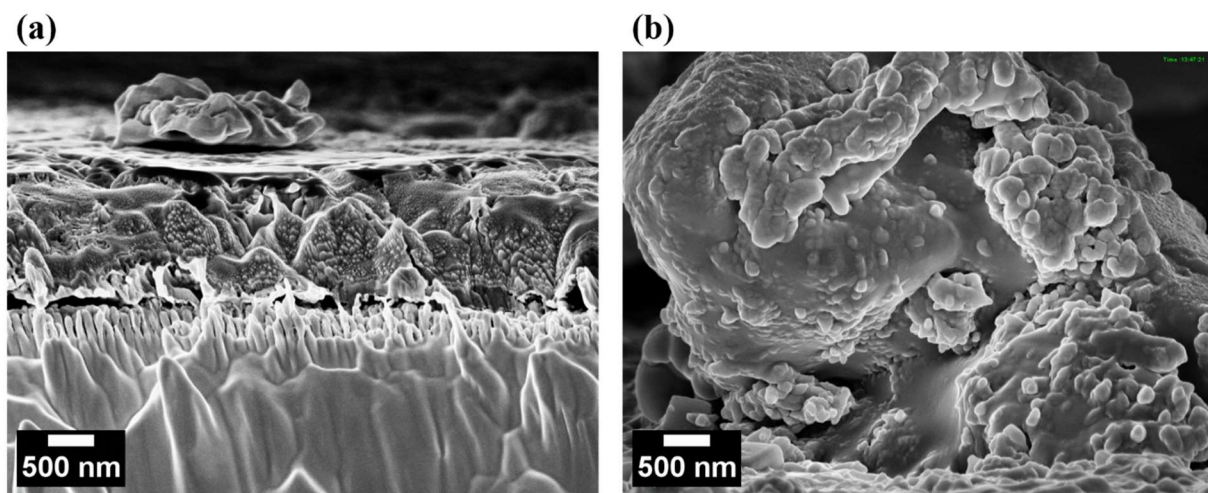


Figure S3: SEM images of agglomerated CuO particles on top of the deposited CuO layer. (a) A CuO particle is deposited on the CuO layer. (b) A detailed image of the CuO particle.

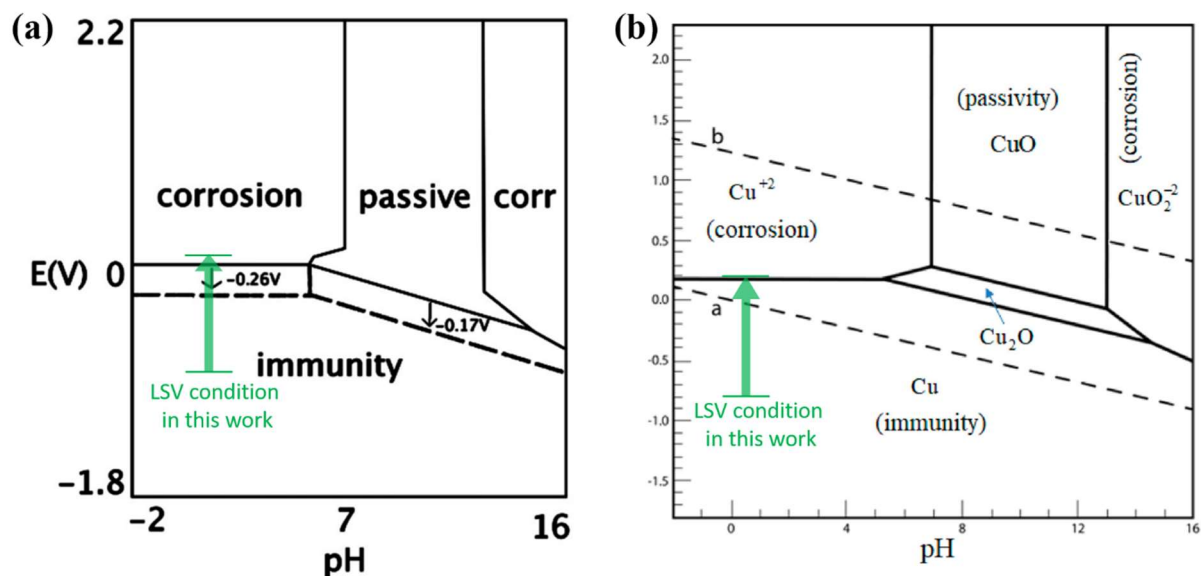


Figure S4: Modified Pourbaix diagrams for Cu with green arrows marking the experimental condition. (a) Cu nanomaterials have a negative shift of the dissolution balance potential leading to a reduction in the immunity area and an expansion of both the passivity and corrosion areas. Reproduced with permission from Taylor et al.¹⁷ (b) A Pourbaix diagram features the oxidation reactions ($2Cu + H_2O \rightarrow Cu_2O + 2H^+ + 2e^-$) at electrode potentials above the “a” line for hydrogen evolution. Reproduced with permission from Hamidah et al.¹⁸

References

- (1) Yan, Y.; Wang, C.; Huang, Z.; Fu, J.; Lin, Z.; Zhang, X.; Ma, J.; Shen, J. Highly Efficient and Robust Catalysts for the Hydrogen Evolution Reaction by Surface Nano Engineering of Metallic Glass. *J. Mater. Chem. A* **2021**, *9* (9), 5415–5424. <https://doi.org/10.1039/D0TA10235K>.
- (2) Boukhvalov, D. W.; Cheng, J.; D’Olimpio, G.; Bocquet, F. C.; Kuo, C.-N.; Sarkar, A. B.; Ghosh, B.; Vobornik, I.; Fujii, J.; Hsu, K.; Wang, L.-M.; Azulay, O.; Daptary, G. N.; Naveh, D.; Lue, C. S.; Vorokhta, M.; Agarwal, A.; Zhang, L.; Politano, A. Unveiling the Mechanisms Ruling the Efficient Hydrogen Evolution Reaction with Mitrofanovite Pt_3Te_4 . *J. Phys. Chem. Lett.* **2021**, *12* (35), 8627–8636. <https://doi.org/10.1021/acs.jpcclett.1c01261>.
- (3) Bae, D.; Park, K.; Kwon, H.; Won, D.; Ling, N.; Baik, H.; Yang, J.; Park, H. J.; Cho, J.; Yang, H.; Jeong, S.; Cho, S. Mitrofanovite, Layered Platinum Telluride, for Active Hydrogen Evolution. *ACS Appl. Mater. Interfaces* **2021**, *13* (2), 2437–2446. <https://doi.org/10.1021/acsami.0c16098>.
- (4) Scremin, J.; Joviano Dos Santos, I. V.; Hughes, J. P.; García-Miranda Ferrari, A.; Valderrama, E.; Zheng, W.; Zhong, X.; Zhao, X.; Sartori, E. J. R.; Crapnell, R. D.; Rowley-Neale, S. J.; Banks, C. E. Platinum Nanoparticle Decorated Vertically Aligned Graphene Screen-Printed Electrodes: Electrochemical Characterisation and Exploration towards the Hydrogen Evolution Reaction. *Nanoscale* **2020**, *12* (35), 18214–18224. <https://doi.org/10.1039/D0NR04336B>.
- (5) Wei, Y.; Fu, J.; Song, H.; Zhang, B.; Pi, C.; Xia, L.; Zhang, X.; Gao, B.; Zheng, Y.; Chu, P. K. N-Doped TiO_2 Nanotube Arrays with Uniformly Embedded Co_xP Nanoparticles for

- High-Efficiency Hydrogen Evolution Reaction. *RSC Adv.* **2019**, *9* (21), 11676–11682. <https://doi.org/10.1039/C9RA01184F>.
- (6) Devendra, B. K.; Praveen, B. M.; Tripathi, V. S.; Nagaraju, D. H.; Nayana, K. O. Hydrogen Evolution Reaction by Platinum Coating. *Iran J Sci Technol Trans Sci* **2021**, *45* (6), 1993–2000. <https://doi.org/10.1007/s40995-021-01220-2>.
- (7) Wang, Z.-J.; Li, M.-X.; Yu, J.-H.; Ge, X.-B.; Liu, Y.-H.; Wang, W.-H. Low-Iridium-Content IrNiTa Metallic Glass Films as Intrinsically Active Catalysts for Hydrogen Evolution Reaction. *Advanced Materials* **2020**, *32* (4), 1906384. <https://doi.org/10.1002/adma.201906384>.
- (8) Gao, S.; Jia, J.; Chen, S.; Luan, H.; Shao, Y.; Yao, K. Oxide-Derived Nanostructured Metallic-Glass Electrodes for Efficient Electrochemical Hydrogen Generation. *RSC Adv.* **2017**, *7* (43), 27058–27064. <https://doi.org/10.1039/C7RA02954C>.
- (9) Zhang, G.; Ming, K.; Kang, J.; Huang, Q.; Zhang, Z.; Zheng, X.; Bi, X. High Entropy Alloy as a Highly Active and Stable Electrocatalyst for Hydrogen Evolution Reaction. *Electrochimica Acta* **2018**, *279*, 19–23. <https://doi.org/10.1016/j.electacta.2018.05.035>.
- (10) Jia, Z.; Nomoto, K.; Wang, Q.; Kong, C.; Sun, L.; Zhang, L.-C.; Liang, S.-X.; Lu, J.; Kruzic, J. J. A Self-Supported High-Entropy Metallic Glass with a Nanosponge Architecture for Efficient Hydrogen Evolution under Alkaline and Acidic Conditions. *Advanced Functional Materials* **2021**, *31* (38), 2101586. <https://doi.org/10.1002/adfm.202101586>.
- (11) Konkana, B.; Junge Puring, K.; Sinev, I.; Piontek, S.; Khavryuchenko, O.; Dürholt, J. P.; Schmid, R.; Tüysüz, H.; Muhler, M.; Schuhmann, W.; Apfel, U.-P. Pentlandite Rocks as Sustainable and Stable Efficient Electrocatalysts for Hydrogen Generation. *Nat Commun* **2016**, *7* (1), 12269. <https://doi.org/10.1038/ncomms12269>.
- (12) Liu, L.; Wang, Y.; Zhao, Y.; Wang, Y.; Zhang, Z.; Wu, T.; Qin, W.; Liu, S.; Jia, B.; Wu, H.; Zhang, D.; Qu, X.; Chhowalla, M.; Qin, M. Ultrahigh Pt-Mass-Activity Hydrogen Evolution Catalyst Electrodeposited from Bulk Pt. *Advanced Functional Materials* **2022**, *32* (20), 2112207. <https://doi.org/10.1002/adfm.202112207>.
- (13) Islam, Md. N.; Ahmed, J.; Faisal, M.; Algethami, J. S.; Aoki, K.; Nagao, Y.; Harraz, F. A.; Hasnat, M. A. Efficient Electrocatalytic Hydrogen Evolution Reaction on CuO Immobilized Stainless-Steel Electrode Prepared by the SILAR Method. *ChemistrySelect* **2023**, *8* (28), e202301077. <https://doi.org/10.1002/slct.202301077>.
- (14) Farahbakhsh, N.; Sanjabi, S. Activated Cu/Cu₂O Foam with Ni Nanoparticles for Electrocatalytic Activity Enhancement of Hydrogen Evolution Reaction (HER) in Acidic Media. *Journal of Industrial and Engineering Chemistry* **2019**, *70*, 211–225. <https://doi.org/10.1016/j.jiec.2018.10.018>.
- (15) Naaz, F.; Sharma, A.; Shahzad, M.; Ahmad, T. Hydrothermally Derived Hierarchical CuO Nanoflowers as an Efficient Photocatalyst and Electrocatalyst for Hydrogen Evolution. *ChemistrySelect* **2022**, *7* (33), e202201800. <https://doi.org/10.1002/slct.202201800>.
- (16) Wang, M.; Cheng, X.; Ni, Y. Simple Vapor–Solid-Reaction Route for Porous Cu₂O Nanorods with Good HER Catalytic Activity. *Dalton Trans.* **2019**, *48* (3), 823–832. <https://doi.org/10.1039/C8DT03572E>.

- (17) Taylor, C. D.; Neurock, M.; Scully, J. R. First-Principles Investigation of the Fundamental Corrosion Properties of a Model Cu₃₈ Nanoparticle and the (111), (113) Surfaces. *Journal of The Electrochemical Society* **2008**, *155* (8). <https://doi.org/10.1149/1.2926598>.
- (18) Hamidah, I.; Solehudin, A.; Hamdani, A.; Hasanah, L.; Khairurrijal, K.; Kurniawan, T.; Mamat, R.; Maryanti, R.; Nandiyanto, A. B. D.; Hammouti, B. Corrosion of Copper Alloys in KOH, NaOH, NaCl, and HCl Electrolyte Solutions and Its Impact to the Mechanical Properties. *Alexandria Engineering Journal* **2021**, *60* (2), 2235–2243. <https://doi.org/10.1016/j.aej.2020.12.027>.

Appendix

1. Declaration on the use of AI-based tools in this dissertation

Object	Share of AI (in %)	Tool/version	Annotation	Reference to prompting
linguistic revision	5	Grammarly Premium	Improve linguistic readability (i.e. orthographic, grammatical and stylistic help)	oc.unileoben.ac.at/myprompts
linguistic revision	2.5	QuillBot Free	Paraphrasing	oc.unileoben.ac.at/myprompts
linguistic revision	2.5	DeepL Free	Paraphrasing	oc.unileoben.ac.at/myprompts

2. Manual of the upgraded TPF apparatus described in section 4.3.2.

Manual of Heating Plates Add-ons for Zwick Z100 Design for Thermoplastic Forming (TPF)

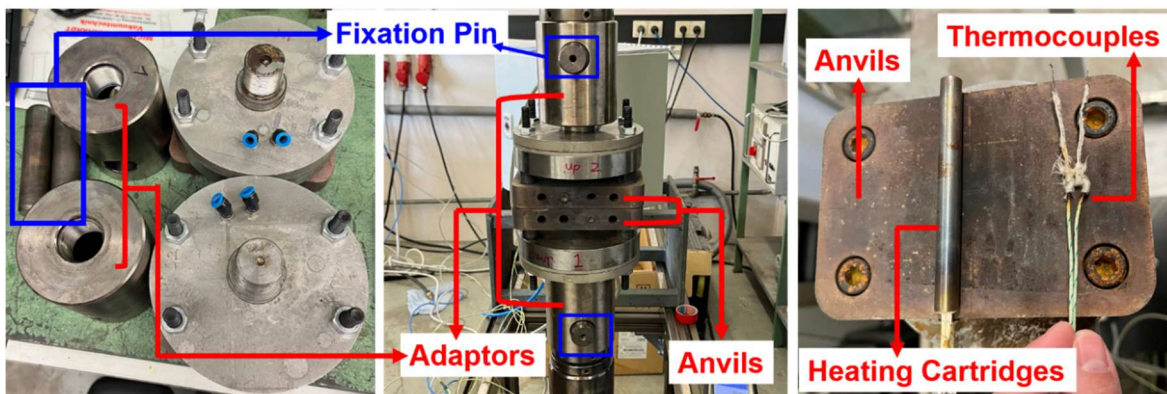


Author: Fei-Fan Cai

Email: feifan.cai.tec@gmail.com

Components

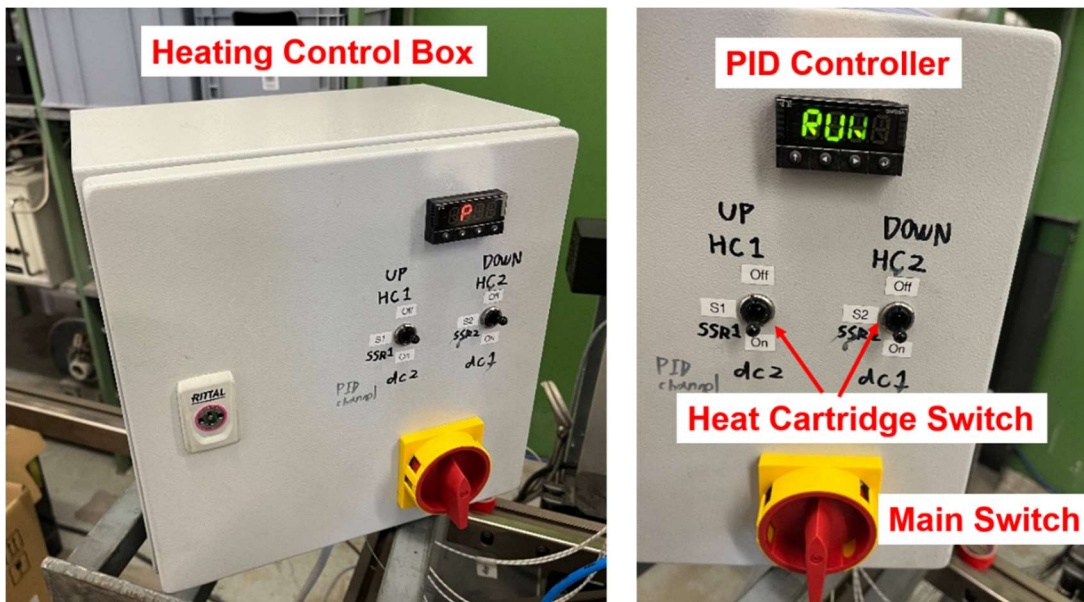
1. Anvils / Adaptors & Fixation Pins / Heating Elements



2. Water-Cooling System



3. Heating Control Elements

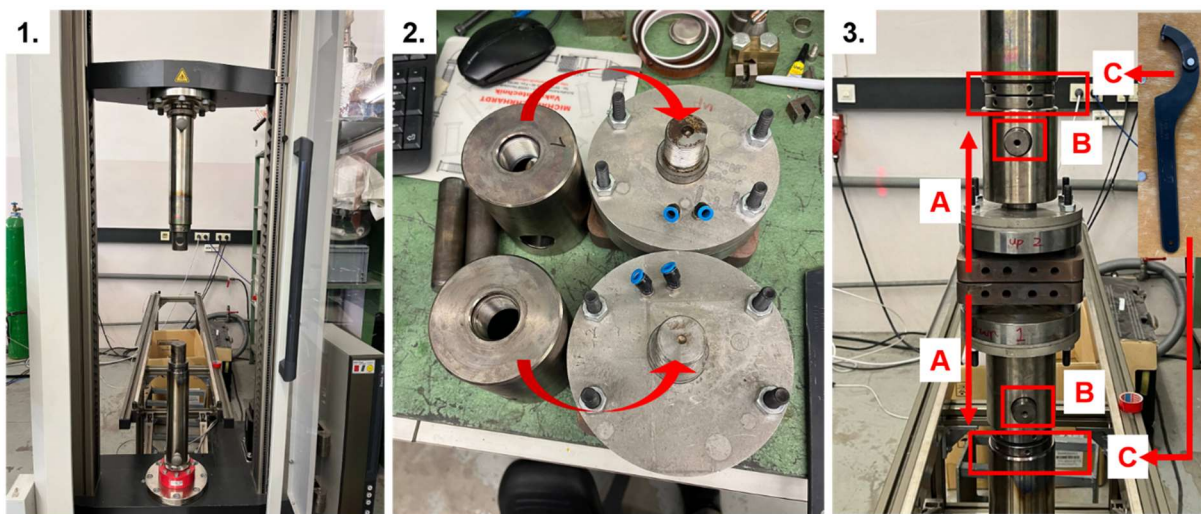


Caution

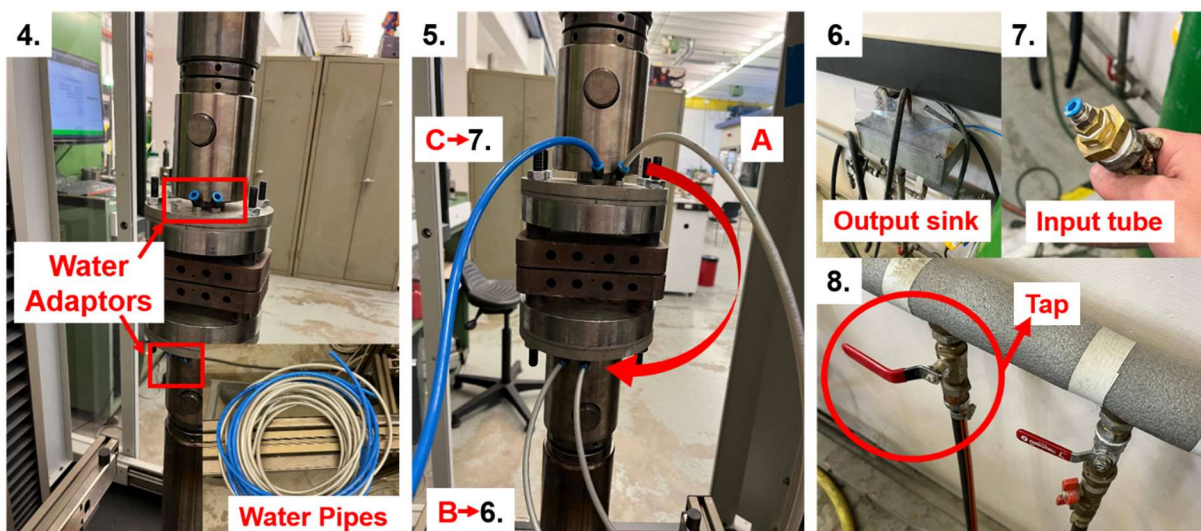
1. The user must have the proper training for Zwick Z100 by Anton Hohenwarter / Peter Kutlesa / the person in charge before working with this Heating Plate add-on.
2. Always turn on the water-cooling system before heating up the plate.
3. Always check if there is a leak from the water-cooling system.
4. The heating cartridges and the thermocouples must be fitted into the reserved holes before switching on the heating. Never start heating before fitting heating cartridges!
5. The setup is designed for a maximum temperature of 500°C.
6. Even though the Zwick Z100 is capable of 100kN, the maximum force of 90kN is recommended. (Add-on its own has weight)
7. Be careful that anvils and water-cooling plates have sharp edges. Don't cut your hands!
8. Adaptors & fixation pins are stock components from Zwick Z100 and do not belong to this add-on. Please return them back to the correct place so others can find them!
9. After the removal of the water-cooling add-on, the water tube connected to the tap needs to be put into the sink or bucket because the water tube will release a large amount of water even if the tap is closed.

Installation

1. Make sure the Zwick Z100 is in the correct configuration and there is enough space between the upper and lower shafts to install the add-on.
 2. Find the adapters and fixation pins. Install adapters on the heating plate add-ons.
 3. A. Fit the heating plate add-ons to the shaft.
B. Use the fixation pins to hold the add-ons.
C. Rotate the locking rings to apply pressure on the fixations pins to fix the add-ons.
- P.S: Please make sure the add-ons are install in the correct direction (water adaptors on the back!) and both two anvils are aligned to each other.

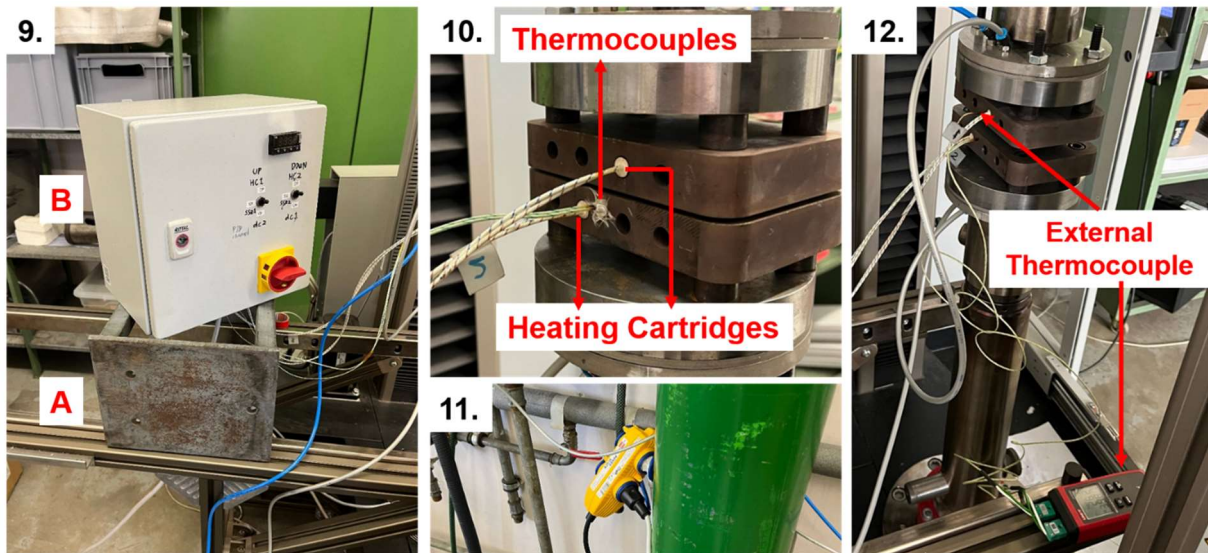


4. There are three water pipes to install on water adaptors, one in blue, two in gray.



5. Connect the **short gray** tube between the upper and lower water-cooling plates as shown in **5.A**.

6. Connect the **long gray** tube to the lower cooling plate, as shown in **5.B**, and fix the other end of the tube to the sink.
7. Connect the **blue** tube to the upper cooling plate, as shown in **5.C**, and connect the other end of the tube to the freshwater input tube.
8. Turn on the water tap to check if the water-cooling system works properly and inspect if there is any leak.



9. Place the bottom rack on the frame as shown in **9.A** and then place the heating control box on the bottom rack as shown in **9.B**.
10. Fit **heating cartridge 1** to the **upper anvil** and **heating cartridge 2** to the **lower anvil** (larger holes). Fit the system thermocouples (both) into the small hole of the **lower anvil**.
11. Connect the plug of place the heating control box to the power socket.
12. Because the PID controller has only one input source (thermocouple) for two outputs (heating cartridge), it is recommended to add an external thermocouple to monitor the upper anvil (fit into the small hole) and another one for testing the sample temperature.

Operation

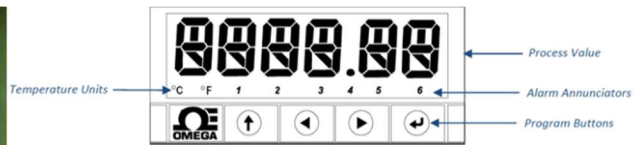
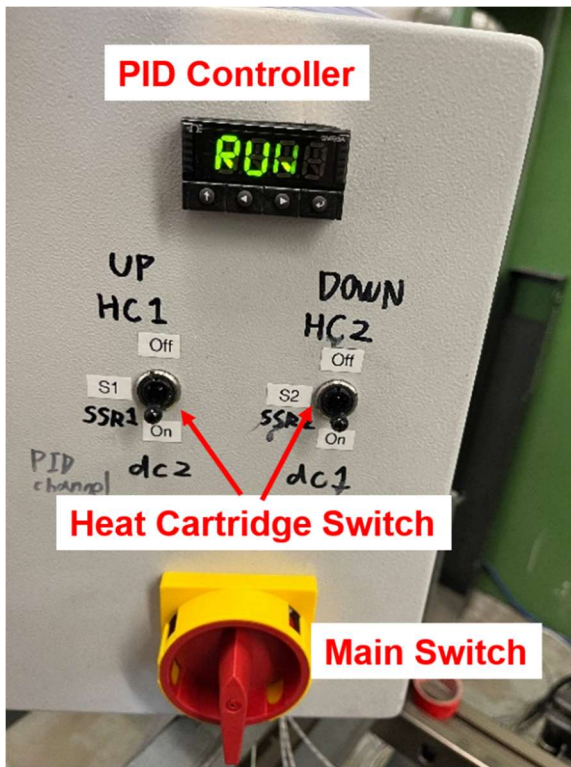


Figure 8 – PLATINUM Series Displays (CN8DPt and CN8EPT Shown)

4.3 Level 1 Menu

- INIT** Initialization Mode: These settings are rarely changed after initial setup. They include transducer types, calibration, etc. These settings can be password-protected.
- PRoG** Programming Mode: These settings are frequently changed. They include Set points, Control Modes, Alarms, etc. These settings can be password-protected.
- oPER** Operating Mode: This mode allows users to switch between Run Mode, Standby Mode, Manual Mode, etc.

4.4 Circular Flow of Menus

The following diagram shows how to use the LEFT and RIGHT buttons to navigate around a menu.

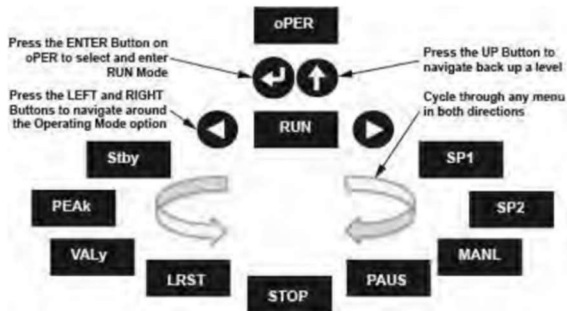


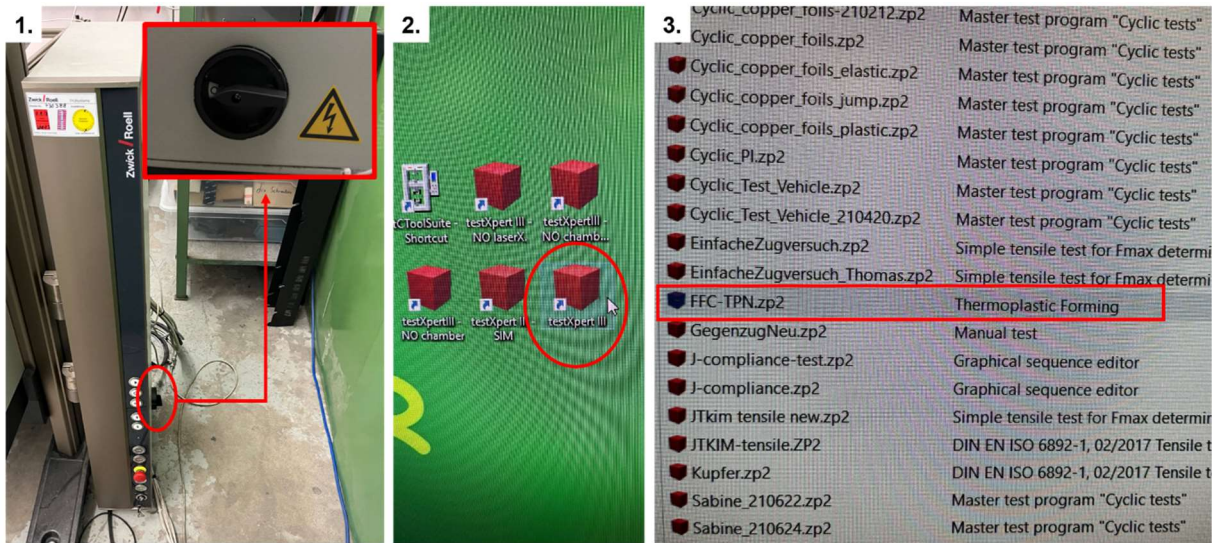
Figure 9 – Circular Flow of Menus.

1. Switch on the device with Main Switch and wait PID controller to be ready.
2. Select **oPER** mode → Select **SP1** to adjust setting temperature and press enter
3. Before start the heating procedure, check if everything working properly. Ex: if water-cooling is ON and there is no leak? Do heating cartridges and thermocouples are fitted in the correct place?
4. Switch on Heat Cartridge Switches (**HC1** & **HC2**) and select **RUN** to start heating.
5. Monitor the temperature from time to time, also with the external thermocouples.
6. **Important:** The setting temperature **is not** equal to the sample temperature! Hence, it is necessary to calibrate / adjust your setting temperature to achieve your sample temperature. Ideally, the calibration should be done as similar as your experiments and before each experiment. Also consider the following factors: any materials and the gap between two anvils, apply some force to have better contact for heat conduction.
7. Run your experiments; see section **Zwick Control with Software**.
8. After your experiments, switch off the Heat Cartridge Switches. Select **PAUS** in PID.
- 9a. If you want to keep the add-ons on the machine, switch off the Main Switch.

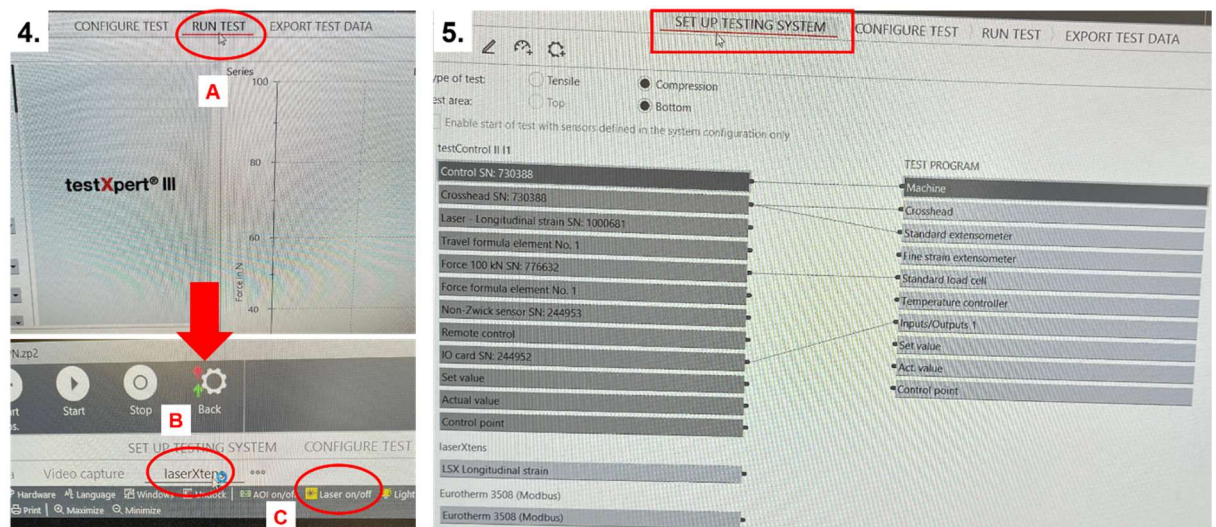
9b. If you want to remove the add-ons, wait until the anvils are below 40°C. Removing order: Heating Control Box (+ cartridges & thermocouples) → Water pipes → Water-cooling plates (Anvils) / Adaptors & Fixation Pins.

Zwick Control with Software

1. Switch on the Zwick Z100 (on the side of *testControl II control electronics*).
2. Open the **testXpert III** software.
3. Select and open the testing program **FFC-TPN.zp2** (Thermoplastic Forming).



4. Turn off the Laser to protect eyes (4.A click **RUN TEST** → 4.B click **laserXtens** → 4.C click **Laser on/off**).
5. Click **SET UP TESTING SYSTEM** to check if the machine configuration is correct.

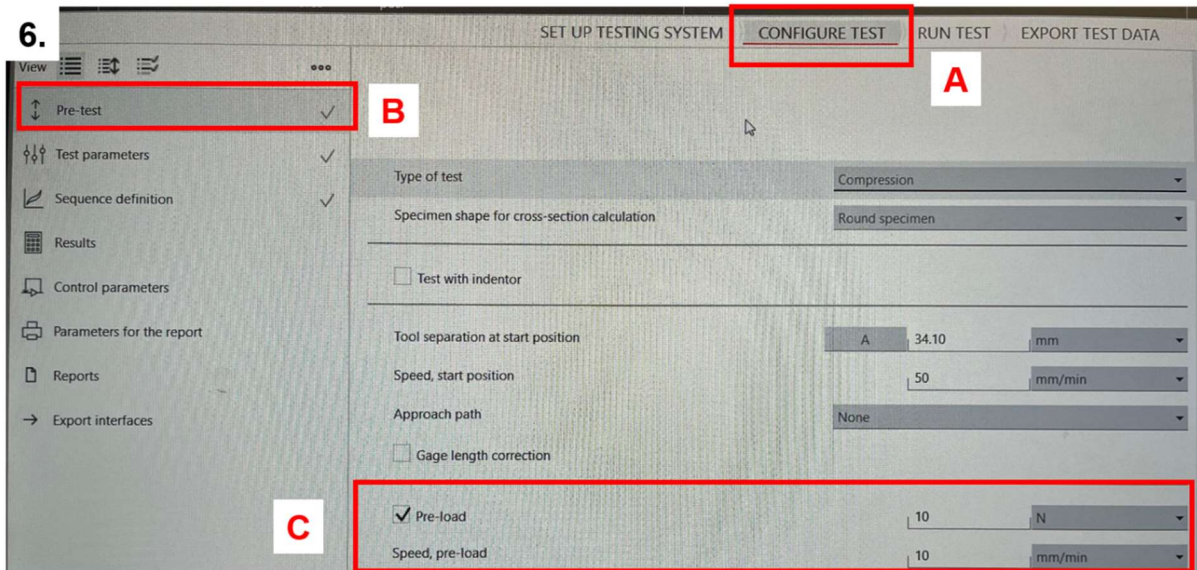


6. Click **CONFIGURE TEST** (6.A) to program the experimental parameters

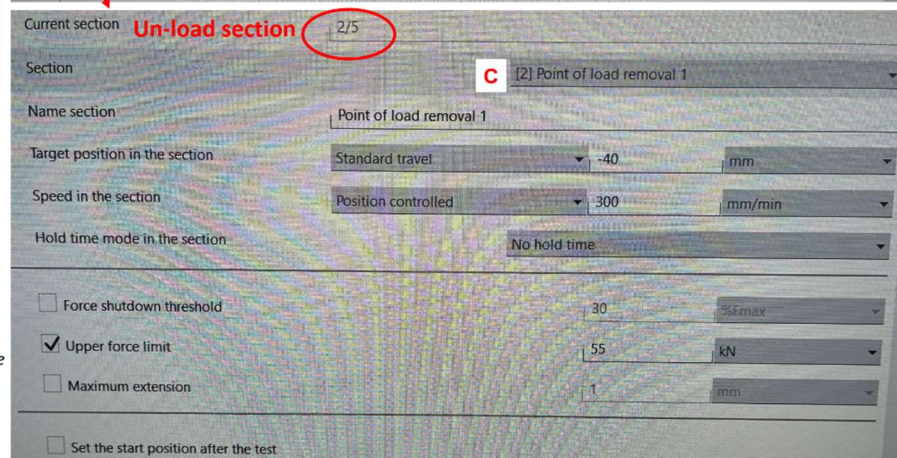
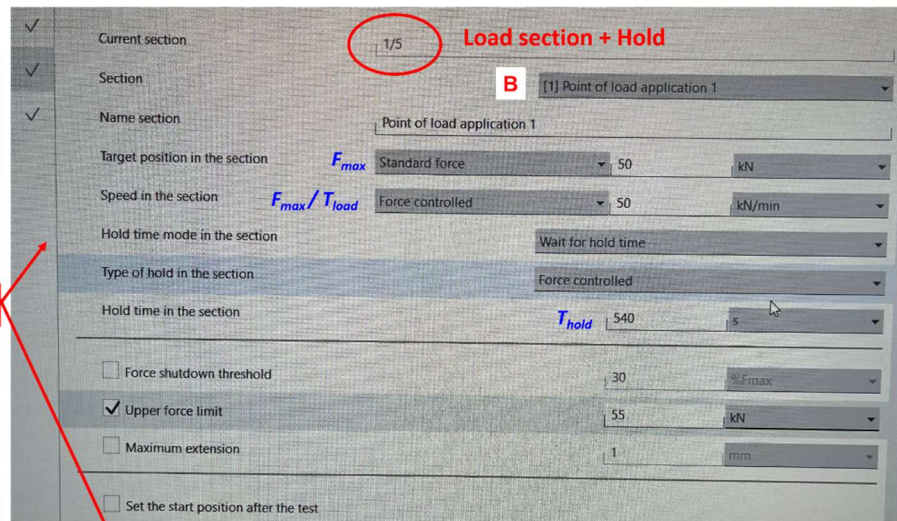
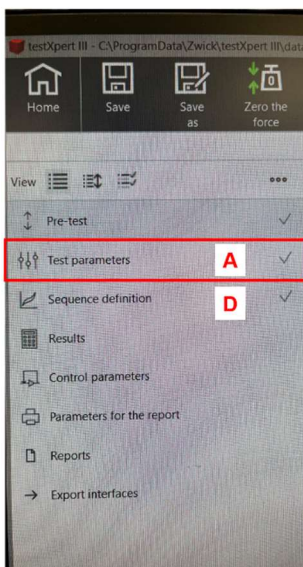
Pre-test (6.B): How anvils approach the sample before the experiment starts.

Normally, only **Pre-load** and **Speed, preload** are relevant (6.C).

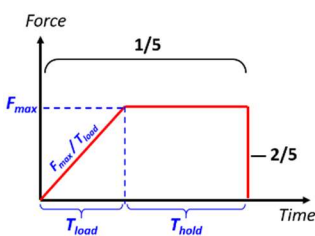
Other parameters can stay the same as Figure 6.



7.



Preset:



7. Click **Test parameters (7.A)** to set experimental parameters (still in **CONFIGURE TEST** page) for two sections. Go to **7.B** (1/5 section) to program the force, load rate, and holding time. Go to **7.C** (2/5 section) to program the un-loading step.
PS: If you want to edit the processing path (ex: multiple loading-unloading steps), go to **7.D Sequence definition**.